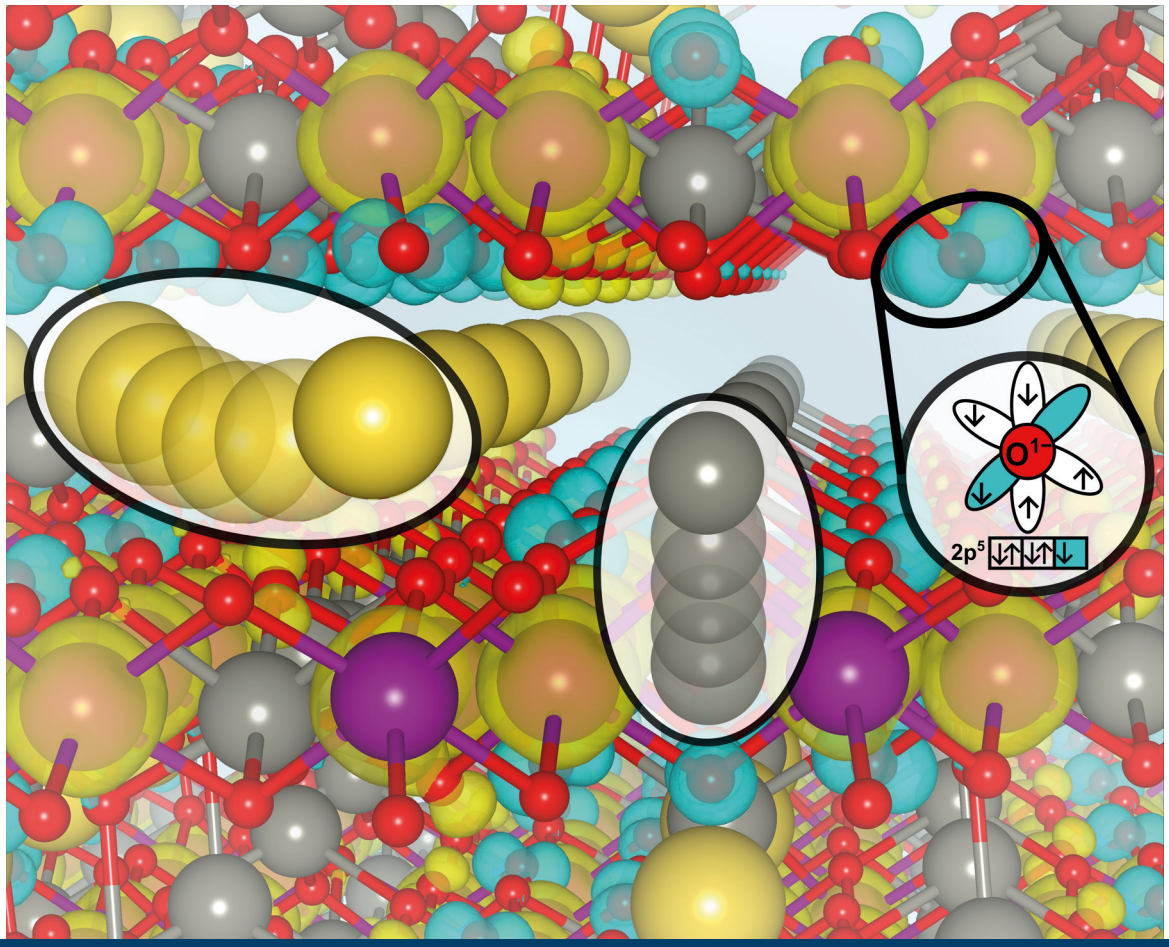

Ab Initio-based large-scale Atomistic Simulations of Cathode Materials for Secondary Batteries: From Computational Methodologies to Applications towards improved Structural and Chemical Stability

Konstantin Köster

Energie & Umwelt / Energy & Environment
Band / Volume 699
ISBN 978-3-95806-898-8

UNIVERSITY OF TWENTE.

JÜLICH Forschungszentrum

Schriften des Forschungszentrums Jülich
Reihe Energie & Umwelt / Energy & Environment Band / Volume 699

Forschungszentrum Jülich GmbH
Institute of Energy Materials and Devices (IMD)
Werkstoffsynthese und Herstellungsverfahren (IMD-2)

Ab Initio-based large-scale Atomistic Simulations of Cathode Materials for Secondary Batteries: From Computational Methodologies to Applications towards improved Structural and Chemical Stability

Konstantin Köster

Schriften des Forschungszentrums Jülich
Reihe Energie & Umwelt / Energy & Environment Band / Volume 699

ISSN 1866-1793 ISBN 978-3-95806-898-8

Bibliografische Information der Deutschen Nationalbibliothek.
Die Deutsche Nationalbibliothek verzeichnet diese Publikation in der
Deutschen Nationalbibliografie; detaillierte Bibliografische Daten
sind im Internet über http://dnb.d-nb.de abrufbar.

Herausgeber und Vertrieb:	Forschungszentrum Jülich GmbH Zentralbibliothek, Verlag 52425 Jülich Tel.: +49 2461 61-5368 Fax: +49 2461 61-6103 zb-publikation@fz-juelich.de www.fz-juelich.de/zb
Umschlaggestaltung:	Grafische Medien, Forschungszentrum Jülich GmbH
Druck:	Grafische Medien, Forschungszentrum Jülich GmbH
Copyright:	Forschungszentrum Jülich 2026

Schriften des Forschungszentrums Jülich
Reihe Energie & Umwelt / Energy & Environment, Band / Volume 699

(Diss. University of Twente, 2026)

ISSN 1866-1793
ISBN 978-3-95806-898-8

ISBN (print): 978-90-365-7040-4 (University of Twente)
ISBN (digital): 978-90-365-7041-1 (University of Twente)

Vollständig frei verfügbar über das Publikationsportal des Forschungszentrums Jülich (JuSER)
unter www.fz-juelich.de/zb/openaccess.

SUMMARY

Transformation towards renewable energy sources and reduction of greenhouse gas emissions to mitigate climate change are among the most severe challenges of humankind today. Energy storage bears the potential to enable this transformation when applied as grid energy storage, which could enhance the utilization of renewable energy sources. Electrification of the transport sector by energy storage can potentially further reduce greenhouse gas emissions. Secondary batteries are promising energy-storage systems for these purposes and lithium-ion batteries (LIBs) are already applied. However, LIBs often rely on critical raw materials such as cobalt, raising sustainability concerns for growing larger-scale application. To partially overcome these issues, materials that do not contain critical raw materials are researched. Under these sustainability measures sodium-ion batteries (SIBs) are discussed as a promising alternative to LIBs due to the high abundance of sodium and the possibility to reduce the critical/costly elements in batteries. For both of these battery technologies, the cathode materials dominate their electrochemical performance and layered oxides are among the most promising materials. In general, layered oxides allow for tailored tuning, raising the demand for rational design approaches by in-depth characterisation and efficient pre-selection of interesting compositions. This can be achieved by first principles simulation studies on the atomistic scale that usually involve three simulation steps, namely configuration selection, geometry relaxation/evolution, and electronic structure calculation. In this thesis, computational techniques to study cathode materials are discussed and for each of these simulation steps relevant methods are developed, tested, and applied. The last chapter describes several practical examples how computational studies, in concert with experimental results, can advance the understanding of cathode materials for LIBs and SIBs. The contents of the chapters are as follows:

In Chapter 2 the first simulation step of configuration selection is discussed. This problem arises due to partial occupations on crystal sites that need to be described by just full occupancies to apply further simulation steps. For complex materials (many substituents) configurational optimization is a formidable combinatorial problem. First, it is highlighted that the relative energy of various configurations in ionic crystals such as layered oxide cathodes can be efficiently assessed in terms of simple pairwise electrostatic interactions. Due to the pairwise character of electrostatic energies, an optimization problem with pre-computed energy terms can be formulated. This implies that there is a computationally inexpensive proxy to obtain low(est) energy configurations for follow-up simulations by optimizing the total electrostatic energy. The optimization is enabled by implementation of various efficient Monte Carlo-based and Genetic Algorithm-based optimizers and also an interface to external solvers is pointed-out. These implementations ultimately result in a new code, GOAC (Global Optimization of Atomistic Configurations by Coulomb), that is significantly faster than existing software for the given problem. Application to multiple extremely large configurational

optimization problems proves the efficiency of the code, providing a valuable tool for computational material, and especially cathode material, research.

Chapter 3 discusses the selection of a structural model but with a focus on stacking phase. Layered oxide cathodes in SIBs show various phases in terms of the stacking sequence and relative shift of the layers towards each other. These phases significantly influence their electrochemical performance such as capacity and/or sodium diffusivity. Moreover, transitions between the phases happen during operation of the cathode materials, causing degradation and capacity fading. However, the phase stability and phase transitions can be optimized by tuning the cathode composition and therefore it would be highly desirable to relate compositions to the associated most stable stacking phase. Here, it is shown that comparing the electrostatic energies of different stacking phases at their respective lowest energy configurations can be an efficient *ab initio* predictor of phase stability. In order to increase the predictive power of this computationally inexpensive approach, electrostatic parameters such as lattice parameters and inter-layer distances are optimized to maximize the correlation of relative phase energies to density functional theory (DFT) calculations. The established prediction scheme allows for high-throughput studies while still being fully *ab initio* and achieves a prediction accuracy of 80 % on experimental data. Moreover, the method allows to capture ordering phenomena (transition metals (TM) and sodium) and to consider all kinds of stacking phases, e.g., O1, O2, O3, P2, P3, OP2, OP4. Therefore, the method is useful to design novel cathode materials with tailored phase stabilities for further experimental or simulational studies.

In Chapter 4 the phase stability in layered oxide cathodes for SIBs is studied further. Next to the thermodynamic phase stability also the process and mechanism of phase transitions (kinetics) is important to understand. In order to simulate phase transitions, a Coulomb-Buckingham potential is fitted to reproduce interatomic interactions in the Na_xCoO_2 cathode material. An extensive dataset of DFT reference calculations is created and the potential is fitted to energies and forces. As a novelty, the potential was fitted as a function of sodium-concentration, thus allowing to capture the cathode material at all states of charge. Results show that the phase-transition barrier for the O2-P2 phase transition decreases on desodiation (charging). It is further shown that in dynamic molecular dynamics (MD) simulations at finite temperatures the barrier is lowered even further and that the transition mechanism involves gliding of a TMO_6 layer. As a highlight, the O2-P2 phase transition in $Na_{0.67}CoO_2$ is directly observed on atomistic scale and at standard lab conditions (*NpT* with 300 K and 1 bar) on the µs time-scale. Finally, the sodium diffusivity as function of progress of phase transition is analyzed, showing satisfactory agreement to experimental values reported in the literature. In conclusion, new insights on the phase transitions of layered oxide cathodes for SIBs are described and the applied classical potential approach is shown to boost computational battery materials research by allowing for larger and longer simulations.

Chapter 5 is about the electronic structure calculation of layered oxide cathode materials. Electronic structure calculations of TM oxides are known to be challenging but are extremely important for cathode materials to comment about their redox mechanism. To improve on this issue, different electronic structure calculations are thoroughly benchmarked here. Namely, hybrid functionals and their Hartree-Fock mixing parame-

ter α is assessed and optimized by the so-called *GW* calculations. It is shown that especially the hybridization of $2p$ oxygen orbitals and $3d$ TM orbitals is affected by α, which substantially influences the assigned redox mechanism of a cathode material. By applying different levels of *GW* calculations and providing various hybrid functional starting-points, two promising ranges for α are determined. The first range is highlighted to show satisfactory agreement to experimentally reported band gaps but corresponding α values of approximately 8.5 % are significantly lower than the default of 25 % employed in most hybrid functionals. However, the other determined range yields an α of approximately 22 % which is fairly close to the aforementioned default value. Finally, the results give some guidance on electronic structure calculations of layered oxide cathodes by summarizing effects and optimization strategies for varying the α parameter.

The last chapter (Chapter 6) focuses on the combination of experimental and theoretical studies on cathode materials. First, a work on a lithium-rich layered oxide cathode for LIBs is shown that aims to improve energy density over conventional cathodes. Especially the determination of the redox mechanism by computational studies is discussed while also configurational optimization by electrostatics and MD simulations to observe structural evolutions are performed. In the second work, large-scale configurational optimizations are leveraged to study lithium iron phosphate (LFP) that is discussed as a more sustainable LIB cathode material. The optimizations successfully reproduced the single-phase/two-phase charging mechanism in LFP on the multi-nanometer length-scale, proving the value and necessity of large-scale configurational optimizations by electrostatics. In the third example, it is shown how a layered oxide SIB cathode can be stabilized by surface modification in terms of a coating. Experimental results highlight significantly improved cycling stability due to the coating and *ab initio* MD simulations reveal the degradation of the bare cathode material by electrolyte species while the coating is found to be mostly inert. The last presented study focuses mainly on the determination of the redox process from electronic structure calculations in layered oxide SIB cathodes. It is highlighted that detailed electronic structure analysis can be directly related to experimentally observed effects such as subtle, yet important, changes in the shape of the voltage curve.

In summary, all of the case studies presented in the last chapter highlight how the methodologies developed in the previous chapters and computational methods in general can contribute to improved characterization of novel cathode materials. Ultimately, these introduced methodologies in conjunction with the detailed insights on specific cathode materials and comparisons to experimental data might contribute, together with many other works in the literature, to more rational cathode material design in the future that enables tailoring the next generation of batteries to specific needs such as sustainability and higher energy density.

SAMENVATTING

De transitie naar hernieuwbare energiebronnen en de vermindering van broeikasgasemissies om klimaatverandering tegen te gaan, is een van de grootste uitdagingen waar de mensheid vandaag de dag voor staat. Energieopslag biedt mogelijkheden om deze transitie mogelijk te maken door energieopslag in te zetten om het gebruik van hernieuwbare energiebronnen te vergroten. Elektrificatie van de transportsector door middel van energieopslag kan mogelijk leiden tot een verdere vermindering van broeikasgasemissies. Secundaire batterijen zijn veelbelovende energieopslagsystemen voor deze doeleinden en lithium-ionbatterijen (LIBs) worden al routinematig toegepast. LIBs zijn echter vaak afhankelijk van kritieke grondstoffen zoals kobalt, wat vragen oproept over de duurzaamheid bij toepassing op grotere schaal. Om deze problemen gedeeltelijk op te lossen, wordt onderzoek gedaan naar materialen die geen kritieke grondstoffen bevatten. In het kader van deze duurzaamheidsmaatregelen worden natrium-ionbatterijen (SIBs) gezien als een veelbelovend alternatief voor LIBs vanwege de grote beschikbaarheid van natrium en de mogelijkheid om het aantal kritieke/dure componenten in batterijen te verminderen. Voor beide batterijtechnologieën domineren de kathodematerialen de elektrochemische prestaties en behoren gelaagde oxiden tot de meest veelbelovende materialen. Over het algemeen maken gelaagde oxiden flexibele afstemming mogelijk, waardoor de vraag naar rationele ontwerpbenaderingen toeneemt door middel van diepgaande karakterisering en efficiënte voorselectie van interessante samenstellingen. Dit kan worden bereikt door simulatiestudies op basis van eerste principes op atomaire schaal, die gewoonlijk drie simulatiestappen omvatten, namelijk configuratieselectie, geometrische relaxatie/evolutie en berekeningen van de elektronische structuur. In dit proefschrift worden computationele technieken voor het bestuderen van kathodematerialen besproken en voor elk van deze simulatiestappen worden methoden ontwikkeld, getest en toegepast. Het laatste hoofdstuk toont ook verschillende praktische voorbeelden van hoe computationele studies, in combinatie met experimentele resultaten, het begrip van kathodematerialen voor LIBs en SIBs kunnen bevorderen. De inhoud van de hoofdstukken is als volgt:

In hoofdstuk 2 wordt de eerste simulatiestap van configuratieselectie besproken. Dit probleem ontstaat door gedeeltelijke bezettingen op kristallocaties die alleen door volledige bezettingen kunnen worden beschreven om verdere simulatiestappen toe te passen. Voor complexe materialen (veel substituenten) is configuratieoptimalisatie een enorm combinatorisch probleem. Allereerst wordt benadrukt dat de relatieve energie van verschillende configuraties in ionische kristallen, zoals gelaagde oxidekathodes, efficiënt kan worden beoordeeld in termen van eenvoudige paarsgewijze elektrostatische interacties. Vanwege het paarsgewijze karakter van elektrostatische energieën kan een optimalisatieprobleem met vooraf berekende energietermen worden geformuleerd.

This text was translated from the English text in the previous section with the help of translation software, and checked by a native Dutch speaker. For possible unclarities it is referred to the original English version.

Dit impliceert dat er een computationeel goedkope proxy is om configuraties met de laagste energie te verkrijgen voor vervolgsimulaties door de totale elektrostatische energie te optimaliseren. De optimalisatie wordt mogelijk gemaakt door de implementatie van verschillende efficiënte op Monte Carlo en genetische algoritmen gebaseerde optimizers, en er wordt ook gewezen op het gebruik van externe solvers. Deze implementaties resulteren uiteindelijk in een nieuwe code, GOAC (Global Optimization of Atomistic Configurations by Coulomb), die aanzienlijk sneller is dan bestaande software voor het gegeven probleem. Toepassingen op diverse, waaronder extreem grote, configuratie-optimalisatieproblemen bewijzen de efficiëntie van de code, waardoor deze een waardevol hulpmiddel is voor computationeel materiaalonderzoek, en met name onderzoek naar kathodemateriaal.

Hoofdstuk 3 bespreekt de keuze van een structureel model, maar met de nadruk op de stapelfase. Gelaagde oxidekathodes in SIB's vertonen verschillende fasen wat betreft de stapelvolgorde en de relatieve verschuiving van de lagen ten opzichte van elkaar. Deze fasen hebben een aanzienlijke invloed op hun elektrochemische prestaties, zoals capaciteit of natriumdiffusie. Bovendien vinden er tijdens het gebruik van de kathodematerialen overgangen tussen de fasen plaats, wat leidt tot degradatie en capaciteitsverlies. De fasestabiliteit en faseovergangen kunnen echter worden geoptimaliseerd door de samenstelling van de kathode aan te passen. Hier wordt aangetoond dat het vergelijken van de elektrostatische energieën van verschillende stapelfasen bij hun respectievelijke laagste energieconfiguraties een efficiënte *ab initio* voorspeller van fasestabiliteit kan zijn. Om de voorspellende kracht van deze computationeel goedkope benadering te vergroten, werden elektrostatische parameters zoals roosterparameters en interlaagafstanden geoptimaliseerd om de correlatie van relatieve fase-energieën met berekeningen op basis van de dichtheidsfunctionaaltheorie (DFT) te maximaliseren. Het vastgestelde voorspellingsschema maakt studies met hoge doorvoer mogelijk, terwijl het nog steeds volledig *ab initio* is en een voorspellingsnauwkeurigheid van 80 % op experimentele gegevens bereikt. Bovendien maakt de methode het mogelijk om ordeningsverschijnselen (overgangsmetalen (TM) en natrium) vast te leggen en rekening te houden met alle soorten stapelfasen, bijvoorbeeld O1, O2, O3, P2, P3, OP2, OP4. Daarom is de methode nuttig voor het ontwerpen van nieuwe kathodematerialen met op maat gemaakte fasestabiliteit voor verdere experimentele of simulatiestudies.

In hoofdstuk 4 wordt de fasestabiliteit in gelaagde oxidekathodes voor SIB's verder onderzocht. Naast de thermodynamische fasestabiliteit is het ook belangrijk om het proces en het mechanisme van faseovergangen (kinetiek) te begrijpen. Om faseovergangen te simuleren, wordt een Coulomb-Buckingham-potentiaal aangepast om interatomaire interacties in het Na_xCoO_2 kathodemateriaal te reproduceren. Er wordt een uitgebreide dataset van DFT-referentieberekeningen gemaakt en de potentiaal wordt aangepast aan energieën en krachten. Als nieuwigheid werd de potentiaal aangepast als een functie van de natriumconcentratie, waardoor het kathodemateriaal in alle laadtoestanden kan worden vastgelegd. De resultaten tonen aan dat de faseovergangsdrempel voor de O2-P2-faseovergang afneemt bij desodatie (opladen). Verder wordt aangetoond dat in dynamische moleculaire dynamica (MD)-simulaties bij eindige temperaturen de drempel nog verder wordt verlaagd en dat het overgangsmechanisme gepaard gaat met het glijden van een TMO_6-laag. Als hoogtepunt wordt de O2-P2-faseovergang in $Na_{0.67}CoO_2$

direct waargenomen op atomaire schaal en bij standaard laboratoriumomstandigheden (*npT* met 300 K en 1 bar) op de tijdschaal van µs. Ten slotte wordt de natriumdiffusiviteit als functie van de voortgang van de faseovergang geanalyseerd, wat een bevredigende overeenstemming laat zien met de experimentele waarden die in de literatuur worden gerapporteerd. Concluderend worden nieuwe inzichten beschreven over de faseovergangen van gelaagde oxidekathodes voor SIBs en wordt aangetoond dat de toegepaste klassieke potentiaalbenadering het computationele onderzoek naar batterijmaterialen stimuleert door grotere en langere simulaties mogelijk te maken.

Hoofdstuk 5 gaat ten slotte over de berekening van de elektronische structuur van gelaagde oxidekathodematerialen. Berekeningen van de elektronische structuur van TM-oxiden staan bekend als een uitdaging, maar zijn uiterst belangrijk voor kathodematerialen om iets te kunnen zeggen over hun redoxmechanisme. Om dit probleem aan te pakken, worden hier verschillende berekeningen van de elektronische structuur grondig getoetst. Namelijk, hybride functionalen en hun Hartree-Fock-mengparameter α worden beoordeeld en geoptimaliseerd door middel van zogenaamde *GW*-berekeningen. Er wordt aangetoond dat met name de hybridisatie van $2p$-zuurstoforbitalen en $3d$-TM-orbitalen wordt beïnvloed door α, wat een aanzienlijke invloed heeft op het toegewezen redoxmechanisme van een kathodemateriaal. Door verschillende niveaus van *GW*-berekeningen toe te passen en verschillende hybride functionele uitgangspunten te bieden, worden twee veelbelovende bereiken voor α bepaald. Het eerste bereik wordt gemarkeerd om aan te tonen dat het in overeenstemming is met experimenteel gerapporteerde bandgaten, maar de overeenkomstige α-waarden van ongeveer 8,5 % zijn aanzienlijk lager dan de standaardwaarde van 25 % die in de meeste hybride functionelen wordt gebruikt. Het andere bepaalde bereik levert echter een α op van ongeveer 22 %, wat vrij dicht bij de bovengenoemde standaardwaarde ligt. Ten slotte geven de resultaten enige richtlijnen voor elektronische structuurberekeningen van gelaagde oxidekathodes door de effecten en optimalisatiestrategieën voor het variëren van de parameter α samen te vatten.

Het laatste hoofdstuk (Hoofdstuk 6) richt zich op de combinatie van experimentele en theoretische studies naar kathodematerialen. Eerst wordt een werk aan een lithiumrijke gelaagde oxidekathode voor LIBs getoond dat tot doel heeft de energiedichtheid ten opzichte van conventionele kathodes te verbeteren. Met name de bepaling van het redoxmechanisme door middel van computationele studies wordt besproken, terwijl ook configuratie-optimalisatie door middel van elektrostatica en MD-simulaties wordt uitgevoerd om structurele evoluties te observeren. In de volgende studie worden grootschalige configuratie-optimalisaties gebruikt om lithiumijzerfosfaat (LFP) te bestuderen, dat wordt beschouwd als een duurzamer LIB-kathodemateriaal. De optimalisaties hebben met succes het eenfasige/tweefasige laadmechanisme in LFP op de multi-nanometerlengteschaal gereproduceerd, wat de waarde en noodzaak van grootschalige configuratie-optimalisaties door middel van elektrostatica aantoont. In het derde voorbeeld wordt getoond hoe een gelaagde oxide SIB-kathode kan worden gestabiliseerd door middel van oppervlaktemodificatie in de vorm van een coating. Experimentele resultaten wijzen op een aanzienlijk verbeterde cyclische stabiliteit dankzij de coating, en *ab initio* MD-simulaties tonen de degradatie van het onbeklede kathodemateriaal door elektrolytspecies aan, terwijl de coating grotendeels inert blijkt te zijn. De

laatste gepresenteerde studie richt zich voornamelijk op de bepaling van het redoxproces op basis van elektronische structuurberekeningen in gelaagde oxide SIB-kathodes. Er wordt benadrukt dat gedetailleerde elektronische structuuranalyse direct kan worden gerelateerd aan experimenteel waargenomen effecten, zoals subtiele, maar belangrijke veranderingen in de vorm van de spanningscurve.

Samenvattend laten alle casestudy's die in het vorige hoofdstuk zijn gepresenteerd zien hoe de methodologieën die in de voorgaande hoofdstukken zijn ontwikkeld en rekenmethoden in het algemeen kunnen bijdragen aan een betere karakterisering van nieuwe kathodematerialen. Uiteindelijk kunnen deze geïntroduceerde methodologieën, in combinatie met de gedetailleerde inzichten in specifieke kathodematerialen en vergelijkingen met experimentele gegevens, samen met veel ander werk in de literatuur bijdragen aan een rationeler ontwerp van kathodematerialen in de toekomst, waardoor de volgende generatie batterijen kan worden afgestemd op specifieke behoeften, zoals duurzaamheid en een hogere energiedichtheid.

CONTENTS

1

INTRODUCTION

1.1 Motivation and Background

The increasing demand for energy in combination with greenhouse gas emissions associated with energy production requires innovative energy supply strategies [1–5]. The strategy of decoupling electricity generation from its use with the help of secondary batteries can facilitate a transition to a more sustainable energy supply. Such batteries store energy via reversible charge/discharge reactions, allowing them to be reused for several cycles [1, 2]. Applied on an industrial-scale, batteries enable storing energy from renewable sources when it is abundant, for example, when it is windy for wind turbines or sunny for photovoltaics, and releasing it on demand. Thus, pairing renewables with batteries helps to reduce energy production from fossil fuels [1, 2, 4–8]. Moreover, the sector of transportation currently relies heavily on fossil fuels, but there are efforts for its electrification through batteries [3, 9, 10]. The sectors of grid energy production and transportation are known to contribute substantially to the global greenhouse gas emissions [9–11]. Therefore, (secondary) energy storage systems are commonly believed to be crucial to limit emissions and to ultimately slow down global climate change in the future [3–10, 12].

The applications and demand of secondary energy storage significantly increased in the past decades and are expected to continue growing [3, 4, 6, 7, 13–17]. While the growth was governed by consumer electronics, for example, laptops or mobile phones/tablets, in the past, it is assumed that it will be dominated by the markets of electrification of transportation and industrial-scale stationary energy storage in the future [3, 6, 7, 12, 17, 18]. The different sectors of the secondary energy storage market along with selected specific applications and their expected market trends are visualized in Figure 1.1. To summarize the economic perspectives on secondary batteries, there will most likely be a strongly increasing demand driven by ecological challenges, e.g., greenhouse gas emissions.

Historically, the market of secondary batteries was started in the 19^{th} century with the lead-acid battery and gradually evolved by nickel-cadmium and nickel-metal-hydride and finally lithium-ion batteries (LIBs) while an average yearly growth in gravimetric energy density of 3 Wh kg^{-1} from 1950 to 2010 was achieved [19, 20]. Since the commercialization of LIBs by Sony in 1991, they became the major technology in secondary energy storage applications [3, 18, 19, 21, 22]. Due to the great importance of LIBs in today's applications of secondary batteries along with the huge impact that this

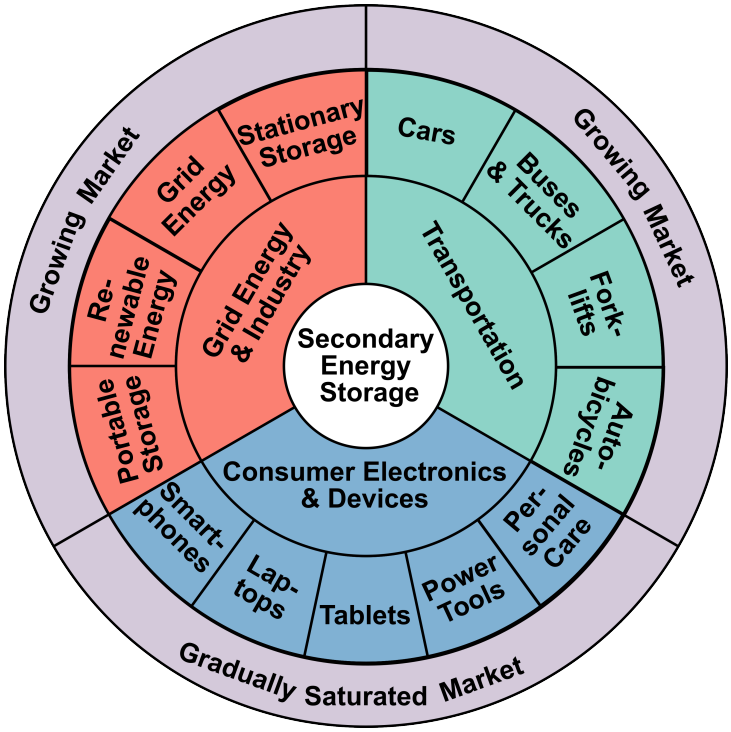

Figure 1.1: Possible applications of secondary energy storage divided into three sectors. For each sector several selected specific applications are shown and on the outer circle market maturity and trend is indicated for each sector. Contents and figure design were mostly recreated from Ding *et al.* [3].

technology had and has on humankind, three of the pioneers of energy storage research, namely John B. Goodenough, M. Stanley Whittingham, and Akira Yoshino, were even honored with the Nobel Prize in Chemistry in 2019 [18, 23–25].

The working principle of such LIBs is sketched in Figure 1.2 and can be described as follows: There are two host structures that can accommodate lithium, the anode and the cathode, with an electrolyte in-between them that are separated by a separator and connected via an external electronic circuit. During operation, the Li-ions (Li^+) travel from one host structure to the other through the electrolyte while electrons (e^-) move through the external circuit. To ensure there is no short circuit for the electrons to travel directly between the anode and cathode, a separator (electronic insulator) is employed. However, the separator can be passed by the Li-ions and the traveling of Li-ions is facilitated by an electrolyte with dissolved lithium salts. On charge, an external potential is applied to the electronic circuit pulling the Li-ions from the cathode towards the anode, or more specific, the lithium is deintercalated from the cathode that is oxidized (loss of electron) and then lithium is intercalated into the anode. On discharge, the opposite reaction takes place accompanied by a flow of electrons in the external circuit, thus allowing to extract the stored electric energy. The cycle is enabled by a difference in the chemical potential of the reactions taking place at anode and cathode side (difference

in Gibbs free energy of the electrochemical reactions) that manifests in the voltage of the cell [6, 12, 26, 27]. Neglecting any possible side reactions, the charge and discharge process is also fully reversible and thus constitutes a secondary energy storage. Also in reality with careful design thousands of charge cycles can be achieved before failure and severe capacity loss [4]. For such a performant and safe battery each basic battery component (cathode, anode, electrolyte, separator) must be optimized and a harmonic interplay of them must be secured to mitigate capacity fading, gas generation, increased internal resistances, short circuits, or even a thermal runaway during continuous cycling [27, 28]. Consequently, past and present research focuses to improve each of these components [26, 27, 29–35]. Despite the importance of all components, the focus of this thesis lies solely on the cathode materials, which also contribute, depending on the exact material, around one-third of the total cell costs [13]. Therefore, only cathodes are discussed further in the following.

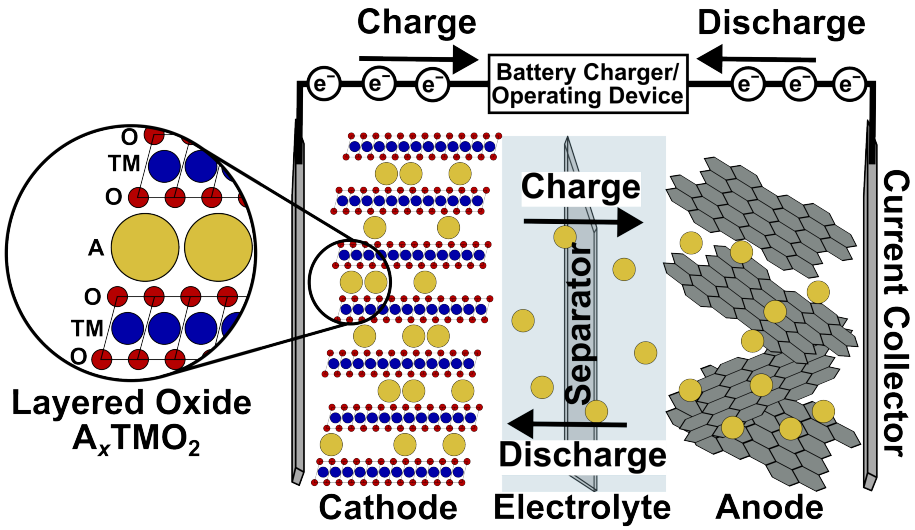

Figure 1.2: Schematic representation of a secondary battery. In this example a layered oxide cathode is shown and its structure motif is labeled in the zoomed circle along with its general chemical formula A_xTMO_2 with A (yellow) being the charge carrier, TM (blue) a transition metal, and O (red) oxygen. For the anode a hard-carbon structure is indicated. Parts of the figure inspired by Yabuuchi *et al.* [36].

Among various different material classes that have been researched for LIB cathodes, layered oxide materials have become the most widely used technology as of today [13, 26, 37, 38]. In Figure 1.2 a layered oxide type cathode material is schematically drawn. Layered oxides follow the general chemical formula A_xTMO_2 with A being the charge carrier (e.g., Li) and TM a transition metal. The material is assembled from layers of TMO_2 that consist of edge-sharing TMO_6 octahedra. The unit cells for layered oxides are usually defined such that the TMO_2 layer lies within the *ab*-plane and the layers are stacked in an alternating ABCABC... pattern (letters indicate 3 different relative oxygen shifts in the *ab*-pane) along the *c*-direction. Therefore, layered oxides can be considered as 2D materials. Between the TMO_2 layers charge-carrier ions such as Li are reversibly

(de-)intercalated while (mainly) the TMs are oxidized (reduced) [26, 37, 39]. Also the first commercialized LIB that was mentioned before leveraged a layered oxide cathode, namely $LiCoO_2$ (LCO). While this material enabled the first LIBs and is still used today, its practical reversible capacity is limited below its theoretical one, the long-term capacity retention is low, and it has a rather low ignition temperature for a thermal runaway (poor safety) [6, 37]. These disadvantages render this cathode material less practical for the discussed future use cases in transportation and large-scale stationary energy storage. However, to mitigate these issues novel layered oxide cathode materials have been developed in the past and the currently most promising candidates and widely employed ones are $Li[Ni_xCo_yMn_{1-x-y}]O_2$ (NCM) and $Li[Ni_xCo_yAl_{1-x-y}]O_2$ (NCA) [3, 6, 28, 37, 38]. These compositions highlight another advantage of the layered oxide class, their wide tunability by optimizing the TM composition which opens many directions for further research. It should be mentioned that next to optimization of the cathode material also surface modifications have proven to be effective in boosting the cathode performance; those are not the main focus of this thesis and are thus omitted here in favor of the bare cathode materials [37]. Despite substantial advances since the introduction of the first LIBs, there are still challenges and new challenges arising, especially, when facing the aforementioned expected market growth and intensified focus on sustainability [3, 12, 16, 40]. Therefore, challenges and possible directions for the next generation of (layered) cathode materials are outlined in the next section.

1.2 Challenges and Perspectives for Cathode Materials

There are still many challenges to overcome in cathode-material research while also promising perspectives exist. As mentioned before, LIBs are already successfully commercialized since several decades while Sodium-ion batteries (SIBs), that will be introduced in this section, are not broadly commercially available today. Due to the exchanged charge-carrier ions and the different market readiness it appears useful to discuss the challenges separately for LIBs and SIBs and this is done in the following subsections.

1.2.1 Lithium-Ion Cathodes

As discussed before, modern LIBs meet many of the most important market requirements regarding energy density/capacity and safety for now, while new applications always demand improvements on these performance metrics. Especially for a broader usage in the electric-vehicle market an increased energy density is highly desirable and a direction of current research on LIBs. Besides further tuning of the NCM (especially Ni-rich) and NCA materials another approach for high energy cathode-materials for layered oxide cathodes are lithium-rich materials with the general formula of $Li[Li_xTM_{1-x}]O_2$ with $0 \leq x \leq 0.33$ [39]. These Li-rich materials offer the opportunity for extremely high energy densities due to the increased lithium content while they suffer from capacity loss, voltage hysteresis, and a poor rate performance. Regarding the structure it is debated whether these materials are single-phase solid solutions or two-phase domain materials. However, it is commonly assumed that in the Li-rich phase a $LiTM_6$ (mainly TM=Mn) honeycomb ordering with Li in the center of a TM_6 comb is formed in the TM

layers of Li-rich layered oxides [39, 41]. Moreover, the additional capacity is generally attributed to the activation of anionic redox (oxygen redox from O^{2-} to $O^{2-+\delta}$) which allows for the extraction of excess lithium because the TMs are usually not oxidized beyond a charge of 4+. During long-term cycling, these materials possess the risk for TM migrations and irreversible anionic redox, e.g., formation of oxygen dimers that leave the cathode material. Ultimately, these mechanisms can lead to undesirable phase transitions to a spinel phase causing capacity degradation [39, 41, 42]. To conclude, Li-rich layered oxides are an interesting perspective for high energy cathode-materials but several challenges on the material side such as phase transitions, TM migration, and irreversible oxygen redox need to be overcome to improve their long-term cyclability.

Next to the desired increase in energy density another challenge frequently discussed for LIBs is the sustainability perspective. Current LIBs rely on relatively rare, toxic materials such as Co whose supplies are spread unevenly over the world (strategic supply risk), which is considered to be mined under critical conditions, and which is officially classified as critical raw material. Also the lower relative abundance of lithium itself and respective difficulties to efficiently source it, is sometimes considered problematic. Finally, the sourcing processes of the raw materials for LIBs are often described as harmful to the environment [3, 13, 16, 26, 40, 43]. These constitute direct limitations and challenges in the large-scale application of LIBs as it would be required for the electrification of transportation and grid energy storage to mitigate climate change. Also, an increasing demand for energy storage and limited raw materials (shortage of materials supply) could cause high costs for batteries thus limiting their application potential [13]. Moreover, energy costs associated with the manufacturing and recycling of LIBs are also high, lowering the possible environmental benefits of energy storage applications discussed in the previous section. However, when used long enough (a few hundreds of charge and discharge cycles), classical LIBs still can have a beneficial effect on energy consumption and greenhouse gas emissions [12, 44]. Another huge challenge for LIBs is therefore to improve their sustainability by relying on more abundant, cheaper, and non-critical materials, and especially eliminating or reducing cobalt in the compositions. It should be mentioned that the high energy, Li-rich cathode materials discussed before as well as modern NCM and NCA cathodes already improve on this issue to some extent as they mainly rely on low cobalt contents [6, 37, 39, 41, 42]. Furthermore, also different cathode chemistries than layered oxides are discussed to mitigate the dependence on costly metals and an interesting material is lithium iron phosphate (LFP) [45]. LFP shows excellent cycling stability, is more safe than layered materials, and utilizes abundant and economically-friendly materials, especially iron. The lower cost of LFP compared to $LiCoO_2$ rendering it a promising cathode material while its lower voltage, capacity, ionic conductivity, and electronic conductivity still introduce additional challenges [3, 26, 28, 46]. Despite the cost reduction and improvements in sustainability by using iron instead of cobalt, this still does not improve on the possible cost (price fluctuations) and supply issues of lithium [43]. Therefore, technologies that not just replace rare TMs by more abundant ones but also exchange the charge carrier from lithium to more abundant (alkali-)metals are desirable. An interesting direction in that regard are the aforementioned SIBs that are discussed in more detail in the next section [40].

1

1.2.2 Sodium-Ion Cathodes

SIBs provide an interesting alternative to LIBs as sodium is more than 1000-times more abundant on the earth than lithium, which secures a steady, cheap, and more sustainable supply. Moreover, SIBs might reduce usage of critical materials as a broad variety of metals is electrochemically active in SIB cathodes and materials relying, for example, on Na, Mn, Ti, and Al can be designed [4, 47–49]. SIBs further allow to replace the copper current collectors by cheaper aluminum as sodium does not alloy with aluminum and the expensive graphite anode in LIBs can be replaced by cheaper and more sustainable hard carbon (cf. Figure 1.2). It should be mentioned that currently a transition to SIBs does not significantly reduce the cost per capacity unit, but with increasing demand in the future and further technological advancements, SIBs can become cost-competitive with LIBs [4, 13, 50]. From the performance perspective, SIBs can advance over LIBs for some properties such as charge rates and (lower) operating temperatures. However, especially the capacity and the operating voltage is lower compared to LIBs because of the smaller redox potential and larger atomic mass/ionic radii of sodium compared to lithium [13, 48]. Therefore, a significant challenge for the future development of SIBs is to improve the insufficient battery performance especially by increasing the reversible energy density [50]. Due to the possibility of more cost-efficient and more sustainable batteries compared to LIBs, research on SIBs intensified significantly during the last decade while before the commercial success of LIBs they were also similarly intensely studied as LIBs [51].

Among different cathode materials for SIBs layered oxides were studied most as they are direct analogues to the most successful LIBs discussed before. For SIBs, layered cathode materials offer among the highest capacities and voltages along with decent electron conduction and reasonable rate performance. Their similarity to the current market standard of LIBs could further allow to use existing production lines once this technology is brought to the market. Despite the considerable research that was already spend on layered oxide cathodes for SIBs, the ultimate step towards (broader) commercialization remains challenging as of today [48, 50, 51]. One of the major challenges with layered oxides for SIBs is the increased variety of phases compared to LIBs due to the larger ionic radius of sodium over lithium. Sodium shows less preferences for a certain oxygen environment-coordination and can be stable in both, an octahedral and prismatic oxygen coordination. These coordination environments can be realized by different shifts of the TMO_6 layers relative to each other in the *ab*-plane, thus introducing different stacking sequences of the layers along the *c*-direction. The different phases resulting from these stacking sequences were classified by Delmas *et al.* [52] based on their sodium coordination (O for octahedral or P for prismatic) and periodicity in terms of TMO_6 layers along the *c*-direction. The most commonly synthesized phases for layered oxide SIB cathodes according to this nomenclature are P2, P3, and O3. The structures can be further classified by their oxygen layer stacking out of three different oxygen layers (A, B, C), each shifted by 1/3 in the *ab*-plane [47, 51]. The most common phases obtained in layered oxide SIB cathodes along with their sodium-coordination and oxygen stacking labels are presented in Figure 1.3.

The stability of the phases is strongly related to the sodium concentration and P-phases are usually observed in the intermediate sodium-concentration range and O-

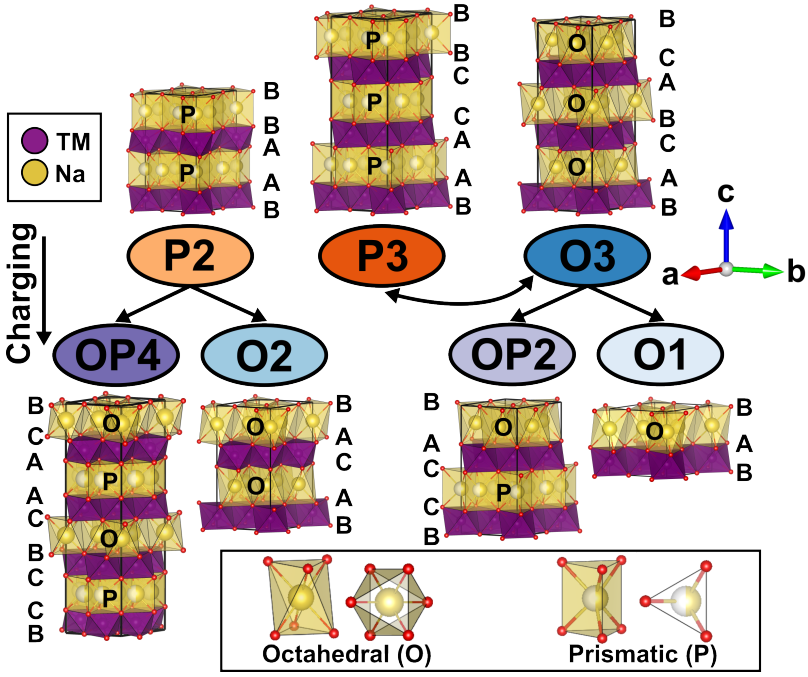

Figure 1.3: Stacking phases of layered oxide sodium-ion battery (SIB) cathodes. The top row shows the most commonly synthesized phases while arrows and the lower row highlight phase transitions that are often observed on charging (desodiation). For each phase structure models are visualized and the oxygen layers as well as the sodium coordination-environments are labelled in the structures. The purple color indicates transition metal (TM) layers and yellow color sodium layers. At the bottom detailed structures of the octahedral (left) and prismatic (right) sodium coordination environments are shown. Parts of the figure inspired by Zhang *et al.* [47]. Structure models were visualized with VESTA [53].

phase at the high and low sodium concentrations. Furthermore, P-structures have two sodium sub-lattices in the sodium layers while at higher concentrations only one of them is occupied due to the electrostatic repulsion between the sodium ions. The inter-layer spacing in P-phases is also larger than in O-phases as the oxygen ions are positioned face to face in the prismatic coordination. These characteristics of the different phases also go along with altered properties of the cathode material. While its high sodium content increases the capacity of O-phases (O3 phase), the P2 phase shows better sodium conductivity due to the two sodium sub-lattices and also better cycling stability [47]. This proves that the electrochemical performance characteristics of a layered oxide cathode for SIBs are strongly correlated to its phase. While the presence of more different phases for layered oxide cathodes in SIBs is intrinsically not a problem, phase transitions during operation of cathode material are. Transition between the phases during cycling goes along with drastic volume changes of the cathode material because of the aforementioned different inter-layer spacings. Such volume changes can yield degradation of the cathode material and steps (multiple plateaus) in the voltage profile because of the different properties of the phases, e.g., sodium diffusivity. Phase transitions also might

be irreversible which limits the cyclability of the cathode materials. Moreover, sodium-vacancy orderings can influence the shape of the voltage plateau, the phase transitions, and sodium diffusion significantly [47–50]. The most commonly observed phases obtained during charging are also indicated in Figure 1.3. It should be noted that the phases are not fully interconnected and usually transitions that just require layer gliding and no breaking/formation of TM-oxygen bonds are observed [48]. However, next to the bare phases presented in the figure, also smaller distortions that reduce the symmetries of the structures often take place during operation and associated phases are commonly indicated by adding a dash to the phase name. Regarding the commercialization of SIBs it can be concluded that the capacity degradation due to phase transitions is among the biggest challenges for layered oxide cathodes [47–50].

To mitigate phase transitions and their negative effects on the electrochemical performance of layered oxide SIB cathodes, the materials can be tuned by element substitution in the TM sites [47]. This highlights the importance of optimizing the composition, while also other strategies such as phase-mixtures are proposed to approach the phase-stability challenges of SIBs [49]. In order to improve the capacity and voltage of SIBs as well and to make them more competitive to LIBs, utilization of anionic redox is frequently proposed [54]. The general principle was already described for the Li-rich LIB cathodes and the oxygen redox also can enable additional capacity at high voltage in SIBs. The voltage is increased as the oxygen ions are oxidized instead of the TM cations. While the additional capacity and the increased voltage are appealing, anionic redox also possesses the risk of oxygen dimerization and ultimately irreversible oxygen loss that leads to degradation of the cathode material. Moreover, oxygen redox can facilitate irreversible migration of TMs to the sodium layers and finally also affect the phase stability and transition behavior. The existence and strength of anionic redox in layered oxide cathodes is also closely related to the TM composition [47, 54]. It can be concluded that tailored design of the cathode-material composition (mainly TM mixture) of layered oxide SIBs can significantly improve their electrochemical performance in terms of capacity, voltage, and cyclability, and it is therefore a promising and interesting research field. It should be mentioned that also poor air/water stability and interfacial reactions with the electrolyte are challenges as well that can be (partially) addressed by element substitution. Another strategy to improve on these challenges are surface modifications, especially for the electrolyte interface. Coating layers were reported to show improved cycling stability and water resistance [48].

All of these challenges and potential directions for improvements result in a huge number of possible cathode-material combinations (compositions) to explore and it would be desirable to design the materials with more rational to obtain deeper understanding as well as to pre-screen the most promising materials before experimental synthesis. For exactly these purposes, computational studies can be leveraged and are therefore discussed in the next section [55].

1.3 Computational Methods to Study Cathode Materials

Overcoming the aforementioned challenges of LIB and SIB cathodes purely by exhaustive experimental studies might be time-consuming and expensive, given the broad compositional and structural space of cathode materials that requires sampling many

combinations. Designing a limited number of the most promising cathode materials for further tests by experimental synthesis would be a more efficient approach. However, such rational design requires atomistic insights of the cathode materials which are difficult to obtain even by advanced experimental characterization methods. Modern computational studies can provide these insights and are therefore inevitable to fully understand cathode materials and thereby enable more rational design. So-called first principles or *ab initio* techniques leverage known physical concepts such as quantum mechanics for cathode material simulations. The great advantage of these methods is that they do not rely on experimental parameters such that they can be readily applied to any (not yet synthesized) cathode material and are not influenced by possible experimental characterization errors. Moreover, the computational studies are usually less expensive and time-consuming than experimental synthesis and thus can allow for efficient screening of candidate cathode materials [56, 57]. Consequently, first principles calculations became an increasingly important tool for the characterization and prediction/selection of novel cathode materials for LIBs and SIBs [55, 57–65]. Especially in combination with experimental studies these computational tools can be highly valuable in the thorough characterization of novel cathode materials as they often provide insights complementary to experiment. Properties that can be approached by computational methods are, for example, crystal structures, cation orderings/disorderings, cation migrations, defect energies, phase diagrams (stability and transition), grain facets, mechanical characteristics, interface reactions, ion transport behaviors (diffusivity), electronic features (e.g., band gaps), redox mechanisms as well as operating voltage and capacity [57–59, 64, 65]. Thus, first principles simulations can allow for both, prediction and characterization of cathode material properties [55, 56, 58].

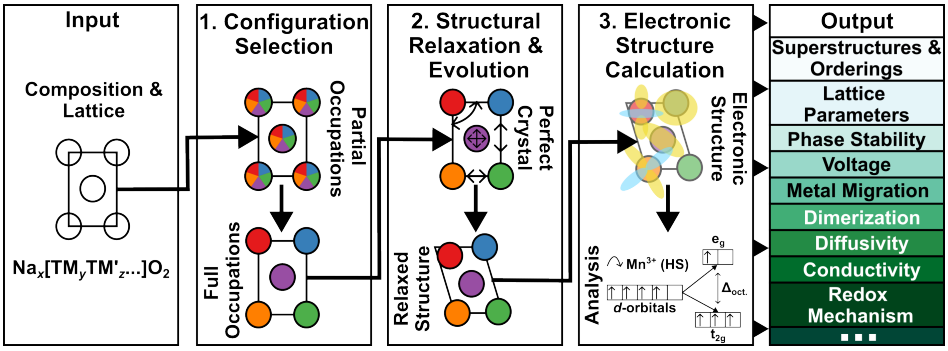

Figure 1.4: Three-step simulation procedure employed in *ab initio* simulations of cathode materials. In the first simulation step a distinct configuration with full occupancies is selected for the further simulation steps. In the second simulation step the structure is optimized by relaxation and/or structural evolution. Finally, in the third simulation step the electronic structure of the relaxed geometry is calculated and analyzed. The combined insights of all of these three simulation steps can predict numerous important properties of cathode materials and some of them are listed in the output box.

Ab initio calculations for cathode materials can follow a general three-step procedure. It should be noted that some materials might require different procedures or fewer/additional steps but the computational studies performed in this thesis follow a

three-step simulation framework for cathode materials. This framework is discussed in detail in the following and the corresponding workflow is visualized in Figure 1.4.

In the very beginning of computational studies on cathode materials usually a desired composition that should be tested is provided along with a crystal lattice. In case of a layered oxide cathode this could be the sodium concentration and the TM composition as well as the unit cell of the structure. Of course, multiple cells can be tested to assess, e.g., the stability of different phases. These inputs go then through the three-step simulation procedure with the configuration selection being the first step.

1.3.1 Configuration Selection

To represent a desired multi-element cathode composition in a crystal lattice it appears useful to assign the fractional occupancies to each lattice site. The combination of elements of various types with the given ratio (composition) results in partial occupancy of a corresponding lattice site. While this approach is useful for representation of the structure, in reality it is nonphysical as multiple species cannot occupy a single site and it cannot be used by the methods typically employed in the following simulation steps as they require just full occupancies on each site. Moreover, only if the partial occupancies are distributed to full occupancies important phenomena such as charge-carrier, e.g., Li or Na, orderings or TM super-structures can be observed [55, 57, 58]. Therefore, the supercell approach can be applied to model the given composition using a multiple of the unit cell with full occupancies distributed over the lattice sites such that the overall composition of the supercell matches the desired composition (cf. Figure 1.4). This generates a combinatorial problem of arranging atoms on a fixed lattice and each arrangement is a configuration of the system [66]. As mentioned before, novel cathode materials comprise of several TMs along with partial Li or Na occupations that need to be considered simultaneously, resulting in a combinatorial explosion for the total number of configurations in a supercell. Thus, selection of a suitable configuration can be extremely challenging [66, 67]. A suitable configuration can be either the most random structure, e.g., Special Quasirandom Structure [68], or for battery materials, where ordering is expected, the lowest energy configuration [55]. No matter how suitability is defined for the configuration search, the huge number of possible configurations in complex systems requires heuristic search methods such as Monte Carlo algorithms or evolutionary approaches. Moreover, often evaluation of many configurations is required such that a computationally in-expensive proxy to the total energy of a configuration needs to be applied. Commonly leveraged methods are cluster expansion (CE) [69] that tries to mimic higher level of theory calculations or the utilization of strongly simplified energy models such as the electrostatic energy [55, 58, 66, 67, 70].

In general, it can be concluded that the configuration selection is a challenging combinatorial optimization problem that needs to be addressed to continue with any of the further simulations steps for cathode materials. More details about this problem and how to approach it are discussed in Chapter 2. Once a configuration with just full occupancies is selected, structural relaxation can be employed in the next step.

1.3.2 Structure Relaxation & Evolution

Given a suitable configuration with just full occupancies, the structure can be optimized by quantum mechanics methods in the next step of the three-step simulation procedure (cf. Figure 1.4). At this step lattice parameters, lattice angles, and atomic positions are optimized through relaxation or their evolution over time at a finite temperature is studied. These structural optimizations are usually conducted by density functional theory (DFT) calculations that are described next.

Density Functional Theory (DFT)

DFT aims to approach the time-independent, non-relativistic, many-body Schrödinger equation that determines the quantum mechanical properties of a system such as its ground-state energy. In its most simplified form, the Schrödinger equation can be written as [55, 71]:

$$H\Psi = E\Psi, \tag{1.1}$$

with the many-body wave function Ψ, the Hamilton operator H, and the ground state energy E. The equation constitutes an eigenvalue problem. In this case, Ψ depends on the coordinates of both, the electrons and nuclei in a system of atoms introducing a high-dimensional numerical problem. To reduce the dimensionality, the significantly different masses of electrons (lighter) and nuclei (protons and neutrons) as well as the corresponding different time scales of their movement can be leveraged to separate the movement of electrons and nuclei. This famous simplification is known as the Born-Oppenheimer approximation [72] and transforms the nuclei positions in the many-body Schrödinger equation from variables into fixed parameters. By writing the Hamilton operator explicitly and applying the Bonn-Oppenheimer approximation, the electronic Schrödinger equation can be derived for a system of N electrons [55, 71]:

$$\left[-\frac{\hbar^2}{2m} \sum_{i=1}^{N} \nabla_i^2 + \sum_{i=1}^{N} V(r_i) + \sum_{i=1}^{N} \sum_{j<i}^{N} U(r_i, r_j) \right] \Psi = E\Psi. \tag{1.2}$$

The first term denotes the kinetic energy with m being the mass of an electron and $\hbar$ reduced Planck's constant. The next term describes the electrostatic interaction of the electrons and (fixed) nuclei and the last term every pairwise electrostatic interaction between two electrons. It should be mentioned that the middle term also contains the positions of the nuclei (R) but due to the aforementioned separation only as parameters and not as variables (due to the fixed geometry). To obtain the total energy also an additional term that describes the electrostatic interaction between the fixed nuclei needs to be considered. Moreover, r_i is defined as the general coordinates of the electrons including, next to the spatial dimensions, also the spins of the electrons. Thus, the wave function Ψ is still high dimensional despite the utilization of the Born-Oppenheimer approximation. However, Ψ might be approximated by a product of separated electron wave functions Ψ_i (Hartree product) but the electron-electron interaction (U) still requires to consider the interaction of one electron with all other electrons simultaneously (many-body character). Still, this description of Ψ allows to define the density of electrons n as [55, 71]:

$$n(r) = 2\sum_i \Psi_i^*(r)\Psi_i(r), \tag{1.3}$$

with Ψ_i^* being the complex-conjugate and the factor of 2 accounting for the two possible spins of electrons. For the density $n(r)$, r indicates just the three spatial dimensions rendering $n(r)$ a low (3) dimensional property compared to $\Psi(r_1, r_2, ..., r_N)$. Hohenberg and Kohn [73] proved that the ground state energy of the Schrödinger equation is a unique functional (a function of a function) of the electron density. This highlights that the ground-state energy of a system can be expressed by its electron density which is just 3-dimensional and not high dimensional as Ψ. This greatly reduces the complexity of the initial Schrödinger equation and Hohenberg and Kohn [73] showed even further that finding the electron density that minimizes the total energy is the true electron density and therefore the full solution of the Schrödinger equation. While it is proven as well that an exact functional exists, its precise functional form is unknown. However, with Equation 1.2 several known contributions can be defined but with integrals instead of sums as a density is considered. All quantum mechanical effects that are not captured in the known terms can finally be summed up in an additional term, $E_{\mathrm{XC}}[n(r)]$. This term is the exchange-correlation functional which needs to be approximated to leverage the dimensionality reduction of considering an electron density. However, determining the electron density holistically is still challenging (orbital-free DFT) and Kohn and Sham [74] finally showed that the problem can be expressed by a set of single-electron equations [55, 71]:

$$\left[-\frac{\hbar^2}{2m}\nabla^2 + V(r) + V_{\mathrm{H}}(r) + V_{\mathrm{XC}}(r)\right]\Psi_i(r) = \epsilon_i\Psi_i(r). \tag{1.4}$$

In the Kohn-Sham equations V is the interaction of electrons and nuclei, V_{H} is the Hartree potential that describes the interaction of an electron with the total electron density, and V_{XC} is the derivative of E_{XC} that accounts for additional quantum mechanical effects. It becomes evident that the Hartree potential introduces a self-interaction error as the electron interacts with the total electron density that includes the electron itself. Therefore, the unknown V_{XC} part should also correct for this error. To solve these equations an initial electron density can be guessed and the single electron wave-functions are determined by the Kohn-Sham equations. The corresponding new electron density can be calculated from the single electron wave-functions. To obtain the ground-state electron density this process is repeated iteratively in a self-consistent manner until the initial electron density is the same as the new one calculated from the single electron wave-functions. Practically, comparing the energies is more straightforward to achieve than comparing the densities directly. In summary, these steps and equations define the theoretical core of DFT calculations [55, 71].

The crucial part to perform DFT calculations within this scheme is to define an approximation for the exchange-correlation functional. The most simplistic approach for that purpose is the local density approximation (LDA) that includes the exchange-correlation energy of a homogeneous electron gas for a given local density value. Thus, LDA is a local functional. To overcome this locality, generalized gradient approximation (GGA) functionals were developed. As the name suggests, these functionals not

just consider the local electron density but also its gradient and thereby indirectly overcome locality (GGAs are considered semi-local). The most renown GGA functional that is also mostly employed in this thesis is the Perdew-Burke-Ernzerhof (PBE) functional [75]. However, as the exact exchange-correlation functional is unknown, numerous further approximations (functionals) exist that are not discussed here and it cannot be simply determined which is the most accurate for a given problem [55, 71].

Some further considerations must be made for periodic systems such as the cathode materials discussed in this thesis. For simulations under periodic conditions it is computationally beneficial to perform the calculations in reciprocal (k) space rather than in in real (r) space. Furthermore, the wave functions must obey the same periodicity as the simulation cell and according to Bloch's theorem [76] the solution of the Schrödinger equation can be written as a sum of plane waves of the following form [71]:

$$\Phi_k(r) = \exp(ikr)u_k(r). \tag{1.5}$$

Here $u_k(r)$ is periodic within the supercell and the Schrödinger equation can be solved separately at each k and integrals that are computationally demanding in the DFT procedure can be evaluated more efficiently. Technically, the $u_k(r)$ can generate an infinite amount of plane waves that satisfy the periodicity constraint, constituting a complete set of plane waves that must be considered for each point (k) in reciprocal space. As this is not practical, the set of plane waves is only considered up to a kinetic energy cut-off. For actual DFT calculations in periodic systems this means that the results need to be converged in both, the k-point sampling and the energy cut-off. When converging the energy cut-off, core electrons require high cut-offs while providing usually the least insights (valance electrons are more important to describe most properties). To overcome this imbalance in value of insights and computational cost, pseudo-potentials are employed. These potentials freeze the core together with its core electrons (frozen core approximation) and replace it by a smoothed effective potential. The smoother (softer) the pseudo-potentials, the lower are the required energy cut-offs. These pseudo-potentials must be, however, designed in a transferable way such that a database with potentials for each element can be simply leveraged to perform DFT calculations on a system of interest. There are different approaches to construct pseudo-potentials but, in this thesis, the projector-augmented wave (PAW) method from Blöchl [77] is employed. Carefully designed pseudo-potentials are able to reach the accuracy of calculations that considered all electrons while drastically reducing the computational costs. The described DFT methods therefore finally allow to study solids such as cathode materials [71].

Geometry Relaxation and Molecular Dynamics

As described before, in DFT initially the energy of given positions of atoms is determined. In order to allow for actual structural optimization, the atoms in the cell need to be displaced and corresponding energies must be calculated. As also the energy is changing on moving the atoms, the derivative of the energy with respect to the atom coordinates corresponds to the forces acting on the atoms. With the forces, gradient-based methods can be applied that move the atoms strategically (e.g., choice of proper step size) along their forces until a convergence criterion is fulfilled, e.g., the forces on all ions are below a certain threshold. By that procedure, DFT calculations allow to perform structural

optimizations. Moreover, similar optimization strategies based on stresses can be employed on lattice parameters and lattice angles such that simultaneous optimization of all degrees of freedom can be achieved for periodic systems like cathode materials [71].

By just following the energy gradient to the next minimum no kinetic energy and dynamic evolution of the atoms is considered and thus no temperature (zero temperature). To simulate the system at a finite temperature Newtons second law can be applied to the nuclei [78]:

$$-\frac{\mathrm{d}V}{\mathrm{d}r} = m\frac{\mathrm{d}^2 r}{\mathrm{d}t^2} \equiv F = ma. \tag{1.6}$$

Here V is the interatomic potential, r the spatial atomic coordinates, m the particle mass and t the time, and F is the force and a the acceleration. To evolve a system of particles, the equation must be solved numerically by defining a small time step Δt. With help of a Taylor expansion and the current particle positions (r_i) the positions at a short time step before (r_{i-1}) or after (r_{i+1}) can be determined [78]:

$$r_{i\pm1} = r_i \pm \frac{\partial r}{\partial t}(\Delta t) + \frac{\partial^2 r}{2\partial t^2}(\Delta t)^2 \pm \frac{\partial^3 r}{6\partial t^3}(\Delta t)^3 + \dots . \tag{1.7}$$

In this expansion the first derivative corresponds to the particle velocity and the second derivative to its acceleration. By utilizing the descriptions for r_{i-1} and r_{i+1} and cutting the expansion off at the second (third) order an expression for r_{i+1} is derived [78]:

$$r_{i+1} = (2r_i - r_{i-1}) + a_i(\Delta t)^2. \tag{1.8}$$

This equation is known as the Verlet algorithm [79] and allows to perform evolutions over time of a system of particles while the previous particle positions (r_{-1}) before the starting point (r_0) can be obtained by introducing an initial velocity v_0. There are slightly different equations to the ones shown here that bring some numerical advantages while the key assumption always is that a sufficiently small time step Δt (smaller than the fastest process in the system) must be chosen to render these equations accurate. Consequently, systems must be propagated in very small time steps and simulations over long time-scales are demanding. Such simulations over time are referred to as molecular dynamics (MD) simulations. The total energy E during the simulations is given by the sum of kinetic and potential energy while the kinetic energy is proportional to the associated temperature of the system. Thus, the simulations run at finite temperatures. Depending on the properties that are fixed during the simulations, different ensembles can be considered such as NVE, NVT, or NpT with the particle number N and system volume V while for the latter also thermostats and barostats must be introduced to control the temperature T and pressure p, respectively. Several strategies to implement such thermostats and barostats were proposed that are not discussed in detail here. More important is the fact that to apply the Verlet algorithm, a potential (more precisely the derivative of it which is the force) is required. This potential can be realized by different levels of theory, including also the aforementioned quantum mechanics approach in DFT calculations. Such simulations are called *ab initio* MD (AIMD) simulations. However, also classical potentials (also called force fields) comprising simple analytical terms can be

considered for the potential in MD simulations (actually also for the geometry optimization described before) [78]. An example for that is discussed in more detail in Chapter 4 of this thesis. More recently, also (on-the-fly) machine learning force fields (MLFF) became popular in MD simulations. MLFF are trained on *ab initio* calculations and aim to reproduce their accuracy at significantly reduced computational cost by leveraging machine learning techniques. On-the-fly MLFF further try to estimate the uncertainty of the current MLFF prediction and perform an *ab initio* calculation if the expected uncertainty is large [80]. Independent of the underlying potential, MD simulations allow to study the evolution of a system over time at a finite temperature and also can enable more strong structural distortions than geometry optimizations. These properties can be highly valuable for cathode materials when phenomena such as cation migration or oxygen dimerization are expected.

1.3.3 Electronic Structure Calculations

After obtaining a satisfactory relaxed geometry, electronic structure calculations can be performed, constituting the third and last step of the three-step simulation workflow (cf. Figure 1.4). Strictly speaking, electronic structure calculations were already performed in the previous steps as DFT is an electronic structure method. The calculations in this step also mostly employ DFT. However, accurate electronic structure descriptions of TM oxides such as layered oxide cathode materials are known to be challenging and therefore more accurate functionals than the ones discussed in the previous section (e.g., PBE) are required. In particular, GGAs over-delocalize the electrons due to the aforementioned self-interaction error resulting in unreasonable descriptions of the *d*-orbitals that are important to correctly asses the redox mechanism of cathode materials [81]. Besides DFT, another famous approach to approximate the Schrödinger equation exists: The Hartree-Fock (HF) method [82, 83]. While the details are not discussed here, this approach does not consider a density but directly the wave function. By design (Slater determinant), it is ensured that the wave function obeys Pauli's exclusion principle. Mathematically, HF shows the opposite tendency to GGA-DFT in the electronic structure, namely the over-localization of electrons as no correlation is included in the method. However, in contrast to DFT, the exchange part is described exactly. Due to the fact that both methods are complementary and a combination could benefit from compensation of errors as well as the consideration of a portion of exact exchange, mixed DFT/HF methods were developed. These methods are so-called hybrid functionals and are of the general form of [78, 84, 85]:

$$E_{\mathrm{XC}} = \alpha E_{\mathrm{X}}^{\mathrm{HF}} + (1-\alpha) E_{\mathrm{X}}^{\mathrm{PBE}} + E_{\mathrm{C}}^{\mathrm{PBE}}. \tag{1.9}$$

Through the inclusion of exact exchange obtained from the HF method more accurate descriptions of the electronic structure in layered oxides can be achieved, even though at significantly increased computational costs. The choice of the mixing parameter α and more advanced designs that further separate the contributions in short- and long-range are discussed more detailed in Chapter 5 of this thesis [55, 78]. Also, more elaborated, yet even more computationally demanding methods within the random phase approximation (RPA) exist that are also briefly discussed in the aforementioned chapter. For the three-step simulation procedure applied to study cathode materials in this work, DFT

with hybrid functionals was utilized to study their redox mechanism from the electronic structure. While it is conceptually possible to also employ these functionals during the structure dynamics in the second step, this is usually prohibitively expensive in terms of computational cost, giving rise to a separate step for the electronic structure calculation.

To summarize, cathode materials can be modelled by the three-step procedure sketched in Figure 1.4 while at each step unique challenges arise that need to be tackled by suitable and feasible methods. As also pointed out, a full simulation of a cathode material including all three steps can deliver valuable insights on several properties of the material and thereby significantly contribute to its characterization and materials prediction. How exactly this thesis relates to the presented three-step simulation framework is outlined in more detail in the next section.

1.4 Thesis Objectives

The objective of this thesis is to explore and develop new methods for the computational exploration of cathode materials for LIBs and SIBs, especially layered oxides. While most of the work builds up on existing and well-established computational methodologies such as Monte Carlo simulations, Ewald summation, Buckingham Potentials, DFT calculations, and *GW* calculations, new approaches with a focus on cathode materials are evaluated and implemented. The thesis is therefore centered around methodology developments to improve computational studies of battery materials. These improvements can be assigned to two main objectives:

I) The reduction of computational costs to allow for more, larger, and faster simulations that offer new insights or support rational materials selection.

II) The assessment and advancement of the calculation accuracy to improve the understanding of fundamental mechanisms in layered oxide cathode materials.

However, also practical case-studies that showcase the applicability and relevance of the newly developed methods are presented in this work. Thus, the third objective of the thesis is:

III) The utilization of computational methods in close combination with experimental measurements to support characterizations and to enable more rational materials design.

In the previous introduction section about computational methods for studying cathode materials a three-step modelling procedure that consists of 1. Configuration Selection, 2. Geometry Relaxation and Evolution, and 3. Electronic Structure Calculation was introduced (cf. Figure 1.4). The objectives of the thesis include contributions of methodical advancements to all of these three steps. Consequently, the chapters and their corresponding specific objectives are also aligned to this trinity of simulation steps. This allows to specify the objectives of the thesis more precisely for each presented contribution.

As outlined before, for the first step extensive configurational optimization is required and the thesis aims to address this challenge by introducing a new software with efficient implementations of several heuristic optimizers. The goal of the thesis in this modelling step is to speed-up configurational selection and thereby enable faster material screening in computational studies while also expanding the use of such optimizations to much larger systems. Thus, enabling new atomistic insights for systems and particles at the length-scale of several nanometers that were not accessible before due to prohibitively high computational costs.

As also pointed-out in the introduction, for SIBs the phase stability in terms of the stacking sequence of the layers along the *c*-direction is rather important and can influence many electrochemical properties of the cathode. Therefore, it would be highly desirable to have a computational tool that can estimate the phase stability of a given layered oxide SIB cathode at low costs and another aim of this thesis is to provide such a

tool. To that extend, the aforementioned developed code for configurational optimization is employed and a new scheme to evaluate the stability of different phases is determined. This part of the thesis bears the opportunity for more rational cathode design for SIBs and therefore constitutes another contribution to the first step of the three-step modelling procedure (cf. Figure 1.4) while mainly targeting the first thesis objective (I).

Another goal of the thesis is to go beyond thermodynamic stability of the layered oxide phases and to also explore the actual phase-transition mechanism under realistic simulation conditions, at long time-scales and at large length-scales. Thus, classical potentials are developed and employed that enable direct observation of phase-transitions under standard lab conditions. This specific contribution therefore also focuses on the objective of reduction of computational costs to allow for larger and longer simulations of battery materials which can yield novel and fundamental insights that are also of relevance to experimental studies. As dynamic structural relaxations are performed, the method is assigned to the second-step of the general three-step simulation hierarchy (cf. Figure 1.4).

To achieve the second objective of assessing and improving the accuracy of the computational methods, higher level of theory calculations of the electronic structures of layered oxides are performed. Precisely, *GW* calculations are conducted and electronic structures are compared to those of various hybrid functionals while also their Hartree-Fock mixing parameter is scanned. These tests can deliver valuable insights for the last step of the three-stop modelling procedure (cf. Figure 1.4) at which mostly hybrid functionals are applied. The redox mechanism is determined in these calculations and comparisons to higher level of theory calculations can help to understand how well default hybrid functionals describe the electronic structure of layered oxide cathodes and if it might be worth and justified to alter their Hartree-Fock mixing parameters. While these considerations are crucial to perform accurate electronic structure calculations in simulation studies, they are also extremely valuable when a comparison of the predicted redox mechanism to experimental data is aimed for.

To specifically address the third and last objective of the thesis, several collaborative studies with experimental experts are performed, each involving the whole three-step simulation protocol (cf. Figure 1.4). These specific contributions aim to highlight how simulations provide insights that cannot be obtained from experiment and that a combination of theory and experiment is required to fully understand the mechanisms in novel cathode materials. These studies also highlight the predictive power of computational approaches and how they can be applied in discovering new materials. Furthermore, next to targeting the third objective of the thesis, case studies serve as a motivation and proof of concept for the computational methodologies that were developed throughout this thesis. A more detailed overview of how all these specific contributions relate to the chapters of this thesis as well as more details on their contributions to the different thesis objectives and advances in the three-step modelling procedure (cf. Figure 1.4) for cathode materials is given in the next section.

1.5 Thesis Outline

The thesis is outlined into 7 Chapters with the first (current) chapter (Chapter 1) being the introduction that motivates the thesis topic by highlighting the urge for the development of secondary batteries. Some general background information on the research of cathode materials and applied computational methods are given and the objectives of the thesis are outlined as well. The following 5 chapters compile the main contributions of the thesis. Their relation between the previously mentioned three-step simulation procedure (cf. Figure 1.4) and the thesis objectives listed above is sketched in Figure 1.5. It can be seen that the thesis and its chapters are structured along both dimensions, the simulations steps and thesis objectives.

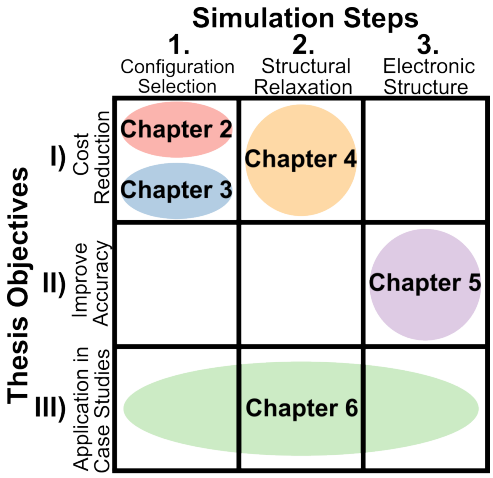

Figure 1.5: Matrix of thesis objectives (given in previous section) and simulation steps (given in Figure 1.4). While the contributions (chapters) often contribute to multiple fields of the matrix, they are located in the matrix fields with their strongest contribution.

Chapter 2 mainly addresses thesis objective I) and the first simulation step (cf. Figure 1.4) by introducing a code to achieve the configurational optimization problem in ionic crystals. An efficient implementation of various heuristic optimizers is provided, coupled with pre-calculated electrostatic energy terms. It is shown that such configurational optimizations are crucial in model selection for further DFT calculations. The focus of this contribution is on the efficient, parallel, and holistic implementation of several heuristic solvers that allow tackling significantly larger configurational problems in drastically reduced computational time. Such advancements are required for the computational research on cathode materials due to the ever-increasing complexity in terms of richer TM substitutions in combination with Li-/Na-vacancy orderings (especially for Na and P-phases) that are crucial to capture the material's properties correctly. Ultimately, the computational tools developed in this chapter are provided to the community of computational (battery) material researchers by an easy-to-use command-line tool.

The next chapter (Chapter 3) also mainly focuses on the first thesis objective (I) and the first simulation step (cf. Figure 1.4). The chapter employs the configurational optimization methodology developed in the previous chapter and extends it by considering the layered oxide phase in SIBs in terms of the stacking sequence of the layers along the *c*-direction as well. By optimization of electrostatic parameters to DFT references, it is aimed to develop a computationally inexpensive scheme to predict phase stabilities for a given cathode composition. Promising agreement to DFT data is achieved, which enables the method to pre-select phases for further DFT calculations of novel materials. As the determination of the most stable phase also goes beyond the bare configurational selection, this chapter also partially contributes to the second simulation step. It is outlined that the developed predictor matches reasonably well with experimentally observed phase stabilities as an overall prediction accuracy of 80 % is achieved on more than 270 experimental compositions. Thus, this chapter also targets thesis objective III). In conclusion, this chapter presents an efficient *ab initio* predictor for the phase stability of layered oxide cathodes for SIBs.

In Chapter 4 a Coulomb-Buckingham potential for layered oxide cathodes for SIBs is fitted and applied. Again, a focus on phase stability is targeted, but in contrast to the previous chapter, in a fully dynamic manner in terms of MD simulations. The chapter therefore aims to provide improvements for the second step of the general simulation procedure (cf. Figure 1.4) while its main objective is to also reduce the computational costs, corresponding to thesis objective I). The fitted Coulomb-Buckingham potential is applied in large-scale MD simulations allowing to directly observe phase transitions under standard lab conditions (*NpT* with 300 K and 1 bar) on the µs time-scale. This constitutes a significant advancement to existing studies as such simulations are prohibitively expensive with computationally less efficient methods. Moreover, also practical conclusions such as the decrease of the transition barrier on desodiation are made that are helpful for experimental studies and therefore contribute to the third thesis objective (III) as well. In summary, this chapter shows how the application of classical potentials to battery materials can allow simulations that are not possible by other, more expensive yet more accurate, methods while delivering valuable insights for experimental studies.

Chapter 5 is a deep-dive into the third step of the three-step modelling procedure for cathode materials (cf. Figure 1.4), namely the electronic structure calculation, while it is targeting thesis objective II). In particular, the chapter highlights that hybrid functionals, often used for electronic structure calculations, have at least one parameter, the Hartree-Fock mixing parameter α, that can be easily tuned. For evaluation of the hybrid functionals higher level of theory calculations within the so-called *GW* approximation are performed and the influence of α is thoroughly checked. Conclusions on how to choose a suitable α-value for the special material class of layered oxide LIB cathodes are made that can be of use in future simulational studies. It is also shown how the α-parameter affects the predicted redox mechanisms which is crucial in comparison to experimental studies and thus constitutes a contribution to the third thesis objective (III) too. To conclude, the accuracy of electronic structure calculations in layered oxide cathodes is assessed and directions for improvements are given.

The following chapter (Chapter 6) aims to combine all simulation steps (cf. Figure 1.4) into holistic computational studies of cathode materials. These studies can have significant contributions to the understanding and interpretation of experimental results. Therefore, this chapter mainly covers the third thesis objective (III). In particular, this chapter aims to showcase possible and actual applications of the methodologies developed in the previous chapters. To that extent, four case studies are shown of which three highlight how extensive computational simulations can yield insights on novel cathode materials that cannot be (easily) obtained experimentally, but help to identify and understand experimentally observed phenomena. Another case study is fully computational, proving that advancements made through the developed methods can allow for new simulational insights. In summary, this chapter motivates the method developments conducted in the previous theory chapters by highlighting direct applications in various studies. It is pointed out that these new methods and computational studies in general can contribute significantly to the in-depth understanding of cathode materials which is of great help for experimental studies and to allow for more rational material design in the future.

In the last chapter (Chapter 7) the main conclusions of the works presented in this thesis are summarized and some proposals for possible future research directions are made. The thesis is closed by listing all publications and conference contributions of the author followed by a brief self-introduction of the author as well as the acknowledgements.

REFERENCES

1. Guney, M. S. & Tepe, Y. Classification and assessment of energy storage systems. *Renewable and Sustainable Energy Reviews* **75,** 1187–1197 (2017).
2. Gallo, A. B., Simões-Moreira, J. R., Costa, H., Santos, M. M. & Moutinho dos Santos, E. Energy storage in the energy transition context: A technology review. *Renewable and Sustainable Energy Reviews* **65,** 800–822 (2016).
3. Ding, Y., Cano, Z. P., Yu, A., Lu, J. & Chen, Z. Automotive Li-Ion Batteries: Current Status and Future Perspectives. *Electrochemical Energy Reviews* **2,** 1–28 (2019).
4. Hounjet, L. J. Comparing lithium– and sodium–ion batteries for their applicability within energy storage systems. *Energy Storage* **4** (2022).
5. McIlwaine, N. *et al.* A state-of-the-art techno-economic review of distributed and embedded energy storage for energy systems. *Energy* **229,** 120461 (2021).
6. Zubi, G., Dufo-López, R., Carvalho, M. & Pasaoglu, G. The lithium-ion battery: State of the art and future perspectives. *Renewable and Sustainable Energy Reviews* **89,** 292–308 (2018).
7. Pimm, A. J., Palczewski, J., Barbour, E. R. & Cockerill, T. T. Using electricity storage to reduce greenhouse gas emissions. *Applied Energy* **282,** 116199 (2021).
8. Letcher, T. M. in *Storing Energy* 3–12 (Elsevier, 2022).
9. Sacchi, R., Bauer, C., Cox, B. & Mutel, C. When, where and how can the electrification of passenger cars reduce greenhouse gas emissions? *Renewable and Sustainable Energy Reviews* **162,** 112475 (2022).
10. Chakraborty, P. *et al.* Addressing the range anxiety of battery electric vehicles with charging en route. *Scientific reports* **12,** 5588 (2022).
11. Lamb, W. F. *et al.* A review of trends and drivers of greenhouse gas emissions by sector from 1990 to 2018. *Environmental Research Letters* **16,** 073005 (2021).
12. Armand, M. & Tarascon, J.-M. Building better batteries. *Nature* **451,** 652–657 (2008).
13. Vaalma, C., Buchholz, D., Weil, M. & Passerini, S. A cost and resource analysis of sodium-ion batteries. *Nature Reviews Materials* **3** (2018).
14. Yoshio, M., Brodd, R. J. & Kozawa, A. *Lithium-Ion Batteries* (Springer New York, New York, NY, 2009).
15. Shojaeddini, E., Alonso, E. & Nassar, N. T. Estimating price elasticity of demand for mineral commodities used in Lithium-ion batteries in the face of surging demand. *Resources, Conservation and Recycling* **207,** 107664 (2024).
16. Yang, X., Zhang, H., Liu, Q. & Jiang, G. The Li-ion battery industry and its challenges. *Nature reviews. Chemistry* **9,** 497–498 (2025).

17. Duffner, F. *et al.* Post-lithium-ion battery cell production and its compatibility with lithium-ion cell production infrastructure. *Nature Energy* **6,** 123–134 (2021).
18. Yoshino, A. The birth of the lithium-ion battery. *Angewandte Chemie (International ed. in English)* **51,** 5798–5800 (2012).
19. Zu, C.-X. & Li, H. Thermodynamic analysis on energy densities of batteries. *Energy & Environmental Science* **4,** 2614 (2011).
20. Scrosati, B. History of lithium batteries. *Journal of Solid State Electrochemistry* **15,** 1623–1630 (2011).
21. Nishi, Y. Lithium ion secondary batteries; past 10 years and the future. *Journal of Power Sources* **100,** 101–106 (2001).
22. Hwang, J.-Y., Myung, S.-T. & Sun, Y.-K. Sodium-ion batteries: present and future. *Chemical Society reviews* **46,** 3529–3614 (2017).
23. Kamat, P. V. Lithium-Ion Batteries and Beyond: Celebrating the 2019 Nobel Prize in Chemistry – A Virtual Issue. *ACS Energy Letters* **4,** 2757–2759 (2019).
24. Whittingham, M. Chemistry of intercalation compounds: Metal guests in chalcogenide hosts. *Progress in Solid State Chemistry* **12,** 41–99 (1978).
25. Mizushima, K., Jones, P. C., Wiseman, P. J. & Goodenough, J. B. LixCoO2 (0<x<-1): A new cathode material for batteries of high energy density. *Materials Research Bulletin* **15,** 783–789 (1980).
26. Da Deng. Li–ion batteries: basics, progress, and challenges. *Energy Science & Engineering* **3,** 385–418 (2015).
27. Liu, Y.-K. *et al.* Research Progresses of Liquid Electrolytes in Lithium-Ion Batteries. *Small (Weinheim an der Bergstrasse, Germany)* **19,** e2205315 (2023).
28. Li, M., Lu, J., Chen, Z. & Amine, K. 30 Years of Lithium-Ion Batteries. *Advanced materials (Deerfield Beach, Fla.),* e1800561 (2018).
29. Manthiram, A. A reflection on lithium-ion battery cathode chemistry. *Nature communications* **11,** 1550 (2020).
30. Schipper, F. *et al.* Review—Recent Advances and Remaining Challenges for Lithium Ion Battery Cathodes. *Journal of The Electrochemical Society* **164,** A6220–A6228 (2017).
31. Nzereogu, P. U., Omah, A. D., Ezema, F. I., Iwuoha, E. I. & Nwanya, A. C. Anode materials for lithium-ion batteries: A review. *Applied Surface Science Advances* **9,** 100233 (2022).
32. Cheng, H., Shapter, J. G., Li, Y. & Gao, G. Recent progress of advanced anode materials of lithium-ion batteries. *Journal of Energy Chemistry* **57,** 451–468 (2021).
33. Xu, K. Li-ion battery electrolytes. *Nature Energy* **6,** 763 (2021).
34. Lagadec, M. F., Zahn, R. & Wood, V. Characterization and performance evaluation of lithium-ion battery separators. *Nature Energy* **4,** 16–25 (2019).
35. Luiso, S. & Fedkiw, P. Lithium-ion battery separators: Recent developments and state of art. *Current Opinion in Electrochemistry* **20,** 99–107 (2020).

36. Yabuuchi, N., Kubota, K., Dahbi, M. & Komaba, S. Research development on sodium-ion batteries. *Chemical reviews* **114,** 11636–11682 (2014).

37. Myung, S.-T. *et al.* Nickel-Rich Layered Cathode Materials for Automotive Lithium-Ion Batteries: Achievements and Perspectives. *ACS Energy Letters* **2,** 196–223 (2017).

38. Andre, D. *et al.* Future generations of cathode materials: an automotive industry perspective. *Journal of Materials Chemistry A* **3,** 6709–6732 (2015).

39. Liu, J. *et al.* Recent breakthroughs and perspectives of high-energy layered oxide cathode materials for lithium ion batteries. *Materials Today* **43,** 132–165 (2021).

40. Chayambuka, K., Mulder, G., Danilov, D. L. & Notten, P. H. L. From Li–Ion Batteries toward Na–Ion Chemistries: Challenges and Opportunities. *Advanced Energy Materials* **10** (2020).

41. De Biasi, L. *et al.* Chemical, Structural, and Electronic Aspects of Formation and Degradation Behavior on Different Length Scales of Ni-Rich NCM and Li-Rich HE-NCM Cathode Materials in Li-Ion Batteries. *Advanced materials (Deerfield Beach, Fla.)* **31,** e1900985 (2019).

42. Hu, S. *et al.* Li-Rich Layered Oxides and Their Practical Challenges: Recent Progress and Perspectives. *Electrochemical Energy Reviews* **2,** 277–311 (2019).

43. Sun, X., Hao, H., Hartmann, P., Liu, Z. & Zhao, F. Supply risks of lithium-ion battery materials: An entire supply chain estimation. *Materials Today Energy* **14,** 100347 (2019).

44. Larcher, D. & Tarascon, J.-M. Towards greener and more sustainable batteries for electrical energy storage. *Nature chemistry* **7,** 19–29 (2015).

45. Padhi, A. K., Nanjundaswamy, K. S. & Goodenough, J. B. Phospho–olivines as Positive–Electrode Materials for Rechargeable Lithium Batteries. *Journal of The Electrochemical Society* **144,** 1188–1194 (1997).

46. Ahsan, Z. *et al.* Recent Progress in Capacity Enhancement of LiFePO4 Cathode for Li-Ion Batteries. *Journal of Electrochemical Energy Conversion and Storage* **18** (2021).

47. Zhang, J. & Li, X. Perspective on Phase Transition in Layered Oxide Cathodes for Sodium-Ion Batteries: Mechanism, Influenced Factors, and Inhibition Strategies. *Energy & Fuels* **38,** 13906–13933 (2024).

48. Guo, Y.-J. *et al.* Sodium layered oxide cathodes: properties, practicality and prospects. *Chemical Society reviews* **53,** 7828–7874 (2024).

49. Wang, J. *et al.* Routes to high-performance layered oxide cathodes for sodium-ion batteries. *Chemical Society reviews* **53,** 4230–4301 (2024).

50. Wang, P.-.-F., You, Y., Yin, Y.-.-X. & Guo, Y.-.-G. Layered Oxide Cathodes for Sodium–Ion Batteries: Phase Transition, Air Stability, and Performance. *Advanced Energy Materials* **8** (2018).

51. Delmas, C. Sodium and Sodium–Ion Batteries: 50 Years of Research. *Advanced Energy Materials* **8** (2018).

52. Delmas, C., Fouassier, C. & Hagenmuller, P. Structural classification and properties of the layered oxides. *Physica B+C* **99,** 81–85 (1980).

53. Momma, K. & Izumi, F. VESTA : a three-dimensional visualization system for electronic and structural analysis. *Journal of Applied Crystallography* **41,** 653–658 (2008).

54. Gu, M., Xu, J., Shi, X., Shao, L. & Sun, Z. Research progress of oxygen redox in sodium–layered oxides. *Battery Energy* **3** (2024).

55. Euchner, H. & Groß, A. Atomistic modeling of Li- and post-Li-ion batteries. *Physical Review Materials* **6** (2022).

56. Das, T., Yang, M. Y., Merinov, B. V. & Goddard, W. A. in *Computational Design of Battery Materials* (ed Hanaor, D. A. H.) 13–76 (Springer International Publishing, Cham, 2024).

57. Bai, Q., Yang, L., Chen, H. & Mo, Y. Computational Studies of Electrode Materials in Sodium–Ion Batteries. *Advanced Energy Materials* **8** (2018).

58. Zhao, S. *et al.* First-principles computational insights into lithium battery cathode materials. *Electrochemical Energy Reviews* **5,** 1–31 (2022).

59. Ma, Y. Computer Simulation of Cathode Materials for Lithium Ion and Lithium Batteries: A Review. *Energy & Environmental Materials* **1,** 148–173 (2018).

60. Hanaor, D. A. H. *Computational Design of Battery Materials* (Springer International Publishing, Cham, 2024).

61. Hautier, G. *Prediction of new battery materials based on ab initio computations* in *Proceedings of the 2nd International Freiberg Conference on Electrochemical Storage Materials* (AIP Publishing, 2016), 020009.

62. Lu, Z., Zhu, B., Shires, B. W. B., Scanlon, D. O. & Pickard, C. J. Ab initio random structure searching for battery cathode materials. *The Journal of chemical physics* **154,** 174111 (2021).

63. Islam, M. S. & Fisher, C. A. J. Lithium and sodium battery cathode materials: computational insights into voltage, diffusion and nanostructural properties. *Chemical Society reviews* **43,** 185–204 (2014).

64. Yan, L.-M., Su, J.-M., Sun, C. & Yue, B.-H. Review of the first principles calculations and the design of cathode materials for Li-ion batteries. *Advances in Manufacturing* **2,** 358–368 (2014).

65. Kansara, S., Kang, H., Ryu, S., Sun, H. H. & Hwang, J.-Y. Basic guidelines of first-principles calculations for suitable selection of electrochemical Li storage materials: a review. *Journal of Materials Chemistry A* **11,** 24482–24518 (2023).

66. Okhotnikov, K., Charpentier, T. & Cadars, S. Supercell program: a combinatorial structure-generation approach for the local-level modeling of atomic substitutions and partial occupancies in crystals. *Journal of cheminformatics* **8,** 17 (2016).

67. d'Avezac, M. & Zunger, A. Identifying the minimum-energy atomic configuration on a lattice: Lamarckian twist on Darwinian evolution. *Physical Review B* **78** (2008).

68. Wei, S., Ferreira, L. G., Bernard, J. E. & Zunger, A. Electronic properties of random alloys: Special quasirandom structures. *Physical review. B, Condensed matter* **42,** 9622–9649 (1990).

69. Laks, D. B., Ferreira, L. G., Froyen, S. & Zunger, A. Efficient cluster expansion for substitutional systems. *Physical review. B, Condensed matter* **46,** 12587–12605 (1992).

70. Sanchez, J. M. Cluster expansions and the configurational energy of alloys. *Physical review. B, Condensed matter* **48,** 14013–14015 (1993).

71. Sholl, D. S. & Steckel, J. A. *Density functional theory: A practical introduction* (Wiley, Hoboken N.J., 2009).

72. Born, M. & Oppenheimer, R. Zur Quantentheorie der Molekeln. *Annalen der Physik* **389,** 457–484 (1927).

73. Hohenberg, P. & Kohn, W. Inhomogeneous Electron Gas. *Physical Review* **136,** B864–B871 (1964).

74. Kohn, W. & Sham, L. J. Self-Consistent Equations Including Exchange and Correlation Effects. *Physical Review* **140,** A1133–A1138 (1965).

75. Perdew, J. P., Burke, K. & Ernzerhof, M. Generalized Gradient Approximation Made Simple. *Physical review letters* **77,** 3865–3868 (1996).

76. Bloch, F. ber die Quantenmechanik der Elektronen in Kristallgittern. *Zeitschrift für Physik* **52,** 555–600 (1929).

77. Blöchl, P. E. Projector augmented-wave method. *Physical review. B, Condensed matter* **50,** 17953–17979 (1994).

78. Jensen, F. *Introduction to computational chemistry* Third edition (Wiley, Chichester UK and Hoboken NJ, 2017).

79. Verlet, L. Computer "Experiments" on Classical Fluids. I. Thermodynamical Properties of Lennard-Jones Molecules. *Physical Review* **159,** 98–103 (1967).

80. Jinnouchi, R., Karsai, F. & Kresse, G. On-the-fly machine learning force field generation: Application to melting points. *Physical Review B* **100** (2019).

81. Iori, F., Gatti, M. & Rubio, A. Role of nonlocal exchange in the electronic structure of correlated oxides. *Physical Review B* **85** (2012).

82. Hartree, D. R. The Wave Mechanics of an Atom with a Non-Coulomb Central Field. Part I. Theory and Methods. *Mathematical Proceedings of the Cambridge Philosophical Society* **24,** 89–110 (1928).

83. Fock, V. Nherungsmethode zur Lsung des quantenmechanischen Mehrkrperproblems. *Zeitschrift fr Physik* **61,** 126–148 (1930).

84. Becke, A. D. A new mixing of Hartree–Fock and local density-functional theories. *The Journal of chemical physics* **98,** 1372–1377 (1993).

85. Becke, A. D. Density-functional thermochemistry. IV. A new dynamical correlation functional and implications for exact-exchange mixing. *The Journal of chemical physics* **104,** 1040–1046 (1996).

2

CONFIGURATIONAL OPTIMIZATION:

OPTIMIZATION OF COULOMB ENERGIES IN GIGANTIC CONFIGURATIONAL SPACES OF MULTI-ELEMENT IONIC CRYSTALS

Most of the novel energy materials contain multiple elements occupying a single site in their lattice. The exceedingly large configurational space of these materials imposes challenges in determining low(est) energy structures. Coulomb energies of possible configurations generally show a satisfactory correlation to computed energies at higher levels of theory and thus allow to screen for minimum-energy structures. Employing an expansion into a binary optimization problem, an efficient Coulomb energy optimizer is obtained using Monte Carlo and Genetic Algorithms. The presented optimization package, GOAC (Global Optimization of Atomistic Configurations by Coulomb), can achieve a speed up of several orders of magnitude compared to existing software. In this work, heuristic optimization on various material classes is performed. Thus, GOAC provides an efficient method for constructing low-energy atomistic models for ionic multi-element materials with gigantic configurational spaces.

This chapter is published as: **Köster, K.**, Binninger, T. & Kaghazchi, P. Optimization of Coulomb energies in gigantic configurational spaces of multi-element ionic crystals. npj Comput Mater **11**, 202 (2025).

2.1 Introduction

Many state-of-the-art solid-state high performance materials are composed of several different types of elements sharing the same lattice sites. Examples for application areas are, but not limited to, energy conversion and storage systems[1–11] as well as other special-purpose applications[12–16]. In some of the most interesting materials for these applications (e.g., layered oxides, ionic conductors), numerous element types with various concentration ratios are combined in a single-crystal phase. While such compositions can be represented with the help of partial site occupations, the configurational complexity becomes a severe challenge for simulation methods that require structural models with integer site occupations, such as commonly used density functional theory (DFT)[17, 18]. The problem of determining reasonable atomistic configurations out of all possible configurations therefore constitutes a serious challenge for modelling and simulation[19–24]. To represent complex compositions with integer occupations the so-called supercell approach is frequently employed, where multiple periodic images of the unit cell are treated explicitly. For computational studies it is often of interest to determine low(est)-energy atomistic configurations which can be a hard combinatorial problem for large supercells. For complex compositions it is generally infeasible to evaluate all possible configurations (even when accounting for symmetry), especially when using high-level methods such as DFT. Therefore, special techniques such as the Coherent Potential Approximation (CPA) [25], Special Quasirandom Structure (SQS)[26], Cluster Expansion (CE)[27, 28], Virtual Crystal Approximation (VCA) [29], or Small Set of Ordered Structures (SSOS) [30] have been developed that approximate the energy and/or are able to find special atomistic configurations that have relevant properties for further investigations. Approximations such as CE where many-particle interaction terms up to a certain order are taken into account can reduce the computational demand drastically[31]. Other approaches that try to mimic highly accurate energies at low computational costs include machine-learned potentials and/or try to reduce the amount of configurations that must be evaluated with other machine learning approaches, e.g., active learning[32–37].

Naturally, the number of possible configurations becomes higher if the supercell contains more sites, more positions per site, and also when more elements can occupy a site, especially when elements are mixed in equimolar amounts. All of these factors generally apply to novel energy materials and yield a combinatorial explosion of the total number of possible configurations. For highly symmetric cells, this number can be reduced by several orders of magnitude if symmetry operations are taken into account and only symmetrically irreducible configurations are considered[38]. There are several software packages and methods such as the site-occupancy disorder (SOD) code[39], ENUMLIB[40] (also accessible through PYMATGEN[41]), the solid-solution tools[42, 43] in the commercial CRYSTAL code[44], the so-called SUPERCELL software[45], the DISORDER code[46] and its recently published tree search algorithm[38], and the SHRY package[47] that all focus explicitly on determining symmetry in-equivalent structures. The number of available software and considerable computational effort spent highlights the importance of the atomistic combinatorial problem in computational materials research.

For ionic crystals, the Coulomb energy with ionic point charges represents a simple energy model allowing to evaluate numerous atomistic configurations with limited computational resources. In practice, the model requires the assignment of the ion valencies and the electrostatic energy is calculated by Ewald summation [48] to obtain the exact Coulomb energy of the periodic lattice[49]. This allows to consider plenty of atomistic configurations explicitly and, in some cases, even the complete enumeration of all possible configurations for practical simulation supercells. This full enumeration approach, sometimes also referred to as brute force method or exhaustive sampling, is implemented with Coulomb energy evaluation in the so-called SUPERCELL software[45]. More recently, the EWALDSOLIDSOLUTION software[50] was released offering the brute-force approach with an option for sparser sampling of the density of states based on Coulomb energy evaluation. In addition, EWALDSOLIDSOLUTION also features a post-processing gradient-descent-like algorithm for optimizing atomistic configurations. However, treating complex combinatorial problems as they appear in modern energy materials by brute forcing is computationally very demanding, even for simple Coulomb energy evaluation. Therefore, classical optimization approaches and the use of heuristics is commonly required.

The atomistic combinatorial sampling can be considered as a general optimization problem and commonly used meta heuristics can be applied. Do Lee *et al.*[51] applied some well-known heuristics, including genetic algorithms, particle swarm optimization, harmony search, cuckoo search, bayesian optimization, and deep Q-networks, to configurational optimization in argyrodite utilizing Coulomb energies. Out of the vast amount of meta heuristics especially the Genetic Algorithm (GA)[52] should be mentioned that is known to be effective for the atomistic combinatorial problem[51, 53], as well as for global optimization of complex chemical structures in general[54]. Next to these classical approaches, more physically motivated approaches such as Monte Carlo (MC)[55] simulations were also shown to be efficient in approaching the atomistic configurations problem[32, 56–58], with the respective Monte Carlo methods implemented, e.g., for determination of SQS in the MCSQS code[59] as part of the ALLOY THEORETIC AUTOMATED TOOLKIT (ATAT)[60] or for general cluster expansions within the recently released STATISTICAL MECHANICS ON LATTICES package[61]. Binninger *et al.*[56] recently also demonstrated that the configuration problem can be solved on existing quantum-computing hardware by formulating it as a binary optimization problem that can be mapped onto a quantum annealer.

The aforementioned software and approaches for determining lowest energy atomistic configurations are either effectively or explicitly limited in the size of the configurational space[39, 41–43, 45, 51, 56, 61] or do not specifically aim to determine the low(est) Coulomb energy structures by optimization[38, 40, 46, 50, 59]. As modern high performance materials introduce more and more species, approaches are required that can reliably and quickly optimize even large combinatorial problems comprising of ten to the power of several hundreds of configurations. For that purpose, either heuristics or general purpose optimization software can be used while the latter one bears the opportunity for exact global optimization within limited computational resources. Even though some works already employed heuristic optimization methods to the configuration problem, as discussed before, there is still, to the best of our knowledge, no pub-

lished tool that allows for optimization of such complex problems yet. Efficient energy evaluation methods, even faster than the commonly applied Ewald summation, along with specifically tailored heuristics must be employed to achieve optimization in difficult atomistic combinatorial problems within reasonable computation time. Creating optimized atomistic configurations for complex problems in a high-throughput manner allows for efficient structure pre-selection for computational studies, such as DFT calculations, of novel materials and thereby offers the opportunity to enhance computational materials discovery in several important research fields.

In this work, the atomistic combinatorial problem in novel energy materials is approached as an optimization problem utilizing a basic but reformulated Coulomb energy model. A Python-based code, termed GOAC (Global Optimization of Atomistic Configurations by Coulomb) is presented, that enables to interface any configuration problem of ions with distinctive valancies given as a crystallographic information file (CIF)[62] to existing (free or commercial) optimization software. CIFs are read with help of the PYMATGEN[41] package. Moreover, several Fortran-based routines are introduced that can be called from the Python code to apply various heuristics to the configurational optimization problem, including GA and MC. To provide a highly efficient implementation, the Coulombic energy is expressed by a binary optimization problem and the optimization heuristics are parallelized using OpenMP[63]. The methodological details of the implementations and the capabilities of the GOAC code are discussed in the next section, followed by a discussion of the results and benchmarking to alternative methods.

2.2 Results

2.2.1 Implementation and Theoretical Background

A supercell is assumed comprising S sites with partial occupations and each site having P_s positions within the cell. Moreover, a site should be occupied by $N_{s,e}$ ions of the element e while in total E_s elements can occupy the given site s. The total number of possible configurations C in the supercell, without considering any symmetries, is then given by:

$$C = \prod_{s=1}^{S} \frac{P_s!}{\prod_{e=1}^{E_s} N_{s,e}!}. \tag{2.1}$$

For a given problem, the Global Optimization of Atomistic Configurations by Coulomb (GOAC) code aims to determine low(est) energy atomistic configuration(s) out of all possible configurations employing various optimization techniques. To this end, GOAC offers a command line interface to provide a CIF with partial occupations and assumed charge states (valencies) for the different ions. The general workflow of GOAC is sketched in Figure 2.1.

In a first step, GOAC calculates the required pairwise Ewald energy matrix-elements, which is discussed in the next section. Then, a binary optimization problem is constructed by expansion to site-specific terms that can be either interfaced to external optimizers, e.g., the GUROBI solver[64], or solved by internal Fortran heuristics. Both approaches are discussed in the following sections. Finally, the n lowest energy atomistic configurations are outputted as a CIF along with the respective Coulomb energies.

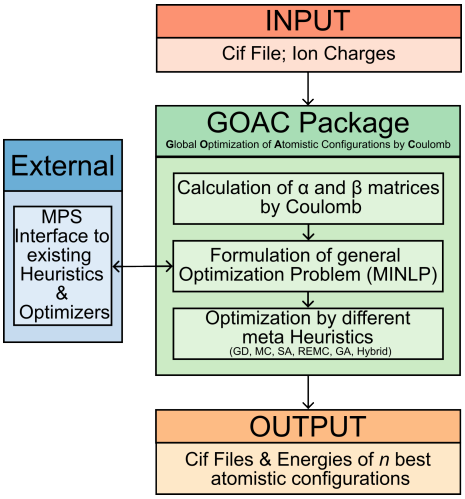

Figure 2.1: Schematic workflow of the GOAC code and connection to external packages.

It should be noted that, in its current implementation, GOAC is not able to identify symmetry-equivalent structures and all optimizers run on the full configurational space. However, filtering by energy is possible to only include structures that are different in energy, which can be useful for many problems but might exclude symmetry in-equivalent structures in some problems.

Pre-Calculation of Coulomb Energy Terms

As optimization methods generally require evaluating the energy of many different atomistic configurations, GOAC implements an ionic Coulomb energy model due to the low computational demand. Naturally, such simple point charge models cannot account for quantum mechanical effects and there is no guarantee that the order of different ionic configurations by Coulomb energy is aligned with the one obtained by more accurate calculations, e.g., based on DFT. However, several studies showed that structures with a low Coulomb energy are often also good candidates for low DFT energies[50, 51, 56, 58, 65]. As an example, a satisfactory correlation between DFT and Coulomb energies at randomly selected configurations is shown in Figure 2.2 for ionic configurations in the layered oxide $Na[Li_{0.33}Mn_{0.67}]O_2$ (assumed ionic charges: Na: +1; Li: +1; Mn: +4; O: −2) that was synthesized by Wang *et al.*[66]. The relative energies show a strong correlation between DFT and Coulomb models and the linear fit well matches the diagonal representing perfect correlation. A commonly employed approach therefore consists in pre-selecting a certain number of low Coulomb energy structures to be used for more accurate DFT calculations and eventually determine low DFT energy configurations[65, 67–70].

Following this approach, GOAC utilizes point-charge Coulomb energies and expands them into a binary optimization model with site coefficients up to the second order. It is noted that for the specific case of the point-charge Coulomb energy this expansion is exact due to the pairwise character of Coulomb point-charge interactions. This allows

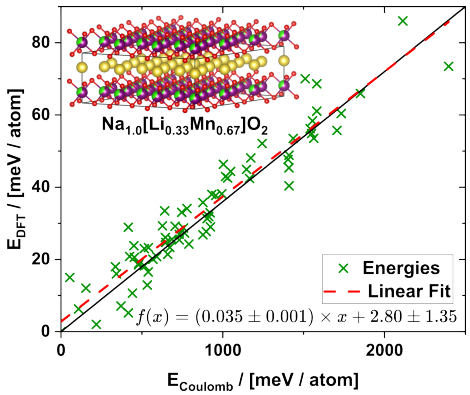

Figure 2.2: Correlation between relative DFT (details are described in the Method section) and Coulomb energies of different ionic configurations for $Na[Li_{0.33}Mn_{0.67}]O_2$. Coulomb energies were obtained with the following ionic valencies: Na: +1; Li: +1; Mn: +4; O: −2. A linear fit of the data points is shown as a red dashed line, along with the ideal correlation diagonal (black solid line).

for an efficient evaluation of different atomistic configurations during optimization as the energy can be expressed as a sum of pre-calculated coefficients. In periodic systems, Coulomb energies are, however, difficult to converge and the Ewald summation technique is required for the energy calculation.

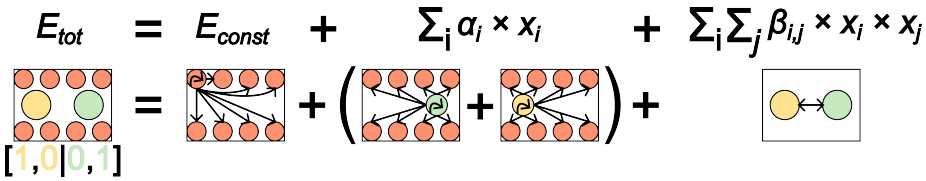

Figure 2.3: The energy calculation approach. Schematic visualization of the expansion approach to binary variables for iterative sites for the energy calculation of atomistic configurations along with the simplified energy formula and an example on how to map specific atomistic configurations on a binary vector. Arrows indicate pairwise interaction terms in the Ewald matrix while for the constant term only interactions for one site are shown exemplary.

The procedure of expressing the atomistic combinatorial problem as a binary optimization problem is sketched in Figure 2.3. The total energy (E_{tot}) of a given atomistic configuration can be expressed as a sum of the energy of the fixed ions (zero-order term, E_{const}), the interaction of each placed iterative ion with the fixed ions as well as its self-interaction due to periodic boundary conditions (first-order term, α), and all particle-particle interactions between all placed iterative sites (second-order term, β). All interactions in the resulting binary optimization model can be pre-calculated for efficient energy evaluation during optimization. In order to do this, the elements of the pairwise interaction matrix of the Ewald energy x^{total} can be calculated by:[71]

$$x_{ij}^{\text{real}} = q_i q_j \sum_{\mathbf{L}} \frac{\operatorname{erfc}(\eta \cdot d_{ij})}{d_{ij}} \tag{2.2}$$

$$x_{ij}^{\text{recip}} = \frac{q_i q_j}{\pi V} \sum_{\mathbf{k}} \frac{\exp\left(\frac{-|\dot{k}|^2}{4\eta^2}\right)}{|\dot{k}|^2} \cdot \cos\left(\dot{k}\left(\dot{r}_i - \dot{r}_j\right)\right) \tag{2.3}$$

$$x_{ii}^{\text{self}} = \frac{-q_i^2 \eta}{\sqrt{\pi}} \tag{2.4}$$

$$x_{ij}^{\text{total}} = x_{ij}^{\text{real}} + x_{ij}^{\text{recip}} + x_{ij}^{\text{self}} \tag{2.5}$$

In these equations i and j are the indices of two sites, $\dot{r}$ is their position, q their charge, and d_{ij} the Euclidean distance between them. The cell volume is denoted as V, $\mathbf{L}$ is the sum over all real-space lattice vectors and $\mathbf{k}$ over (non-zero) reciprocal-space lattice vectors within the respective cut-off radii and η is the screening length. While the theory and implementation of Ewald summation is already extensively discussed in the literature, for example by Faber *et al.*[71], it should be highlighted that for the energy calculation of configurational optimization problems, the real-space and reciprocal-space terms can be split into an charge-dependent (q-dependent) and position-dependent (r-dependent or d-depended) term. The computationally demanding parts are in the position-depended expressions as the sum over all real-space ($\mathbf{L}$) and reciprocal-space ($\mathbf{k}$) lattice vectors has to be considered. As the pre-calculation of all pairwise interactions of a configurational optimization problem requires to evaluate multiple charges on fixed positions, the position-dependent terms of the real- and reciprocal-parts only have to be considered once for each site-pair. This can result in an additional speed-up compared to standard Ewald summations of different configurations as not just every pairwise interaction is only considered once, but also the computationally demanding summations over lattice vectors are only performed once for each pair of different positions. GOACs implementation to calculate the pairwise interaction Ewald summation energy matrix for configurational optimization problems utilizes this shortcut and in addition parallelizes the calculation of the matrix elements. From the Ewald summation matrix it is straight forward to construct the binary optimization problem by summing up the matrix elements that correspond to the black arrows in Figure 2.3 to obtain the values for E_{const} and all expansion coefficients α and β. It is noted, that this expansion can be considered as special case of a general second-order cluster expansion without the requirements for any distance cut-offs as periodic pair-wise interactions are considered exactly by Ewald summation. Thus, cutting the expansion at the second interaction order yields the exact Coulomb energy of a configuration.

GOAC also allows to consider Gaussian smeared charges instead of point-charges by applying to following correction to the point-charge energy-terms:[72]

$$x_{ij} = x_{ij}^{Point} - \frac{1}{2} q_i q_j \sum_{\mathbf{L}} \frac{\operatorname{erfc}\left(\frac{\sigma_i \sigma_j}{\sqrt{\sigma_i^2 \sigma_j^2}} d_{ij}\right)}{d_{ij}}. \tag{2.6}$$

In this equation σ is related to the smearing width $\hat{\sigma}$ of the Gaussian shaped charge by $1/(\sqrt{2}\sigma)$. It should be noted that no correction to the self-energy is applied to ensure

a convergence towards the point-charge energy for $\hat{\sigma} \to 0$. This does practically also do not influence the configuration search as the self-energy cancels out when two different configurations are compared.

For the exemplary problem in Figure 2.3 with two sites that are both occupied by 50 % by two different species, all possible configurations can be expressed by a binary solution vector x that has a position for each site for each species. A possible solution would than have a 1 on every position where a species is placed and a 0 everywhere else. By that, the total energy of a given instance becomes a simple sum of products of pre-calculated first-order (α) and second-order (β) coefficients and the binary solution vector x. To ensure that only second-order terms are counted where both ions are placed, the β-coefficients are multiplied by the two corresponding positions in the binary solution vector. Due to the pairwise character of Coloumb energies such an expansion to a binary optimization problem is able to give the correct periodic energy for each configuration by pre-calculated coefficients.

For implementing the binary optimization problem, a slight reformulation of the equation in Figure 2.3 appears to be practical where the solution vector x has two dimensions, one for the site-species (i) and one for the positions this site-species can occupy (j). Consequently, the expansion coefficients α and β become higher in dimensionality as well. By reformulation of the sums it is ensured that each interaction is only counted in one direction and just one half of the diagonal α and β matrices must be stored. Lastly, for a full optimization problem the constraints have to be defined. Beyond the binary constraint for the x variables (Equation 2.10) it must be also ensured by additional constraints that the desired total occupancy (O_i) is matched for each site-species i (Equation 2.8) and that a certain position j is not occupied by multiple species i (Equation 2.9). In summary, the optimization problem of atomistic configurations is implemented in GOAC as shown in Equation 2.7-2.10.

$$\begin{aligned} \min_{E_{tot}} \quad & E_{tot} = E_{const} + \sum_{i=1}^{S} \sum_{j=1}^{P_i} \alpha_{i,j} \cdot x_{i,j} + \\ & \sum_{i=1}^{S} \sum_{j=1}^{P_i} \sum_{l=j+1}^{P_i} \beta_{i,j,i,l} \cdot (x_{i,j} \cdot x_{i,l}) + \\ & \sum_{i=1}^{S} \sum_{j=1}^{P_i} \sum_{k=i+1}^{S} \sum_{l=1}^{P_k} \beta_{i,j,k,l} \cdot (x_{i,j} \cdot x_{k,l}) \end{aligned} \tag{2.7}$$

subject to:

$$\sum_{j=1}^{P_i} x_{i,j} = O_i \quad \forall i \in S \tag{2.8}$$

$$\sum_{i=1}^{S} x_{i,j} \leq 1 \quad \forall j \in P_i \tag{2.9}$$

$$x_{i,j} \in \{0;1\} \quad \forall i \in S; \quad \forall j \in P_i \tag{2.10}$$

Even though Coulomb (Ewald summation) calculations are computationally comparably inexpensive, for high-throughput evaluations of atomistic configurations Equations 2.7-2.10 represent a significant speed-up compared to a full Ewald summation for each atomistic configuration. Moreover, by storing the expansion coefficients (α and β), the pre-calculated energy terms conveniently allow to test multiple optimization approaches without performing energy calculations every time.

2.2.2 Optimization Strategies for Atomistic Configurations

Two main categories of optimizers, namely exact and heuristic optimizers, can be distinguished. A successful run of an exact optimizer guarantees that the global optimum is found or, if specified, not just the global optimum but the n lowest energy structures while n can be freely chosen by the user. The heuristic optimizers guarantee to output a valid, low energy structure that might be the global minimum or just a local minimum or no minimum at all, depending on the optimizer. The focus of heuristics is to create valid, high-quality solutions fast, while exact optimizers spend significant effort on proving optimality without improving the actual minimum solution. Depending on the needs of the user, both approaches can be valuable and are accessible via the GOAC code as described in the next sections.

Interfacing to External Exact Optimizers

Generally speaking, Equations 2.7-2.10 describe a so-called mixed integer non-linear programming (MINLP) problem with the special circumstance that all variables are not just integer but binary variables which technically allows for a reformulation to a mixed integer linear programming (MILP) problem. Problems of the same type frequently appear in the context of business economics under the collective term *Operations Research*, where the aim is, e.g., to determine the optimal (shortest/fastest) delivery route[73] or to optimize production planning[74]. Due to the economic value connected to this problem type plenty of optimizers exist[75]. Their aim is to find the global optimum and also prove that the global optimum was found employing advanced mathematical strategies that can be faster than a full enumeration of all possible solutions (brute forcing), which, by definition, is also an exact optimization method.

For a given atomistic combinatorial problem, GOAC can create a standard MINLP with the help of the licensed Gurobi[64] software and the full problem statement is written to a standard MPS (Mathematical Programming System) file. By default, GOAC passes this MINLP also to Gurobi for solving, however, it should be noted that the MPS file can be used to run the problem in other (commercial or free) optimization software. GOAC supports interfacing to the Gurobi optimizer and its solver parameters. It is worth noting that Gurobi (and other software) is technically capable of linearizing the quadratic terms in the MINLP to an MILP due to the binary character of the integer variables. This is not done by default in GOAC but was found to be efficient for some problems. Such a reformulation can also allow the use of other standard optimization software that are not capable of general MINLPs. However, results for exact optimizations presented in this work were obtained with the default Gurobi parameter set in GOAC, which was found to be most robust for different configuration problems. It should be noted that the MPS file of the problem can be also handed to non-exact heuristic solvers.

Internal Fortran Heuristics in GOAC

The core of the GOAC code offers different heuristic optimizers for the atomistic combinatorial problem that are all tailored for this specific problem and implemented in Fortran. All of these heuristics are capable of generating valid low energy structures. The following methods are currently supported in the GOAC code: a random structure generator, a Greedy Heuristic, a Gradient Descent algorithm (GD), a Metropolis Monte Carlo code (MC)[55], a simulated annealing extension of the MC code (SA), a Replica Exchange Monte Carlo scheme (REMC)[76], and a Genetic Algorithm (GA)[52] with roulette wheel selection[77]. The random structure generation occupies sites randomly and resulting structures are not as random as structures obtained by, e.g., SQS. It is also possible to combine some of the aforementioned heuristics to a hybrid approach. Such combinations were already proposed and proven successful for chemical optimization problems[78, 79] and a combination of the REMC and GA heuristic is benchmarked and referred to as HY in the following. The functionalities of the different algorithms are discussed in more detail in the manual and the code can be directly accessed within the project repository (see Code Availability Statement).

Most heuristics that are directly implemented in the GOAC code are of stochastic nature and it can be useful to run the same heuristic multiple times. By that procedure, the probability and confidence that the global minimum and other low energy structures are found can be increased. For convenience, GOAC allows to run the same heuristic multiple times in parallel with the help of OpenMP[63] which allows to achieve an statistic ensemble over multiple runs with the same heuristic. Moreover, trivial parallelizations such as, e.g., parallelization over the different temperatures in REMC are also implemented via OpenMP in GOAC to further boost the performance of the code. The scaling behavior of the different algorithms is also sketched in Supplementary Figure 2.7. Finally, the internal heuristics in GOAC offer abortion by run time or heuristic steps without improvement on the global minimum. More detailed descriptions of GOAC's features and how to employ them can be found in the manual inside the project repository (see Code Availability Statement).

2.2.3 Performance of Exact Optimization Methods

As explained above, GOAC has the possibility to interface to external optimization software for exact optimization of atomistic configurations. For this benchmark, the Gurobi optimizer, which utilizes an advanced branch-and-cut method, is employed with the default parameter set GOAC uses to interface to Gurobi. This parameter set enforces strong pre-solving of the model (Presolve=2) along with a focus on proving optimality (MIPFocus=2). It also ensures that the n lowest energy structures are found by setting the convergence boundaries to zero (MIPGap=0 and MIPGapAbs=0) and the "PoolSearchMode" to 2. To the best of our knowledge, the existing software for exact optimization of configurations, i.e., including proof of optimality, employ the full enumeration approach. An efficient implementation of the latter can be found in the SUPERCELL software, which is used as a reference for timings of full enumeration. Here it should be noted that the SUPERCELL software only considers the symmetry in-equivalent structures which reduces the number of explicitly considered atomistic configurations drastically compared to the total number of configurations when ignoring symmetry.

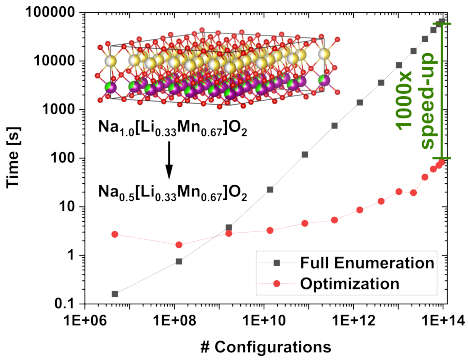

Figure 2.4: Scaling of full enumeration versus optimization. $\log_{10}$-$\log_{10}$ representation of run time (estimated from outputted timings of the software) to find the global optimum atomistic configuration versus number of total possible configurations using the full enumeration approach and external optimization software.

The SUPERCELL software and the optimization with Gurobi of the model prepared by GOAC were tested on a layered-oxide sodium-ion-battery cathode material ($Na[Li_{1/3}Mn_{2/3}]O_2$)[66] with one layer in the *c*-direction and partial occupations in both the transition-metal and sodium-ion sites, cf. Figure 2.4. By changing the sodium-ion stoichiometry from 1.0 to 0.52, configuration combinatorics with steadily increasing number of total possible configurations ranging from ca. 10^7 to 10^{14} were created and evaluated by both approaches. Such variation of the sodium concentration is also a practical example as it is a common task of battery material simulations to find sodium configurations at various concentrations that are suitably low in energy to predict accurate operation voltages.[80] Charge states of Na^+, Li^+, Mn^{4+} and a variable oxidation state of oxygen ranging from -2.0 (for a Na stoichiometry of 1) to -1.75926 (for a Na stoichiometry of 0.52) to ensure charge-neutrality were assumed as the compound is reported to show anionic redox from O^{2-} to O^{n-} ($n < 2$)[66]. As both approaches guarantee to determine the global optimum after a successful run, it is only of interest to benchmark the run time of both methods. The timings on 128 physical processor cores are plotted against the total number of configurations in Figure 2.4. For smaller problem instances with up to ca. 10^9 configurations, full enumeration was faster than optimization due to the overhead of interfacing to an external optimization code combined with the capability of the SUPERCELL software to reduce the solution space to just symmetry in-equivalent structures. However, it should be noted that timings on these problem instances are well below 10 seconds and therefore computationally inexpensive in both approaches. For more complex problems the full enumeration approach scales perfectly linearly while run time of the branch-and-cut optimization method increased more irregularly from the small offset caused by the overhead. In general, the computation time of the branch-and-cut optimization was significantly lower for more complex instances of this problem and also appeared to scale lower towards problems with many configurations. Overall, a speed-up of up to three orders of magnitude was achieved by the optimization with Gurobi compared to full enumeration with the SUPERCELL software at the most difficult considered problem instance with ca. 10^{14} total configurations. The

respective run times to find the global optimum atomistic configuration in Coulomb energy were ca. 18 hours by full enumeration versus ca. 1.5 minutes by Gurobi optimization.

Figure 2.4 clearly highlights the computational advantages that can be accessed by using GOAC to formulate a general optimization problem for the combinatorial ground-state search that can be handed to external optimization software. However, extrapolating the scaling behavior to much larger problems also reveals that even with the significant speed up achieved, still only problems of intermediate difficulty/size can be tackled. It must be also noted that the actual performance of the branch-and-cut optimization is very much problem dependent. By introducing (slight) changes to the presented problem (e.g., more species per site or more sodium sites by using a P-type layered structure[81]), problems can be constructed where optimization of the complete configuration space is even slower than full enumeration of symmetry in-equivalent structures or problems that formally have as many as 10^{230} configurations, but are being optimized within seconds, might be obtained.

In summary, the performance of applying standard optimization software to the atomistic combinatorial problem is strongly problem (material) dependent. However, the results indicate that especially for problems of intermediate difficulty (ca. 10^{10} to 10^{20} possible configurations), such as configuration of charge carriers in rechargeable energy storage materials, optimization can give a significant computational advantage over full enumeration approaches, even if the full enumeration method accounts for symmetry equivalents.

2.2.4 Benchmark of Heuristics in GOAC

As the heuristics do not guarantee to find the global minimum, a suitable benchmark could either compare the lowest energy that is found within given computational resources or the time that it takes to find a known global optimum. However, the implemented heuristics are of stochastic nature which makes it important to average their performance over multiple runs. Such comparisons of the different internal heuristics in GOAC are discussed for several examples with various complexity in the following. Moreover, an additional benchmark of $FeSbO_4$ is shown in the supplementary information (Supplementary Table 2.2). All examples in the following were executed on the same hardware and run times (given in real time) were estimated by the CPU time required to perform each calculation.

Atomistic Configurations in NaCl

The site occupation in NaCl is not a true combinatorics problem as the unit cell contains two distinctive sites, one for Na and one for Cl. However, for testing purposes both sites can be modified such that each site is occupied by 50 % of each species, yielding an atomistic combinatorial problem. With this model, in a 3×3×3-supercell the total number of possible configurations is ca. 10^{64}, a rather difficult combinatorial problem. As the global optimum still remains trivial, a perfectly alternating pattern of Na and Cl in all dimensions, this problem statement is a rather suitable benchmark. Moreover, calculation

of the Madelung constant[82],

$$M_C = \frac{4\pi \times \epsilon_0 \times r \times |E|}{N_{\text{Ions}}/2 \times e}, \tag{2.11}$$

is straight forward and convergence to the literature value of $M = 1.74756...$[83] can be tracked for the different heuristics over run time. In this equation, ϵ_0 is the electric constant, r the lattice distance of two neighbouring sites (2.81 Å), E the Coulomb energy of the considered structure, N_{ions} the total number of ions in the structure (216), and e the elementary charge.

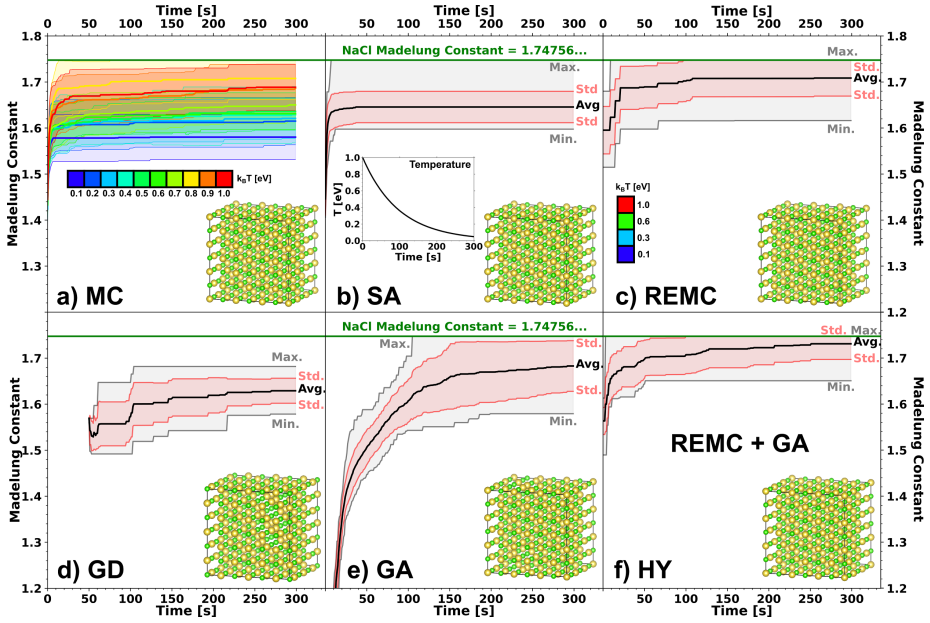

Figure 2.5: Heuristic optimization in NaCl. Single-Core (1 physical CPU core, 1 OpenMP thread) performance of the MC (a), SA (b), REMC (c), GD (d), GA (e), and HY (f) approaches as implemented in GOAC on the atomistic combinatorial problem of NaCl in a 3×3×3-supercell with 10^{64} possible configurations. All heuristics were run for 300 seconds and averages over 16 independent runs along with their statistics (standard deviations, minimum, maximum) and the obtained minimum structure are shown in the plots. For MC, averages and standard deviations over 16 runs are visualized for 10 different temperatures, respectively. The temperature evolution for SA is shown in the respective inset and the REMC parallel temperatures are indicated in the corresponding plot.

The convergence towards the Madelung constant for the heuristics implemented in GOAC is plotted in Figure 2.5. It is observed that the Gradient Descent heuristic requires some time before the first solutions can be obtained. In this algorithm, the first solution is written as soon as the local minimization from a random starting point is finished and then the next random starting structure is optimized. The time required to reach this first solution is also different for random starting structures as different amounts of optimization steps are necessary to reach a local minimum. Therefore, in the beginning of the GD plot, averages over less than 16 runs are contained, which also explains the

drop in the average caused by more independent runs that obtained their first solution being included. Even though the average becomes flatter and standard deviations as well as min-max differences become smaller towards the end of the 5 minutes run time, no run was able to find the global minimum. This highlights the problem of this algorithm as it guarantees to find a local minimum but on shallow energy surfaces with many local minima it becomes highly unlikely to find the global minimum as there is a high chance to get trapped in another local minimum. However, in other use cases one might also be interested in studying these local minima.

The same tendency can be observed in Figure 2.5 for Monte Carlo performed at low temperatures (ca. 0.1–0.5 eV) as the average quickly flattens to a constant value since the algorithm gets trapped in local minima at a low sampling temperature, similar to the outcome of the GD method. At higher temperatures (ca. 0.6–0.8 eV), however, the averages are observed to get closer to the Madelung constant (corresponding to the global energy minimum) over time as local barriers can be passed with a certain probability to eventually find lower minima. At high temperatures (ca. 0.9–1.0 eV) the algorithm is able to pass even higher energy barriers, thus spending only short times for local optimization and resulting in a decrease of average performance. In this example, the best result (on average) was obtained at a temperature of 0.8 eV and the performance was quite sensitive to the simulation temperature, even though multiple runs at various temperatures were able to find the global optimum within five minutes of run time. To overcome these temperature sensitivity, methods that make use of temperature variation to improve the optimization performance are discussed next.

The average performance of Simulated Annealing was similar to that of MC at lower to intermediate temperatures with a relatively high variance in solutions, as some runs returned the global optimum. This behaviour can be explained by the rather fast cooling rate chosen, which exponentially decreased from an initial simulation temperature of 1.0 eV to almost 0 eV during the run time (cf. inset in Figure 2.5). Such a high cooling rate, which was required to scan a sufficiently large temperature range within the given run time limit, makes it more unlikely that a sufficient temperature is present at the crucial optimization steps leading to a high risk of local minima trapping. Nevertheless, SA was able to find the global optimum in some runs.

The last tested approach from the MC family, namely Replica Exchange Monte Carlo, shows a better performance than SA. The algorithm showed a pronounced optimization, especially in the first ca. 100 seconds, before almost constant values for average, standard deviation, and min-max were reached. This behaviour indicates that the optimization got trapped in local minima for some runs, while in other runs the global optimum was successfully reached. As only about one third of the run time (ca. the first 100 seconds) was effectively used for optimization, the performance might be improved by using more than four temperatures in REMC, including also largely-different and higher temperatures. Compared to the other heuristics, REMC performed very well within the given run time.

Among the approaches compared in Figure 2.5, the Genetic Algorithm shows the slowest increase in average performance versus run time. Several generations and selection procedures are required to obtain more optimized structures resulting in the steep improvement of average energy. Even though some GA runs successfully reached

the global optimum, the average over all runs was still substantially below the correct Madelung constant after 300 seconds of run time, showing that some runs got trapped in local minima. The trapping also goes along with high standard deviations and a large min-max difference. This occurs if the structural variation in the generations becomes low and centered around a deep local minimum. Another problem can be that the generation consists of symmetry equivalents of the same local minimum or if the local minimum is so deep that it can not be exited at small mutation rates which are required for a systematic optimization.

To overcome these limitations the Hybrid approach can be employed which provided the best performance among the methods compared in Figure 2.5. Here, a pre-trained (from REMC) generation was used for the GA which greatly improved the average performance within the first seconds of the run. Moreover, the REMC steps between the GA runs can help to improve the variation in the generation pool of the GA. Vice versa, the GA offers a systematic procedure to make rather large steps on the potential energy surface that cannot be efficiently achieved by pure REMC. Therefore, both approaches can complement each other and the results demonstrate that HY was very effective with the average of 16 independent runs being fairly close to the correct Madelung constant after just 5 minutes of run time and with many runs ending in the global optimum. Moreover, the average kept increasing at longer run times indicating that most of the runs would eventually converge to the global optimum. Notably, the HY strategy performed better than the two individual approaches (GA and REMC) and was the best out of all investigated methods, indicating that a beneficial synergy effect between GA and REMC was achieved.

Li-Site Occupation and Ta Doping in LLZO

$Li_7La_3Zr_2O_{12}$ (LLZO) is a widely studied electrolyte for all-solid-state batteries and therefore of high practical interest. However, the global minimum energy structure or in general low energy configurations are rather hard to approach computationally due to its large unit cell (8 formula units). The computational challenge becomes even more severe when dopants and defects are introduced that require even larger supercells. For these cases, the configurational space is extremely large, representing an interesting test for GOAC to obtain optimized atomistic configurations in terms of Coulomb energies. As an example, $Li_6La_{2.969}Zr_{0.906}Ta_{1.094}O_{12}$ (Charges: Li^{1+}, La^{3+}, Zr^{4+}, Ta^{5+}, O^{2-}) is considered which can be modelled by a 2×2×1 supercell (32 formula units). The modelled composition is in good agreement with the experimental one reported by Redhammer *et al.*[84]. The structure is defined such that all lithium ions can be placed in both the tetrahedral and octahedral sites, resulting in a total of ca. 10^{159} possible atomistic configurations. The corresponding structure model is also shown in Supplementary Figure 2.8.

Performances over 10 independent optimization runs are visualized for each heuristic of GOAC in Figure 2.6. As discussed previously at the example of NaCl, the GD algorithm requires some time before the first local optimizations are finished and therefore the average plot begins at ca. 1000 seconds in Figure 2.6. The overall performance of GD was found to be among the worst out of the GOAC heuristics. The GA solutions converged to a similar average energy as GD, but also had the largest variation between the best and worst independent runs, hinting at local minima trapping. This behavior might

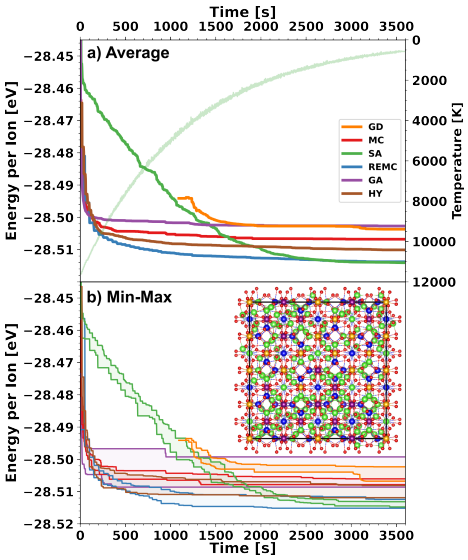

Figure 2.6: Heuristic optimization in LLZO. Average (a) and min/max (b) energies per ion for the LLZO atomistic combinatorial problem with ca. 10^{159} configurations over 10 independent runs of 1 hour at 128 physical CPU cores (128 OpenMP threads) for GD, MC, SA, REMC, GA, and HY as implemented in GOAC. In the upper plot, also the average temperature profile used for the SA simulations is shown. The structure inset in the lower plot corresponds to the minimum energy structure that was obtained across all optimizations. An enlarged version of the minimum energy structure is also given in Supplementary Figure 2.9.

be reasoned by the different parallelization approaches as discussed in the supplementary information and the code documentation in the project repository (see Code Availability statement). However, averages shown in Figure 2.6 are still a fair comparison of optimization performance versus CPU time, revealing that the heuristics including some sort of MC are more efficient than a pure GA for LLZO.

The MC approach returned an intermediate average energy per ion, while the SA and REMC methods yielded significantly lower energies after one hour of run time. For most heuristics the convergence was rather flat beyond the first ca. 500 seconds, but SA showed an exponential decrease over the whole run time which was matching the exponential decrease of the respective simulation temperature from ca. 12000 K to almost 0 K (cf. Figure 2.6). Interestingly, also the variance between the best and worst runs became rather small for the SA approach. In contrast to the results obtained for NaCl, SA performed well for the present example due to the longer run times that allowed for a slower cooling rate. The final average energies obtained from SA and REMC were similar, but the energy of the best REMC run was slightly lower than that of the best SA run, and the corresponding minimum-energy structure is shown in Figure 2.6. The superior performances of SA and REMC over the other methods demonstrate that MC approaches with some temperature variation are very effective for the complex LLZO configuration problem. While in this example, the HY approach was not able to improve on the performance of REMC, still a much lower average energy than for the pure GA was found. The overall performance of HY might be increased by longer run times and adjusted heuristic

parameters.

The determined minimum energy structure can be analysed in terms of the ratio of lithium ions in tetrahedral versus octahedral coordination of oxygen as all lithium ions were freely iterated over both classes of sites during optimization. A ratio of $\frac{77}{115} \approx 0.67$ is obtained which is in very good agreement with the ratios of 0.74, 0.64, and 0.59 (after different treatments) and an average of 0.66 reported from experiments[84]. This highlights again the predictive quality of point-charge Coulomb energies for the configuration of ions in complex structures and validates the approach of pre-selecting atomistic low energy configurations by Coulomb energies for higher-level calculations. It should be mentioned that in a practical study one might be interested in the n lowest energy configurations as the material probably encounters some disorder in experiment. However, referencing to the lowest energy configuration is desirable to assess which metastable configurations might exist at a given temperature. Moreover, the discussed LLZO example can hardly be approached by exact optimization or computationally more demanding energy evaluation models proving the practicability of heuristic optimization with Coulomb energies. To the best of our knowledge, heuristic configurational optimization of Coulomb energies has not been reported before for any comparably complex atomistic combinatorial problem. However, it should be mentioned that heuristic optimization was carried out on different, more complex problem settings beyond site-configurational optimization and Coulomb energies such as, e.g., protein folding[85].

Layered Oxide Cathode Materials

To further demonstrate the optimization capabilities of GOAC, the atomistic combinatorial problem in a high-entropy layered sodium-ion-battery cathode material was addressed. The composition of O3-$Na_{2/3}[Li_{1/6}Fe_{1/6}Co_{1/6}Ni_{1/6}Mn_{1/3}]O_2$ was recently proposed by Yao *et al.*[86], while O3 indicates that the structure has three layers in the c-direction and octahedral coordination of the sodium ions[81]. The system was modelled in a $\sqrt{3}$-unit cell ($a = 5.0$ Å, $c = 19.2$ Å) assuming ionic charges of Na^+, Li^+, $Fe^{2.5+}$, $Co^{3.5+}$, Ni^{2+}, Mn^{4+}, and $O^{1.75-}$. The cationic charges were chosen to agree with the ones observed in experiment[86] while the charge of Fe was decreased by 0.5 and the one of Co was increased by 0.5 to ensure that all configurations are distinguishable in Coulomb energy. The oxygen charge was set to achieve a overall charge-neutral compound and can be reasoned by the experimentally reported oxygen redox. All sodium ions were iterated over all sodium positions in every layer (one sodium site in the whole structure with nine positions in the unit cell) and all ions in the transition metal layers were iterated over all positions in each layer (one transition metal site in the whole structure with nine positions in the unit cell), allowing for the maximal configurational space. To highlight the scalability and limitations of GOAC, this configuration problem was solved in supercells of different sizes ranging from 4 unit cells (2×2×1, $Na_{24}[Li_6Fe_6Co_6Ni_6Mn_{12}]O_{72}$) to 108 unit cells (6×6×3, $Na_{648}[Li_{162}Fe_{162}Co_{162}Ni_{162}Mn_{324}]O_{1944}$). Structure models for the smallest and largest considered supercells are visualized in Supplementary Figure 2.10. Results for optimizing the atomistic configurations with the heuristics in GOAC within a given run time (given computational resources) are summarized in Table 2.1.

Remarkably, all solvers were capable to find the same minimum, likely the global minimum, for the smallest problem of a 2×2×1 supercell within just one hour of run time. It should be also noted that most heuristics identified this minimum within the

Table 2.1: Energies per ion of the lowest energy structures obtained for differently sized supercells of O3-$Na_{2/3}[Li_{1/6}Fe_{1/6}Co_{1/6}Ni_{1/6}Mn_{1/3}]O_2$ with the different heuristics implemented in GOAC (all calculations performed on 128 physical CPU cores and using 128 OpenMP threads). Even though energy differences appear to be small as they are scaled per ion to allow for comparisons, they are very significant (usually more than 1 eV) when the energy of a whole supercell is considered. The table also shows the total number of configurations (N_{Conf}) of the different combinatorial problems along with the required time to calculate the Coulomb matrices and expansion coefficients (t_C). The run times for each heuristic were limited to t_R for the shown problems. Minimum energies found for each of the problem sizes are highlighted in bold.

				Energy per ion [eV]					
$\sqrt{3}$-Cell	N_{Conf}	t_C [s]	t_R [h]	GD	MC	SA	REMC	GA	HY
2×2×1	10^{31}	0.0	1	**-22.080**	**-22.080**	**-22.080**	**-22.080**	**-22.080**	**-22.080**
2×2×2	10^{64}	0.0	1	-22.071	-22.082	**-22.096**	**-22.096**	**-22.096**	**-22.096**
4×4×1	10^{132}	0.1	1	-22.040	-22.027	**-22.087**	**-22.087**	-22.042	**-22.087**
4×4×2	10^{269}	0.5	2	-22.013	-22.006	**-22.096**	**-22.096**	-21.772	-22.040
6×6×1	10^{303}	0.5	2	-	-22.003	-22.078	**-22.083**	-21.814	-22.029
8×8×1	10^{543}	1.6	4	-	-21.975	**-22.031**	-22.022	-21.625	-21.986
6×6×2	10^{611}	1.9	8	-	-21.984	**-22.040**	-22.031	-21.589	-21.992
6×6×3	10^{920}	3.8	16	-	-21.970	**-22.018**	-22.006	-21.548	-21.975

first minutes (cf. the convergence versus run time plots in Supplementary Figures 2.11–2.16). Compared to the exact solvers presented in the previous section, this represents a huge speed up as a problem with 10^{31} total configurations would be (almost) impossible to solve with an exact solver in a reasonable run time, especially not within just one hour. This highlights the practicability of GOAC as problems of this size regularly appear when high-entropy structures or similarly complex structures are to be pre-selected for DFT calculations. The suitability to pre-select low(est) energy structures for DFT calculations was also checked by performing single-point DFT calculations on the 10 lowest energy configurations obtained by the REMC approach (Supplementary Figure 2.17). This is particularly practical as one is usually interested in selecting a sufficiently low or several low energy configurations but in the following just the global minimum is discussed to better compare the performances of the different heuristic optimizers.

For the next larger problem, a 2×2×2 supercell, only the more advanced heuristics, namely SA, REMC, GA, and HY, were able to find the same lowest energy structure, which makes it again a likely candidate for the global minimum in Coulomb energy. The respective minimum energy is lower than the minimum energy obtained for the smaller problem, because the increased problem size allows for larger, energetically more favourable superstructures. The same applies to the 4×4×1 supercell where SA, REMC, and HY obtained the same best candidate configuration for the global minimum. As the periodicity is extended in a different direction compared to the 2×2×2 supercell, the minimum energy is still lower than for the 2×2×1 case but higher than for the 2×2×2 supercell. For a 4×4×2 supercell, only SA and REMC were capable to find a likely candidate for the global minimum. The respective minimum energy is identical to the one of the 2×2×2 problem as both consider the same periodicity, and thus same degrees of freedom, in the *c*-direction. The additional degrees of freedom in *a* and *b*-direction, on the other hand, did not seem to allow for the formation of lower energy superstructures.

These findings highlight another aspect why it is important to consider sufficiently large supercells in the construction of structural models with occupational disorder, because suitable supercell sizes are required for lowest energy superstructures. To efficiently select suitable supercell sizes and to account for the fact that it becomes increasingly hard to obtain the lowest energy configuration in larger supercells even if it is already known from a smaller commensurately cell, GOAC also allows to systematically scan for increasing supercell sizes to find low(est) energy configurations.

For an even larger 6×6×1 supercell, the GD heuristic was not able to reach any local minimum within the given run time since more complex problems not only increase the expected number of optimization steps required to reach a local minimum from a random starting structure but also heavily increase the amount of neighbouring structures that need to be evaluated to follow the steepest descent path. Within the given framework, 10^{269} configurations seemed to be the maximum where GD could be applied within reasonable computational resources, which is arguably already a quite large configurational space. For the 6×6×1 supercell, REMC returned the lowest energy structure, lower in energy than the 2×2×1 minimum, which was expected given that the 6×6×1 is a multiple of the 2×2×1 supercell. SA also returned a low-energy solution, albeit not the same minimum, probably because the cooling rate was too fast for the given problem size and run time limitation.

For all supercells larger than 6×6×1, SA found the lowest energy structure out of all heuristics implemented in GOAC. However, the obtained minima did not correspond to the respective global minima as they were higher in energy than the minimum energy structures of one of the smaller problems with matching multiplicity. While it is still possible to run optimizations on these extremely large problems, the results show the limitations of the heuristics implemented in GOAC as one cannot expect to find lowest energy configurations within reasonable run times for such large configurational spaces. Due to the combinatorial explosion in large cells it is also not surprising that it is nearly impossible to find minimum energy structures in configurational spaces with up to 10^{920} configurations, a number even larger than the estimated total number of atoms in the entire universe [87] to the power of ten (The actual number of atoms in the universe must be estimated from measured densities and hydrogen/helium distributions and is in the range of ca. 10^{80} atoms).

The pure MC heuristic performed inferior to the more elaborate SA and REMC extensions for all problem sizes. As it was shown for NaCl, the MC method is quite sensitive to the simulation temperature which was not re-optimized for every problem in the benchmark (fixed to 0.75 eV). The GA performed rather poor for problems with a complexity of 10^{269} or more in its current implementation. Combining the GA with REMC in the HY approach did not resolve this issue for the larger problem sizes as the gain in performance compared to the pure GA stemmed almost exclusively from the REMC part. Therefore, the overall performance of the HY method was still inferior to using all computational resources on REMC. More advanced HY combination schemes or different crossing strategies in the GA might resolve this under-performance in the future.

2.3 Discussion

In this work, it was shown that the problem of finding low(est) energy configurations in the huge configurational space of modern energy materials can be effectively approached by using advanced optimization methods in combination with Coulomb energy models. The Coulomb energy variations between different configurations often align well with energies from higher levels of theory, e.g., DFT, and sampling by Coulomb energies is therefore an attractive method to pre-select low-energy structure candidates. As a tool for conveniently and effectively exploring the vast configurational space of atomistic configurations in complex materials, the GOAC code was introduced that can be conveniently accessed as a command line tool.

The calculation of energies of different configurations was significantly sped up by expressing the Coulomb energy cost function as an expansion to a binary optimization problem, which enables the use of pre-calculated coefficients in the optimization procedure, thus providing significant improvements over performing Ewald summations at each optimization step. This reformulation transforms the atomistic combinatorial problem statement into an MINLP problem and allows to employ various advanced optimization methods. It was shown that the exact optimization of the MINLP, interfaced via GOAC to existing optimization software, was several orders of magnitude faster than the full enumeration approach often applied for the atomistic combinatorial problem, allowing to exactly solve configuration problems for larger system sizes.

Due to the combinatorial explosion of the configurational space in complex multi-element materials, exact solving strategies cannot be applied to more complex materials. For such problems, several heuristics were implemented in GOAC, including Gradient Descent, Monte Carlo, Simulated Annealing, Replica Exchange Monte Carlo, Genetic Algorithms, and hybrid approaches. With these heuristics, GOAC produced high-quality low-energy structures within limited computational resources for extremely large configuration problems, which is of interest to model complex compositions and identify possible superstructures. As a highlight, it was shown that GOAC was able to find likely candidates for global minimum structures of problems with 10^{303} configurations in just about 2 hours of run time on 128 CPU cores. It should be mentioned that this usually implies that also the n lowest energy configurations that are of interest for further computational studies are obtained as well. Moreover, it was demonstrated that for problem combinatorics up to 10^{920}, it was still possible to perform optimizations using the GOAC package even though finding minimum energy configurations in reasonable computation time cannot be expected at such large problems.

For the results presented in this work, simple point-charge Coulomb energies were employed, which represent a rough estimation that does not guarantee to coincide in the lowest energy configuration with higher level of theory approaches, e.g., DFT. Moreover, atomistic combinatorial problems with charge-neutral ions (atoms) or ions with identical valencies cannot be optimized on the basis of Coulomb energies alone. In general, one can expect to get reasonable energetic alignments of DFT and Coulomb when the charges are more localized as this is more well-described by point-charges. When studying systems with more delocalized charges, e.g., highly charged cathode materials, the alignment of DFT and Coulomb energies might decrease. To potentially overcome the issue of too delocalized charges and also allow to treat different ions with the same

charge, GOAC also supports Gaussian smeared charges. Future studies will show if or how smearing out the point-charges can improve the accuracy of the Coulomb model in cases with strong delocalization and help to deal with different species that have the same valency.

Finally, it should be mentioned that GOAC can perform well on several other research questions concerning configurations, also beyond the scaling tests and configurational selections shown in this work. For example, GOAC might be employed to study charge-ordering of ions that disproportionate into different valances (cf. Supplementary Figure 2.18) or charge-ordering in general. In fact, results at the example of a layered oxide sodium-ion cathode material in Supplementary Figure 2.19 indicate that a strong correlation of energies of charge-orderings of differently charged Mn ions exists between Coulomb and DFT energies. In the case of layered oxide cathodes GOAC optimizations also allow to study transition metal layer charge-orderings and Na-orderings in a coupled fashion to get an idea if and how theses two orderings are coupled. The examples presented in Supplementary Figure 2.20 indicate that GOAC might also be successfully applied to this problem setting as DFT calculations show similar trends to the GOAC optimizations. Further studies might show in more detail how GOAC can be employed to study various types of orderings in layered oxide materials and how well the results match selected references, e.g., DFT calculations. Lastly, GOAC was recently also applied to study the single-phase — two-phase charging characteristics of lithium iron phosphate (LFP)[88]. Results showed that electrostatic optimization can reproduce the critical particle size from experiment for the switch from the single-phase to the two-phase charging mechanism as well as the energetically most favourable interface orientation between the two phases. This indicates that GOAC could be used to study similar materials in the future.

In summary, GOAC can be a valuable tool for computational research on novel energy materials and other complex materials to determine likely candidate structures for low or lowest energy atomistic configurations with comparably little computational resources.

2.4 Methods

2.4.1 DFT Reference Calculations

The DFT reference calculations shown in Figure 2.2 were performed with the VIENNA AB INITIO SIMULATION PACKAGE (VASP)[89] in the projector augmented wave (PAW) scheme[90] with the Perdew-Burke-Ernzerhof (PBE) exchange-correlation functional[91]. An energy cut-off of 520 eV along with a convergence criterion of 10^{-4} eV, a $1\times1\times2$ Γ-centered k-point grid, and spin-polarization was employed. Single-point calculations without any geometry optimization were performed to allow for a fair comparison to Coulomb energies. The exact geometries can be found in the “Examples” folder of the project repository (see Data Availability statement). Structure models in this work were visualize with the VESTA software[92].

Data Availability

All raw data and input files for the examples shown in this work can be found in the Forschungszentrum Jülich GitLab project of this study in the ”Examples“ folder under: `https://iffgit.fz-juelich.de/k.koester/goac`.

Code Availability

The underlying code, GOAC, that was designed for this study is openly available on the Forschungszentrum Jülich GitLab and can be found here: `https://iffgit.fz-juelich.de/k.koester/goac`.

Supporting Information

Scalability of the GOAC Functionalities

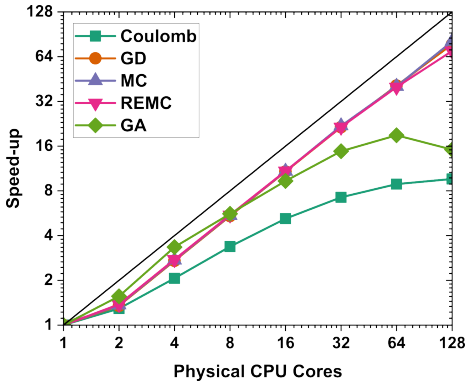

Supplementary Figure 2.7: $\log_2 - \log_2$-plot of the speed-up versus the number of CPU cores (OpenMP threads) for the different parallelized methods in the GOAC code. Ideal scaling behavior is indicated by the black diagonal.

The scalability plot in Figure 2.7 shows that the internal parallelizations for GD, MC, and REMC work rather well. This is also to expect for GD and MC as the parallelization simply consist of running multiple runs in parallel which is effectively the same as running the code multiple times manually. For REMC, however, it proves that also the internal parallelizations over the simulation temperatures are implemented effectively. For the Coulomb calculation (Coulomb matrix and expansion coefficients calculation) the scaling becomes slightly worse at many cores and the same applies to the GA where the generation creation is parallelized. These lower scalabilities probably stem from the fact that in these methods parallelization is less trivial than just running the same code multiple times. Moreover, the problems used for this benchmark might have been too simple such that the actual scaling behavior was masked by some overhead. Nevertheless, all methods show a suitable scaling behavior to be effectively employed on machines with multiple cores.

Structure Models of Ta-doped LLZO

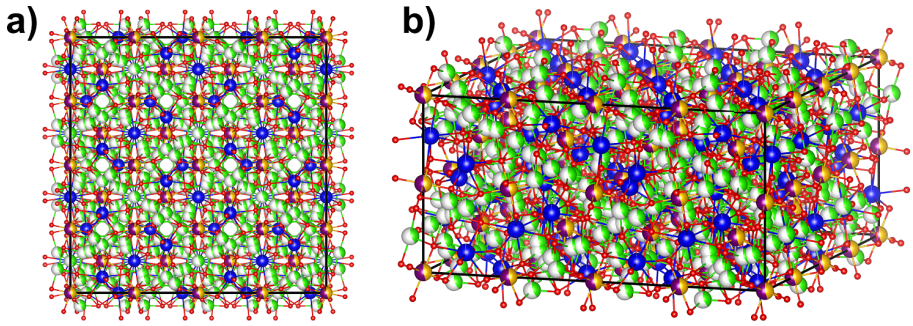

Supplementary Figure 2.8: Input structure with partial occupations for the optimization of the Ta-doped LLZO presented in the main text in the front (a) and perspective (b) view. A single-site was defined for the Li positions such that all positions shown here were freely iterated for Li. The color-coding is as follows: Li: green, La: blue, Ta: purple, Zr: orange, O: red.

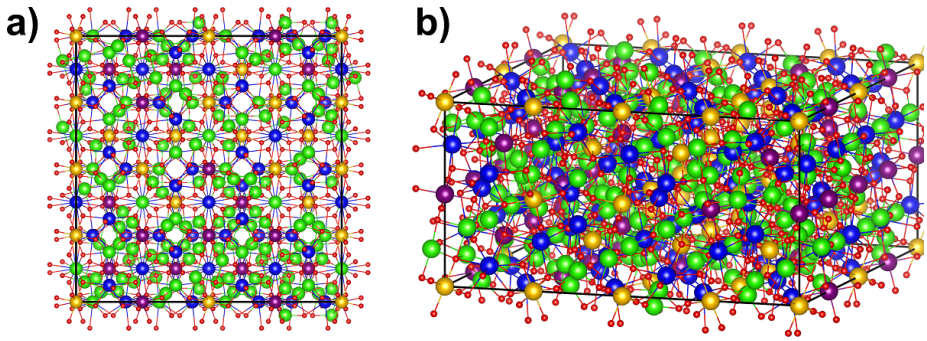

Supplementary Figure 2.9: Lowest energy structure for the optimization of the Ta-doped LLZO presented in the main text in the front (a) and perspective (b) view. The color-coding is as follows: Li: green, La: blue, Ta: purple, Zr: orange, O: red.

Case Study on $FeSbO_4$

Yang *et al.*[50] published their EWALDSOLIDSOLUTION software very recently which allows to sample the density of states for an atomistic combinatorial problem by Coulomb energies. This technique is also able to determine minima and their code even features a local minimization algorithm similar to GD in GOAC. In their work, they solved the largest atomistic combinatorial problem by Coulomb that is, to the best of our knowledge, reported in literature. The problem is a 3×3×14 supercell of $FeSbO_4$ (Fe^{3+}, Sb^{5+}, $O^{-2.0}$) with roughly 10^{75} possible configurations. However, similarly to NaCl, the global minimum is still trivial and known from smaller supercells. Timings to reach the global optimum are shown for each heuristic implemented in GOAC in Table 2.2.

The average timings for GD to find the global optimum are rather high and also show large deviations. The random sampling of the starting points for local minimization can

Supplementary Table 2.2: Average timings and statistics over 5 independent runs (each on 128 physical CPU cores, 128 OpenMP threads) with GD, MC, SA, REMC, GA, and HY as implemented in GOAC on the 3×3×14 $FeSbO_4$ supercell with ca. 10^{75} configurations. Calculations of the Coulomb matrix and the expansion coefficients, which took 0.1 seconds, are excluded.

	Run Time Statistics [s]			
Method	Avg.	Std.	Min.	Max.
GD	5568	5877	3645	16610
MC	41	17	24	73
SA	17	2	15	20
REMC	45	10	33	57
GA[1]	100	74	29	199
HY	35	14	15	58

be quite inefficient for this problem as there is a high probability that the algorithm ends up in a local minima. That GOAC's GD is still able to find the global minimum despite the huge computational effort spend in the many local minimization steps proves that the expansion into a binary optimization problem of the atomistic combinatorial problem is rather efficient approach.

The other heuristics in GOAC are all much faster with GA being the slowest approach. It must be also noted that not all GA runs did end in the global minimum and some got trapped in local minima. This behavior might be explained by the slightly different implementation/parallelization in GA compared to the other heuristics as the parallelization is restricted to the pool creation to allow for large structure pools while for all other heuristics multiple independent runs of the same heuristic are parallelized. The SA heuristic performs best for the $FeSbO_4$ problem with the lowest average time to find the global minimum and also the lowest deviation in run time. REMC and HY also perform well on the problem but it becomes evident that their overhead in run time is larger than the actual gain in optimization performance for this problem.

It should be mentioned that the timings for GOAC correspond to the pure optimization task of the lowest energy structure and do not include any search for the density of states at higher energies. Moreover, GOAC is of heuristic nature and if the global minimum was unknown some additional run time would be required to reach a convergence criteria, e.g., n heuristic steps without improvement in the global minimum, to have some certainty that the determined minimum is the global one.

Structure Models and Convergence Plots for Optimization in High Entropy Layered Oxides

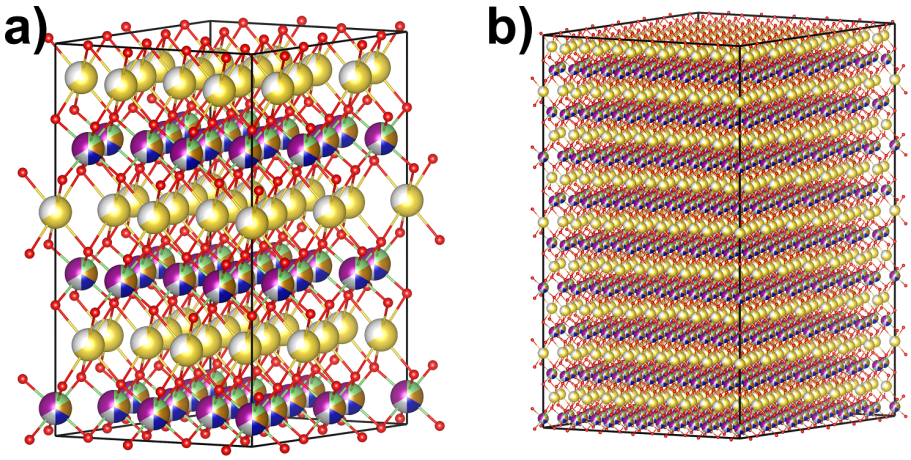

Supplementary Figure 2.10: Considered structure models of the O3-$Na_{2/3}[Li_{1/6}Fe_{1/6}Co_{1/6}Ni_{1/6}Mn_{1/3}]O_2$ material with partial occupations. In a), the smallest simulated supercell (2×2×1) is shown and the largest one (6×6×3) in b). Each structure contained just one class of Na and one class of transition-metal sites such that iteration over all shown positions in the structures was performed.

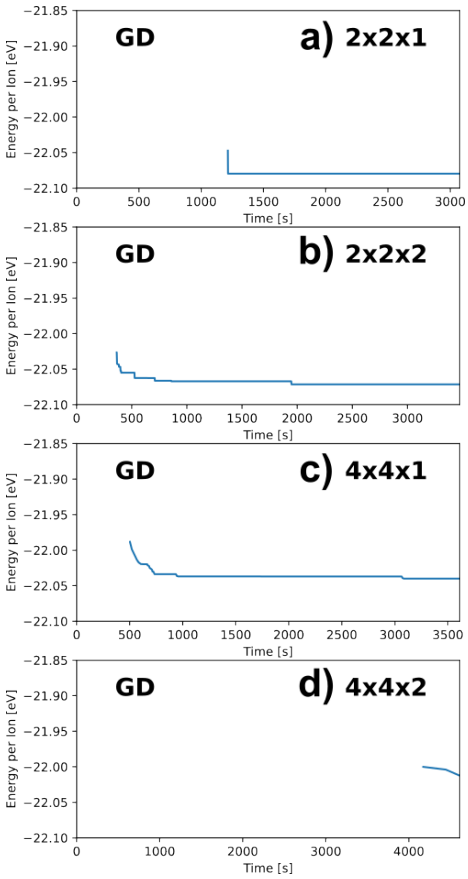

Supplementary Figure 2.11: Convergence plots for O3-$Na_{2/3}[Li_{1/6}Fe_{1/6}Co_{1/6}Ni_{1/6}Mn_{1/3}]O_2$ with the GD method for increasing supercell size 2×2×1 (a), 2×2×2 (b), 4×4×1 (c), 4×4×2 (d). As discussed in the main text, only for supercells up to 4×4×2 solutions were obtained within the given time for this method. The first solutions start later for the 2×2×1 case as many more structures could be generated and treated in parallel by GD than for the more complex supercells. Moreover, the timings in the 4×4×2 supercell are slightly off as less structures could be considered in parallel than available CPU-cores to finish within the given run time constraint. As timings in the plots were estimated from CPU times, timings are slightly shifted in this case.

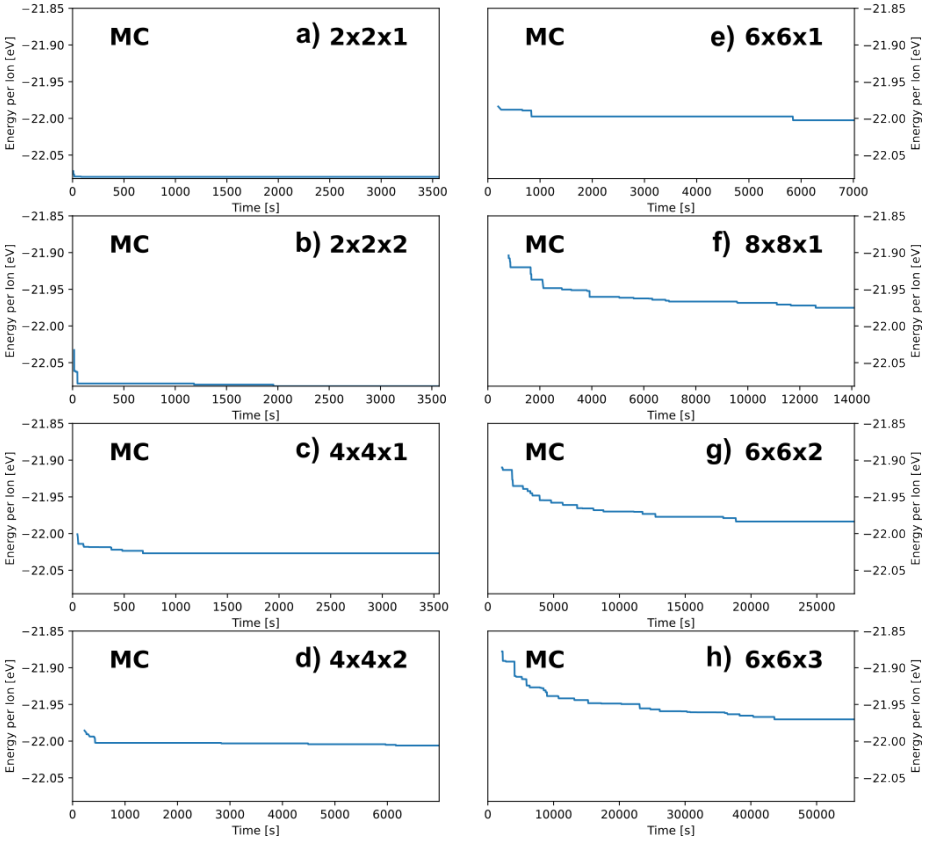

Supplementary Figure 2.12: Convergence plots for O3-$Na_{2/3}[Li_{1/6}Fe_{1/6}Co_{1/6}Ni_{1/6}Mn_{1/3}]O_2$ with the MC method for increasing supercell size 2×2×1 (a), 2×2×2 (b), 4×4×1 (c), 4×4×2 (d), 6×6×1 (e), 8×8×1 (f), 6×6×2 (g), 6×6×3 (h). The plots nicely show that for more easy problems (small supercells) the best solution is almost found instantly, while in larger supercells a slow convergence over run time can be observed.

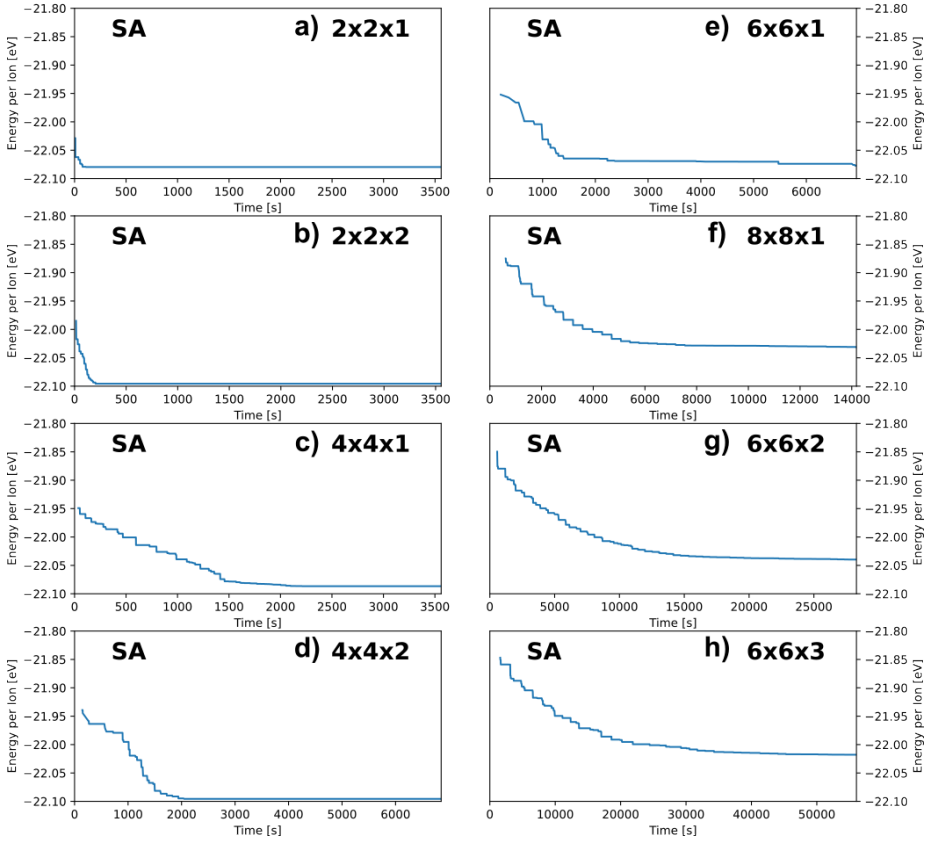

Supplementary Figure 2.13: Convergence plots for O3-$Na_{2/3}[Li_{1/6}Fe_{1/6}Co_{1/6}Ni_{1/6}Mn_{1/3}]O_2$ with the SA method for increasing supercell size 2×2×1 (a), 2×2×2 (b), 4×4×1 (c), 4×4×2 (d), 6×6×1 (e), 8×8×1 (f), 6×6×2 (g), 6×6×3 (h). The convergence trends are similar to the pure MC method but convergence over time is more pronounced and even looks like an exponential decay for larger supercells. This is in good agreement with the temperature evolution of the SA method that also decreases the temperature exponentially over run time.

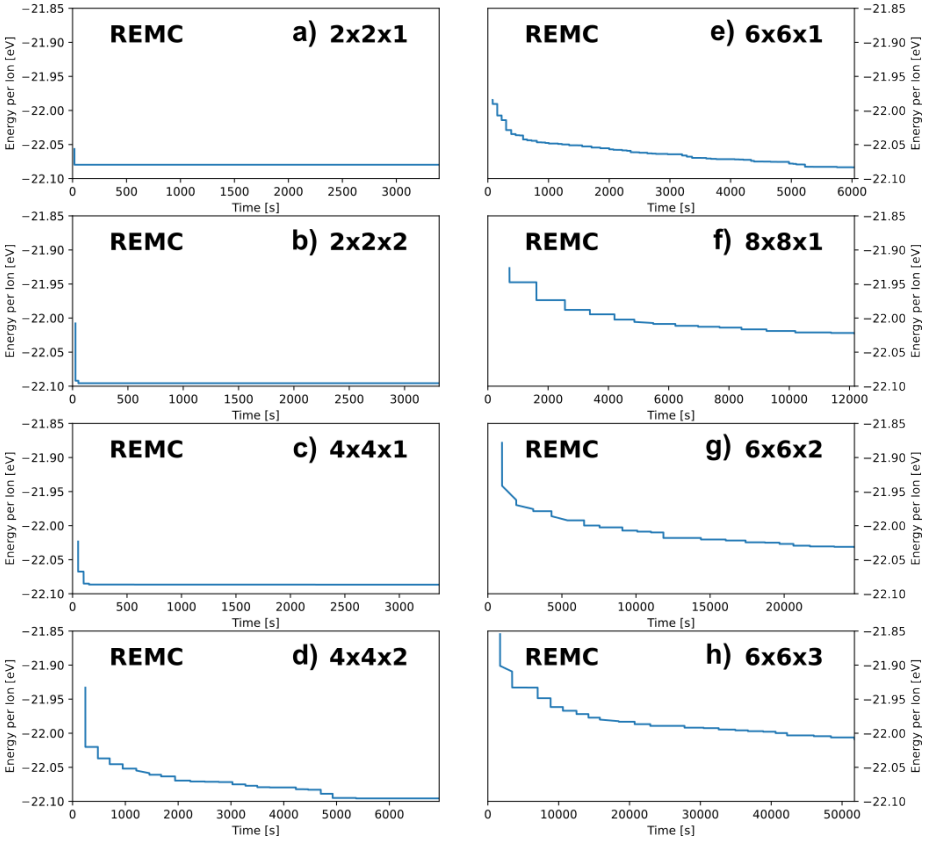

Supplementary Figure 2.14: Convergence plots for O3-$Na_{2/3}[Li_{1/6}Fe_{1/6}Co_{1/6}Ni_{1/6}Mn_{1/3}]O_2$ with the REMC method for increasing supercell size 2×2×1 (a), 2×2×2 (b), 4×4×1 (c), 4×4×2 (d), 6×6×1 (e), 8×8×1 (f), 6×6×2 (g), 6×6×3 (h). Also REMC converges almost instantly in the smaller supercells and shows almost in all examples a steep decrease in energy within the first seconds of run time.

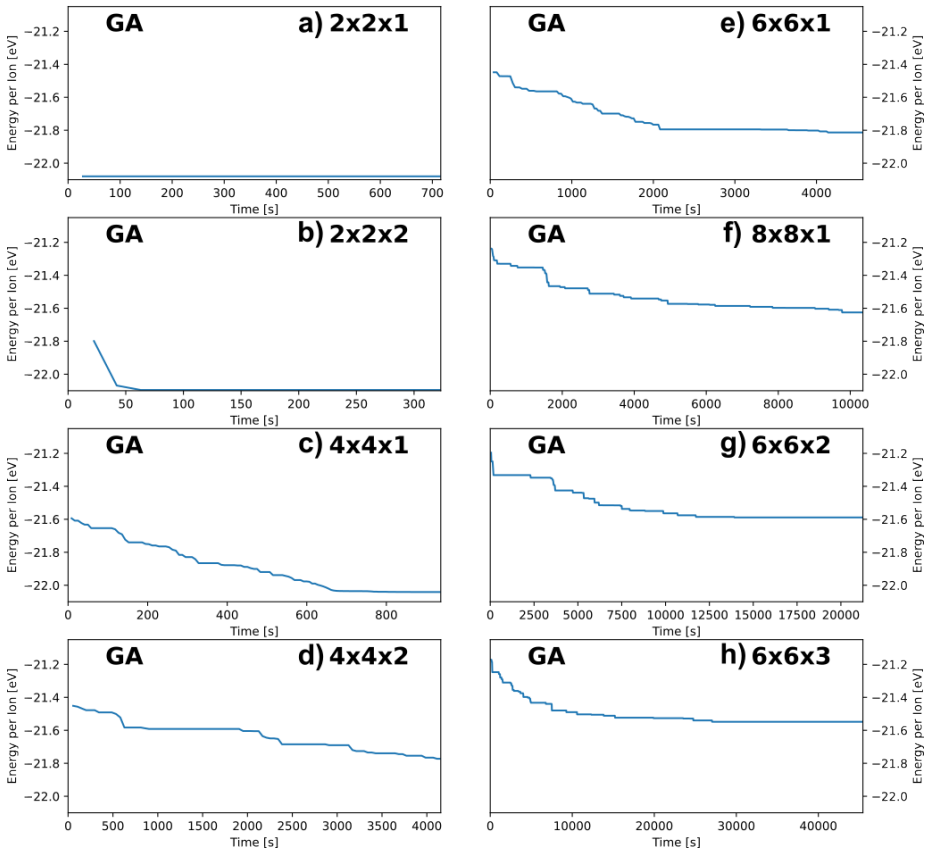

Supplementary Figure 2.15: Convergence plots for O3-$Na_{2/3}[Li_{1/6}Fe_{1/6}Co_{1/6}Ni_{1/6}Mn_{1/3}]O_2$ with the GA method for increasing supercell size 2×2×1 (a), 2×2×2 (b), 4×4×1 (c), 4×4×2 (d), 6×6×1 (e), 8×8×1 (f), 6×6×2 (g), 6×6×3 (h). The GA also converges within almost no run time for the small supercells. While for intermediate sized supercells (4×4×1 to 8×8×1) a steady, even though slowing down by supercell size, convergence is observed. For even larger supercells the GA gets trapped in one solution after roughly half of the run time. This highlights that the GA is prone to get trapped in local minima for complex problems.

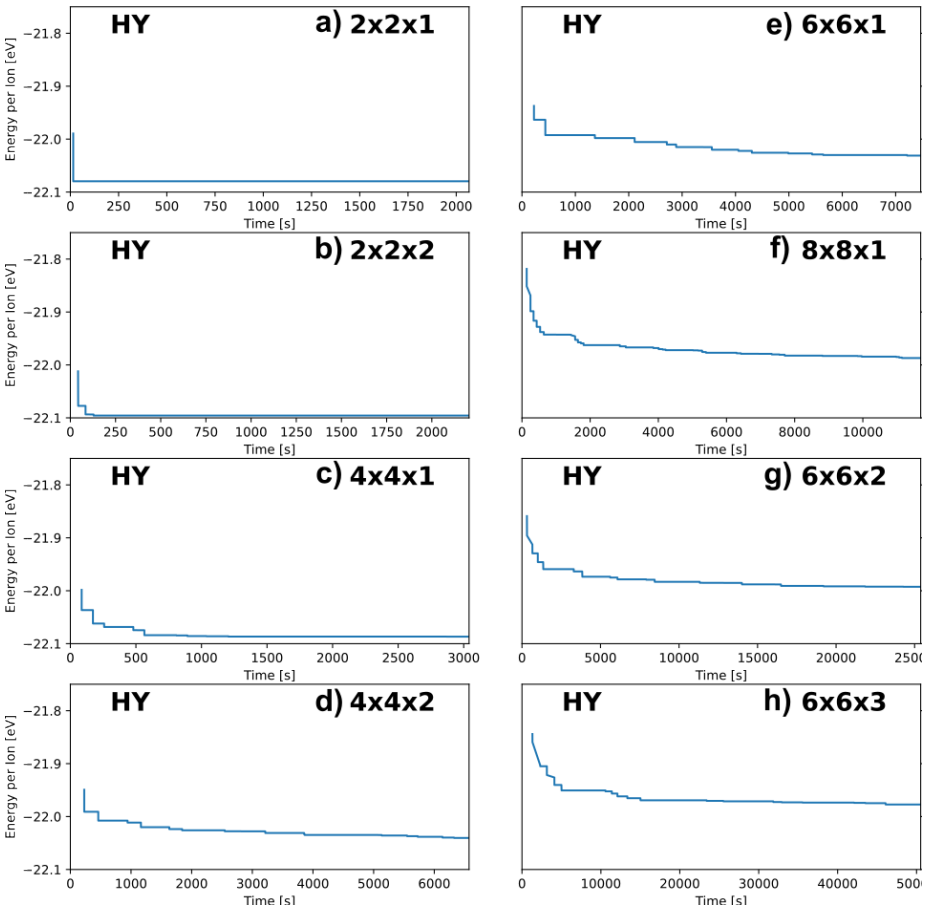

Supplementary Figure 2.16: Convergence plots for O3-$Na_{2/3}[Li_{1/6}Fe_{1/6}Co_{1/6}Ni_{1/6}Mn_{1/3}]O_2$ with the HY (REMC + GA) method for increasing supercell size 2×2×1 (a), 2×2×2 (b), 4×4×1 (c), 4×4×2 (d), 6×6×1 (e), 8×8×1 (f), 6×6×2 (g), 6×6×3 (h). For the small supercells similar trends than for the pure methods can be observed. At larger supercells, however, the convergence is slowed down compared to the pure REMC method. In contrast to the pure GA, even after longer run times small improvements in energy are observed. For the most complex problems it appears that the HY approach is only beneficial for the first seconds/minutes while at longer run times the pure REMC method clearly outperforms the HY approach.

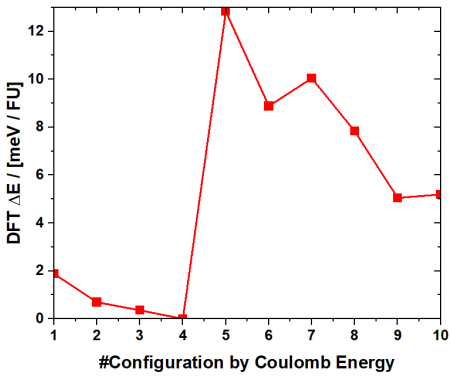

Supplementary Figure 2.17: The 10 lowest energy configurations of O3-$Na_{2/3}[Li_{1/6}Fe_{1/6}Co_{1/6}Ni_{1/6}Mn_{1/3}]O_2$ obtained by the REMC method in the $2 \times 2 \times 1$-supercell evaluated by DFT single-points. Same DFT settings as described in the method part of the main text were employed using just the Γ-point. Apparently, the 4th lowest energy structure is a likely candidate for a global minimum in DFT enegies in this example.

Examples of Charge-Ordering

Another example where GOAC might be applied is to study different kinds of charge-orderings in layered oxide materials. For example, charge orderings in the transition metal layer can be studied alongside the ordering of Na ions in the Na-layer and how these different orderings are coupled.

Figure 2.18 depicts the example of $Na_{1.00}[Mg_{0.33}Mn_{0.67}]O_2$ that is expected to show some sort of charge-ordering as Mn is known to be likely to disproportionate into ions of different charges rather than showing a delocalized average charge. Therefore, and to ensure charge balancing, the transition metal layer was modelled by 1/3 Mg^{2+}, 1/3 Mn^{3+}, and 1/3 Mn^{4+}. It was also checked by the scan-supercell-size feature of GOAC that no lower energy charge-ordering can be obtained in cells up to twice as large in the *a*- and *b*-dimensions as the presented one. The optimized charge-ordering in the transition-metal layer obtained using GOAC is shown in the inlet in Figure 2.18. The pattern shows a superstructure that maximizes the distances between the ions of the highest charge (minimizes Coulomb repulsion). As a sodium concentration of 1 was modelled in an O-type stacking sequence (octahedral Na sites) along the *c*-direction, no different orderings of the sodium layer can be observed in this example.

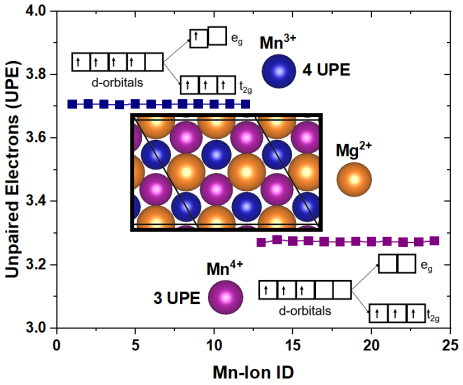

Supplementary Figure 2.18: Charge-ordering obtained for $Na_{1.00}[Mg_{0.33}Mn_{0.67}]O_2$ by optimization with GOAC assuming charges of Na^+, Mg^{2+} (orange), disproportionation into Mn^{3+} (blue) and Mn^{4+} (purple), and O^{2-}. Unpaired electrons (UPE) per Mn ion obtained from an HSE06 single-point are shown alongside their assigned charges following ligand-field theory

To verify the obtained charge-ordering, a DFT single-point calculation using the same settings described in the method part of the main text but the HSE06[93] hybrid functional was performed. Initial magnetic moments for Mn were chosen to coincide with the charge-ordering obtained in the GOAC optimization. The unpaired electrons (UPE) per Mn ion in the optimized electronic structure prove the charge-ordering proposed by Coulomb as 3+ sites in Coulomb show 4 UPE (high-spin Mn^{4+}, $t_{2g}{}^3$ $e_g{}^1$ electronic configuration) while 4+ sites in Coulomb show 3 UPE (Mn^{3+}, $t_{2g}{}^3$ $e_g{}^0$ electronic configuration). Thus, the charge ordering obtained from Coulomb energy optimization by GOAC coincides perfectly with the electronic structure obtained from DFT calculations with a hybrid functional for the depicted example. However, it should be noted that also some bias to the initial magnetic moment exists, however, the DFT electronic

structure was also not constrained such that the obtained result still is an indication that the proposed transition-metal layer charge-ordering is at least a local minimum in DFT.

To further verify the optimality of the obtained Mn charge ordering, HSE06 calculations for the 16 lowest orderings in Coulomb energy were performed. Again, initial magnetic moments were provided to coincide with the Mn ordering observed in electrostatics. The calculated Coulomb energies are plotted versus their obtained DFT energy in Figure 2.19. Results are split into 2 groups: Orderings where the initial magnetic moment was maintained in the electronic structure optimization (blue points) and orderings where another magnetic ordering than the initially provided one was obtained (orange points). As it can be seen from the dashed blue line, energies of charge-orderings where the initial magnetic moment was maintained in the electronic structure calculation are perfectly aligned to their Coulomb energies.

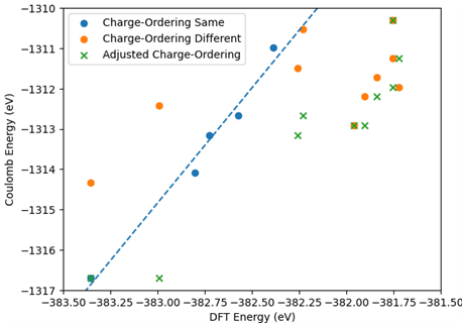

Supplementary Figure 2.19: Coulomb energies of the 16 lowest energy charge-orderings obtained for $Na_{1.00}[Mg_{0.33}Mn_{0.67}]O_2$ versus their DFT energy within the HSE06 functional. For the HSE06 calculations initial magnetic moments in agreement to the charge-ordering found in Coulomb were provided. For the blue points, the initial magnetic moments (charge-orderings) were maintained during electronic structure optimization while for the orange points it was not. The green crosses indicate the Coulomb energy that corresponds to the charge ordering in the HSE06 calculations for the orange points.

Outliers from the alignment between DFT and Coulomb energy of different orderings are observed for cases where another charge-ordering was obtained during the electronic structure optimization (HSE06 calculation). However, these points can be corrected by calculating the Coulomb energy of the actually observed charge-ordering (green crosses in Figure 2.19). Using the adjusted points along with the points where the charge-ordering was maintained, a Pearson correlation coefficient of more than 88 % between DFT and Coulomb energies can be observed proving a strong correlation between electrostatic energies and DFT energies of various transition-metal layer charge-orderings. Most importantly, the lowest energy Coulomb energy charge-orderings are also lowest in energy in DFT. This is particularly remarking as also different magnetic moments due to high- or low-spin Mn were seen for the electronic structures of some charge-orderings. The fact that the charge-orderings are still aligned to Coulomb energies indicates that electrostatics are the determining factor for charge-orderings while other magnetic effects (e.g., high-spin, low-spin, ferromagnetic, anti-ferromagnetic) only play a secondary role.

Finally, also the coupling of the transition-metal layer charge-ordering and the

sodium-ordering was studied at the example of $Na_{1/6}Mn_{1.00}O_2$. The two lowest energy orderings optimized by GOAC are shown in panel a) and b) of Figure 2.20. A coupling between the Na-ordering an the transition-metal layer charge-ordering can be observed: The sodiums are always placed on top of the transition-metal ion with the lowest charge (Mn^{3+}) to reduce the electrostatic repulsion. While, the two lowest energy orderings are rather close in energy, it should be noted that the next lowest energy structure in electrostatics is separated by more than 80 meV per formula unit (FU). To check the validity of the observed pattern, two HSE06 electronic structure calculations were performed for each of the orderings: one providing initial magnetic moments in agreement to the ordering observed in Coulomb (c, d in Figure 2.20) and one giving no specific initial guess for the magnetic moments (e, f in Figure 2.20). As the results in Figure 2.20 prove, in both cases the same ordering as in electrostatics is observed after the electronic structure optimizations with HSE06. Both configurations are also very similar in energy (in agreement to Coulomb) while the energetic order is reversed. This highlights that it is worth to study several low energy configurations from Coulomb to find the lowest energy configuration in DFT.

To verify the coupling between the transition-metal layer charge-ordering and Na-ordering observed in electrostatics, the models were cross-checked by providing the initial magnetic orderings of one configuration to the Na-ordering of the other structure (models are shown in Figure 2.20, g and h). The outcomes when optimizing the electronic structure of these cross-check models by HSE06 are shown in panel i9 and j) of Figure 2.20, respectively. While in one case (j) the same coupling of the transition-metal layer charge-ordering and Na-ordering is obtained, in the other case (i) only partial coupling is observed. However, also the corresponding energy of the partially-coupled configuration is much higher compared to the very small energy difference between the two coupled-configurations known from electrostatics (a, b in Figure 2.20). Overall, the results suggest that GOAC can also be employed to study transition-metal layer charge-orderings and Na-orderings in a coupled fashion as DFT electronic structure calculations of low Coulomb energy configurations are seemingly well aligned.

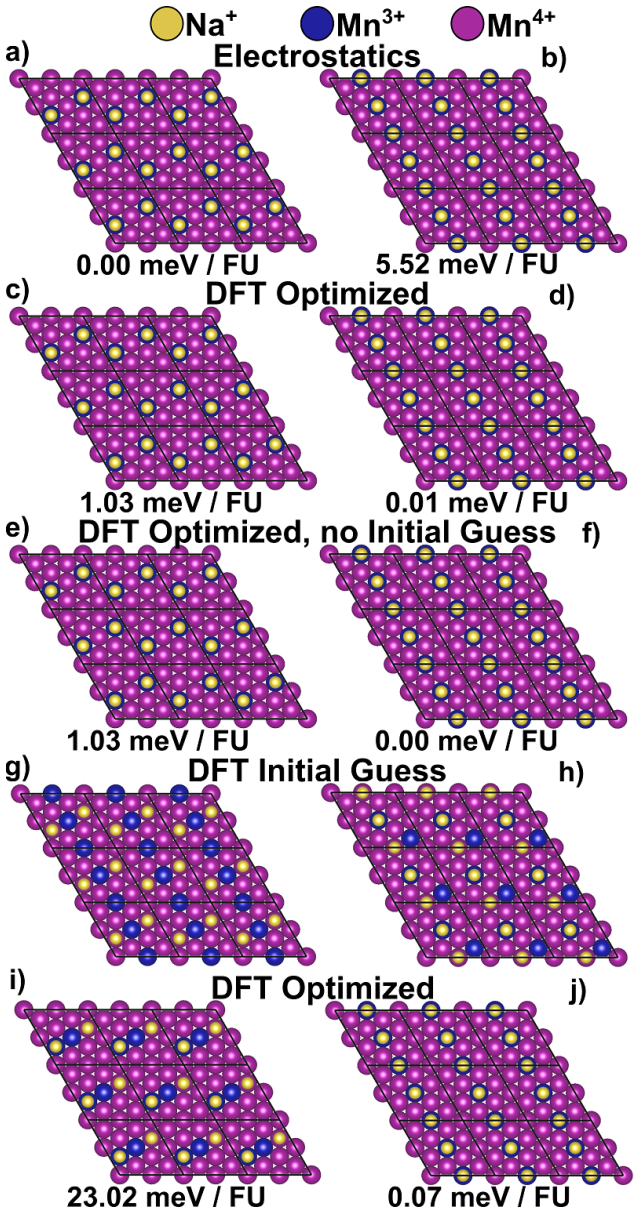

Supplementary Figure 2.20: Coupling of transition-metal layer orderings and Na-ordering in electrostatics and DFT. The two lowest energy transition-metal layer orderings and Na-orderings of $Na_{1/6}Mn_{1.00}O_2$ as optimized by GOAC (a and b) or DFT HSE06 calculations (with initial guess: c, d, and without initial guess: e, f). g) and h) show models to cross-check the Na- and transition-metal charge-orderings and i) and j) the corresponding optimized structures employing DFT HSE06.

REFERENCES

1. Chen, S. *et al.* Compositional dependence of structural and electronic properties of Cu 2 ZnSn(S,Se) 4 alloys for thin film solar cells. *Physical Review B* **83** (2011).
2. Boyd, C. C., Cheacharoen, R., Leijtens, T. & McGehee, M. D. Understanding Degradation Mechanisms and Improving Stability of Perovskite Photovoltaics. *Chemical reviews* **119,** 3418–3451 (2019).
3. Anantharamulu, N. *et al.* A wide-ranging review on Nasicon type materials. *Journal of Materials Science* **46,** 2821–2837 (2011).
4. Li, W., Erickson, E. M. & Manthiram, A. High-nickel layered oxide cathodes for lithium-based automotive batteries. *Nature Energy* **5,** 26–34 (2020).
5. Lun, Z. *et al.* Cation-disordered rocksalt-type high-entropy cathodes for Li-ion batteries. *Nature materials* **20,** 214–221 (2021).
6. Sarkar, A. *et al.* High entropy oxides for reversible energy storage. *Nature communications* **9,** 3400 (2018).
7. Fabbri, E., Pergolesi, D. & Traversa, E. Materials challenges toward proton-conducting oxide fuel cells: a critical review. *Chemical Society reviews* **39,** 4355–4369 (2010).
8. Yan, S. *et al.* Perovskite Solid-State Electrolytes for Lithium Metal Batteries. *Batteries* **7,** 75 (2021).
9. Bai, X., Duan, Y., Zhuang, W., Yang, R. & Wang, J. Research progress in Li-argyrodite-based solid-state electrolytes. *Journal of Materials Chemistry A* **8,** 25663–25686 (2020).
10. Shin, D. O. *et al.* Synergistic multi-doping effects on the Li7La3Zr2O12 solid electrolyte for fast lithium ion conduction. *Scientific reports* **5,** 18053 (2015).
11. Wang, C. *et al.* Garnet-Type Solid-State Electrolytes: Materials, Interfaces, and Batteries. *Chemical reviews* **120,** 4257–4300 (2020).
12. Oses, C., Toher, C. & Curtarolo, S. High-entropy ceramics. *Nature Reviews Materials* **5,** 295–309 (2020).
13. Li, H., Lai, J., Li, Z. & Wang, L. Multi–Sites Electrocatalysis in High–Entropy Alloys. *Advanced Functional Materials* **31** (2021).
14. Kumar Katiyar, N., Biswas, K., Yeh, J.-W., Sharma, S. & Sekhar Tiwary, C. A perspective on the catalysis using the high entropy alloys. *Nano Energy* **88,** 106261 (2021).
15. Ma, Z. *et al.* High Entropy Semiconductor AgMnGeSbTe 4 with Desirable Thermoelectric Performance. *Advanced Functional Materials* **31** (2021).

16. Yarema, O., Yarema, M. & Wood, V. Tuning the Composition of Multicomponent Semiconductor Nanocrystals: The Case of I–III–VI Materials. *Chemistry of Materials* **30,** 1446–1461 (2018).

17. He, Q., Yu, B., Li, Z. & Zhao, Y. Density Functional Theory for Battery Materials. *Energy & Environmental Materials* **2,** 264–279 (2019).

18. Zhang, T., Li, D., Tao, Z. & Chen, J. Understanding electrode materials of rechargeable lithium batteries via DFT calculations. *Progress in Natural Science: Materials International* **23,** 256–272 (2013).

19. Wang, Y., Yu, B., Xiao, J., Zhou, L. & Chen, M. Application of First Principles Computations Based on Density Functional Theory (DFT) in Cathode Materials of Sodium-Ion Batteries. *Batteries* **9,** 86 (2023).

20. d'Avezac, M. & Zunger, A. Identifying the minimum-energy atomic configuration on a lattice: Lamarckian twist on Darwinian evolution. *Physical Review B* **78** (2008).

21. Islam, M. S. & Fisher, C. A. J. Lithium and sodium battery cathode materials: computational insights into voltage, diffusion and nanostructural properties. *Chemical Society reviews* **43,** 185–204 (2014).

22. Zhang, R.-Z. & Reece, M. J. Review of high entropy ceramics: design, synthesis, structure and properties. *Journal of Materials Chemistry A* **7,** 22148–22162 (2019).

23. Toda-Caraballo, I., Wróbel, J. S., Nguyen-Manh, D., Pérez, P. & Rivera-Díaz-del-Castillo, P. E. J. Simulation and Modeling in High Entropy Alloys. *JOM* **69,** 2137–2149 (2017).

24. Huo, W. *et al.* High-entropy materials for electrocatalytic applications: a review of first principles modeling and simulations. *Materials Research Letters* **11,** 713–732 (2023).

25. Velický, B. Theory of Electronic Transport in Disordered Binary Alloys: Coherent-Potential Approximation. *Physical Review* **184,** 614–627 (1969).

26. Wei, S., Ferreira, L. G., Bernard, J. E. & Zunger, A. Electronic properties of random alloys: Special quasirandom structures. *Physical review. B, Condensed matter* **42,** 9622–9649 (1990).

27. Laks, D. B., Ferreira, L. G., Froyen, S. & Zunger, A. Efficient cluster expansion for substitutional systems. *Physical review. B, Condensed matter* **46,** 12587–12605 (1992).

28. Sanchez, J. M. Cluster expansions and the configurational energy of alloys. *Physical review. B, Condensed matter* **48,** 14013–14015 (1993).

29. Bellaiche, L. & Vanderbilt, D. Virtual crystal approximation revisited: Application to dielectric and piezoelectric properties of perovskites. *Physical review. B, Condensed matter* **61,** 7877–7882 (2000).

30. Sorkin, V., Tan, T. L., Yu, Z. G. & Zhang, Y. W. Generalized small set of ordered structures method for the solid-solution phase of high-entropy alloys. *Physical Review B* **102** (2020).

31. Ångqvist, M. *et al.* ICET – A Python Library for Constructing and Sampling Alloy Cluster Expansions. *Advanced Theory and Simulations* **2** (2019).
32. Kostiuchenko, T., Körmann, F., Neugebauer, J. & Shapeev, A. Impact of lattice relaxations on phase transitions in a high-entropy alloy studied by machine-learning potentials. *npj Computational Materials* **5** (2019).
33. Yuan, X. *et al.* Active learning to overcome exponential-wall problem for effective structure prediction of chemical-disordered materials. *npj Computational Materials* **9** (2023).
34. Ferrari, A. *et al.* Frontiers in atomistic simulations of high entropy alloys. *Journal of Applied Physics* **128** (2020).
35. Tetsassi Feugmo, C. G., Ryczko, K., Anand, A., Singh, C. V. & Tamblyn, I. Neural evolution structure generation: High entropy alloys. *The Journal of Chemical Physics* **155,** 044102 (2021).
36. Peng, Q. *et al.* Active-learning search for unitcell structures: A case study on Mg3Bi2-xSbx. *Computational Materials Science* **226,** 112260 (2023).
37. Yaghoobi, M. & Alaei, M. Machine learning for compositional disorder: A comparison between different descriptors and machine learning frameworks. *Computational Materials Science* **207,** 111284 (2022).
38. Lian, J.-C. *et al.* Highly efficient tree search algorithm for irreducible site-occupancy configurations. *Physical Review B* **105** (2022).
39. Grau-Crespo, R., Hamad, S., Catlow, C. R. A. & de Leeuw, N. H. Symmetry-adapted configurational modelling of fractional site occupancy in solids. *Journal of Physics: Condensed Matter* **19,** 256201 (2007).
40. Hart, G. L. W. & Forcade, R. W. Algorithm for generating derivative structures. *Physical Review B* **77** (2008).
41. Ong, S. P. *et al.* Python Materials Genomics (pymatgen): A robust, open-source python library for materials analysis. *Computational Materials Science* **68,** 314–319 (2013).
42. Mustapha, S. *et al.* On the use of symmetry in configurational analysis for the simulation of disordered solids. *Journal of Physics: Condensed Matter* **25,** 105401 (2013).
43. D'Arco, P. *et al.* Symmetry and random sampling of symmetry independent configurations for the simulation of disordered solids. *Journal of Physics: Condensed Matter* **25,** 355401 (2013).
44. Erba, A. *et al.* CRYSTAL23: A Program for Computational Solid State Physics and Chemistry. *Journal of Chemical Theory and Computation* **19,** 6891–6932 (2023).
45. Okhotnikov, K., Charpentier, T. & Cadars, S. Supercell program: a combinatorial structure-generation approach for the local-level modeling of atomic substitutions and partial occupancies in crystals. *Journal of cheminformatics* **8,** 17 (2016).
46. Lian, J.-C., Wu, H.-Y., Huang, W.-Q., Hu, W. & Huang, G.-F. Algorithm for generating irreducible site-occupancy configurations. *Physical Review B* **102** (2020).

47. Prayogo, G. I. *et al.* Shry: Application of Canonical Augmentation to the Atomic Substitution Problem. *Journal of chemical information and modeling* **62,** 2909–2915 (2022).

48. Ewald, P. P. Die Berechnung optischer und elektrostatischer Gitterpotentiale. *Annalen der Physik* **369,** 253–287 (1921).

49. Toukmaji, A. Y. & Board, J. A. Ewald summation techniques in perspective: a survey. *Computer Physics Communications* **95,** 73–92 (1996).

50. Jang, S.-H., Jalem, R. & Tateyama, Y. EwaldSolidSolution: A High-Throughput Application to Quickly Sample Stable Site Arrangements for Ionic Solid Solutions. *The journal of physical chemistry. A* **127,** 5734–5744 (2023).

51. Lee, B. D. *et al.* Argyrodite configuration determination for DFT and AIMD calculations using an integrated optimization strategy. *RSC advances* **12,** 31156–31166 (2022).

52. Fraser, A. S. Simulation of Genetic Systems by Automatic Digital Computers I. Introduction. *Australian Journal of Biological Sciences* **10,** 484 (1957).

53. Han, W. G., Park, W. B., Singh, S. P., Pyo, M. & Sohn, K.-S. Determination of possible configurations for Li0.5CoO2 delithiated Li-ion battery cathodes via DFT calculations coupled with a multi-objective non-dominated sorting genetic algorithm (NSGA-III). *Physical chemistry chemical physics : PCCP* **20,** 26405–26413 (2018).

54. Dieterich, J. M. & Hartke, B. OGOLEM: Global cluster structure optimisation for arbitrary mixtures of flexible molecules. A multiscaling, object-oriented approach. *Molecular Physics* **108,** 279–291 (2010).

55. Metropolis, N., Rosenbluth, A. W., Rosenbluth, M. N., Teller, A. H. & Teller, E. Equation of State Calculations by Fast Computing Machines. *The Journal of Chemical Physics* **21,** 1087–1092 (1953).

56. Binninger, T., Ting, Y.-Y., Kowalski, P. M. & Eikerling, M. H. Optimization of ionic configurations in battery materials by quantum annealing. *Physical Review B* **110** (2024).

57. Ferrari, A., Körmann, F., Asta, M. & Neugebauer, J. Simulating short-range order in compositionally complex materials. *Nature computational science* **3,** 221–229 (2023).

58. Binninger, T., Marcolongo, A., Mottet, M., Weber, V. & Laino, T. Comparison of computational methods for the electrochemical stability window of solid-state electrolyte materials. *Journal of Materials Chemistry A* **8,** 1347–1359 (2020).

59. van de Walle, A. *et al.* Efficient stochastic generation of special quasirandom structures. *Calphad* **42,** 13–18 (2013).

60. van de Walle, A., Asta, M. & Ceder, G. The alloy theoretic automated toolkit: A user guide. *Calphad* **26,** 539–553 (2002).

61. Barroso-Luque, L. *et al.* smol: A Python package for cluster expansions and beyond. *Journal of Open Source Software* **7,** 4504 (2022).

62. Hall, S. R., Allen, F. H. & Brown, I. D. The crystallographic information file (CIF): a new standard archive file for crystallography. *Acta Crystallographica Section A Foundations of Crystallography* **47,** 655–685 (1991).

63. Dagum, L. & Menon, R. OpenMP: an industry standard API for shared-memory programming. *IEEE Computational Science and Engineering* **5,** 46–55 (1998).

64. Gurobi Optimization, L. L. *Gurobi Optimizer Reference Manual* 2023. `https://www.gurobi.com`.

65. Moradabadi, A. & Kaghazchi, P. Defect chemistry in cubic Li6.25Al0.25La3Zr2O12 solid electrolyte: A density functional theory study. *Solid State Ionics* **338,** 74–79 (2019).

66. Wang, Q. *et al.* Unlocking anionic redox activity in O3-type sodium 3d layered oxides via Li substitution. *Nature materials* **20,** 353–361 (2021).

67. Kim, J. C. *et al.* Direct Observation of Alternating Octahedral and Prismatic Sodium Layers in O3–Type Transition Metal Oxides. *Advanced Energy Materials* **10** (2020).

68. Voronina, N. *et al.* Unveiling the Role of Ruthenium in Layered Sodium Cobaltite Toward High–Performance Electrode Enabled by Anionic and Cationic Redox. *Advanced Energy Materials* **13** (2023).

69. Kim, H.-J. *et al.* Synergetic impact of dual substitution on anionic–Cationic activity of P2-type sodium manganese oxide. *Energy Storage Materials* **66,** 103224 (2024).

70. Pahari, D., Chowdhury, A., Das, D., Paul, T. & Puravankara, S. The evolution of structure–property relationship of P2-type Na0.67Ni0.33Mn0.67O2 by vanadium substitution and organic electrolyte combinations for sodium-ion batteries. *Journal of Solid State Electrochemistry* **27,** 2067–2082 (2023).

71. Faber, F., Lindmaa, A., von Lilienfeld, O. A. & Armiento, R. Crystal structure representations for machine learning models of formation energies. *International Journal of Quantum Chemistry* **115,** 1094–1101 (2015).

72. Gingrich, T. R. & Wilson, M. On the Ewald summation of Gaussian charges for the simulation of metallic surfaces. *Chemical Physics Letters* **500,** 178–183 (2010).

73. Zhang, H., Ge, H., Yang, J. & Tong, Y. Review of Vehicle Routing Problems: Models, Classification and Solving Algorithms. *Archives of Computational Methods in Engineering* **29,** 195–221 (2022).

74. Shamsaei, F. & van Vyve, M. Solving integrated production and condition-based maintenance planning problems by MIP modeling. *Flexible Services and Manufacturing Journal* **29,** 184–202 (2017).

75. Kronqvist, J., Bernal, D. E., Lundell, A. & Grossmann, I. E. A review and comparison of solvers for convex MINLP. *Optimization and Engineering* **20,** 397–455 (2019).

76. Thachuk, C., Shmygelska, A. & Hoos, H. H. A replica exchange Monte Carlo algorithm for protein folding in the HP model. *BMC bioinformatics* **8,** 342 (2007).

77. Lipowski, A. & Lipowska, D. Roulette-wheel selection via stochastic acceptance. *Physica A: Statistical Mechanics and its Applications* **391,** 2193–2196 (2012).

78. Dugan, N. & Erkoç, Ş. Genetic algorithm–Monte Carlo hybrid geometry optimization method for atomic clusters. *Computational Materials Science* **45,** 127–132 (2009).

79. Sakae, Y., Hiroyasu, T., Miki, M., Ishii, K. & Okamoto, Y. Conformational search simulations of Trp-cage using genetic crossover. *Molecular Simulation* **41,** 1045–1049 (2015).

80. Kim, H. *et al.* Ab Initio Study of the Sodium Intercalation and Intermediate Phases in Na 0.44 MnO 2 for Sodium-Ion Battery. *Chemistry of Materials* **24,** 1205–1211 (2012).

81. Delmas, C., Fouassier, C. & Hagenmuller, P. Structural classification and properties of the layered oxides. *Physica B+C* **99,** 81–85 (1980).

82. Madelung, E. Das elektrische Feld in Systemen von regelmäßig angeordneten Punktladungen. *Phys. Z* **19,** 32 (1918).

83. Sakamoto, Y. Madelung Constants of Simple Crystals Expressed in Terms of Born's Basic Potentials of 15 Figures. *The Journal of Chemical Physics* **28,** 164–165 (1958).

84. Redhammer, G. J. *et al.* Wet-Environment-Induced Structural Alterations in Single- and Polycrystalline LLZTO Solid Electrolytes Studied by Diffraction Techniques. *ACS applied materials & interfaces* **13,** 350–359 (2021).

85. Kannan, S. & Zacharias, M. Simulated annealing coupled replica exchange molecular dynamics–an efficient conformational sampling method. *Journal of structural biology* **166,** 288–294 (2009).

86. Yao, L. *et al.* High–Entropy and Superstructure–Stabilized Layered Oxide Cathodes for Sodium–Ion Batteries. *Advanced Energy Materials* **12** (2022).

87. Ade, P. A. R. *et al.* Planck 2015 results. *Astronomy & Astrophysics* **594,** A13 (2016).

88. Binninger, T. *et al.* Simulating charging characteristics of lithium iron phosphate by electro-ionic optimization on a quantum annealer. *Physical Review B* **112** (2025).

89. Kresse, G. & Furthmüller, J. Efficient iterative schemes for ab initio total-energy calculations using a plane-wave basis set. *Physical review. B, Condensed matter* **54,** 11169–11186 (1996).

90. Blöchl, P. E. Projector augmented-wave method. *Physical review. B, Condensed matter* **50,** 17953–17979 (1994).

91. Perdew, J. P., Burke, K. & Ernzerhof, M. Generalized Gradient Approximation Made Simple. *Physical review letters* **77,** 3865–3868 (1996).

92. Momma, K. & Izumi, F. VESTA : a three-dimensional visualization system for electronic and structural analysis. *Journal of Applied Crystallography* **41,** 653–658 (2008).

93. Krukau, A. V., Vydrov, O. A., Izmaylov, A. F. & Scuseria, G. E. Influence of the exchange screening parameter on the performance of screened hybrid functionals. *The Journal of Chemical Physics* **125,** 224106 (2006).

3

PHASE STABILITY PREDICTIONS:

HIGH-THROUGHPUT PREDICTIONS OF PHASE-STABILITIES OF LAYERED OXIDE CATHODES BY OPTIMIZED ELECTROSTATICS

Layered oxide cathodes are among the most promising materials for sodium ion batteries. They are reported in various stacking sequences along the *c*-direction such as P2 and O3. These phases can influence important material properties such as capacity or ionic conductivity. Moreover, the layered sodium materials are also prone to undergo phase transitions during cycling which is considered to be a key reason for voltage fade and capacity degradation. Thus, predicting the most stable phase is highly desirable to enable rational design of layered oxide sodium ion cathodes. In this work, an *ab initio* phase stability predictor that is solely based on electrostatics is presented. The approach utilizes high throughput Monte-Carlo-based heuristic optimizations in huge configurational spaces (e.g., 10^{100} configurations) of a large number (15000 materials) of possible cathode compositions and phases (O1, O2, O3, P2, P3, OP2, OP4). It is shown that the resulting predictor is able to reproduce experimentally observed phase stabilities with an accuracy of 80 % and also captures trends of phase stabilities and transitions during desodiation correctly. Thus, the *ab initio* electrostatics predictor will support the rational design of layered oxide sodium ion cathode materials.

This chapter is based on: **Köster, K.**, ten Elshof, J. E., Huijben, M., *et al.* High-Throughput Predictions of Phase-Stabilities of Layered Oxide Cathodes by Optimized Electrostatics. *In Preparation for Re-Submission to eScience* (2025).

3.1 Introduction

Sodium ion batteries (SIBs) gained significant interest during the last years as a promising, potentially more cost-effective and sustainable alternative to today's market standard for secondary batteries, lithium ion batteries (LIBs).[1–4] Among the various types of SIBs cathodes layered oxides are among the most promising ones as they can offer high capacities. They are routinely employed in commercial LIBs. However, when lithium is exchanged by sodium several challenges arise, mainly due to the increased ionic size of sodium compared to lithium. This impacts especially the sequence at which the layers are stacked along the *c*-direction. While lithium shows usually an octahedral coordination, SIBs are mostly reported in a prismatic environment while also octahedral coordination is found.[2] The layered oxide materials are therefore classified by the charge carrier coordination, e.g., octahedral (O) or prismatic (P), and the stacking periodicity along the *c*-direction.[5] Using this formalism, SIBs are mostly reported in P2 and O3 phases.[6] In contrast to LIBs, SIBs also usually undergo several phase transitions between various stacking phases during cycling which causes a stepped voltage profile. Such phase transitions often lead to large and sudden changes in the *c*-lattice parameter which can cause cracking and is believed to be a major reason for capacity degradation during cycling.[7] A common approach is to design the composition of the cathode material such that the desired phase is obtained during synthesis and phase transitions are suppressed or controlled during cycling.[8–12] Next to stability, the stacking phases can also influence other properties such as the maximal sodium concentration (capacity), ionic conductivity, moisture sensitivity, and average voltage. In general, O-phases (O3) allow for higher sodium concentrations (possibly higher capacity) while P-phases show better ionic conductivity at intermediate to low sodium concentrations and are often stable over a broader voltage window.[2, 6, 13]

Thus, predictors that relate the chemical composition of a cathode material to its most stable stacking phase are highly desirable to allow for the rational design of layered oxide cathodes for SIBs. Zhao *et al.* [6] published a simple yet effective predictor named "cationic potential", based on the ionic potential [14], that relates chemical compositions to their most stable stacking sequence. In their work, they show that a linear fit in the two dimensional space of sodium concentration (sodium ionic potential) and cationic potential separates as-synthesized sodium ion layered oxides into P2 and O3. As the ionic potential aims to quantify the charge density of ions by their valency and ionic radii the success of the cationic potential classifier indicates that electrostatic interactions and sodium concentration are the determining factor for phase stabilities in layered oxides. Indeed, Shin *et al.* [15] tried to explain the stability of P over O phases by electrostatics. For all of these approaches a guess for the valencies of the transition-metal layer ions must be made, e.g., by their electronegativity. However, when explicit and not only averaged electrostatics are considered, the site occupation must be determined first. This gives raise to a huge configurational space for materials where multiple transition metals occupy one lattice site and/or sodium orderings must be determined. This gigantic configurational space renders the main challenge in comparing phase stabilities by direct electrostatics. To judge the thermodynamic stability of different phases it is desirable to compare the lowest energy configurations of each phase which requires configurational optimization as, for example, implemented in the recently published

GOAC (Global Optimization of Atomistic Configurations by Coulomb) package. [16]

In this work, it is shown show that with the help of heuristic optimizations it is possible to evaluate phase stabilities at their respective lowest energy configuration by direct calculation of periodic electrostatic interaction energies. To maximize the prediction quality, it is shown that lattice parameters can be optimized by maximizing the correlation to density functional theory (DFT) energy differences between different stacking sequences for various layered oxide cathode materials. Thus, the prediction approach remains fully *ab initio*. It is continued by employing the approach to predict experimental structures and finally prove that the approach is computationally still fast enough to be used in high throughput studies. By such high-throughput screening a detailed overview of the phase stabilities of several ternary cathode materials at different sodium concentrations (15000 compounds) is provided. The *ab initio* predictor based on electrostatics can be employed to predict phase stability of various stacking sequence phases such as O1, O2, O3, P2, P3, OP2, and OP4 and also delivers predictions at lower sodium concentrations (cycled materials).

3.2 Framework Electrostatic Prediction Approach

For ionic crystals such as layered oxide cathode materials it is to expect that electrostatic interactions are the driving force for structural arrangements and that Coulomb energies are sufficiently correlated to energies of higher level of theory approaches such as density functional theory (DFT). Even though Coulomb calculations are *ab initio* by definition, performing an energy calculation on a layered oxide cathode still has some parameters that can be, to some extend, freely chosen. Tuning the parameters can increase the agreement to DFT energies even further. These parameters are the inter-layer separation along the *c*-axis ($d_{\text{O-Na-O}}$), the intra-layer separation ($d_{\text{O-TM-O}}$), and the *a*-lattice parameter (which is equal to the *b*-lattice parameter in the space group). If smeared charges instead of point charges are considered in the electrostatic calculations also the smearing width of the charges (σ) is a free parameter. All parameters are visualized in the left box in the upper part of Figure 3.1. Moreover, technically also the magnitude of the (point-) charges, the lattice angles and the ion positions could be varied as well. Due to the high complexity of including these parameters and the decrease of predictive power by introducing more degrees of freedom these parameters are omitted in this work. Regarding the considered geometry related parameters ($d_{\text{O-Na-O}}$, $d_{\text{O-TM-O}}$, *a*-lattice parameter) it must be mentioned that with Coulomb energies, unlike in other approaches such as DFT or complete force fields, no optimization can be performed as bare Coulomb forces would result in a collapse of the structure due to the missing Born repulsion at short distances. Therefore, all parameters should be fixed *a priori*. To do so, in this work it is proposed to fit the parameters to DFT references such that the Pearson correlation of energies between all the different stacking sequences shown in Figure 3.2 is maximized. By fitting to DFT data, the overall prediction approach also remains fully *ab initio*. To fit the parameters of the Coulomb calculations it is desirable to apply fully optimized DFT structures as the obtained DFT energies are usually more reliable than DFT single points and such a fitting approach bears the potential to still capture a portion of the energy contribution of the structural relaxation in the optimized Coulomb energies. In summary, the framework for high throughput predictions of phase stabilities in layered

oxides proposed in this work can be summarized by the scheme in Figure 3.1: A database with the energies of 231 fully optimized DFT structures (cf. Figure 3.2) is used to find a optimal set of parameters ($d_{\text{O-Na-O}}$, $d_{\text{O-TM-O}}$, a, σ) for the Coulomb energy calculations of the undistorted structures and finally these parameters are applied to screen a broad composition space with low computational cost. Optimality of the parameters is defined such that the correlation of energies over the different stacking sequences between Coulomb and DFT is maximized.

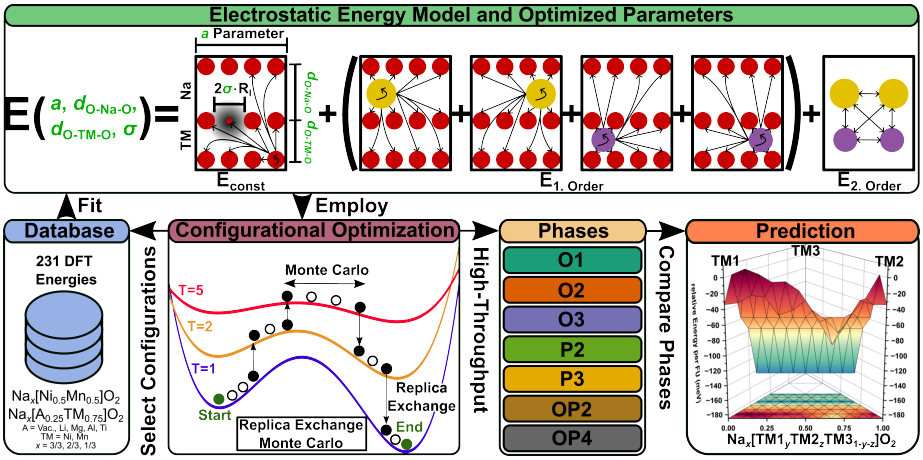

Figure 3.1: Framework of the high throughput prediction scheme employed in this work. First, electrostatic optimization was employed to find favourable configurations. Configurational energy optimization was performed by Replica Exchange Monte Carlo (REMC) based on an additive function of pairwise electrostatic interactions. The energy calculation is sketched in the top box of the Figure while red ions indicate oxygen, yellow ions sodium, and purple ions transition metals (TM). Pairwise interactions including the self-interaction are indicated by arrows but for the constant term just for one of the oxygen ions. The total electrostatic energy of the system is constructed from interactions of fixed ions (E_{const}), interactions of iterative ions, e.g., sodium or transition metals, and fixed ions ($E_{1.\text{ Order}}$) and interactions between iterative sites ($E_{2.\text{ Order}}$). Next, with help of DFT geometry optimizations of lowest electrostatic energy configurations a DFT energies database of 231 materials was created. Electrostatic parameters ($d_{\text{O-Na-O}}$ (oxygen-layer separation around Na along the c-axis), $d_{\text{O-TM-O}}$ (oxygen-layer separation around TM along the c-axis), a (a-lattice parameter that equals b-lattice parameter), and σ (Gaussian smearing width of point charges)) were optimized to maximize the correlation over different stacking sequences to the DFT energies. Finally, the optimized parameters are employed within the electrostatic configurational optimization framework to predict the energies of various stacking sequences of a large composition space in a high throughput manner. These energies are then used to describe the phase-stability energy-surface as function of composition. The compositions space of $Na_x[A_yNi_zMn_{1-y-z}]O_2$ with x in [0/6, 1/6, 2/6, 3/6, 4/6, 5/6, 6/6], A in [Vac^0, Li^{1+}, Mg^{2+}, Al^{3+}, and Ti^{4+}], y in [0/12, 1/12, 2/12, 3/12, 4/12, 5/12, 6/12], and z in [0/12, 1/12, 2/12, 3/12, 4/12, 5/12, 6/12, 7/12, 8/12, 9/12, 10/12, 11/12, 12/12] was considered in all 7 most common stacking sequences (O1, O2, O3, P2, P3, OP2, OP4).

To create the DFT database, configurational optimization by Coulomb energies was performed with the Replica Exchange Monte Carlo (REMC) scheme followed by DFT full geometry optimizations on the lowest Coulomb-energy configuration for 231 compositions of $Na_x[Ni_{0.5}Mn_{0.5}]O_2$ and $Na_x[A_{0.25}TM_{0.75}]O_2$ with A = Vac, Li, Mg, Al, Ti, TM = Ni, Mn. Moreover, x = 3/3, 2/3, and 1/3, and all in O1, O2, O3, P2, P3, OP2, and OP4 stacking sequence along c direction (cf. Fig. 3.2), respectively. In the REMC scheme, multiple Monte Carlo (MC) runs are performed at different temperatures and samples

are exchanged between those from different temperatures (cf. corresponding panel in Figure 3.1). While low temperatures are well suited to determine local minima, MC runs at higher temperatures allow to overcome local energy barriers. Thus, the combination of different temperatures in REMC can allow efficient heuristic optimizations towards the global minima. During the runs energies are evaluated by pairwise electrostatic interactions while energy terms are split into constant as well as first- and second-order terms to allow for efficient energy evaluation. More details of the energy calculation and optimization methods can be found in the work of Köster *et al.*.[16] The valencies for the electrostatic calculations can be calculated assuming fixed charges of Na^{+}, Vac^{0}, Li^{+}, Mg^{2+}, Al^{3+}, Ti^{4+}, and O^{2-} and variable charges between 2+ and 4+ for Ni and Mn to ensure overall charge balancing for each composition. Mn was first oxidized to Mn^{4+} before Ni was oxidized to any oxidation state larger than 2+, which yields a redox mechanism accordingly to the electronegativities of the transition metals. Lastly, the oxygen was oxidized to charges higher than 2− if the structure was not charge balanced by full oxidation to 4+ for Ni and Mn. The degrees and mechanisms of oxygen redox in layered cathodes is a topic of intense discussion[17, 18] but in the electrostatic model simply the charge of all oxygen anions was increased to charge balance the material (full delocalization of charges). Consequently, compositions with just Ni or Mn should yield exactly the same phase stability (correlation of energies over different stackings) if the transition metal ion type plays only a secondary role (transition metals have same charges and similar ionic radii) and phase stability is mainly determined by electrostatics as Ni and Mn would be indistinguishable in these compositions. Indeed, the relative phase-energies of fully optimized DFT calculations of Mn and Ni compositions behave often similar as it can be seen in Figure 3.2 as well as in the plots of the energies shown in Figure 3.8. This indicates a strong correlation between Mn and Ni compositions with respect to their stacking sequence which is further quantified in Figure 3.9 where the Pearson correlation coefficients between Ni and Mn are plotted for all compositions revealing that many compositions are strongly positively correlated (correlation greater than 0.7). $Na_{0.67}[Mg_{0.25}TM_{0.75}]O_2$ and especially $Na_{0.33}[Vac_{0.25}TM_{0.75}]O_2$ are outliers that are weakly correlated. The particular weak correlation of ca. 0.2 for the latter composition might be explained by the fact that too strong oxygen redox is required to charge balance this composition which might yield to nonphysical behaviour. However, the overall very strong correlation between Ni and Mn compositions in DFT indicates that an electrostatic model could potentially be successful in predicting the phase stabilities of such layered oxides correctly as it seems that other effects such as local distortions, e.g., Jahn-Teller, or magnetic orderings play only a secondary role for the phase stability.

Assuming the aforementioned fixed point charges as well as a perfect undistorted structure with $d_{\text{O-Na-O}}$ = 3.4 Å, $d_{\text{O-TM-O}}$ = 2.1 Å, and a = 5.0 Å (default parameter set), indeed a decent correlation of Coulomb and DFT energies can be observed for $Na_x[Ni_{0.5}Mn_{0.5}]O_2$ in Figure 3.10, especially at higher sodium concentrations. Interestingly, the Coulomb energies of the perfect structures before DFT optimization show in most cases a reasonable correlation to the ones of fully optimized DFT structures which is especially remarkable as even energies of different structures are compared. The remaining strong correlation indicates that electrostatic interactions are a driving force in phase stability of layered oxides. However, it is still worth mentioning that overall the

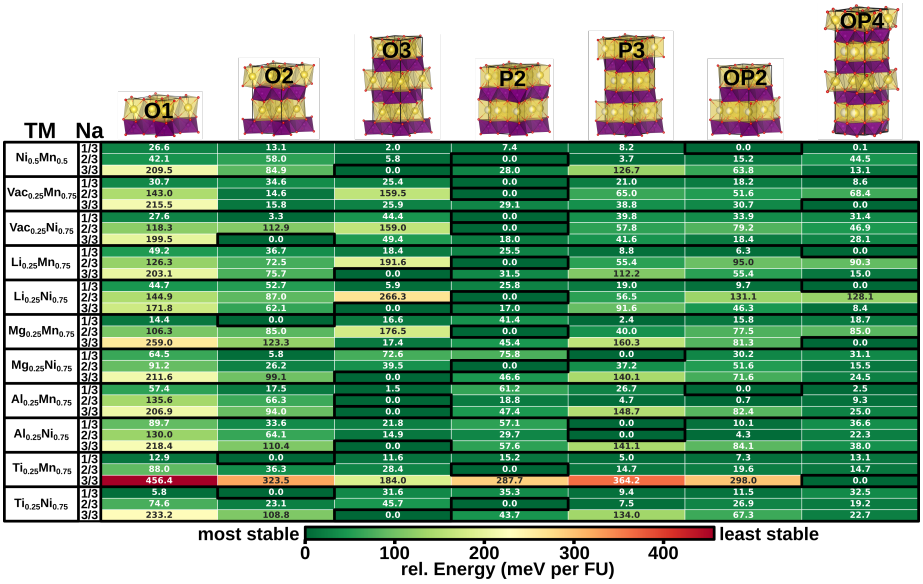

TM	Na	O1	O2	O3	P2	P3	OP2	OP4
$Ni_{0.5}Mn_{0.5}$	1/3	26.6	13.1	2.0	7.4	8.2	0.0	0.1
	2/3	42.1	58.0	5.8	0.0	3.7	15.2	44.5
	3/3	209.5	84.9	0.0	28.0	126.7	63.8	13.1
$Vac_{0.25}Mn_{0.75}$	1/3	30.7	34.6	25.4	0.0	21.0	18.2	8.6
	2/3	143.0	14.6	159.5	0.0	65.0	51.6	68.4
	3/3	215.5	15.8	25.9	29.1	38.8	30.7	0.0
$Vac_{0.25}Ni_{0.75}$	1/3	27.6	3.3	44.4	0.0	39.8	33.9	31.4
	2/3	118.3	112.9	159.0	0.0	57.8	79.2	46.9
	3/3	199.5	0.0	49.4	18.0	41.6	18.4	28.1
$Li_{0.25}Mn_{0.75}$	1/3	49.2	36.7	18.4	25.5	8.8	6.3	0.0
	2/3	126.3	72.5	191.6	0.0	55.4	55.0	30.3
	3/3	203.1	75.7	0.0	31.5	112.2	55.4	15.0
$Li_{0.25}Ni_{0.75}$	1/3	44.7	52.7	5.9	25.8	19.0	9.7	0.0
	2/3	144.9	87.0	266.3	0.0	56.5	131.1	128.1
	3/3	171.8	62.1	0.0	17.0	91.6	46.3	8.4
$Mg_{0.25}Mn_{0.75}$	1/3	14.4	0.0	16.6	41.4	2.4	15.0	18.7
	2/3	106.3	85.0	176.5	0.0	40.0	77.5	85.0
	3/3	259.0	123.3	17.4	45.4	160.3	81.3	0.0
$Mg_{0.25}Ni_{0.75}$	1/3	64.5	5.8	72.6	75.8	0.0	30.2	31.1
	2/3	91.2	26.2	39.5	0.0	37.2	51.6	15.5
	3/3	211.6	99.1	0.0	46.6	140.1	71.6	24.5
$Al_{0.25}Mn_{0.75}$	1/3	57.4	17.5	1.5	61.2	26.7	0.0	2.5
	2/3	135.6	66.3	0.0	18.8	4.7	0.7	9.3
	3/3	206.9	94.0	0.0	47.4	148.7	82.4	25.0
$Al_{0.25}Ni_{0.75}$	1/3	89.7	33.6	21.8	57.1	0.0	10.1	36.6
	2/3	130.0	64.1	14.9	29.7	0.0	4.3	22.3
	3/3	218.4	110.4	0.0	57.6	111.1	84.1	38.0
$Ti_{0.25}Mn_{0.75}$	1/3	12.9	0.0	11.6	15.2	5.0	7.3	13.1
	2/3	88.0	36.3	28.4	0.0	14.7	19.6	14.7
	3/3	456.4	323.5	184.0	287.7	364.2	298.0	0.0
$Ti_{0.25}Ni_{0.75}$	1/3	5.8	0.0	31.6	35.3	9.4	11.5	32.5
	2/3	74.6	23.1	45.7	0.0	7.5	26.9	19.2
	3/3	233.2	108.8	0.0	43.7	134.0	67.3	22.7

Figure 3.2: Top: Most commonly observed stacking sequences (phases) for sodium layered oxides. The letters indicate whether the sodium is in octahedral (O) or prismatic (P) coordination or if the coordination varies between the layers (OP). The number denotes the periodicity along *c*-direction. Bottom: Table with relative energies in meV per formula unit (FU) as obtained from full-geometry optimization in DFT for 11 different compositions, each at 3 different sodium concentrations (Na = 3/3, 2/3, 1/3). Energies are normalized to the most stable phase of each row (highlighted by a black box). In general, energy differences between the phases decrease at lower sodium concentrations rendering predictions of the most stable phase more difficult.

Coulomb energies of the fully optimized DFT geometries are more strongly correlated to the actual DFT energies while DFT single-point calculations of the undistorted structures are also stronger correlated to the Coulomb energies of the corresponding structures. In general, it seems promising that for higher sodium concentrations the energies of Coulomb and fully optimized DFT calculations are mostly aligned as this offers the possibility for a short-cut of *ab initio* phase stability predictions without performing expensive DFT calculations that might allows for high-throughput screening of compositions. Accordingly, it was continued by calculating the correlation over different stacking sequences between the fully optimized DFT energies and electrostatic energies of the undistorted structures for all 231 compositions and obtained an overall Pearson correlation coefficient of 0.508 (cf. Tab. 3.1). Interestingly, the correlation increases to 0.776 when the compositions with low sodium concentration (Na=1/3) are excluded from the data set proving that electrostatic energies are indeed capable to predict phase stabilities of as-synthesized layered oxides in fair agreement to DFT.

It was continued within the proposed prediction framework (cf. Figure 3.1) by optimizing the electrostatic parameters ($d_{\text{O-Na-O}}$, $d_{\text{O-TM-O}}$, a, σ) to increase correlation to DFT energies even further. The sensitivity of the correlation to DFT energies when varying the different parameters is shown in Figure 3.11 (including Na=1/3) and Figure 3.12 (excluding Na=1/3). While all geometry related parameters fail to achieve a high corre-

lation at Na=1/3 some optimization potential can be observed for higher sodium concentrations, especially at Na = 2/3 the correlation is sensitive to parameter variations. To determine optimal parameters for the electrostatic calculations in a holistic approach a three dimensional search on a dense grid (0.1 Å) for the geometry parameters ($d_{\text{O-Na-O}}$, $d_{\text{O-TM-O}}$, a) was performed. For each considered set of parameters the average correlation over stacking sequences (O1, O2, O3, P2, P3, OP2, OP4) to the DFT energies over all compositions can be determined. Resulting correlation values are shown in Figure 3.3 (a). It can be seen that for most points of the grid search a fair average correlation of more than 0.75 exists while towards small $d_{\text{O-Na-O}}$, small $d_{\text{O-TM-O}}$, and large a the correlation generally weakens. The correlations of the electrostatic energies to the DFT energies can also be checked per composition and sodium concentration as shown in the matrix in Figure 3.3 (b). In this matrix correlation values are shown if the most optimal set of electrostatic parameters is chosen individually for every field of the matrix. For most fields very strong correlation (greater than 0.8) exists proving that the prediction approach *via* Coulomb energies can be successful. However, at the lowest considered sodium concentration some outliers can be identified and the correlation becomes weaker. Especially the compositions containing Mg and Ti become weakly correlated (even negatively correlated) at Na=1/3. This might indicate that the proposed electrostatic prediction approach is not well-suited for low sodium-concentrations as no acceptable correlation to DFT energies was obtained. The reasons for this observation can be manifold but are most likely related to the fact that structures become more distorted during DFT geometry optimization at lower sodium concentrations (e.g., compositions containing Mg) which makes it more difficult or even impossible to obtain comparable results from the undistorted structures by electrostatics. Moreover, the computed redox mechanism (localization and delocalization of charges) can become less straight forward at lower sodium concentrations and might be even captured incorrectly by the employed PBE exchange-correlation functional which may especially influence the agreement for compositions containing Ti. Whether the electrostatics prediction approach can be still employed at low sodium concentrations is evaluated in the next section by comparison to experimental results. For the higher sodium concentrations the correlation of DFT and electrostatics is strong for all compositions. Predictability would decrease if a different set of electrostatic parameters is employed to each composition and sodium concentration as this would prevent effective high-throughput screening of unknown systems. Therefore, a single, globally optimal parameter set of the electrostatic parameters for sodium concentrations larger than 1/3 is chosen. As definition for globally optimal it is proposed to either maximize the average correlation (Figure 3.3 (c)) or to maximize the minimum correlation observed in the matrix fields (Figure 3.3 (d)).

It can be seen in Figure 3.3 (c) and (d) that both optimization approaches for the correlation by varying just the geometry parameters ($d_{\text{O-Na-O}}$, $d_{\text{O-TM-O}}$, a) yield strong correlations to the DFT energies, proving that phase-stabilities can be reproduced by electrostatic calculations employing a single set of electrostatic parameters for all compositions and sodium contents greater 1/3. Apparently, the overall performance (agreement to DFT) was slightly better when optimizing the average correlation and the corresponding set of electrostatic parameters is shown in Table 3.1 as "Optimized". Table 3.1 also reveals that the average correlation to DFT for high sodium concentrations is very

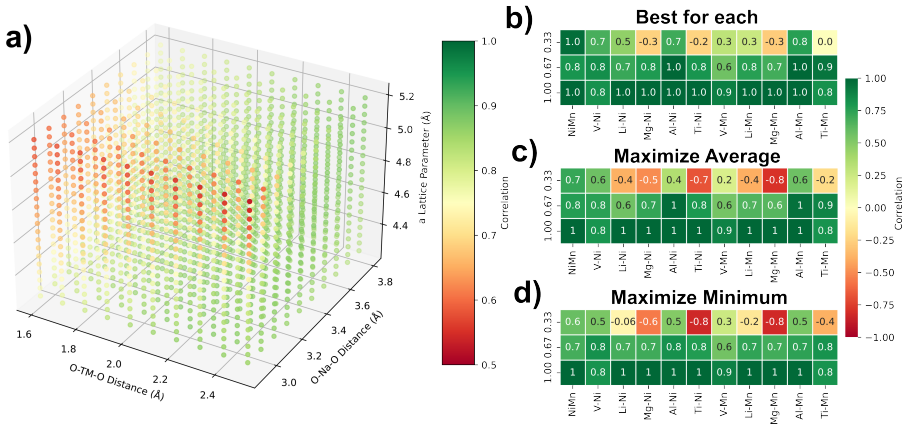

Figure 3.3: a) Grid-based search in the 3D space of considered geometry parameters ($d_{\text{O-Na-O}}$, $d_{\text{O-TM-O}}$, a) for the Coulomb calculations while green highlights stronger correlation to DFT energies and red weaker correlation. b) Correlation achieved by using the best possible set of parameters for each composition (horizontal) and sodium concentration (vertical) individually. c) Correlations to DFT energies per composition and sodium concentration when the parameter set that maximizes the average correlation over all compositions and sodium concentrations larger than 1/3 is chosen. d) Correlations to DFT energies per composition and sodium concentration when the parameter set that maximizes the minimum correlation out of all compositions and sodium concentrations larger than 1/3 is chosen.

high (0.852) with the optimized parameters and significantly improved compared to the default parameters (correlation of 0.776). However, the correlation is still weak (0.552) when also the compositions with 1/3 sodium are considered in the average even though significantly higher than for the default set of parameters (0.508). It was checked in Figure 3.13 if including Na=1/3 and/or excluding the compositions with a vacancy, as a vacancy is arguably very different from having different substituents in the transition-metal layer, can improve the correlation, but no significant improvement over the "Optimized" parameters shown in Table 3.1 was found. Moreover, optimized parameters were often similar to the ones shown in Table 3.1 while sometimes also nonphysical parameter sets (e.g., too small layer separations or a-lattice parameters) yield a high average correlation (cf. Figure 3.13). Finally, it was also tested if introducing two parameters for $d_{\text{O-Na-O}}$ to account for octahedral and prismatic sites can improve the results as different layer separations for these coordinations are reported experimentally [6]. However, it was found that correlations are not significantly improved and that electrostatic energies are in general most comparable when a single (same) parameter for the inter-layer separation is used. Consequently, only one parameter for the inter-layer distance is given in the parameter sets in Table 3.1.

Table 3.1: Different sets of electrostatic parameters determined and employed in this work. First, the default parameters motivated by experimental values that were used as a reference and to obtain most favourable ionic configurations for DFT calculations. Second, optimized parameters that maximize the average correlation to DFT energies considering just geometry related parameters. Third, optimized parameters considering also smeared instead of point-charges in the electrostatic calculations. For all parameter sets the average correlation to DFT energies is given excluding or including compositions with a sodium concentration of 1/3. The last column gives the prediction accuracy when the parameters are employed to predict P2/O3 phase stabilities in a database of 272 experimental compositions.

Name	$d_{O\text{-}TM\text{-}O}$ (Å)	$d_{O\text{-}Na\text{-}O}$ (Å)	a (Å)	Smearing	Cor. DFT (Na ≥ 2/3)	Cor. DFT	Acc. Exp. (%)
Default	2.1	3.4	5.0	0.0	0.776	0.508	68.8
Optimized	2.4	3.5	4.75	0.0	0.852	0.552	79.4
Smearing	2.3	3.4	4.60	0.5	0.883	0.601	79.4

In order to overcome the weaker correlation at low sodium concentrations and to further improve the correlation in general, another parameter was introduced to the Coulomb energy calculation: the scaling factor (σ) to smear the point charges to Gaussian charges. In this approach all point-charges are smeared proportionally to their effective ionic radius while the radius is scaled by the aforementioned scaling factor σ. The total energy in the smeared case is derived by the formulas of Gingrich *et al.* [19]:

$$E_{\text{Smeared}} = E_{\text{Point}} - \frac{1}{2}\sum q_i q_j \frac{\operatorname{erfc}\left(\frac{\eta_i \eta_j}{\sqrt{\eta_i^2+\eta_j^2}} d_{ij}\right)}{d_{ij}}. \tag{3.1}$$

Here, the sum iterates over all pairs of ions i and j for all real-space vectors within the real-space cutoff of the Ewald summation. The Euclidean distances of the ions is given by d_{ij} and their point-charge valencies by q_i and q_j, respectively. Finally, η denotes the smearing width that is derived from:

$$\eta = \frac{1}{\sqrt{2} R_{\text{ionic}} \sigma}, \tag{3.2}$$

with R_{ionic} being the ionic radius of the respective ion and σ the scaling factor for the smearing. It must be mentioned that a total energy calculation with smeared charges would also include a correction to the self-energy which is omitted here to ensure that the energy calculation is numerically stable even when converged towards the point-charge limit. In practice, omitting the self-energy contribution of the smeared charges does not influence the result as relative energies are compared in this work (e.g., energy differences between different stacking sequences or configurations). Finally, the scaling factor σ can be chosen as another free parameter in the electrostatic calculations that can be optimized. However, a constant σ should be used for all ions and compositions to keep the approach as general as possible.

The sensitivity of the correlation to DFT energies when just varying σ can be seen in Figure 3.11 (including Na=1/3) and Figure 3.12 (excluding Na=1/3). Remarkably, the variation of σ shows the highest sensitivity among all parameters. Moreover, σ is apparently the only parameter that can significantly improve the correlation to DFT for some

compositions, e.g. compositions containing Li, Mg, or Ti, even at lower Na concentrations (Na=1/3) when a high value is chosen. To find a global optimum set of parameters a grid-based search was applied again but now in four dimensions ($d_{\text{O-Na-O}}$, $d_{\text{O-TM-O}}$, a, σ). To be consistent with the previous fitting approach that excluded smearing, the average correlation for Na concentrations larger than 1/3 was maximized. Parameter values and corresponding average correlations of the best 30 sets of parameters are shown in Table 3.2. It can be seen, that the maximal average correlation is not very sensitive to different sets of optimal parameters and only changes slightly (less than 0.001) within the top 30 sets of parameters. While some clusters of similar parameter sets can be observed, it seems that due to the higher dimensionality of the parameter space (more degrees of freedom) also quite different sets of parameters can yield high correlations. As changes in the average correlation are insignificant and to avoid choosing an over-fitted set of parameters, the 8$^{\text{th}}$ best parameter set was chosen as the corresponding geometry parameters are in or close to the range of what is typically reported in experimental or computational studies and as the σ-value of the parameter set is 0.5 which is a value commonly observed in the top 20 parameter sets. The chosen optimized set of parameters that is referred to in the following as "Smearing" is given in Table 3.1 along with the obtained correlations to DFT energies. While the average correlation (0.883) slightly improves for sodium concentrations larger than 1/3 compared to the optimized parameters excluding smearing (0.852), the correlation (0.601 to 0.552) improves more significantly when including the low sodium concentration. However, the obtained average correlation of 0.601 still indicates that the issues at low sodium concentrations are also only partially resolved when smearing is included.

To summarize, following the framework sketched in Figure 3.1 a database consisting of 231 fully geometry optimized DFT energies for various compositions and stacking sequences (visualized in Figure 3.2) was created. This database is then used to optimize the parameters of electrostatic calculations. The relevant fitted parameters were $d_{\text{O-Na-O}}$, $d_{\text{O-TM-O}}$, a, and σ when smeared charges were applied. Screening of all parameters was performed on a fine grid (0.1 Å) and optimality was defined such that the correlation over different stacking sequences to the DFT energy differences is maximized while compositions with low sodium concentration are excluded from the average (Na=1/3 is excluded). Following this framework two sets of optimal parameters for electrostatic calculations to predict stacking phase stabilities are obtained, one considering just geometry related parameters ($d_{\text{O-Na-O}}$, $d_{\text{O-TM-O}}$, a) alongside with point charges and another one including charges smeared proportionally to their ionic radius and scaled by another parameter σ. Both parameter sets deliver very high correlation to DFT energies for high sodium concentrations (Na larger than 1/3) while the approach including smearing also shows satisfactory correlation including the low sodium concentrations (Na=1/3).

Due to the low computational costs of stochastic electrostatic optimizations of ionic configurations these parameter sets can be employed to perform high-throughput predictions of phase stabilities in a vast composition range. In the following, the framework is used to predict P2/O3 phase stabilities in a large experimental database with 272 compositions. Afterwards, it is shown how vast compositional spaces can be efficiently screened to identify trends in the most stable stacking sequence from *ab initio* calculations.

3.3 Results

To employ the proposed framework and selected parameter sets for prediction of stacking sequences in sodium layered oxide materials, first the approach is benchmarked against a set of experimental layered oxide cathodes. In the following, the approach is used to perform high-throughput predictions of the most stable stacking sequence in a vast compositional space.

3.3.1 Prediction of Experimental Data

The most commonly observed stacking sequences of layered oxide sodium cathodes in experimental studies are P2 and O3 which also agrees well with the *ab initio* database of DFT references (cf. Figure 3.2). To obtain a comprehensive database of experimental compositions the compilation of 104 compositions from Zhao *et al.* [6] was used and extended the dataset by another 168 compositions that are either P2 or O3 from the ICSD database [20]. To ensure that the additional compositions selected from the ICSD database are really P2 and O3 stackings, *c*-lattice parameters were checked and sodium coordinations were approximated from the structural information. The resulting database with experimental P2 and O3 compositions consists of 272 compositions with various transition-metal combinations and sodium concentrations. A full list with all compositions including their original experimental references is given in Table 3.3.

In a next step, $4\sqrt{3}\times4\sqrt{3}\times1$-supercells were created for each of the 272 compositions and in both considered stacking sequences (P2 and O3) as well as for all three sets of electrostatic parameters shown in Table 3.1. The rather large supercell dimensions allowed to match the experimental compositions within roughly 1 % while partial occupancies were considered for the transition metal as well as the sodium sites. While the large supercells ensure that the experimentally reported composition is matched as precisely as possible, it requires sampling a gigantic configurational space (up to 10^{135} configurations for a single composition) which needs fast heuristic optimizers to identify the lowest (or at least a low) energy configuration. To obtain a discrete ionic configuration and to evaluate the electrostatic energies of the structures, global optimization of the configuration in terms of Coulomb energy was attempted *via* the replica exchange Monte Carlo method as implemented in the GOAC package [16]. The resulting electrostatic energy per formula unit of the most favourable configuration was finally employed to identify the most stable phase out of P2 and O3. The calculated energy differences between P2 and O3 for all 272 experimental compositions are compiled in Figure 3.4 for the "Smearing" electrostatic parameter set (cf. Table 3.1).

Figure 3.4 reveals that the most stable phase (P2 or O3) is predicted correctly for the vast majority of experimental compositions, namely 216 out of 272 which yields an prediction accuracy of almost 80 % (cf. Tab. 3.1). Regarding the sensitivity of the prediction accuracy towards the different electrostatic parameter sets, the values in Table 3.1 indicate that both parameter sets that were optimized to DFT data have essentially the same accuracy while the non-optimized default parameters show a significantly lower accuracy of 69 %. Despite the slightly improved correlation to DFT energies, discussed in the previous section, when smearing is included in the electrostatic calculations, the experimental prediction quality apparently did not profited from the additional parameter. However, considering that the prediction approach is purely *ab initio*, an accuracy

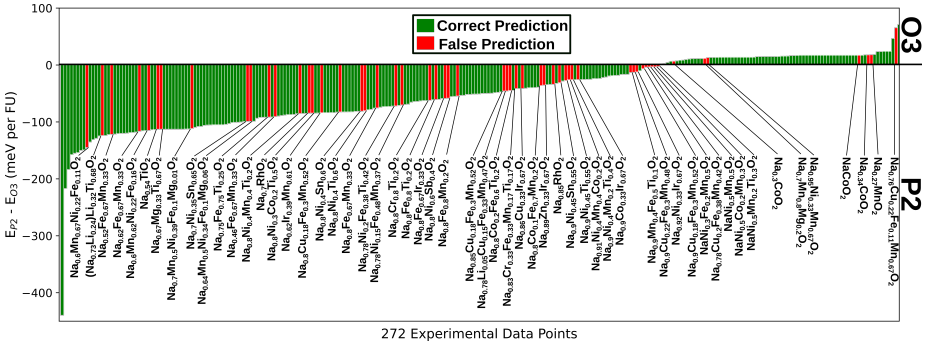

Figure 3.4: Energy differences in meV and per formula unit (FU) of the most favourable ionic configurations between P2 and O3 phases employing the "Smearing" electrostatic parameter set (Tab. 3.1) for all 272 collected experimental compositions. A positive energy difference indicates that the electrostatic approach predicts the O3 stacking sequence to be more stable and a negative energy that the P2 phase is more stable. Colors of the bars indicate whether the prediction is in agreement (green) with the experimentally reported phase or not (red). Compositions for the incorrect predictions are given in the plot.

of 80 % to experimental data is very promising, especially when the overall small energy differences (cf. Fig. 3.2) between layered phases are taken into account.

Regarding the falsely predicted compositions shown in Figure 3.4 it should be first mentioned that some clustering of false predictions happens around energy differences close to zero which highlights that the approach can be also interpreted quantitatively to some extend. Moreover, the dataset also includes more exotic (complex electronic structure, possibly very different behaviour) and practically less frequent discussed materials such as, e.g., $Na_{0.85}RhO_2$ that is predicted in the wrong phase. Also, for some materials multiple data points that belong to the same experimental reference are predicted in the wrong phase which might be explained by special synthesis procedures that were employed in the corresponding studies. Finally, also three compositions that were reported in both phases were included in the dataset such that the accuracy cannot reach 100 %. Considering all these points the reported accuracy of ca. 80 % is a conservative estimate and the actual prediction accuracy of the discussed *ab initio* framework might be even higher. However, it is quite remarkable that almost 50 % of the wrongly predicted materials contain some fraction of iron. This might indicate that the behavior of iron is more difficult to predict, maybe because of strong cooperative local distortions of active transition metals, e.g., manganese or nickle, that effects the phase stability. Finally, it must be mentioned that in contrast to the DFT correlations that became weak at a low sodium concentrations no significant decrease in the prediction accuracy of the experimental data was observed. More precisely, for compositions with a sodium concentration of 0.5 or less a prediction accuracy of 79 % is maintained in the data set. However, the dataset also includes just 19 compositions with such low sodium concentrations but the results still give a hint that the electrostatic prediction approach might not be as unreliable as suggested from the DFT correlations at low sodium concentrations. A possible reason might be that also the DFT energies become unreliable/less comparable to electrostatics at low sodium concentrations as high oxidation states are enforced to charge bal-

ance the structure. These strong oxidations might be especially over-delocalized in the shown DFT database as the PBE exchange-correlation functional was applied [21]. Consequently, different "ion charges" are obtained in DFT and resulting energies are more different to Coulomb energies with very localized charges. From that perspective it is even questionable which approach might be the most predictive at low sodium concentrations.

To summarize, comparison to experimental data proved that the pure *ab initio* electrostatic prediction approach with parameters optimized to DFT data is capable to correctly reproduce experimentally observed stacking sequences of P2 or O3 with an accuracy of approx. 80 %. Thus, it is evident that the electrostatic calculations have some predictive power for potential experimental studies and are well-suited to be employed in high-throughput predictions of phase stabilities which is shown in the next section.

3.3.2 High-Throughput Predictions

The developed electrostatic prediction approach was used to perform high-throughput screening of huge compositional spaces of Ni-Mn binary mixtures with different substituents with electrostatically distinguishable charges. Formula units of $Na_x[A_yNi_zMn_{1-y-z}]O_2$ with x in [0/6, 1/6, 2/6, 3/6, 4/6, 5/6, 6/6], A in [Vac^0, Li^{1+}, Mg^{2+}, Al^{3+}, and Ti^{4+}], y in [0/12, 1/12, 2/12, 3/12, 4/12, 5/12, 6/12], and z in [0/12, 1/12, 2/12, 3/12, 4/12, 5/12, 6/12, 7/12, 8/12, 9/12, 10/12, 11/12, 12/12] were considered in the study for all 7 stacking sequences (O1, O2, O3, P2, P3, OP2, OP4). In total, ca. 15,000 different materials were included in the high-throughput screening. For all structures electrostatic energies were evaluated after configurational optimization by replica exchange Monte Carlo (REMC). All structures were calculated with all three parameter sets shown in Table 3.1 but in the following only results for the "Smearing" parameter set, which generally is expected to deliver the most accurate predictions also at lower sodium concentrations, are discussed.

Qualitative Predictions of Phase-Stability

Employing configurational optimization and comparing energy differences of the lowest-energy configuration between all stacking sequences, the lowest energy stacking sequence for each composition can be determined. Predicted most stable phases for different sodium concentrations down to 2/3 are shown in Figure 3.5 (a). Results for sodium concentrations down to zero are shown in Figure 3.14 ("Default" parameter set), Figure 3.15 ("Optimized" parameter set), and Figure 3.16 ("Smearing" parameter set).

Figure 3.5 (a) shows a general tendency for O3 phases at very high sodium concentrations, e.g., Na=1.00 while the P2 phase becomes by far the most dominant phase for lower sodium concentrations. These trends are in close agreement to experiment. [2] Interestingly, the predicted overall trend regarding either O3 or P2 being the most stable phase is also consistent throughout all of the different investigated compounds. Besides the dominance of O3 and P2 some compositions with OP2 and especially OP4 are observed at higher sodium concentrations of Na=1.00 and Na=0.83. At lower concentrations even some presence of P3 is observed for all substituents. Even O1 is predicted to be most stable for some compositions with a vacancy at a sodium concentration of Na=0.67. Most importantly, these occurrences of outlier phases of the dominant phase occur for a range

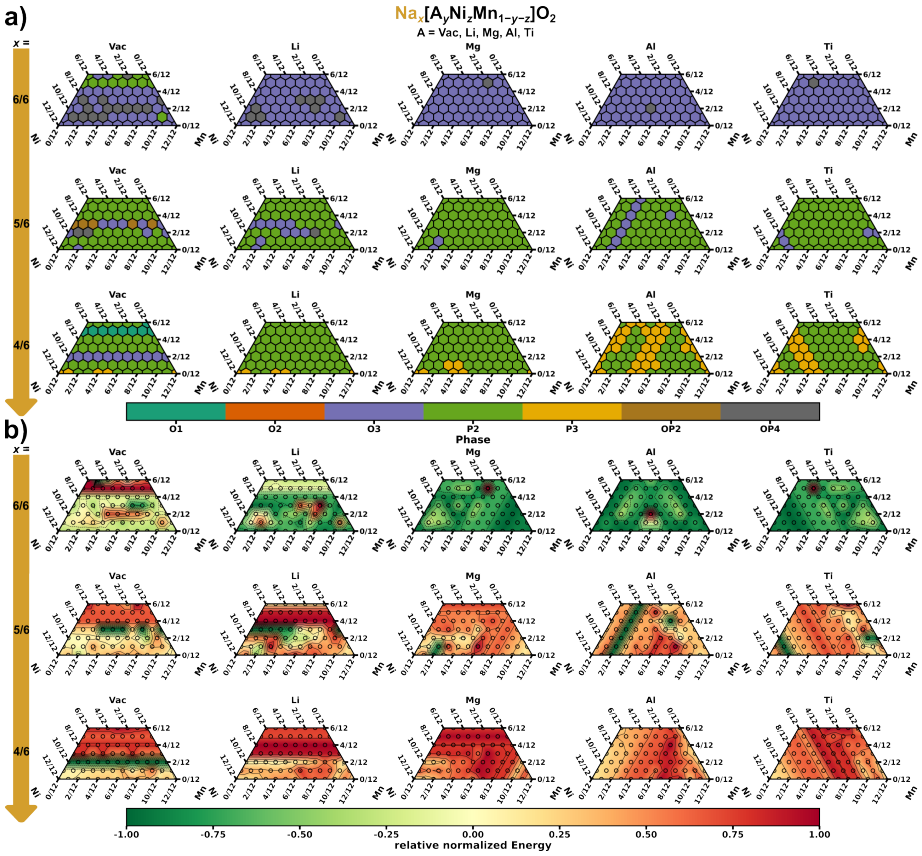

Figure 3.5: High-Throughput predictions using the "Smearing" parameter set (cf. Table 3.1) for various compositions including different substituents (left to right) and Na concentrations (top to bottom). a) For each composition the lowest energy stacking sequence is highlighted in the color coding shown below. A general trend from mainly O3 at Na=1.00 towards P2 being the most dominant phase at lower sodium concentrations can be observed. b) Contour plots of O3 stability versus all other stacking sequences. Energies where normalized such that values below zero indicate O3 being the most stable and values above zero indicate another phase is more stable. The magnitude of the value (-1 to 1) highlights relatively how favourable of unfavourable the O3 phase is compared to the lowest other phases according to the calculated electrostatic energies. For all plots concentrations are shown in steps of 1/12 as $2\sqrt{3}\times2\sqrt{3}\times1$-supercells with 12 transition-metal positions per layer were considered in the predictions.

of substituent concentrations and often in patterns that are parallel to one of the triangle corners. This proves that these are not just outliers due to, e.g., incomplete configurational optimization *via* REMC. However, these outlier patterns can potentially be artifacts of the limited supercell sizes in either the *a*- or *c*-direction which is especially likely for the aforementioned O1 stability of the compositions with 2/12 vacancies. Still, most of these patterns should actually give important physical insights on the phase stability of different compositions and can provide a basis for materials that are interesting to be considered in experimental studies. Phase stabilities in the screened phase space

in Figure 3.5 (a) are mostly parallel to the species with the lowest charge, e.g., Vac, Li, Mg and then Ni^{2+} for Al and Ti. This indicates that having compounds with low valence elements or to design materials such that highly reduced species are present is the most promising approach to engineer phase stability in layered oxide sodium ion cathodes. As valence change during cycling, doping by elements with fixed charges seems to design phase stability. However, the phase stability predictions by the electrostatic approach of this work also indicate that it is extremely challenging to remain a single phase to be thermodynamically the most stable at a broad range of sodium concentrations. Finally, it must be mentioned that the electrostatic model shown in this work predicts phase stabilities and not phase transitions, for phase transitions as they occur during cycling also kinetic effects play a role. Ultimately, the electrostatic phase stability prediction approach suggests that it is impossible to stabilize a single stacking phase over a broad range of sodium concentrations. Therefore, the high throughput predictions imply that kinetic stabilization of phases or cycling in a limited sodium range could be more promising approaches to design sodium ion layered oxide cathodes with a specific phase.

Quantitative Predictions of Phase-Stability

As the electrostatic prediction approach involves the calculation of actual energy differences between the various stacking sequences, also a more quantitative analysis than the qualitative prediction of the most stable phase in Figure 3.5 (a) can be performed. Figure 3.5 (b) depicts the normalized energy differences of the O3 phase towards all other stackings which allows to draw contour plots in the ternary composition phase-diagrams. Figures for all considered parameter sets (cf. Table 3.1) are given in Figure 3.17, Figure 3.18, and Figure 3.19 for sodium concentrations down to zero.

The contour plots of the O3 stability in Figure 3.5 (b) allow for a more quantitative analysis of the phase stability and to see trends regarding phase stability as function of composition more clearly. Firstly, the contour plots of the relative normalized energy also show pronounced trends in the phase stability and almost no outliers/peaking of energy indicating the predictive power of the applied electrostatic optimization approach and also that the REMC configurational optimizations were sufficiently converged. Again, the energy contours appear to be mostly parallel to one of the elements of the phase diagram, mostly the element with the lowest ionic charge. Figure 3.5 (b) shows that an O3 phase is for non of the studied compositions the (thermodynamically) most stable phase over a broader sodium concentration range. However, energy differences between the phases are smaller in the lower parts of the phase diagram (low substituent concentration), for substituents with lower charges, e.g., Vac, Li. The results therefore suggest that a vacancy concentration of 8 % to 25 % could potentially best stabilize an O3 phase over a broader sodium concentration. However, to obtain O3 in as-synthesized materials with high Na concentration, e.g., Na=1.00 or 0.83, it appears more favourable to dope with highly charged elements such as Al or Ti as the corresponding contour plots show some dark green areas for particular composition ranges. Interestingly, doping with Mg for sodium concentrations less than one seems to be least beneficial for stabilizing an O3 phase. Another interesting feature to mention is that the contour plots for Na=1.00 are symmetric for Mg an Ti but mirrored along the vertical axis and that the plot for Al is symmetric to that axis as well (cf. Figure 3.5 (b)). This behavior can be explained

by the used charges as all of these phase diagrams have one species with a charge of 2+, 3+, and 4+, respectively. Again, this proves that the performed configurational optimizations are sufficiently converged, however, it also shows that the predicted phase stabilities and corresponding energies are mainly determined by the electrostatic interactions and not strongly influenced by the applied smearing of the charges. In agreement, also the contour plots with the optimized parameters without smearing (cf. Figure 3.18) show qualitatively similar trends. This is also in agreement to the parameter optimizations shown in Table 3.1 that also indicate a small increase in correlation for high sodium concentrations when smearing is applied. Thus, smearing is probably most beneficial at lower sodium concentrations.

Even though the proposed electrostatic prediction approach does not consider any kinetic effects of phase transitions, it is still worth to explore how it performs for lower sodium concentrations. Figure 3.6 depicts the energies of the P2 stability over the phases to which P2 is often transitioning to, e.g. O2 and OP4, at the example of $Na_x[Li_yNi_zMn_{1-y-z}]O_2$. [22–24] The results suggest that P2 is generally not stable at very high (Na=1.00) and very low (Na=0.00) sodium concentrations. However, at intermediate concentrations a broader P2 stability is observed. This is in excellent agreement to experimental studies that suggest a P2 stability between Na=0.7 and Na=0.3. [2]

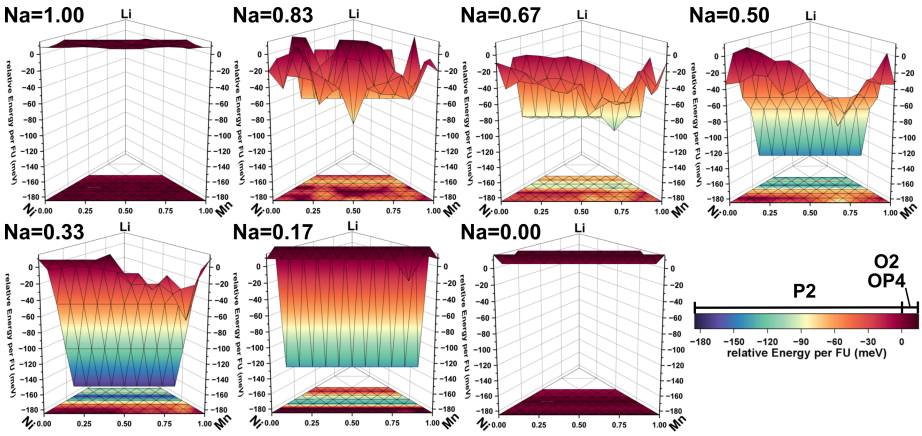

Figure 3.6: Energies of the P2 phase versus the O2 and OP4 phase for compositions in $Na_x[Li_yNi_zMn_{1-y-z}]O_2$. It can be observed that the P2 phase is the most stable for intermediate sodium concentrations while being unstable at the extreme points of 1 and 0 sodium.

When using lithium as substituent at transition metal sites it can stabilize the P2 phase over a broader sodium range and the plots in Figure 3.6 show that a lithium concentration of at least ca. 20-25 % is required. Compositions with such lithium substitutions are calculated by the electrostatic prediction approach to be most stable in P2 for sodium concentrations between ca. Na=0.67 and Na=0.17. Thus, stabilization of the P2 phase over broader sodium concentration ranges appears to be a promising design methodology for layered oxide cathodes. Indeed, the predictions regarding P2 stability and phase transition match very well with existing experimentally reported results. Yang *et al.* [25] showed that P2-$Na_{0.67}[Li_{0.2}Ni_{0.2}Mn_{0.6}]O_2$ shows no phase transition while

both, $Na_{0.67}[Ni_{0.4}Mn_{0.6}]O_2$ and $Na_{0.67}[Ni_{0.2}Mn_{0.8}]O_2$ exhibit a phase transition during cycling. Another experimental example for P2 stabilization during cycling by lithium substitution was found by Yabuuchi *et al.* [26] for P2-$Na_{0.83}[Li_{0.25}Mn_{0.75}]O_2$. Despite the slightly higher sodium concentration, the stabilization mechanism appears to be well captured by the electrostatic prediction approach proposed in this work.

Overall, the obtained trends regarding phase stability and composition obtained from the high-throughput screenings seem to be quite useful to select promising cathode materials in which phase stability matters. It should be mentioned that due to the quantitative nature of the proposed electrostatic phase stability prediction approach contour plots could be obtained for other phases besides O3 and P2 to determine promising compositions (or ranges) where that particular phase of interest is thermodynamically more stable. Although the electrostatic prediction approach does not capture any kinetics, apparently it can not only match phases of as-synthesized materials but is also able to capture phase transitions during cycling well. The results of the high-throughput screenings are available online (cf. Supplementary Data Statement).

3.4 Discussion

The presented results prove that the proposed electrostatic prediction approach for phase stabilities of layered oxide sodium cathodes is capable of predictions in satisfactory agreement to both, theory (DFT) and experiment while being fully *ab initio*. It should be mentioned that the high-throughput study was enabled by using fast heuristic optimizers (REMC as implemented in GOAC) to determine lowest energy configurations in the vast configurational space for each composition and phase. That the phase stability should be governed by electrostatics is also assumed in the well-known cationic potential approach [6] that aims to emulate effective electrostatic interactions by a simplified formula that solely depends on the composition of interest. However, to the best of our knowledge, no study considered the electrostatic interactions explicitly and on a structural level for a large composition range, most likely due to the emerging configurational explosion when more complex compositions are considered that is not straight forward to handle. The cationic potential relies implicitly on electrostatics for phase predictions, but the approach in this work considers electrostatics explicitly. Both approaches rely on the ionic charges of the different ions and also aim to include the polarizibility or delocalization of the ionic charges by including the ionic radii. In both approaches, the electrostatic interaction of an ion is weaker the larger its ionic radii is. Finally, both approaches require some fitting to reference materials to achieve some predictive power. However, the two approaches for phase stability predictions also have some differences which come with their advantages and disadvantages. While both approaches are fitted to reference materials, the approach proposed in this work relies on DFT data which renders the whole approach fully *ab initio* while the cationic potential uses experimental data. On the one hand, fitting to *ab initio* data eliminates the risk to introduce a bias to certain, potentially wrong or inaccurate, experimental data points while fitting to experiment bears the potential for more accurate predictions that also implicitly account for experimental effects that are not covered in *ab initio* data, e.g., temperatures, cation migrations, other kinetics related effects. More precisely, when the cationic potential is applied to the experimental data set in Figure 3.4, a prediction accu-

racy of ca. 90 % is achieved, which is about 10 % higher than the electrostatic prediction approach proposed in this work. The higher accuracy must be interpreted with care as the cationic potential was also fitted to a substantial amount of the considered data points but it can still be concluded that the cationic potential achieves a higher accuracy than considering electrostatics explicitly. However, the cationic potential separation line is less interpretable than the parameters ($d_{\text{O-Na-O}}$, $d_{\text{O-TM-O}}$, a, σ) and resulting electrostatic energies employed in this work . Moreover, the cationic potential is of qualitative nature (either O3 or P2) and strictly speaking does not allow for any quantitative statements while direct calculations of electrostatic energies allow for quantitative comparisons (energy differences) of different phase, also beyond O3 and P2 (such as O1, O2, P3, OP2, OP4). The bare electrostatic results can also be interpreted further by looking at specific pair-wise interactions or at the superstructures that are possibly found during configuration optimization. Finally, it should be mentioned that the cationic potential is probably still the best trade-off of predictive power and simplicity, e.g., can be calculated by hand, compared to the explicit calculation of electrostatic energies as in this work. However, another advantage of the interpretable, physics-based models is that out-of-sample predictions, e.g., predictions of points that are not in-between the points considered for fitting, are more likely to be successful. Therefore the approach is potentially more transferable to different sodium concentrations. This can be seen in Figure 3.7 where all compositions shown in Figure 3.5, but down to a sodium concentration of zero, are evaluated by the cationic potential line versus their most stable phase (out of O3 and P2) calculated by electrostatics. While Figure 3.7 shows the results for the "Smearing" parameter set (cf. Table 3.1), similar plots are given for all three parameter sets in Figure 3.20.

While the cationic potential matches the predictions of the electrostatic model proposed in this work rather well for high sodium concentrations (Φ_{Na} larger than 6, Na greater 0.6), the cationic potential fails to capture the trend towards O3 at very low sodium concentrations (Na smaller than or equal to 1/3). While predictions of phase stabilities are usually most relevant at high sodium concentrations to predict as-synthesized phases, also thermodynamically most stable phases during cycling of the cathode materials are of interest. Even though the fitting to DFT data of the electrostatic prediction approach proposed in this work showed some difficulties at low sodium concentrations, the experimental data was still fairly reproducible for low concentrations. The overall trend towards more O-layers (e.g., OP4 or O1) seen in Figure 3.7 is also frequently reported in experiments indicating that the electrostatic prediction approach probably still has some predictive power when investigating low sodium concentrations. However, when a linear line is fitted to the electrostatic prediction in Figure 3.7 in the same way as the cationic potential and for the whole sodium concentration range, the predictive power of the linear fit at high sodium concentrations is strongly reduced compared to the original cationic potential. This highlights that most likely a more complex function is required to obtain a predictive model for the phase stability over a broad sodium range within the cationic potential framework.

However, both approaches (cationic potential, direct electrostatics) are very useful to study and predict phase transitions: The cationic potential for its very good trade off of accuracy and simplicity for high sodium concentrations (as-synthesized), and use of

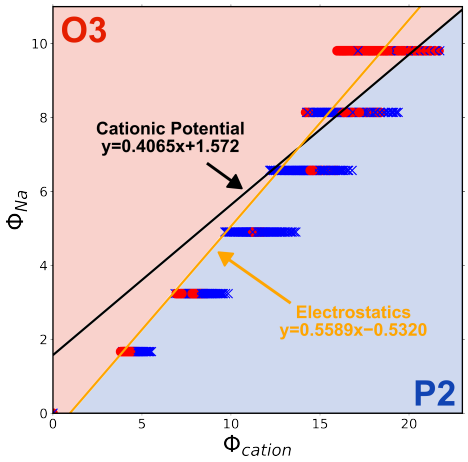

Figure 3.7: Phases (O3 or P2) as predicted by the electrostatic prediction approach using the "Smearing" parameter set (cf. Table 3.1) for all compositions shown in Figure 3.5 down to a sodium concentration of zero in the two dimensional cationic potential space as introduced by Zhao *et al.* [6]. Blue crosses indicate P2 and red circles indicate O3. The linear separation line proposed by the cationic potential approach is shown as black line while the one obtained from re-fitting to the electrostatic predictions is shown in orange. The cationic potential matches the electrostatic data points for high Φ_{Na} (high Na content) even better than the fit over the whole sodium range, however, the predictions differ a lot for low sodium concentrations (low Φ_{Na}). This indicates that the whole sodium concentration range is not sufficiently described by a linear separation line in the two dimensional cationic potential space.

explicit calculation of electrostatics as the approach can be considered fully *ab initio* and is also quantitative and physically interpretable. Moreover, the use of direct electrostatic calculations for the prediciton of layered phases as proposed in this work also offers the possibility to include even more phases beyond P2 and O3 as shown above which is unique compared to the other approaches as sufficient amounts of experimental samples are missing for these phases. Finally, it should be mentioned that the accuracy of the electrostatic approach might be further increased by using larger supercells, e.g., same amount of layers in *c*-direction for all phases and/or more repetitions of the unit cell along the *a*-direction, which increases the computational costs for the configurational search rendering high-throughput screenings as performed in this work infeasible. Such larger supercells might improve the prediction quality further as higher-symmetry (and lower energy) superstructures can form. However, with the use of heuristic solvers such as implemented in GOAC, which is openly provided by our group, these studies would be feasible for certain systems of interest. Therefore, including larger supercells is expected to further boost the predictive power of explicit electrostatic calculations for the phase stabilities of layered oxide sodium-ion cathodes and details will be discussed in further studies.

To summarize, an *ab initio* prediction model for the stability of layered oxide phases of sodium cathodes based solely on electrostatic interactions was proposed. While the energy evaluation by electrostatics is not very demanding, the configurational search for lowest energy structures in materials with complex compositions is very challeng-

ing due to a combinatorial explosion of possible configurations. However, by using advanced heuristics such as Replica Exchange Monte Carlo as implemented in the GOAC optimizer for the configurational search, compositions of high complexity can be evaluated using electrostatic model that treats atomistic interactions explicitly. It was shown that the resulting model can be fitted to DFT data by maximizing the correlation over different stacking phases while varying the intra-layer distances and inter-layer distances along the *c*-direction as well as the *a*-lattice parameter and applying Gaussian smearing of the point charges. Results prove that electrostatic calculations with such optimized parameters are able to reproduce DFT energy differences between various layered oxide stackings (O1, O2, O3, P2, P3, OP2, OP4) with Pearson correlations well above 80 %, indicating the high predictive power of bare electrostatics. It was continued by verifying the pure *ab initio* phase stability prediction model by achieving an accuracy of ca. 80 % on an experimental data set of 272 compositions in either P2 or O3 phase. The high accuracies prove that electrostatics are the driving force when it comes to phase stabilities in layered oxides. Finally, it is highlighted that due to the low computational costs the proposed electrostatic prediction together with the use of heuristic optimizers for the configurational search is capable to be applied in high-throughput studies by performing calculations on 15000 compositions. While techniques fitted to experimental data sets still achieve a slightly higher prediction accuracy on experimental data sets, it is expected that the *ab initio* electrostatics approach has some advantages when considering out-of-sample predictions, e.g. different stacking phases and more importantly lower sodium concentrations. Regarding the lower sodium concentrations it is also worth mentioning that reasonable agreement to experimental studies regarding phase stability and transitions during cycling were found. Thus, the electrostatic prediction approach might not only be able to predict most stable as-synthesized phases but also to predict phase transitions during cycling despite no kinetic effects are considered.

Combining all these aspects together, the *ab initio* electrostatic prediction approach for the phase stability of layered oxide sodium-ion cathodes proposed in this work along with the shown optimized parameter sets offers a highly valuable tool to study phase stabilities in more detail while keeping the computational costs to a minimum. Thus, the approach will enable both, prediction of interesting compositions for future experimental studies as well as the possibility to screen large composition spaces for further theoretical insights.

3.5 Methods

3.5.1 GOAC

To obtain the ionic configurations for the DFT calculations and to compare the stabilities of various phases, configurational optimization of Coulomb energies was performed assuming fixed charges of Na^{+}, Vac^{0}, Li^{+}, Mg^{2+}, Al^{3+}, Ti^{4+}, O^{2-} and a variable oxidation state of Mn and Ni between 2+ and 4+ while always the Mn was first fully oxidized to 4+ before the Ni was oxidized accordingly to their electronegativities. For compositions beyond these elements the typical oxidation states reported by Zhao *et al.* [6] were assumed and again full oxidation of the species with the lowest electronegativity was assumed followed by oxidation of the species with the next lowest electronegativity and so

on. It was always ensured that the overall composition is charge balanced, if this was not possible from the transition metals alone, oxygen oxidation from O^{2-} to O^{2-+n} was applied. In all cases delocalized charges over all species of the same type were applied (same average charge for all species of a type). Moreover, the configurational search was constrained to ensure that the total composition is matched for each layer of the considered stacking. This ensures the same degrees of freedom for stackings with different amounts of layers along the *c*-direction. For the DFT references and the high-throughput screening of various compositions $2\sqrt{3}\times2\sqrt{3}\times1$-supercells were employed while for the structures in the experimental data set $4\sqrt{3}\times4\sqrt{3}\times1$-supercells were considered. For the actual configurational optimization the Replica Exchange Monte Carlo (REMC) heuristic as implemented in the GOAC code [16] was used with parallel tempering at temperatures of 0.1, 0.2, 0.3, 0.4, 0.6, 0.8, 1.0, and 1.2 eV, respectively. For the larger cells in the experimental data set Monte Carlo steps per exchange and total run times per composition were set by the number of total configurations: 1000000 and 90 seconds for less than 10^{30}, 750000 and 180 seconds for up to 10^{50}, 500000 and 300 seconds for up to 10^{75} and for even more configurations 300000 and 480 seconds. For the high throughput screening of the composition spaces always 200000 Monte Carlo steps were used along with run times of 30 (O1), 60 (O2), 75 (O3, P2), 90 (P3), and 120 (OP4) seconds, respectively. The run times correspond to machines with 128 physical CPU cores. As discussed in the Results section, optimizations appeared to be sufficiently converged with these settings and no evidence was found that the results suffer from unconverged configurational optimizations. Energies for the optimization were evaluated by electrostatics within the Ewald summation technique and the parameters (distances and/or Gaussian smearing of charges) described in Framework section. All energies or energy differences always refer to the lowest energy configuration found during optimization for each composition and stacking sequence.

3.5.2 DFT

The lowest energy configuration of each composition obtained from REMC runs (described above) was considered for the DFT calculations. DFT calculations were performed with the Vienna *ab initio* simulation package (VASP) [27] that relies on the projector-augmented wave (PAW) [28] approach. The Perdew-Burke-Ernzerhof (PBE) exchange-correlation functional was employed [29]. Spin-polarization along with an energy cutoff of 520 eV and an electronic and force convergence criterion of 10^{-4} eV and 10^{-2} eV/Å, respectively, were applied. No symmetries were considered and a Γ-centered *k*-point grid of $2\times2\times n$ with n equals 4 for O1, 2 for O2, P2, OP2, O3, and P3, and 1 for OP4 was applied. Standard VASP PAW potentials considering just the valence electrons explicitly were used.

Supplementary Data

Supplementary data to this article can be found in the next section. The data calculated in this work is accessible in an interactive way by a graphical user interface (GUI) at: https://huggingface.co/spaces/KK-JZF/Electrostatic-Phase-Stability

Supporting Information

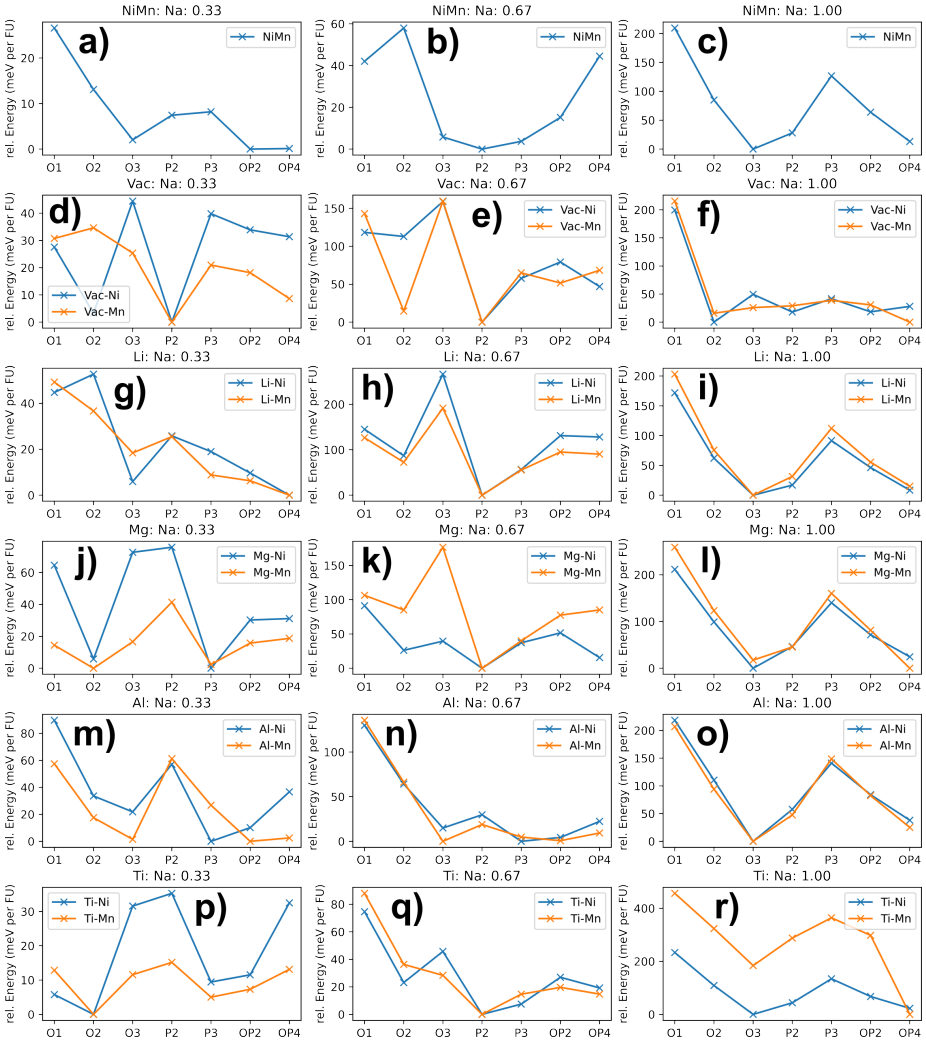

Supplementary Figure 3.8: Normalized DFT energies for various phases (O1, O2, O3, P2, P3, OP2, OP4), sodium concentrations (left to right: 0.33, 0.67, 1.00) and substituents (a, b, c: 1:1 Ni:Mn; d, e, f: 25 % Vac; g, h, i: 25 % Li; j, k, l: 25 % Mg; m, n, o: 25 % Al; p, q, r: 25 % Ti). The blue curves depict materials with Ni and the oranges ones with Mn. Generally, same trends between Ni and Mn compounds can be observed.

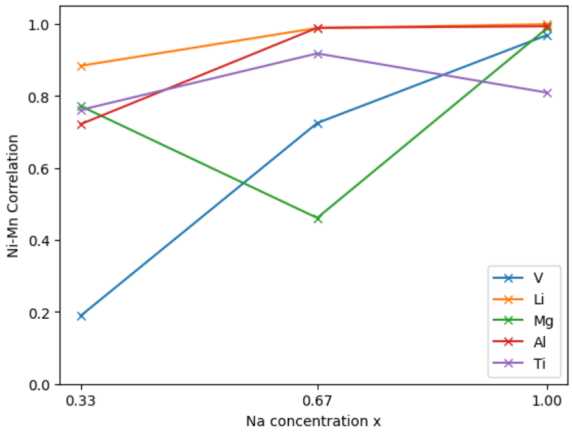

Supplementary Figure 3.9: Correlation of phase stabilities as obtained from DFT between the same compositions containing either Mn or Ni. Curves for various substituents are shown. Generally, the phase stability between Ni and Mn compounds is highly correlated.

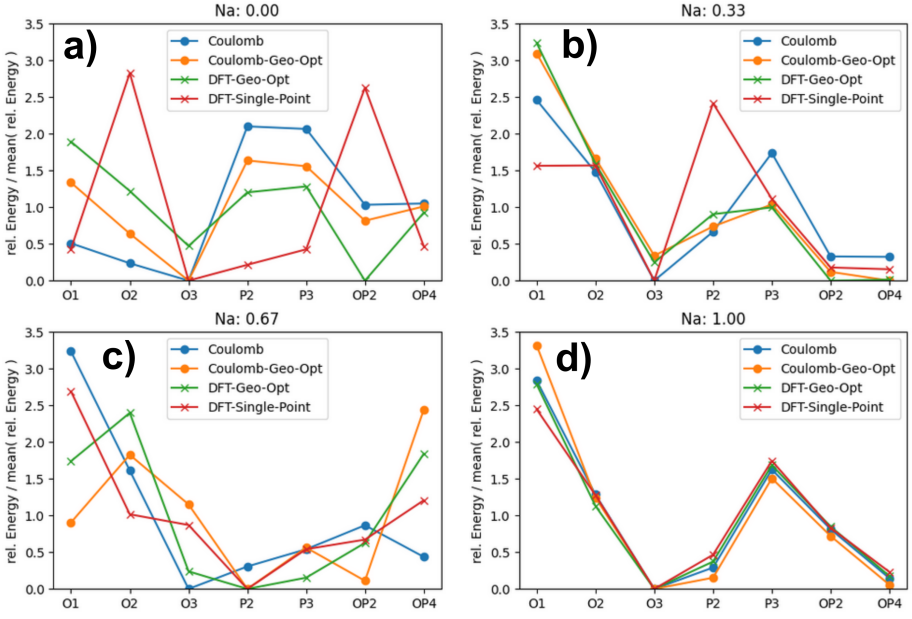

Supplementary Figure 3.10: Relative and normalized DFT and Coulomb energies of $Na_xNi_{0.5}Mn_{0.5}O_2$ at x=0.00 (a), 0.33 (b), 0.67 (c), 1.00 (d) for different stacking sequences. The energies are given for both, a perfect and undistorted structure and for the DFT geometry optimized structures. In general, a strong correlation between the two different energy calculation approaches is observed.

Supplementary Table 3.3: Database of of experimentally reported cathode materials in either the P2 or O3 phase used to evaluate the performance of the electrostatic prediction approach developed in this work. Materials were collected from the work of Zhao *et al.* [30] and the ICSD database. [31] For the compositions in the work of Zhao *et al.* [30] the original references are given or the work itself is cited where the original reference was not available. For the compositions from ICSD the corresponding ICSD Collection Code is given as reference.

Nr.	Composition	Phase	Reference
1	$Na_{0.6}[Mn_{1.0}]O_{2.0}$	P2	Caballero *et al.* [32]
2	$Na_{0.6}[Cr_{0.6}Ti_{0.4}]O_{2.0}$	P2	Wang *et al.* [33]
3	$Na_{0.6}[Mn_{0.65}Ni_{0.25}Co_{0.1}]O_{2.0}$	P2	Nguyen *et al.* [34]
4	$Na_{0.65}[Ni_{0.17}Co_{0.11}Mn_{0.72}]O_{2.0}$	P2	Yu *et al.* [35]
5	$Na_{0.65}[Mn_{0.93}]O_{2.0}$	P2	Zhao *et al.* [36]
6	$Na_{0.66}[Li_{0.22}Ru_{0.78}]O_{2.0}$	P2	Cao *et al.* [37]
7	$Na_{0.66}[Nb_{1.0}]O_{2.0}$	P2	Tyutyunnik *et al.* [38]
8	$Na_{0.67}[Mn_{0.65}Ni_{0.2}Co_{0.15}]O_{2.0}$	P2	Li *et al.* [39]
9	$Na_{0.67}[Co_{0.67}Mn_{0.22}Ni_{0.11}]O_{2.0}$	P2	Valvo *et al.* [40]
10	$Na_{0.67}[Co_{0.25}Mn_{0.65}Cr_{0.1}]O_{2.0}$	P2	Wang *et al.* [41]
11	$Na_{0.67}[Mn_{1.0}]O_{2.0}$	P2	Su *et al.* [42]
12	$Na_{0.67}[Mg_{0.28}Mn_{0.72}]O_{2.0}$	P2	Yabuuchi *et al.* [43]
13	$Na_{0.67}[Mn_{0.78}Zn_{0.22}]O_{2.0}$	P2	Bai *et al.* [44]
14	$Na_{0.67}[Co_{1.0}]O_{2.0}$	P2	Hamada *et al.* [45]
15	$Na_{0.67}[Co_{0.5}Mn_{0.5}]O_{2.0}$	P2	Zhu *et al.* [46]
16	$Na_{0.67}[Li_{0.22}Ti_{0.78}]O_{2.0}$	P2	Wang *et al.* [47]
17	$Na_{0.67}[Ni_{0.33}Mn_{0.67}]O_{2.0}$	P2	Paulsen *et al.* [48]
18	$Na_{0.67}[Ni_{0.23}Mg_{0.1}Mn_{0.67}]O_{2.0}$	P2	Hou *et al.* [49]
19	$Na_{0.67}[Ni_{0.1}Cu_{0.2}Mn_{0.7}]O_{2.0}$	P2	Wang *et al.* [50]
20	$Na_{0.67}[Ni_{0.26}Zn_{0.07}Mn_{0.67}]O_{2.0}$	P2	Wu *et al.* [51]
21	$Na_{0.67}[Ni_{0.33}Mn_{0.5}Ti_{0.17}]O_{2.0}$	P2	Yoshida *et al.* [52]
22	$Na_{0.67}[Ni_{0.22}Cu_{0.11}Mn_{0.56}Ti_{0.11}]O_{2.0}$	P2	Mu *et al.* [53]
23	$Na_{0.67}[Ni_{0.33}Ti_{0.67}]O_{2.0}$	P2	Shin [54]
24	$Na_{0.67}[Fe_{0.67}Mn_{0.33}]O_{2.0}$	P2	Matsumura *et al.* [55]
25	$Na_{0.67}[Fe_{0.2}Mn_{0.8}]O_{2.0}$	P2	Dose *et al.* [56]
26	$Na_{0.67}[Mn_{0.8}Fe_{0.1}Ti_{0.1}]O_{2.0}$	P2	Han *et al.* [57]
27	$Na_{0.67}[Fe_{0.2}Ni_{0.15}Mn_{0.65}]O_{2.0}$	P2	Luo *et al.* [58]
28	$Na_{0.67}[Mn_{0.5}Fe_{0.25}Co_{0.25}]O_{2.0}$	P2	Liu *et al.* [59]
29	$Na_{0.67}[Mn_{0.65}Co_{0.2}Ni_{0.15}]O_{2.0}$	P2	Yuan *et al.* [60]
30	$Na_{0.67}[Ni_{0.4}Co_{0.2}Mn_{0.4}]O_{2.0}$	P2	Sun *et al.* [61]
31	$Na_{0.67}[Cr_{0.33}Ti_{0.67}]O_{2.0}$	P2	Tsuchiya *et al.* [62]; Zhao *et al.* [30]
32	$Na_{0.67}[Ni_{0.67}Te_{0.33}]O_{2.0}$	P2	Evstigneeva *et al.* [63]
33	$Na_{0.7}[Mn_{1.0}]O_{2.0}$	P2	Sehrawat *et al.* [64]
34	$Na_{0.7}[Mn_{0.6}Ni_{0.3}Co_{0.1}]O_{2.0}$	P2	Yoshida *et al.* [65]
35	$Na_{0.72}[Li_{0.24}Mn_{0.76}]O_{2.0}$	P2	Rong *et al.* [66]
36	$Na_{0.75}[Co_{1.0}]O_{2.0}$	P2	Huang *et al.* [67]; Balsys [68]

37	$Na_{0.76}[Cu_{0.22}Fe_{0.11}Mn_{0.67}]O_{2.0}$	P2	Li *et al.* [69]
38	$Na_{0.78}[Ni_{0.2}Co_{0.38}Mn_{0.42}]O_{2.0}$	P2	Zhao *et al.* [30]
39	$Na_{0.8}[Li_{0.12}Ni_{0.22}Mn_{0.66}]O_{2.0}$	P2	Clément *et al.* [70]
40	$Na_{0.8}[Co_{0.8}Ti_{0.2}]O_{2.0}$	P2	Zhao *et al.* [30]
41	$Na_{0.8}[Co_{0.8}Mn_{0.2}]O_{2.0}$	P2	Zhao *et al.* [30]
42	$Na_{1.0}[Ti_{1.0}]O_{2.0}$	O3	Di Wu *et al.* [71]
43	$Na_{1.0}[V_{1.0}]O_{2.0}$	O3	Chamberland & Porter [72]
44	$Na_{1.0}[Cr_{1.0}]O_{2.0}$	O3	Xia & Dahn [73]
45	$Na_{1.0}[Fe_{1.0}]O_{2.0}$	O3	Takeda *et al.* [74]
46	$Na_{1.0}[Mo_{1.0}]O_{2.0}$	O3	Ringenbach, C, Kessler, H, Acad, CR [75]
47	$Na_{1.0}[Rh_{1.0}]O_{2.0}$	O3	Hobbie & Hoppe [76]
48	$Na_{1.0}[Lu_{1.0}]O_{2.0}$	O3	Blasse [77]
49	$Na_{1.0}[Co_{0.5}Fe_{0.5}]O_{2.0}$	O3	Yoshida *et al.* [78]
50	$Na_{1.0}[Ni_{0.5}Mn_{0.5}]O_{2.0}$	O3	Bréger *et al.* [79]
51	$Na_{1.0}[Na_{0.33}Zr_{0.67}]O_{2.0}$	O3	Song *et al.* [80]
52	$Na_{1.0}[Na_{0.33}Ru_{0.67}]O_{2.0}$	O3	Mogare *et al.* [81]
53	$Na_{1.0}[Na_{0.33}Pd_{0.67}]O_{2.0}$	O3	Panin *et al.* [82]
54	$Na_{1.0}[Na_{0.33}Ir_{0.67}]O_{2.0}$	O3	Perez *et al.* [83]
55	$Na_{1.0}[Na_{0.33}Pt_{0.67}]O_{2.0}$	O3	McDaniel [84]
56	$Na_{1.0}[Na_{0.33}Ru_{0.53}Mn_{0.13}]O_{2.0}$	O3	Liu *et al.* [85]
57	$Na_{1.0}[Na_{0.33}Ru_{0.5}Sn_{0.17}]O_{2.0}$	O3	Rozier *et al.* [86]
58	$Na_{1.0}[Na_{0.2}Ni_{0.2}Mn_{0.2}Ru_{0.4}]O_{2.0}$	O3	Su *et al.* [87]
59	$Na_{1.0}[Na_{0.5}Ru_{0.5}]O_{2.0}$	O3	Regan *et al.* [88]; Qiao *et al.* [89]
60	$Na_{1.0}[Ni_{0.67}Bi_{0.33}]O_{2.0}$	O3	Wang *et al.* [90]
61	$Na_{1.0}[Ni_{0.67}Sb_{0.33}]O_{2.0}$	O3	Ma *et al.* [91]
62	$Na_{1.0}[Ni_{0.67}Ru_{0.33}]O_{2.0}$	O3	Li *et al.* [92]
63	$Na_{1.0}[Cu_{0.67}Sb_{0.33}]O_{2.0}$	O3	Smirnova *et al.* [93]
64	$Na_{1.0}[Cr_{0.33}Fe_{0.33}Mn_{0.33}]O_{2.0}$	O3	Cao *et al.* [94]
65	$Na_{1.0}[Mn_{0.33}Fe_{0.33}Co_{0.33}]O_{2.0}$	O3	Zhao *et al.* [30]
66	$Na_{1.0}[Mn_{0.33}Fe_{0.33}Ni_{0.33}]O_{2.0}$	O3	Kim *et al.* [95]
67	$Na_{1.0}[Ni_{0.33}Mn_{0.33}Co_{0.33}]O_{2.0}$	O3	Sathiya *et al.* [96]
68	$Na_{1.0}[Ni_{0.5}Co_{0.2}Mn_{0.3}]O_{2.0}$	O3	Xu *et al.* [97]
69	$Na_{1.0}[Mn_{0.25}Fe_{0.25}Co_{0.25}Ni_{0.25}]O_{2.0}$	O3	Li *et al.* [98]
70	$Na_{1.0}[Ni_{0.32}Fe_{0.13}Co_{0.15}Mn_{0.4}]O_{2.0}$	O3	Hwang *et al.* [99]
71	$Na_{1.0}[Ni_{0.4}Fe_{0.2}Mn_{0.2}Ti_{0.2}]O_{2.0}$	O3	Sun *et al.* [100]
72	$Na_{1.0}[Ni_{0.25}Co_{0.25}Fe_{0.25}Mn_{0.12}Ti_{0.12}]O_{2.0}$	O3	Yue *et al.* [101]
73	$Na_{1.0}[Ti_{0.25}Fe_{0.25}Co_{0.25}Ni_{0.25}]O_{2.0}$	O3	Yue *et al.* [102]
74	$Na_{1.0}[Ni_{0.33}Li_{0.11}Ti_{0.56}]O_{2.0}$	O3	Zhang *et al.* [103]
75	$Na_{1.0}[Li_{0.33}Ir_{0.67}]O_{2.0}$	O3	Perez *et al.* [104]
76	$Na_{1.0}[Na_{0.2}Mn_{0.4}Ir_{0.4}]O_{2.0}$	O3	Zhang *et al.* [105]
77	$Na_{1.0}[Ti_{0.5}Ni_{0.5}]O_{2.0}$	O3	Yu *et al.* [106]

78	$Na_{1.0}[Fe_{0.33}Ni_{0.33}Ti_{0.33}]O_{2.0}$	O3	Wang *et al.* [107]
79	$Na_{1.0}[Ni_{0.5}Mn_{0.2}Ti_{0.3}]O_{2.0}$	O3	Wang *et al.* [108]
80	$Na_{1.0}[Ni_{0.45}Cu_{0.05}Mn_{0.4}Ti_{0.1}]O_{2.0}$	O3	Yao *et al.* [109]
81	$Na_{0.9}[Cu_{0.22}Fe_{0.3}Mn_{0.48}]O_{2.0}$	O3	Mu *et al.* [110]
82	$Na_{0.9}[Ni_{0.45}Ti_{0.55}]O_{2.0}$	O3	Li *et al.* [111]
83	$Na_{0.9}[Ni_{0.4}Mn_{0.2}Ti_{0.4}]O_{2.0}$	O3	Qi *et al.* [112]
84	$Na_{0.9}[Mn_{0.4}Fe_{0.5}Ti_{0.1}]O_{2.0}$	O3	Jiang *et al.* [113]
85	$Na_{0.85}[Rh_{1.0}]O_{2.0}$	O3	Varela *et al.* [114]
86	$Na_{0.83}[Cr_{0.33}Fe_{0.33}Mn_{0.17}Ti_{0.17}]O_{2.0}$	O3	Cao *et al.* [115]
87	$Na_{0.8}[Ni_{0.4}Ti_{0.6}]O_{2.0}$	O3	Guo *et al.* [116]
88	$Na_{0.8}[Ni_{0.3}Co_{0.2}Ti_{0.5}]O_{2.0}$	O3	Guo *et al.* [117]
89	$Na_{0.8}[Fe_{0.8}Mn_{0.2}]O_{2.0}$	O3	Thorne *et al.* [118]
90	$Na_{0.8}[Cr_{0.8}Ti_{0.2}]O_{2.0}$	O3	Zhao *et al.* [30]
91	$Na_{0.8}[Fe_{0.8}Ti_{0.2}]O_{2.0}$	O3	Zhao *et al.* [30]
92	$Na_{0.8}[Ni_{0.4}Mn_{0.4}Ti_{0.2}]O_{2.0}$	O3	Zhao *et al.* [30]
93	$Na_{0.8}[Co_{0.1}Fe_{0.7}Mn_{0.2}]O_{2.0}$	O3	Zhao *et al.* [30]
94	$Na_{0.8}[Co_{0.2}Fe_{0.6}Ti_{0.2}]O_{2.0}$	O3	Zhao *et al.* [30]
95	$Na_{0.8}[Ni_{0.6}Sb_{0.4}]O_{2.0}$	O3	Smirnova *et al.* [119]
96	$Na_{0.78}[Li_{0.05}Cu_{0.15}Fe_{0.33}Mn_{0.47}]O_{2.0}$	O3	Zhao *et al.* [30]
97	$Na_{0.78}[Ni_{0.15}Fe_{0.48}Mn_{0.37}]O_{2.0}$	O3	Zhao *et al.* [30]
98	$Na_{0.78}[Cu_{0.2}Fe_{0.38}Mn_{0.42}]O_{2.0}$	O3	Zhao *et al.* [30]
99	$Na_{0.78}[Ni_{0.2}Fe_{0.38}Ti_{0.42}]O_{2.0}$	O3	Zhao *et al.* [30]
100	$Na_{0.7}[Rh_{1.0}]O_{2.0}$	O3	Varela *et al.* [114]
101	$Na_{0.7}[Ni_{0.35}Sn_{0.65}]O_{2.0}$	O3	Wang *et al.* [120]
102	$Na_{0.67}[Mg_{0.33}Ti_{0.67}]O_{2.0}$	O3	Zhao *et al.* [121]
103	$Na_{1.0}[Li_{0.33}Ti_{0.17}Mn_{0.5}]O_{2.0}$	O3	Zhao *et al.* [30]
104	$Na_{0.67}[Ni_{0.17}Mg_{0.17}Ti_{0.67}]O_{2.0}$	P2	Wang *et al.* [122]
105	$Na_{0.64}[Mn_{0.5}Ni_{0.34}Fe_{0.1}Mg_{0.06}]O_{2.0}$	O3	13770
106	$Na_{0.69}[Mn_{0.5}Ni_{0.39}Fe_{0.1}Mg_{0.01}]O_{2.0}$	O3	13771
107	$Na_{1.0}[Ni_{0.3}Fe_{0.4}Mn_{0.3}]O_{2.0}$	O3	19572
108	$Na_{1.0}[Ni_{0.5}Mn_{0.3}Co_{0.19}Al_{0.01}]O_{2.0}$	O3	49492
109	$Na_{1.0}[Ni_{0.5}Mn_{0.3}Co_{0.18}Al_{0.02}]O_{2.0}$	O3	49493
110	$Na_{1.0}[Cu_{0.2}Fe_{0.4}Mn_{0.4}]O_{2.0}$	O3	49834
111	$Na_{1.0}[Cu_{0.2}Fe_{0.3}Mn_{0.5}]O_{2.0}$	O3	49835
112	$Na_{0.54}[Ti_{1.0}]O_{2.0}$	O3	68872
113	$Na_{0.99}[Ti_{1.0}]O_{2.0}$	O3	85654
114	$Na_{1.0}[Co_{1.0}]O_{2.0}$	O3	96428
115	$Na_{0.73}[Li_{0.32}Ti_{0.68}]O_{2.0}$	O3	96670
116	$Na_{1.0}[Er_{1.0}]O_{2.0}$	O3	97544
117	$Na_{0.8}[Cu_{0.18}Fe_{0.3}Mn_{0.52}]O_{2.0}$	O3	133882
118	$Na_{0.85}[Cu_{0.18}Fe_{0.3}Mn_{0.52}]O_{2.0}$	O3	133884
119	$Na_{0.9}[Cu_{0.18}Fe_{0.3}Mn_{0.52}]O_{2.0}$	O3	133885
120	$Na_{0.92}[Co_{1.0}]O_{2.0}$	O3	155498
121	$Na_{0.32}[Co_{1.0}]O_{2.0}$	O3	155499
122	$Na_{1.0}[Ru_{1.0}]O_{2.0}$	O3	170347

123	$Na_{0.89}[Zn_{0.33}Ir_{0.67}]O_{2.0}$	O3	191296
124	$Na_{0.62}[Fe_{0.67}Mn_{0.33}]O_{2.0}$	O3	252021
125	$Na_{0.46}[Fe_{0.67}Mn_{0.33}]O_{2.0}$	O3	252022
126	$Na_{0.34}[Fe_{0.67}Mn_{0.33}]O_{2.0}$	O3	252023
127	$Na_{0.18}[Fe_{0.67}Mn_{0.33}]O_{2.0}$	O3	252024
128	$Na_{0.8}[Fe_{0.67}Mn_{0.33}]O_{2.0}$	O3	252025
129	$Na_{0.52}[Fe_{0.67}Mn_{0.33}]O_{2.0}$	O3	252026
130	$Na_{0.86}[Cu_{0.33}Ir_{0.67}]O_{2.0}$	O3	426655
131	$Na_{0.92}[Ni_{0.33}Ir_{0.67}]O_{2.0}$	O3	426656
132	$Na_{0.62}[Ir_{0.39}Mn_{0.61}]O_{2.0}$	O3	426657
133	$Na_{0.9}[Co_{0.33}Ir_{0.67}]O_{2.0}$	O3	426658
134	$Na_{0.8}[Fe_{0.67}Ir_{0.33}]O_{2.0}$	O3	426659
135	$Na_{1.0}[Al_{1.0}]O_{2.0}$	O3	22216
136	$Na_{1.0}[Tl_{1.0}]O_{2.0}$	O3	25510
137	$Na_{1.0}[Sc_{1.0}]O_{2.0}$	O3	25729
138	$Na_{0.75}[Fe_{0.75}Ti_{0.25}]O_{2.0}$	O3	27358
139	$Na_{1.0}[In_{1.0}]O_{2.0}$	O3	31932
140	$Na_{1.0}[Na_{0.33}Sn_{0.67}]O_{2.0}$	O3	31933
141	$Na_{1.0}[Ni_{0.48}Mn_{0.3}Ti_{0.2}Zr_{0.02}]O_{2.0}$	O3	33192
142	$Na_{1.0}[Ni_{0.45}Mn_{0.3}Ti_{0.2}Zr_{0.05}]O_{2.0}$	O3	33195
143	$Na_{1.0}[Ni_{0.4}Mn_{0.4}Ti_{0.1}Cu_{0.1}]O_{2.0}$	O3	37649
144	$Na_{1.0}[Ni_{0.2}Fe_{0.35}Mn_{0.45}]O_{2.0}$	O3	37671
145	$Na_{1.0}[Ni_{0.2}Fe_{0.35}Mn_{0.4}Zn_{0.05}]O_{2.0}$	O3	37672
146	$Na_{1.0}[Ni_{0.45}Zn_{0.05}Mn_{0.4}Ti_{0.1}]O_{2.0}$	O3	142010
147	$Na_{1.0}[Ni_{0.3}Fe_{0.2}Mn_{0.5}]O_{2.0}$	O3	147473
148	$Na_{1.0}[Ni_{0.28}Fe_{0.19}Mn_{0.47}Ti_{0.05}]O_{2.0}$	O3	147474
149	$Na_{1.0}[Ni_{0.27}Fe_{0.18}Mn_{0.45}Ti_{0.1}]O_{2.0}$	O3	147475
150	$Na_{1.0}[Ni_{0.26}Fe_{0.17}Mn_{0.42}Ti_{0.15}]O_{2.0}$	O3	147476
151	$Na_{0.6}[Mn_{0.67}Ni_{0.22}Fe_{0.11}]O_{2.0}$	O3	147524
152	$Na_{0.6}[Mn_{0.62}Ni_{0.22}Fe_{0.16}]O_{2.0}$	O3	147528
153	$Na_{1.0}[Ni_{0.4}Mn_{0.4}Co_{0.2}]O_{2.0}$	O3	257298
154	$Na_{0.91}[Ni_{0.4}Mn_{0.4}Co_{0.2}]O_{2.0}$	O3	257299
155	$Na_{0.8}[Ni_{0.4}Sn_{0.6}]O_{2.0}$	O3	264775
156	$Na_{0.9}[Ni_{0.45}Sn_{0.55}]O_{2.0}$	O3	264776
157	$Na_{1.0}[Ni_{0.5}Sn_{0.5}]O_{2.0}$	O3	264777
158	$Na_{1.0}[Y_{1.0}]O_{2.0}$	O3	291907
159	$Na_{1.0}[Ho_{1.0}]O_{2.0}$	O3	291908
160	$Na_{1.0}[Yb_{1.0}]O_{2.0}$	O3	291910
161	$Na_{0.63}[Mn_{0.5}Ni_{0.3}Fe_{0.1}Mg_{0.1}]O_{2.0}$	P2	13772
162	$Na_{0.48}[Mn_{1.0}]O_{2.0}$	P2	19654
163	$Na_{0.44}[Mn_{1.0}]O_{2.0}$	P2	19656
164	$Na_{0.27}[Mn_{1.0}]O_{2.0}$	P2	19657
165	$Na_{0.7}[Mn_{0.8}Mg_{0.2}]O_{2.0}$	P2	19772
166	$Na_{0.7}[Mn_{0.66}Ni_{0.17}Co_{0.17}]O_{2.0}$	P2	32224
167	$Na_{0.62}[Ti_{0.13}Mn_{0.61}Ni_{0.13}Co_{0.13}]O_{2.0}$	P2	32225

168	$Na_{0.77}[Ni_{0.33}Mn_{0.67}]O_{2.0}$	P2	33349
169	$Na_{0.8}[Ni_{0.33}Mn_{0.67}]O_{2.0}$	P2	33350
170	$Na_{0.95}[Ni_{0.33}Mn_{0.67}]O_{2.0}$	P2	33352
171	$Na_{0.67}[Mn_{0.5}Co_{0.4}Fe_{0.1}]O_{2.0}$	P2	35810
172	$Na_{0.67}[Mn_{0.5}Co_{0.3}Fe_{0.2}]O_{2.0}$	P2	35811
173	$Na_{0.74}[Co_{1.0}]O_{2.0}$	P2	50301
174	$Na_{0.41}[Co_{1.0}]O_{2.0}$	P2	55722
175	$Na_{0.67}[Fe_{0.5}Mn_{0.5}]O_{2.0}$	P2	70640
176	$Na_{0.67}[Co_{0.33}Ti_{0.67}]O_{2.0}$	P2	95617
177	$Na_{0.73}[Co_{1.0}]O_{2.0}$	P2	98212
178	$Na_{0.78}[Co_{1.0}]O_{2.0}$	P2	99393
179	$Na_{0.84}[Co_{1.0}]O_{2.0}$	P2	99394
180	$Na_{0.61}[Co_{1.0}]O_{2.0}$	P2	99830
181	$Na_{0.57}[Co_{1.0}]O_{2.0}$	P2	99831
182	$Na_{0.67}[Mn_{0.8}Zn_{0.1}Cu_{0.1}]O_{2.0}$	P2	112715
183	$Na_{0.67}[Mn_{0.8}Zn_{0.1}Al_{0.1}]O_{2.0}$	P2	112716
184	$Na_{0.67}[Mn_{0.8}Zn_{0.1}Ti_{0.1}]O_{2.0}$	P2	112717
185	$Na_{0.67}[Mn_{0.8}Fe_{0.1}Cu_{0.1}]O_{2.0}$	P2	112718
186	$Na_{0.67}[Mn_{0.8}Fe_{0.1}Al_{0.1}]O_{2.0}$	P2	112719
187	$Na_{0.75}[Mn_{0.75}Li_{0.25}]O_{2.0}$	P2	116426
188	$Na_{0.56}[Mn_{0.9}]O_{2.0}$	P2	117923
189	$Na_{0.7}[Cu_{0.2}Fe_{0.1}Mn_{0.7}]O_{2.0}$	P2	127638
190	$Na_{0.7}[Co_{1.0}]O_{2.0}$	P2	138399
191	$Na_{0.52}[Fe_{0.33}Mn_{0.67}]O_{2.0}$	P2	145390
192	$Na_{0.51}[Fe_{0.5}Mn_{0.5}]O_{2.0}$	P2	145391
193	$Na_{0.67}[Mn_{0.6}Ni_{0.2}Li_{0.2}]O_{2.0}$	P2	148780
194	$Na_{0.56}[Mn_{0.75}Ni_{0.25}]O_{2.0}$	P2	149048
195	$Na_{0.3}[Co_{1.0}]O_{2.0}$	P2	150910
196	$Na_{0.71}[Co_{1.0}]O_{2.0}$	P2	151793
197	$Na_{0.76}[Co_{1.0}]O_{2.0}$	P2	151795
198	$Na_{0.67}[Ni_{0.58}Sb_{0.42}]O_{2.0}$	P2	155267
199	$Na_{0.38}[Co_{1.0}]O_{2.0}$	P2	155510
200	$Na_{0.63}[Co_{1.0}]O_{2.0}$	P2	159810
201	$Na_{0.64}[Co_{1.0}]O_{2.0}$	P2	159818
202	$Na_{0.69}[Co_{1.0}]O_{2.0}$	P2	162600
203	$Na_{0.55}[Co_{1.0}]O_{2.0}$	P2	162845
204	$Na_{0.54}[Co_{1.0}]O_{2.0}$	P2	162847
205	$Na_{0.53}[Co_{1.0}]O_{2.0}$	P2	162849
206	$Na_{0.63}[Co_{0.97}Fe_{0.03}]O_{2.0}$	P2	166645
207	$Na_{0.58}[Co_{0.5}Mn_{0.5}]O_{2.0}$	P2	192730
208	$Na_{0.64}[Mn_{0.8}Mg_{0.2}]O_{2.0}$	P2	196275
209	$Na_{0.58}[Mn_{0.8}Mg_{0.2}]O_{2.0}$	P2	196276
210	$Na_{0.66}[Mn_{0.67}Fe_{0.33}]O_{2.0}$	P2	231006
211	$Na_{0.62}[Mn_{0.5}Fe_{0.5}]O_{2.0}$	P2	231007
212	$Na_{0.47}[Mn_{0.8}Mg_{0.2}]O_{2.0}$	P2	235991

213	$Na_{0.62}[Mn_{0.8}Mg_{0.2}]O_{2.0}$	P2	235992
214	$Na_{0.42}[Mn_{0.8}Mg_{0.2}]O_{2.0}$	P2	235993
215	$Na_{0.79}[Co_{1.0}]O_{2.0}$	P2	237123
216	$Na_{0.79}[Co_{0.7}Mn_{0.3}]O_{2.0}$	P2	237125
217	$Na_{0.34}[Co_{1.0}]O_{2.0}$	P2	246579
218	$Na_{0.8}[Co_{1.0}]O_{2.0}$	P2	246584
219	$Na_{1.0}[Co_{1.0}]O_{2.0}$	P2	246585
220	$Na_{0.64}[Co_{0.9}Ru_{0.1}]O_{2.0}$	P2	246744
221	$Na_{0.66}[Co_{0.8}Ru_{0.2}]O_{2.0}$	P2	246745
222	$Na_{0.77}[Co_{0.7}Ru_{0.3}]O_{2.0}$	P2	246746
223	$Na_{0.69}[Co_{0.6}Ru_{0.4}]O_{2.0}$	P2	246747
224	$Na_{0.72}[Co_{0.5}Ru_{0.5}]O_{2.0}$	P2	246748
225	$Na_{0.67}[Cr_{0.67}Ti_{0.33}]O_{2.0}$	P2	253190
226	$Na_{0.67}[Mn_{0.66}Fe_{0.2}Cu_{0.14}]O_{2.0}$	P2	259163
227	$Na_{0.7}[Cr_{0.85}Sb_{0.15}]O_{2.0}$	P2	261554
228	$Na_{0.71}[Mn_{0.65}Co_{0.18}Ni_{0.17}]O_{2.0}$	P2	291156
229	$Na_{0.85}[Ni_{0.34}Mn_{0.66}]O_{2.0}$	P2	19135
230	$Na_{0.85}[Li_{0.12}Ni_{0.22}Mn_{0.66}]O_{2.0}$	P2	19136
231	$Na_{0.69}[Mn_{0.92}Fe_{0.08}]O_{2.0}$	P2	36989
232	$Na_{0.69}[Mn_{0.87}Fe_{0.08}Mg_{0.05}]O_{2.0}$	P2	36990
233	$Na_{0.69}[Mn_{0.82}Fe_{0.08}Mg_{0.1}]O_{2.0}$	P2	36991
234	$Na_{0.69}[Mn_{0.77}Fe_{0.08}Mg_{0.15}]O_{2.0}$	P2	36992
235	$Na_{0.44}[Co_{0.1}Mn_{0.9}]O_{2.0}$	P2	41644
236	$Na_{0.67}[Ni_{0.28}Mn_{0.47}Fe_{0.19}Zr_{0.01}]O_{2.0}$	P2	43092
237	$Na_{0.67}[Mn_{0.7}Ni_{0.2}Mg_{0.1}]O_{2.0}$	P2	45924
238	$Na_{0.7}[Mg_{0.15}Mn_{0.85}]O_{2.0}$	P2	92079
239	$Na_{0.7}[Mg_{0.15}Li_{0.1}Mn_{0.75}]O_{2.0}$	P2	92097
240	$Na_{0.67}[Co_{0.04}Ni_{0.29}Mn_{0.67}]O_{2.0}$	P2	93469
241	$Na_{0.5}[Ti_{0.6}Ni_{0.3}Fe_{0.1}]O_{2.0}$	P2	111262
242	$Na_{0.67}[Ni_{0.25}Mn_{0.75}]O_{2.0}$	P2	113162
243	$Na_{0.8}[Mn_{0.6}Co_{0.4}]O_{2.0}$	P2	113711
244	$Na_{0.66}[Li_{0.01}Mn_{0.48}Ti_{0.01}Fe_{0.5}]O_{2.0}$	P2	116196
245	$Na_{0.66}[Al_{0.05}Mn_{0.95}]O_{2.0}$	P2	130561
246	$Na_{0.64}[Al_{0.1}Mn_{0.9}]O_{2.0}$	P2	130562
247	$Na_{0.67}[Al_{0.2}Mn_{0.8}]O_{2.0}$	P2	130563
248	$Na_{0.67}[Mn_{0.9}Co_{0.1}]O_{2.0}$	P2	138209
249	$Na_{0.67}[Mn_{0.8}Co_{0.2}]O_{2.0}$	P2	138210
250	$Na_{0.54}[Fe_{0.33}Mn_{0.67}]O_{2.0}$	P2	145392
251	$Na_{0.6}[Fe_{0.5}Mn_{0.5}]O_{2.0}$	P2	145393
252	$Na_{0.67}[Mn_{0.49}Fe_{0.5}Zr_{0.01}]O_{2.0}$	P2	146381
253	$Na_{0.6}[Mn_{0.67}Ni_{0.22}Fe_{0.11}]O_{2.0}$	P2	147522
254	$Na_{0.6}[Mn_{0.62}Ni_{0.22}Fe_{0.16}]O_{2.0}$	P2	147526
255	$Na_{0.6}[Fe_{0.5}Mn_{0.49}Zn_{0.01}]O_{2.0}$	P2	147596
256	$Na_{0.6}[Fe_{0.5}Mn_{0.48}Zn_{0.02}]O_{2.0}$	P2	147597
257	$Na_{0.66}[Ni_{0.28}Zn_{0.05}Mn_{0.67}]O_{2.0}$	P2	148427

258	$Na_{0.66}[Ni_{0.23}Zn_{0.1}Mn_{0.67}]O_{2.0}$	P2	148428
259	$Na_{0.66}[Ni_{0.18}Zn_{0.15}Mn_{0.67}]O_{2.0}$	P2	148429
260	$Na_{0.4}[Mn_{0.87}Ni_{0.13}]O_{2.0}$	P2	149008
261	$Na_{0.72}[Li_{0.12}Ni_{0.22}Mn_{0.66}]O_{2.0}$	P2	194426
262	$Na_{0.44}[Mn_{0.6}Ni_{0.4}]O_{2.0}$	P2	235714
263	$Na_{0.44}[Mn_{0.6}Ni_{0.3}Cu_{0.1}]O_{2.0}$	P2	235715
264	$Na_{0.57}[Co_{0.65}Mn_{0.35}]O_{2.0}$	P2	237126
265	$Na_{1.0}[Pu_{0.67}Na_{0.33}]O_{2.0}$	O3	241539
266	$Na_{1.0}[Bi_{0.5}Na_{0.5}]O_{2.0}$	O3	414158
267	$Na_{0.8}[Ni_{0.33}Mn_{0.67}]O_{2.0}$	P2	33351
268	$Na_{0.71}[Co_{1.0}]O_{2.0}$	P2	98211
269	$Na_{0.65}[Li_{0.12}Mg_{0.13}Mn_{0.74}]O_{2.0}$	P2	124528
270	$Na_{0.67}[Cu_{0.17}Ni_{0.17}Mn_{0.67}]O_{2.0}$	P2	125982
271	$Na_{0.5}[Co_{1.0}]O_{2.0}$	P2	21001
272	$Na_{0.67}[Li_{0.17}Co_{0.17}Mn_{0.67}]O_{2.0}$	P2	147641

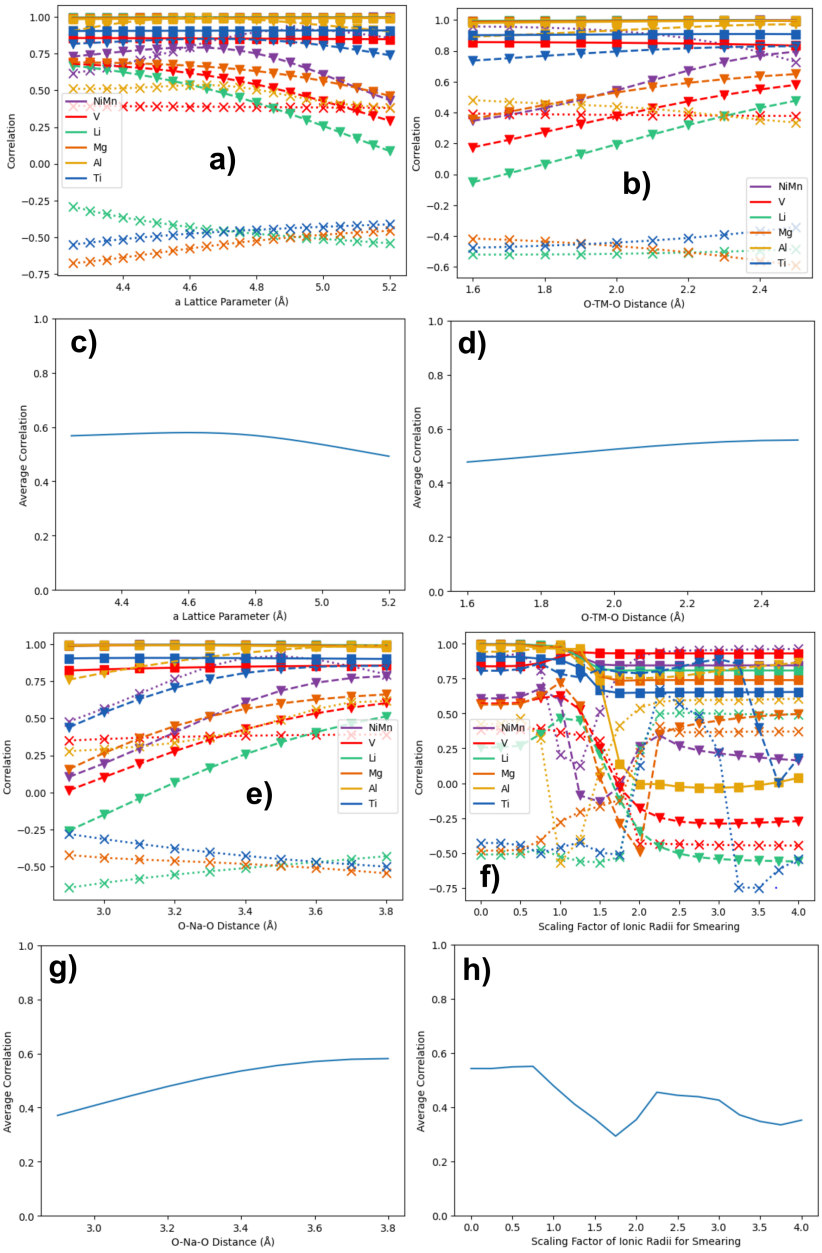

Supplementary Figure 3.11: Sensitivity of correlation to DFT for energy differences of different stacking sequences for changing the free parameters a (a and c), $d_{\text{O-TM-O}}$ (b and d), $d_{\text{O-Na-O}}$ (e and g), and σ (f and h). While a, b, e, and f show the change in correlation for each tested substituent and for all sodium concentrations of 1.00, 0.67, and 0.33, the plots c, d, g, and h show the average over all materials and sodium concentrations.

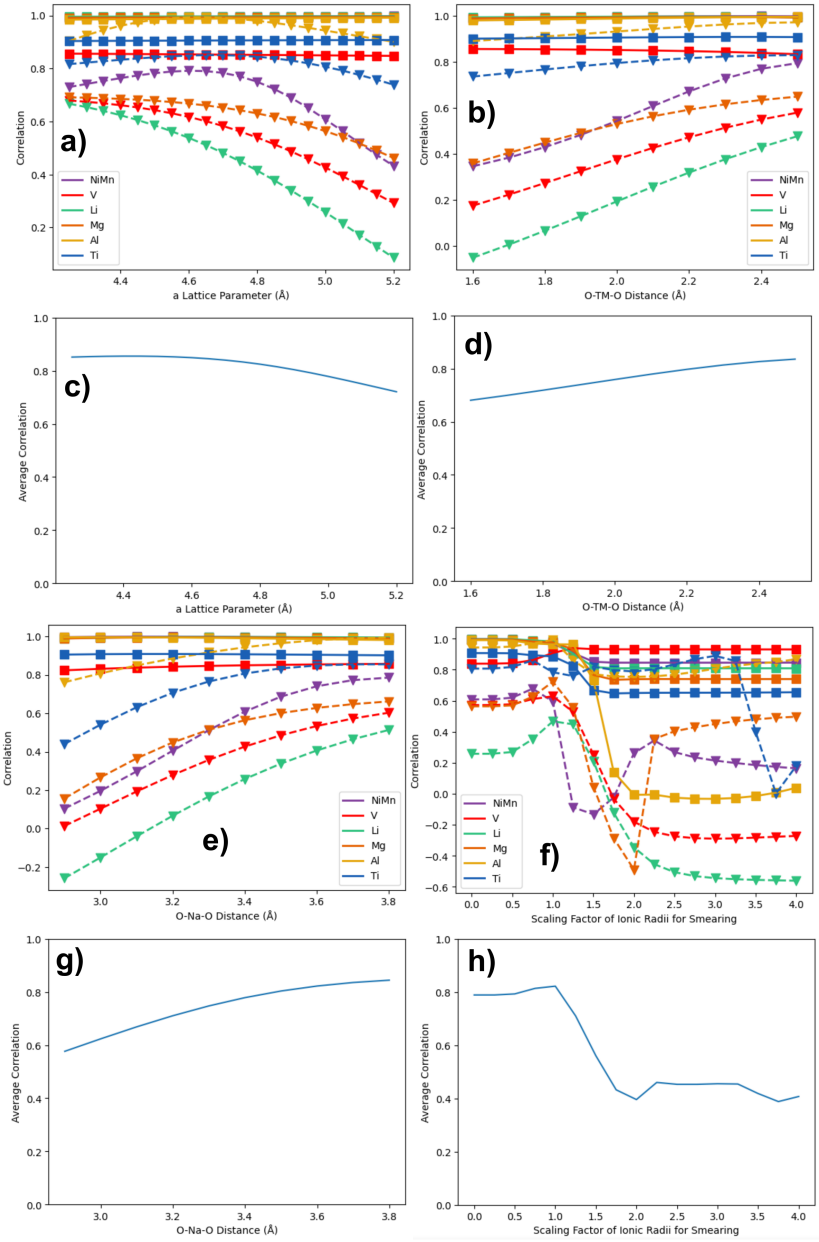

Supplementary Figure 3.12: Sensitivity of correlation to DFT for energy differences of different stacking sequences for changing the free parameters a (a and c), $d_{\text{O-TM-O}}$ (b and d), $d_{\text{O-Na-O}}$ (e and g), and σ (f and h) excluding Na=0.33. While a, b, e, and f show the change in correlation for each tested substituent and for all sodium concentrations of 1.00 and 0.67 (excluding 0.33) the plots c, d, g, and h show the average over all materials and sodium concentrations.

Supplementary Table 3.2: The top 30 parameter sets found during the grid-based screening of all four parameters. The correlation (excluding Na=0.33) is very high for all parameter sets and the chosen parameter set (8) which is also close to experimental values is highlighted in bold.

Nr.	O-TM-O (Å)	O-Na-O (Å)	a (Å)	Smearing	Correlation
1	2.7	2.9	4.5	0.6	0.88304
2	2.6	3.1	4.6	0.6	0.88297
3	2.6	3.0	4.5	0.6	0.88293
4	2.6	3.2	4.7	0.6	0.88286
5	2.2	2.9	4.1	0.5	0.88284
6	2.2	3.0	4.2	0.5	0.88282
7	2.7	3.0	4.6	0.6	0.88279
8	**2.3**	**3.4**	**4.6**	**0.5**	**0.88273**
9	2.6	3.6	5.0	0.6	0.88272
10	2.6	2.9	4.4	0.6	0.88272
11	2.7	3.4	4.9	0.6	0.88271
12	2.3	3.3	4.5	0.5	0.88270
13	2.6	3.5	4.9	0.6	0.88270
14	2.7	3.5	5.0	0.6	0.88269
15	2.2	3.1	4.3	0.5	0.88268
16	2.7	3.3	4.8	0.6	0.88267
17	2.5	3.8	5.1	0.5	0.88267
18	2.7	3.9	5.3	0.6	0.88265
19	2.6	3.7	5.1	0.6	0.88265
20	2.6	3.3	4.8	0.6	0.88264
21	2.0	3.1	4.1	0.1	0.88263
22	2.0	3.1	4.1	0.0	0.88263
23	2.0	3.1	4.1	0.2	0.88263
24	2.0	3.1	4.1	0.3	0.88263
25	2.2	3.4	4.5	0.2	0.88263
26	2.2	3.4	4.5	0.1	0.88263
27	2.2	3.4	4.5	0.0	0.88263
28	2.2	3.4	4.5	0.3	0.88263
29	2.5	3.7	5.0	0.5	0.88262
30	2.4	3.7	4.9	0.2	0.88262

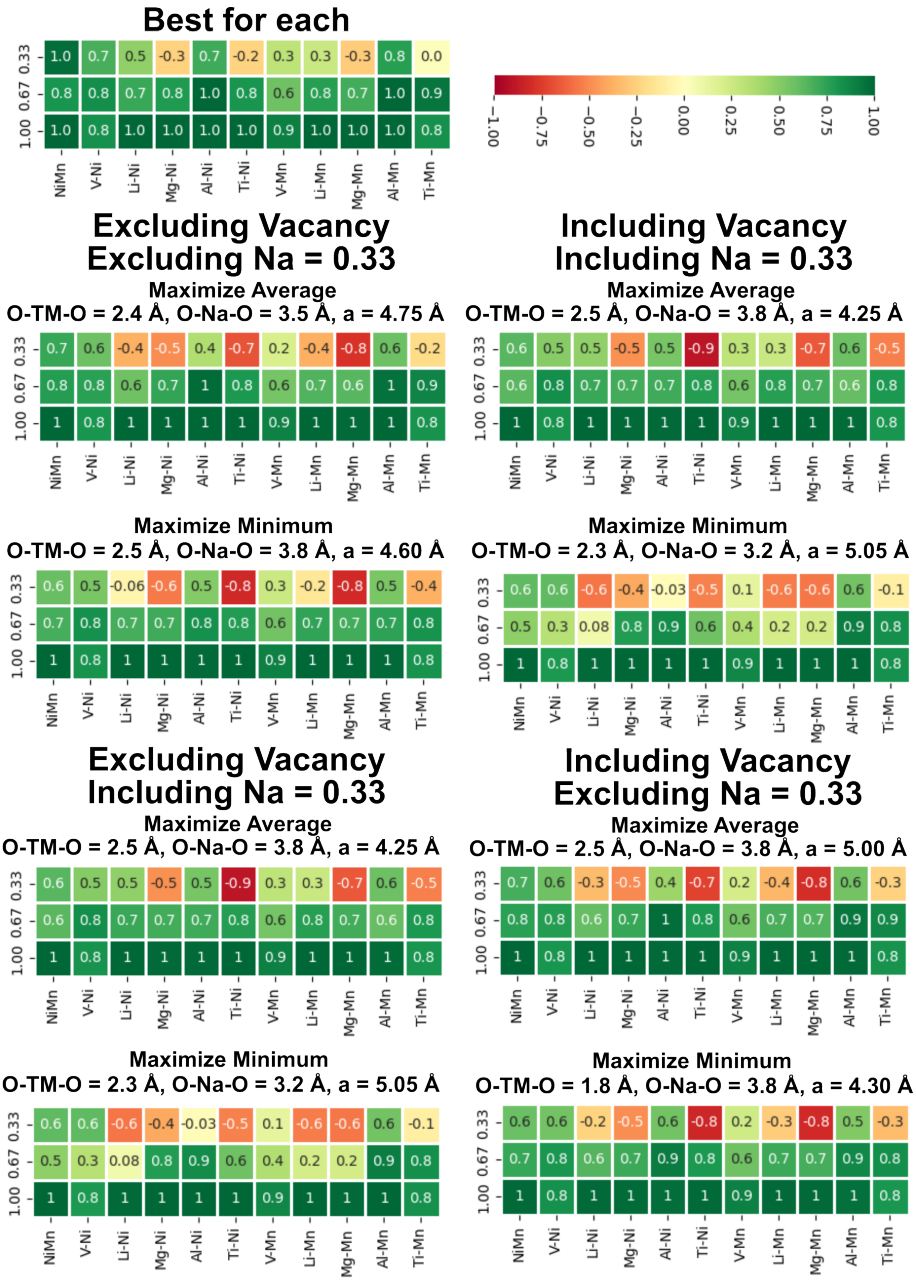

Supplementary Figure 3.13: Correlation of optimized parameter while either the average correlation over all materials and sodium concentrations is maximized or the minimal correlation is maximized. Fits for excluding or including certain materials and sodium concentrations are shown along with the optimal correlation (top left) that could be achieved if an individual set of parameter is used for each composition.

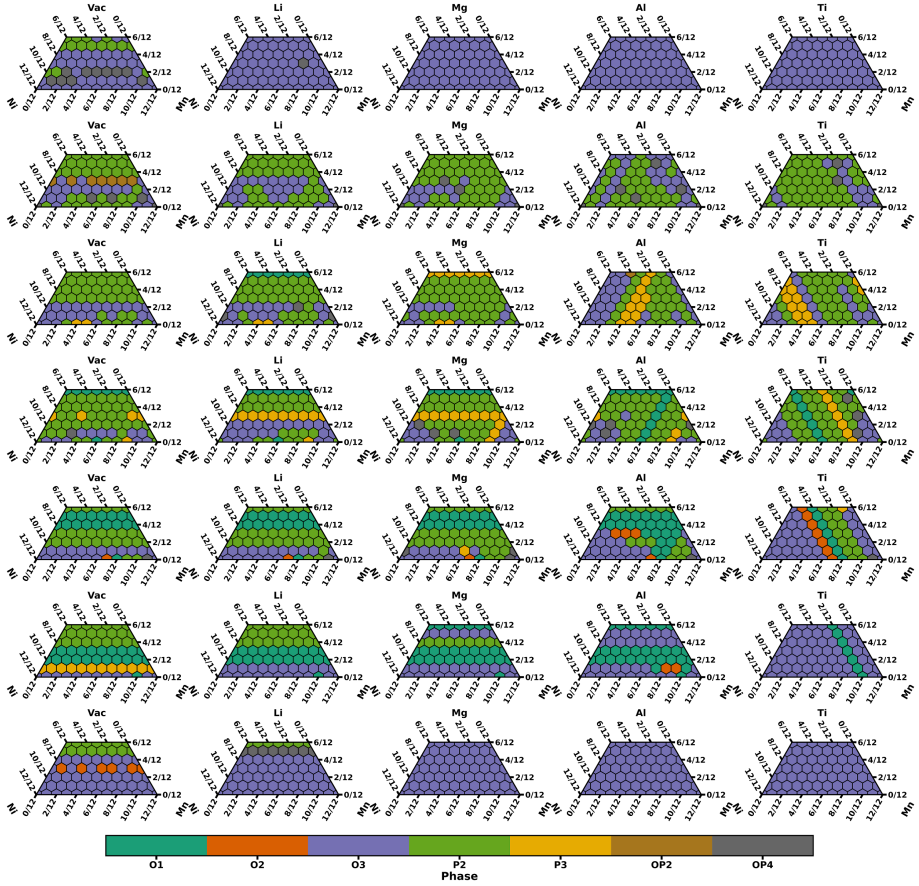

Supplementary Figure 3.14: Phase stabilities for various substituents (left to right) and sodium concentrations (top to bottom: 1.00, 0.83, 0.67, 0.50, 0.33, 0.17, 0.00) when the "default" parameter set discussed in the main text is employed.

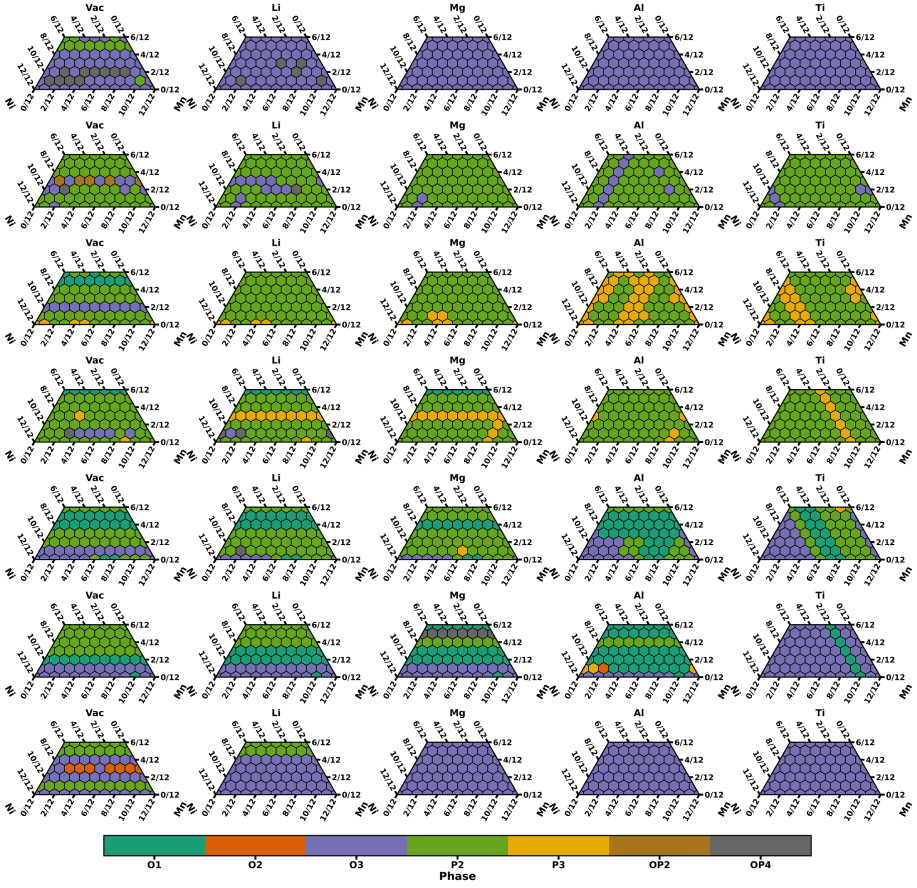

Supplementary Figure 3.15: Phase stabilities for various substituents (left to right) and sodium concentrations (top to bottom: 1.00, 0.83, 0.67, 0.50, 0.33, 0.17, 0.00) when the "optimized" parameter set discussed in the main text is employed.

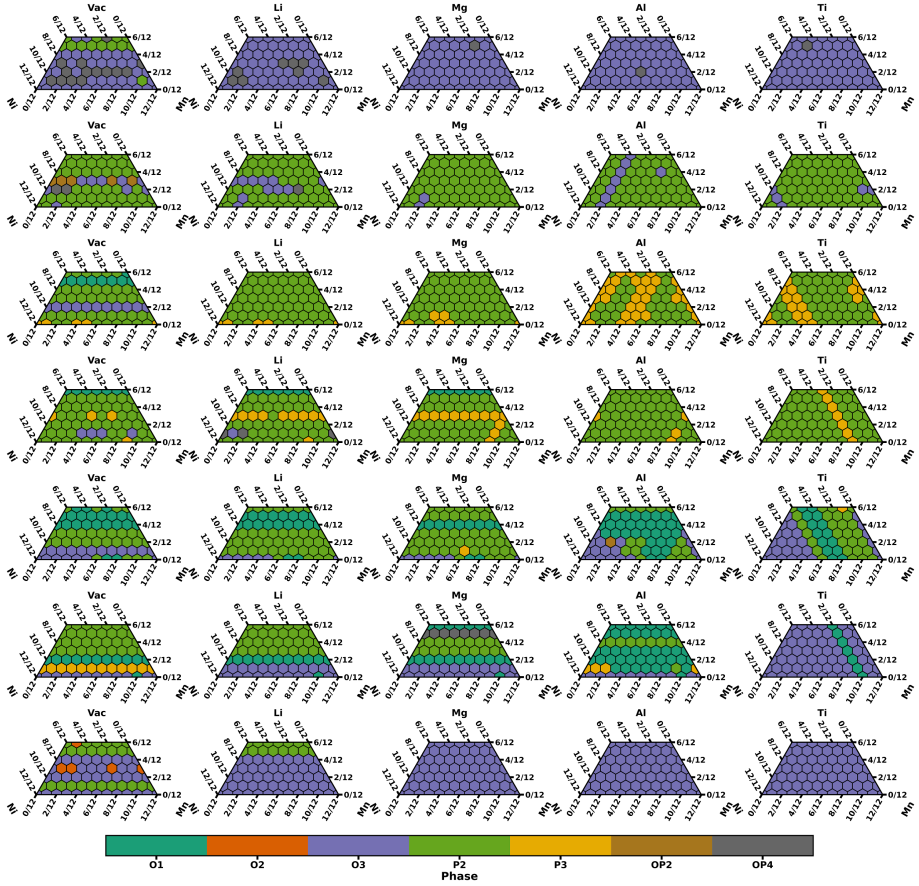

Supplementary Figure 3.16: Phase stabilities for various substituents (left to right) and sodium concentrations (top to bottom: 1.00, 0.83, 0.67, 0.50, 0.33, 0.17, 0.00) when the "Smeared" parameter set discussed in the main text is employed.

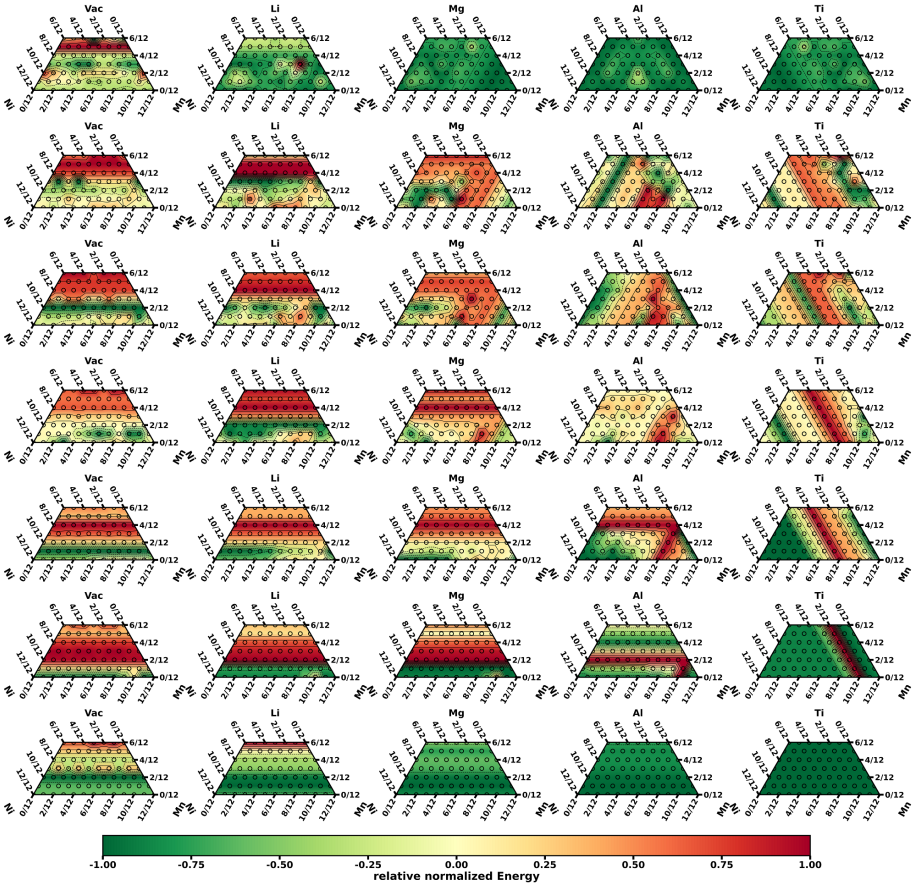

Supplementary Figure 3.17: Heatmaps of O3 stabilities while energies are normalized between -1 and 1 for each plot and negative values indicate O3 being the most stable phase and positive values some other phase is more stable. Plots for different substituents (left to right) and various sodium concentrations (top to bottom: 1.00, 0.83, 0.67, 0.50, 0.33, 0.17, and 0.00) are shown. Energies were obtained using the "default" parameter set discussed in the main text.

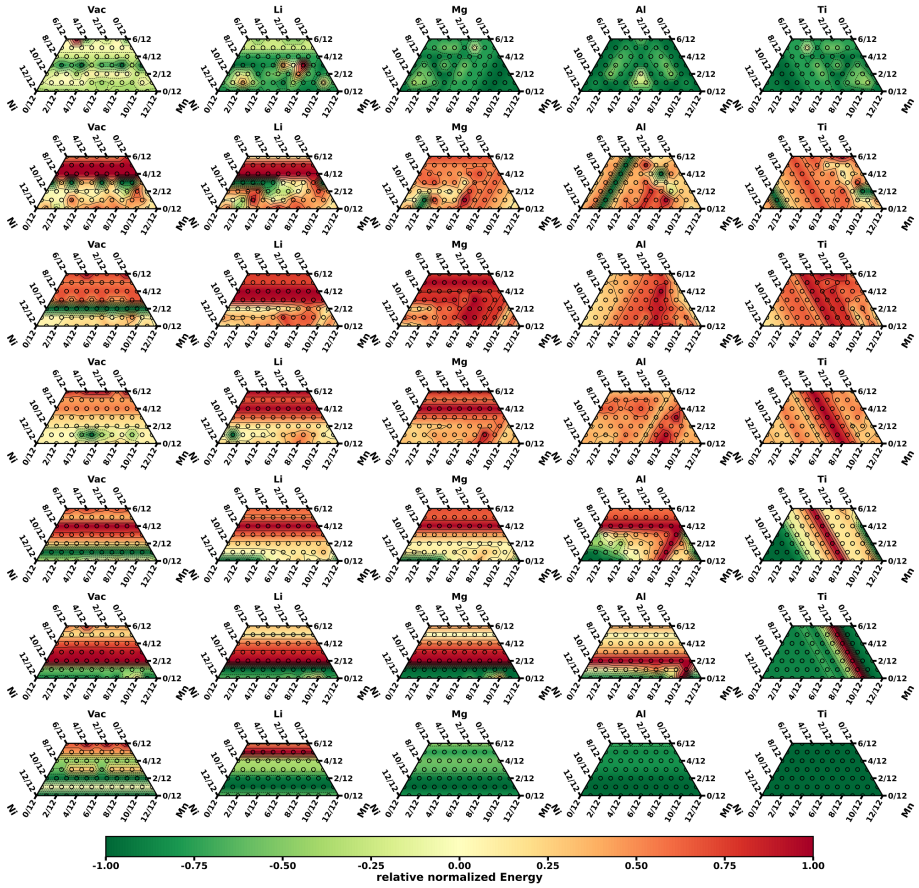

Supplementary Figure 3.18: Heatmaps of O3 stabilities while energies are normalized between -1 and 1 for each plot and negative values indicate O3 being the most stable phase and positive values some other phase is more stable. Plots for different substituents (left to right) and various sodium concentrations (top to bottom: 1.00, 0.83, 0.67, 0.50, 0.33, 0.17, and 0.00) are shown. Energies were obtained using the "optimized" parameter set discussed in the main text.

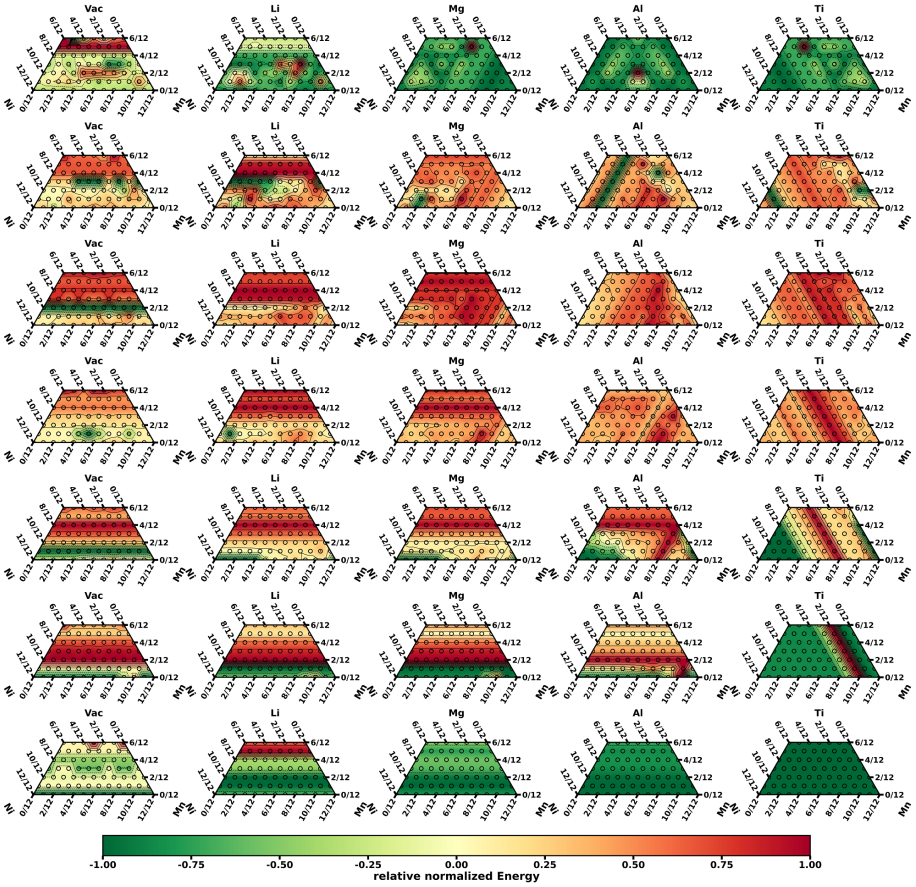

Supplementary Figure 3.19: Heatmaps of O3 stabilities while energies are normalized between -1 and 1 for each plot and negative values indicate O3 being the most stable phase and positive values some other phase is more stable. Plots for different substituents (left to right) and various sodium concentrations (top to bottom: 1.00, 0.83, 0.67, 0.50, 0.33, 0.17, and 0.00) are shown. Energies were obtained using the "smeared" parameter set discussed in the main text.

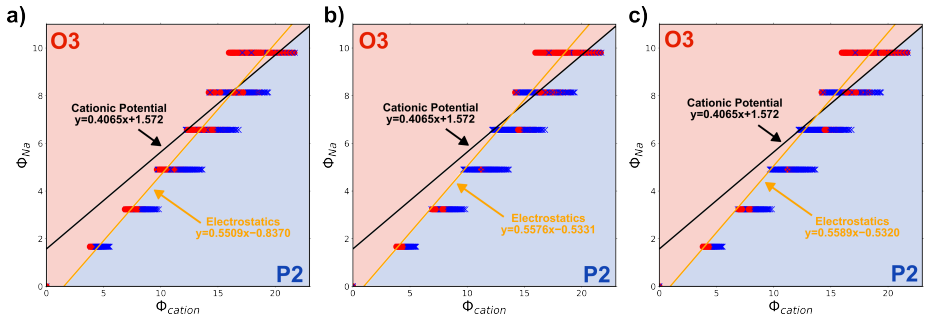

Supplementary Figure 3.20: Phases (O3 or P2) as predicted by the electrostatic prediction approach using the "default" (a), "optimized", and "Smearing" parameter set as discussed in the main text for all compositions shown in Figure S7 down to a sodium concentration of zero in the two dimensional cationic potential space as introduced by Zhao *et al.* [30]. Blue crosses indicate P2 and red circles indicate O3. The linear separation line proposed by the cationic potential approach is shown as black line while the one obtained from re-fitting to the electrostatic predictions is shown in orange.

REFERENCES

1. Yabuuchi, N., Kubota, K., Dahbi, M. & Komaba, S. Research development on sodium-ion batteries. *Chemical reviews* **114,** 11636–11682 (2014).
2. Hwang, J.-Y., Myung, S.-T. & Sun, Y.-K. Sodium-ion batteries: present and future. *Chemical Society reviews* **46,** 3529–3614 (2017).
3. Gao, Y. *et al.* A 30–year overview of sodium–ion batteries. *Carbon Energy* **6** (2024).
4. Phogat, P., Dey, S. & Wan, M. Comprehensive review of Sodium-Ion Batteries: Principles, Materials, Performance, Challenges, and future Perspectives. *Materials Science and Engineering: B* **312,** 117870 (2025).
5. Delmas, C., Braconnier, J., Fouassier, C. & Hagenmuller, P. Electrochemical intercalation of sodium in NaxCoO2 bronzes. *Solid State Ionics* **3-4,** 165–169 (1981).
6. Zhao, C. *et al.* Rational design of layered oxide materials for sodium-ion batteries. *Science (New York, N.Y.)* **370,** 708–711 (2020).
7. Wang, K., Yan, P. & Sui, M. Phase transition induced cracking plaguing layered cathode for sodium-ion battery. *Nano Energy* **54,** 148–155 (2018).
8. Tang, Y. *et al.* Sustainable layered cathode with suppressed phase transition for long-life sodium-ion batteries. *Nature Sustainability* **7,** 348–359 (2024).
9. Xiao, Y. *et al.* A Stable Layered Oxide Cathode Material for High–Performance Sodium–Ion Battery. *Advanced Energy Materials* **9** (2019).
10. Sathiya, M. *et al.* A Chemical Approach to Raise Cell Voltage and Suppress Phase Transition in O3 Sodium Layered Oxide Electrodes. *Advanced Energy Materials* **8** (2018).
11. Wang, P.-F. *et al.* Ti-Substituted NaNi0.5 Mn0.5-x Tix O2 Cathodes with Reversible O3-P3 Phase Transition for High-Performance Sodium-Ion Batteries. *Advanced materials (Deerfield Beach, Fla.)* **29** (2017).
12. Sheng, T. *et al.* Modulating Phase Angle Variations of O3–Type High–Entropy Layered Sodium Oxide for Practical Sodium–Ion Cylindrical Battery. *Advanced Functional Materials* (2025).
13. Mo, Y., Ong, S. P. & Ceder, G. Insights into Diffusion Mechanisms in P2 Layered Oxide Materials by First-Principles Calculations. *Chemistry of Materials* **26,** 5208–5214 (2014).
14. GH Cartledge. *Studies on the Periodic System. I. The Ionic Potential as a Periodic Function 1* (ACS Publications, Journal of the American Chemical Society, 1928).
15. Shin, Y. Preparation and structural properties of layer-type oxides NaxNix/2Ti1−x/2O2 (0.60≤x≤1.0). *Solid State Ionics* **132,** 131–141 (2000).

16. Köster, K., Binninger, T. & Kaghazchi, P. Optimization of Coulomb energies in gigantic configurational spaces of multi-element ionic crystals. *npj Computational Materials* **11** (2025).

17. House, R. A. *et al.* The role of O2 in O-redox cathodes for Li-ion batteries. *Nature Energy* **6,** 781–789 (2021).

18. Gao, X. *et al.* Clarifying the origin of molecular O2 in cathode oxides. *Nature materials* **24,** 743–752 (2025).

19. Gingrich, T. R. & Wilson, M. On the Ewald summation of Gaussian charges for the simulation of metallic surfaces. *Chemical Physics Letters* **500,** 178–183 (2010).

20. Zagorac, D., Müller, H., Ruehl, S., Zagorac, J. & Rehme, S. Recent developments in the Inorganic Crystal Structure Database: theoretical crystal structure data and related features. *Journal of applied crystallography* **52,** 918–925 (2019).

21. Köster, K. & Kaghazchi, P. Hybrid functionals with nonempirical Hartree-Fock parameters for electronic structure calculation of layered oxides. *Physical Review B* **109** (2024).

22. Liu, H. *et al.* Reversible OP4 phase in P2–Na2/3Ni1/3Mn2/3O2 sodium ion cathode. *Journal of Power Sources* **508,** 230324 (2021).

23. Pahari, D. & Puravankara, S. On controlling the P2-O2 phase transition by optimal Ti-substitution on Ni- site in P2-type Na0.67Ni0.33Mn0.67O2 (NNMO) cathode for Na-ion batteries. *Journal of Power Sources* **455,** 227957 (2020).

24. Eom, S., Jeong, S. H., Lee, S. J., Jung, Y. H. & Kim, J.-H. Mitigating the P2–O2 phase transition of Ni–Co–Mn based layered oxide for improved sodium-ion batteries via interlayered structural modulation. *Materials Today Energy* **38,** 101449 (2023).

25. Yang, L. *et al.* Structural Aspects of P2–Type Na 0.67 Mn 0.6 Ni 0.2 Li 0.2 O 2 (MNL) Stabilization by Lithium Defects as a Cathode Material for Sodium–Ion Batteries. *Advanced Functional Materials* **31** (2021).

26. Yabuuchi, N. *et al.* New O2/P2–type Li–Excess Layered Manganese Oxides as Promising Multi–Functional Electrode Materials for Rechargeable Li/Na Batteries. *Advanced Energy Materials* **4** (2014).

27. Kresse, G. & Furthmüller, J. Efficient iterative schemes for ab initio total-energy calculations using a plane-wave basis set. *Physical review. B, Condensed matter* **54,** 11169–11186 (1996).

28. Blöchl, P. E. Projector augmented-wave method. *Physical review. B, Condensed matter* **50,** 17953–17979 (1994).

29. Perdew, J. P., Burke, K. & Ernzerhof, M. Generalized Gradient Approximation Made Simple. *Physical review letters* **77,** 3865–3868 (1996).

30. Zhao, C. *et al.* Rational design of layered oxide materials for sodium-ion batteries. *Science (New York, N.Y.)* **370,** 708–711 (2020).

31. Zagorac, D., Müller, H., Ruehl, S., Zagorac, J. & Rehme, S. Recent developments in the Inorganic Crystal Structure Database: theoretical crystal structure data and related features. *Journal of applied crystallography* **52,** 918–925 (2019).

32. Caballero, A. *et al.* Synthesis and characterization of high-temperature hexagonal P2-Na0.6 MnO2 and its electrochemical behaviour as cathode in sodium cells. *Journal of Materials Chemistry* **12,** 1142–1147 (2002).

33. Wang, Y., Xiao, R., Hu, Y.-S., Avdeev, M. & Chen, L. P2-Na0.6Cr0.6Ti0.4O2 cation-disordered electrode for high-rate symmetric rechargeable sodium-ion batteries. *Nature communications* **6,** 6954 (2015).

34. Nguyen, N.-A. *et al.* Effect of Calcination Temperature on a P-type Na 0.6 Mn 0.65 Ni 0.25 Co 0.10 O 2 Cathode Material for Sodium-Ion Batteries. *Journal of The Electrochemical Society* **164,** A6308–A6314 (2017).

35. Yu, T.-Y., Hwang, J.-Y., Aurbach, D. & Sun, Y.-K. Microsphere Na0.65Ni0.17Co0.11Mn0.72O2 Cathode Material for High-Performance Sodium-Ion Batteries. *ACS applied materials & interfaces* **9,** 44534–44541 (2017).

36. Zhao, C. *et al.* Decreasing transition metal triggered oxygen redox activity in Na-deficient oxides. *Energy Storage Materials* **20,** 395–400 (2019).

37. Cao, X. *et al.* Stabilizing Reversible Oxygen Redox Chemistry in Layered Oxides for Sodium–Ion Batteries. *Advanced Energy Materials* **10** (2020).

38. Tyutyunnik, A. P. *et al.* ChemInform Abstract: Synthesis, Superconducting Properties and Structural (Including Electron Diffraction) Studies of NaxNbO2 and LixNbO2. *ChemInform* **27** (1996).

39. Li, Z.-Y., Gao, R., Sun, L., Hu, Z. & Liu, X. Designing an advanced P2-Na 0.67 Mn 0.65 Ni 0.2 Co 0.15 O 2 layered cathode material for Na-ion batteries. *Journal of Materials Chemistry A* **3,** 16272–16278 (2015).

40. Valvo, M., Doubaji, S., Saadoune, I. & Edström, K. Pseudocapacitive charge storage properties of Na2/3Co2/3Mn2/9Ni1/9O2 in Na-ion batteries. *Electrochimica Acta* **276,** 142–152 (2018).

41. Wang, Y., Tang, J., Yang, X. & Huang, W. A study on electrochemical properties of P2-type Na–Mn–Co–Cr–O cathodes for sodium-ion batteries. *Inorganic Chemistry Frontiers* **5,** 577–584 (2018).

42. Su, D., Wang, C., Ahn, H.-j. & Wang, G. Single crystalline Na(0.7)MnO2 nanoplates as cathode materials for sodium-ion batteries with enhanced performance. *Chemistry (Weinheim an der Bergstrasse, Germany)* **19,** 10884–10889 (2013).

43. Yabuuchi, N. *et al.* A new electrode material for rechargeable sodium batteries: P2-type Na 2/3 [Mg 0.28 Mn 0.72]O 2 with anomalously high reversible capacity. *Journal of Materials Chemistry A* **2,** 16851–16855 (2014).

44. Bai, X. *et al.* Anionic Redox Activity in a Newly Zn–Doped Sodium Layered Oxide P2–Na 2/3 Mn 1−y Zn y O 2 (0 < y < 0.23). *Advanced Energy Materials* **8** (2018).

45. Hamada, N., Imai, T. & Funashima, H. Thermoelectric power calculation by the Boltzmann equation: Na(x)CoO(2). *Journal of physics. Condensed matter : an Institute of Physics journal* **19,** 365221 (2007).

46. Zhu, Y.-E. *et al.* A P2-Na 0.67 Co 0.5 Mn 0.5 O 2 cathode material with excellent rate capability and cycling stability for sodium ion batteries. *Journal of Materials Chemistry A* **4,** 11103–11109 (2016).

47. Wang, Y. *et al.* A zero-strain layered metal oxide as the negative electrode for long-life sodium-ion batteries. *Nature communications* **4,** 2365 (2013).

48. Paulsen, J. M., Donaberger, R. A. & Dahn, J. R. Layered T2-, O6-, O2-, and P2-Type A 2/3 [M‘ 2+1/3 M 4+2/3]O 2 Bronzes, A = Li, Na; M‘ = Ni, Mg; M = Mn, Ti. *Chemistry of Materials* **12,** 2257–2267 (2000).

49. Hou, H., Gan, B., Gong, Y., Chen, N. & Sun, C. P2-Type Na0.67Ni0.23Mg0.1Mn0.67O2 as a High-Performance Cathode for a Sodium-Ion Battery. *Inorganic chemistry* **55,** 9033–9037 (2016).

50. Wang, L. *et al.* Copper-substituted Na 0.67 Ni 0.3−x Cu x Mn 0.7 O 2 cathode materials for sodium-ion batteries with suppressed P2–O2 phase transition. *Journal of Materials Chemistry A* **5,** 8752–8761 (2017).

51. Wu, X. *et al.* P2-type Na 0.66 Ni 0.33–x Zn x Mn 0.67 O 2 as new high-voltage cathode materials for sodium-ion batteries. *Journal of Power Sources* **281,** 18–26 (2015).

52. Yoshida, J. *et al.* New P2 - Na 0.70 Mn 0.60 Ni 0.30 Co 0.10 O 2 Layered Oxide as Electrode Material for Na-Ion Batteries. *Journal of The Electrochemical Society* **161,** A1987–A1991 (2014).

53. Mu, L. *et al.* Water-Processable P2-Na 0.67 Ni 0.22 Cu 0.11 Mn 0.56 Ti 0.11 O 2 Cathode Material for Sodium Ion Batteries. *Journal of The Electrochemical Society* **166,** A251–A257 (2019).

54. Shin, Y. Preparation and structural properties of layer-type oxides NaxNix/2Ti1−x/2O2 (0.60≤x≤1.0). *Solid State Ionics* **132,** 131–141 (2000).

55. Matsumura, T., Sonoyama, N. & Kanno, R. Synthesis, structure and electrochemical properties of layered material, Li2/3[Mn1/3Fe2/3]O2, with mixed stacking states. *Solid State Ionics* **161,** 31–39 (2003).

56. Dose, W. M. *et al.* Structure–Electrochemical Evolution of a Mn-Rich P2 Na 2/3 Fe 0.2 Mn 0.8 O 2 Na-Ion Battery Cathode. *Chemistry of Materials* **29,** 7416–7423 (2017).

57. Han, M. H. *et al.* High-Performance P2-Phase Na 2/3 Mn 0.8 Fe 0.1 Ti 0.1 O 2 Cathode Material for Ambient-Temperature Sodium-Ion Batteries. *Chemistry of Materials* **28,** 106–116 (2016).

58. Luo, C., Langrock, A., Fan, X., Liang, Y. & Wang, C. P2-type transition metal oxides for high performance Na-ion battery cathodes. *Journal of Materials Chemistry A* **5,** 18214–18220 (2017).

59. Liu, L. *et al.* High–Performance P2–Type Na 2/3 (Mn 1/2 Fe 1/4 Co 1/4)O 2 Cathode Material with Superior Rate Capability for Na–Ion Batteries. *Advanced Energy Materials* **5** (2015).

60. Yuan, D. *et al.* Synthesis and electrochemical behaviors of layered Na0.67[Mn0.65Co0.2Ni0.15]O2 microflakes as a stable cathode material for sodium-ion batteries. *Journal of Materials Chemistry A* **1,** 3895 (2013).

61. Sun, X. *et al.* Sodium insertion cathode material Na0.67[Ni0.4Co0.2Mn0.4]O2 with excellent electrochemical properties. *Electrochimica Acta* **208,** 142–147 (2016).

62. Tsuchiya, Y. *et al.* Layered Na x Cr x Ti 1– x O 2 as Bifunctional Electrode Materials for Rechargeable Sodium Batteries. *Chemistry of Materials* **28,** 7006–7016 (2016).

63. Evstigneeva, M. A., Nalbandyan, V. B., Petrenko, A. A., Medvedev, B. S. & Kataev, A. A. A New Family of Fast Sodium Ion Conductors: Na 2 M 2 TeO 6 (M = Ni, Co, Zn, Mg). *Chemistry of Materials* **23,** 1174–1181 (2011).

64. Sehrawat, D. *et al.* Alkali Metal-Modified P2 NaxMnO2: Crystal Structure and Application in Sodium-Ion Batteries. *Inorganic chemistry* **59,** 12143–12155 (2020).

65. Yoshida, H. *et al.* P2-type Na(2/3)Ni(1/3)Mn(2/3-x)Ti(x)O2 as a new positive electrode for higher energy Na-ion batteries. *Chemical communications (Cambridge, England)* **50,** 3677–3680 (2014).

66. Rong, X. *et al.* Anionic Redox Reaction-Induced High-Capacity and Low-Strain Cathode with Suppressed Phase Transition. *Joule* **3,** 503–517 (2019).

67. Huang, Q., Lynn, J. W., Toby, B. H., Foo, M.-L. & Cava, R. J. Characterization of the structural transition in Na 0.75 CoO 2. *Journal of physics. Condensed matter : an Institute of Physics journal* **17,** 1831–1840 (2005).

68. Balsys, R. Refinement of the structure of Na0.74CoO2 using neutron powder diffraction. *Solid State Ionics* **93,** 279–282 (1997).

69. Li, Y. *et al.* Air-Stable Copper-Based P2-Na7/9Cu2/9Fe1/9Mn2/3O2 as a New Positive Electrode Material for Sodium-Ion Batteries. *Advanced science (Weinheim, Baden-Wurttemberg, Germany)* **2,** 1500031 (2015).

70. Clément, R. J. *et al.* Direct evidence for high Na + mobility and high voltage structural processes in P2-Na x [Li y Ni z Mn 1−y−z]O 2 (x, y, z ≤ 1) cathodes from solid-state NMR and DFT calculations. *Journal of Materials Chemistry A* **5,** 4129–4143 (2017).

71. Di Wu *et al.* NaTiO 2 : a layered anode material for sodium-ion batteries. *Energy & Environmental Science* **8,** 195–202 (2015).

72. Chamberland, B. L. & Porter, S. K. A study on the preparation and physical property determination of NaVO2. *Journal of Solid State Chemistry* **73,** 398–404 (1988).

73. Xia, X. & Dahn, J. R. NaCrO2 is a Fundamentally Safe Positive Electrode Material for Sodium-Ion Batteries with Liquid Electrolytes. *Electrochemical and Solid-State Letters* **15,** A1 (2012).

74. Takeda, Y., Akagi, J., Edagawa, A., Inagaki, M. & Naka, S. A preparation and polymorphic relations of sodium iron oxide (NaFeO2). *Materials Research Bulletin* **15,** 1167–1172 (1980).

75. Ringenbach, C, Kessler, H, Acad, CR. *Hatterer. A. Un Nouveau Composé Oxygéné du Molybdène NaMoO2. Propriétés Cristallographiques et Magnétiques* (1969).

76. Hobbie, K. & Hoppe, R. Zum Aufbau von NaRhO 2. *Zeitschrift für anorganische und allgemeine Chemie* **565,** 106–110 (1988).

77. Blasse, G. Sodium lanthanide oxides NaLnO2. *Journal of Inorganic and Nuclear Chemistry* **28,** 2444–2445 (1966).

78. Yoshida, H., Yabuuchi, N. & Komaba, S. NaFe0.5Co0.5O2 as high energy and power positive electrode for Na-ion batteries. *Electrochemistry Communications* **34,** 60–63 (2013).

79. Bréger, J., Kang, K., Cabana, J., Ceder, G. & Grey, C. P. NMR, PDF and RMC study of the positive electrode material Li(Ni0.5Mn0.5)O2 synthesized by ion-exchange methods. *Journal of Materials Chemistry* **17,** 3167 (2007).

80. Song, S. *et al.* Y-Doped Na 2 ZrO 3 : A Na-Rich Layered Oxide as a High-Capacity Cathode Material for Sodium-Ion Batteries. *ACS Sustainable Chemistry & Engineering* **5,** 4785–4792 (2017).

81. Mogare, K. M., Friese, K., Klein, W. & Jansen, M. Syntheses and Crystal Structures of Two Sodium Ruthenates: Na 2 RuO 4 and Na 2 RuO 3. *Zeitschrift für anorganische und allgemeine Chemie* **630,** 547–552 (2004).

82. Panin, R. V. *et al.* Synthesis and crystal structure of the palladium oxides NaPd3O4, Na2PdO3 and K3Pd2O4. *Journal of Solid State Chemistry* **180,** 1566–1574 (2007).

83. Perez, A. J. *et al.* Strong Oxygen Participation in the Redox Governing the Structural and Electrochemical Properties of Na-Rich Layered Oxide Na 2 IrO 3. *Chemistry of Materials* **28,** 8278–8288 (2016).

84. McDaniel, C. L. Phase relations in the systems Na2OIrO2 and Na2OPtO2 in air. *Journal of Solid State Chemistry* **9,** 139–146 (1974).

85. Liu, S. *et al.* Na2Ru0.8Mn0.2O3: A novel cathode material for ultrafast sodium ion battery with large capacity and superlong cycle life. *Journal of Power Sources* **421,** 14–22 (2019).

86. Rozier, P. *et al.* Anionic redox chemistry in Na-rich Na 2 Ru 1−y Sn y O 3 positive electrode material for Na-ion batteries. *Electrochemistry Communications* **53,** 29–32 (2015).

87. Su, N., Lyu, Y. & Guo, B. Electrochemical and in-situ X-ray diffraction studies of Na1.2Ni0.2Mn0.2Ru0.4O2 as a cathode material for sodium-ion batteries. *Electrochemistry Communications* **87,** 71–75 (2018).

88. Regan, K. A., Huang, Q. & Cava, R. J. Isolated spin 3/2 plaquettes in Na3RuO4. *Journal of Solid State Chemistry* **178,** 2104–2108 (2005).

89. Qiao, Y. *et al.* Reversible anionic redox activity in Na 3 RuO 4 cathodes: a prototype Na-rich layered oxide. *Energy & Environmental Science* **11,** 299–305 (2018).

90. Wang, C. *et al.* The top-down synthesis of sequentially controlled architectures for honeycomb-layered Na 3 Ni 2 BiO 6 towards high-voltage and superior performance cathodes for sodium-ion batteries. *Journal of Materials Chemistry A* **7,** 1797–1809 (2019).

91. Ma, J. *et al.* Ordered and Disordered Polymorphs of Na(Ni 2/3 Sb 1/3)O 2 : Honeycomb-Ordered Cathodes for Na-Ion Batteries. *Chemistry of Materials* **27,** 2387–2399 (2015).

92. Li, Q. *et al.* A Superlattice-Stabilized Layered Oxide Cathode for Sodium-Ion Batteries. *Advanced materials (Deerfield Beach, Fla.)* **32,** e1907936 (2020).

93. Smirnova, O. A., Nalbandyan, V. B., Petrenko, A. A. & Avdeev, M. Subsolidus phase relations in Na2O–CuO–Sb2On system and crystal structure of new sodium copper antimonate Na3Cu2SbO6. *Journal of Solid State Chemistry* **178,** 1165–1170 (2005).

94. Cao, M.-H. *et al.* Suppressing the chromium disproportionation reaction in O3-type layered cathode materials for high capacity sodium-ion batteries. *Journal of Materials Chemistry A* **5,** 5442–5448 (2017).

95. Kim, D. *et al.* Layered Na[Ni1/3Fe1/3Mn1/3]O2 cathodes for Na-ion battery application. *Electrochemistry Communications* **18,** 66–69 (2012).

96. Sathiya, M., Hemalatha, K., Ramesha, K., Tarascon, J.-M. & Prakash, A. S. Synthesis, Structure, and Electrochemical Properties of the Layered Sodium Insertion Cathode Material: NaNi 1 / 3 Mn 1 / 3 Co 1 / 3 O 2. *Chemistry of Materials* **24,** 1846–1853 (2012).

97. Xu, H. *et al.* Synthesis and evaluation of NaNi0.5Co0.2Mn0.3O2 as a cathode material for Na-ion battery. *Ceramics International* **42,** 12521–12524 (2016).

98. Li, X. *et al.* O3-type Na(Mn0.25Fe0.25Co0.25Ni0.25)O2: A quaternary layered cathode compound for rechargeable Na ion batteries. *Electrochemistry Communications* **49,** 51–54 (2014).

99. Hwang, J.-Y., Myung, S.-T. & Sun, Y.-K. Quaternary Transition Metal Oxide Layered Framework: O3-Type Na[Ni 0.32 Fe 0.13 Co 0.15 Mn 0.40]O 2 Cathode Material for High-Performance Sodium-Ion Batteries. *The Journal of Physical Chemistry C* **122,** 13500–13507 (2018).

100. Sun, X. *et al.* Na[Ni 0.4 Fe 0.2 Mn 0.4−x Ti x]O 2 : a cathode of high capacity and superior cyclability for Na-ion batteries. *Journal of Materials Chemistry A* **2,** 17268–17271 (2014).

101. Yue, J.-L. *et al.* A quinary layer transition metal oxide of NaNi1/4Co1/4Fe1/4Mn1/8Ti1/8O2 as a high-rate-capability and long-cycle-life cathode material for rechargeable sodium ion batteries. *Chemical communications (Cambridge, England)* **51,** 15712–15715 (2015).

102. Yue, J.-L. *et al.* O3-type layered transition metal oxide Na(NiCoFeTi) 1/4 O 2 as a high rate and long cycle life cathode material for sodium ion batteries. *Journal of Materials Chemistry A* **3,** 23261–23267 (2015).

103. Zhang, S. *et al.* O3-type NaNi0·33Li0·11Ti0·56O2-based electrode for symmetric sodium ion cell. *Journal of Power Sources* **329,** 1–7 (2016).

104. Perez, A. J., Rousse, G. & Tarascon, J.-M. Structural Instability Driven by Li/Na Competition in Na(Li1/3Ir2/3)O2 Cathode Material for Li-Ion and Na-Ion Batteries. *Inorganic chemistry* **58,** 15644–15651 (2019).

105. Zhang, X. *et al.* Manganese-Based Na-Rich Materials Boost Anionic Redox in High-Performance Layered Cathodes for Sodium-Ion Batteries. *Advanced materials (Deerfield Beach, Fla.)* **31,** e1807770 (2019).

106. Yu, H., Guo, S., Zhu, Y., Ishida, M. & Zhou, H. Novel titanium-based O3-type NaTi(0.5)Ni(0.5)O2 as a cathode material for sodium ion batteries. *Chemical communications (Cambridge, England)* **50,** 457–459 (2014).

107. Wang, J. *et al.* O3-type Na[Fe 1/3 Ni 1/3 Ti 1/3]O 2 cathode material for rechargeable sodium ion batteries. *Journal of Materials Chemistry A* **4,** 3431–3437 (2016).

108. Wang, P.-F. *et al.* Ti-Substituted NaNi0.5 Mn0.5-x Tix O2 Cathodes with Reversible O3-P3 Phase Transition for High-Performance Sodium-Ion Batteries. *Advanced materials (Deerfield Beach, Fla.)* **29** (2017).

109. Yao, H.-R. *et al.* Designing Air-Stable O3-Type Cathode Materials by Combined Structure Modulation for Na-Ion Batteries. *Journal of the American Chemical Society* **139,** 8440–8443 (2017).

110. Mu, L. *et al.* Prototype Sodium-Ion Batteries Using an Air-Stable and Co/Ni-Free O3-Layered Metal Oxide Cathode. *Advanced materials (Deerfield Beach, Fla.)* **27,** 6928–6933 (2015).

111. Li, X. *et al.* Na0.9Ni0.45Ti0.55O2 as novel bipolar material for sodium ion batteries. *Solid State Ionics* **334,** 14–20 (2019).

112. Qi, X. *et al.* Sodium–Deficient O3–Na 0.9 [Ni 0.4 Mn x Ti 0.6− x]O 2 Layered–Oxide Cathode Materials for Sodium–Ion Batteries. *Particle & Particle Systems Characterization* **33,** 538–544 (2016).

113. Jiang, X., Hu, F. & Zhang, J. Sodium-deficient O3–Na 0.9 Mn 0.4 Fe 0.5 Ti 0.1 O 2 as a cathode material for sodium-ion batteries. *RSC Advances* **6,** 103238–103241 (2016).

114. Varela, A., Parras, M. & González–Calbet, J. M. Influence of Na Content on the Chemical Stability of Nanometric Layered Na x RhO 2 (0.7 ≤ x ≤ 1.0). *European Journal of Inorganic Chemistry* **2005,** 4410–4416 (2005).

115. Cao, M.-H., Shadike, Z., Zhou, Y.-N. & Fu, Z.-W. Sodium-deficient O3-type Na0.83Cr1/3Fe1/3Mn1/6Ti1/6O2 as a new cathode material for Na-ion batteries. *Electrochimica Acta* **295,** 918–925 (2019).

116. Guo, S. *et al.* High-performance symmetric sodium-ion batteries using a new, bipolar O3-type material, Na 0.8 Ni 0.4 Ti 0.6 O 2. *Energy & Environmental Science* **8,** 1237–1244 (2015).

117. Guo, H. *et al.* Na-deficient O3-type cathode material Na0.8[Ni0.3Co0.2Ti0.5]O2 for room-temperature sodium-ion batteries. *Electrochimica Acta* **158,** 258–263 (2015).

118. Thorne, J. S., Dunlap, R. A. & Obrovac, M. N. Structure and Electrochemistry of Na x Fe x Mn 1-x O 2 (1.0 ≤ x ≤ 0.5) for Na-Ion Battery Positive Electrodes. *Journal of The Electrochemical Society* **160,** A361–A367 (2013).

119. Smirnova, O., Rocha, J., Nalbandyan, V., Kharton, V. & Marques, F. Crystal structure, local sodium environments and ion dynamics in Na0.8Ni0.6Sb0.4O2, a new mixed antimonate. *Solid State Ionics* **178,** 1360–1365 (2007).

120. Wang, P.-F. *et al.* An Abnormal 3.7 Volt O3-Type Sodium-Ion Battery Cathode. *Angewandte Chemie (International ed. in English)* **57,** 8178–8183 (2018).

121. Zhao, C., Avdeev, M., Chen, L. & Hu, Y.-S. An O3-type Oxide with Low Sodium Content as the Phase-Transition-Free Anode for Sodium-Ion Batteries. *Angewandte Chemie (International ed. in English)* **57,** 7056–7060 (2018).

122. Wang, P.-F., Yao, H.-R., Zuo, T.-T., Yin, Y.-X. & Guo, Y.-G. Novel P2-type Na2/3Ni1/6Mg1/6Ti2/3O2 as an anode material for sodium-ion batteries. *Chemical communications (Cambridge, England)* **53,** 1957–1960 (2017).

4

PHASE TRANSITION DYNAMICS:

COMPUTATIONAL STUDIES ON O2-P2 PHASE-TRANSITION DYNAMICS IN LAYERED-OXIDE SODIUM-ION CATHODE MATERIALS

Sodium-ion batteries have gained much interest over the past years and especially layered oxides are highly considered as cathodes for the next generation of batteries. However, there are still significant challenges to overcome in these materials for practical applications mainly related to capacity degradation and voltage fading. A key influence factor for these challenges are phase transitions that occur by gliding of layers during operation of these materials. Until now there is limited atomistic-level understanding on such transitions as simulations of these processes are computationally demanding. In this work, a classical pairwise Coulomb-Buckingham potential is trained versus extensive *ab initio* data using a genetic algorithm to study O2-P2 phase transitions in Na_xCoO_2. The density functional theory (DFT) and classical potential calculations show that phase transition barriers decrease upon desodiation and are further lowered if dynamic conditions are considered through molecular dynamics simulations. The developed classical potential is able to capture phase transitions and its related increase in the Na-ion diffusivity under standard lab conditions at the μs timescale of molecular dynamics simulation. Furthermore, it is found that the phase transition occurs gradually *via* various OP*n* phases.

This chapter is *under review* as: **Köster, K.** & Kaghazchi, P. Computational Studies on O2-P2 Phase-Transition Dynamics in Layered-Oxide Sodium-Ion Cathode Materials. Phys. Rev. B (2025). If accepted for publication the copyright will be by the American Physical Society.

4.1 Introduction

Layered oxide cathode active materials are among the most promising for sodium-ion batteries (SIBs) as they are already successfully applied in the widely commercialized lithium-ion batteries (LIBs). While LIBs are superior over SIBs in terms of total capacity and capacity retention, SIBs can offer several advantages over LIBs when ecological and economical/strategic perspectives are considered. The high, widely-distributed abundance of Na compared to Li can yield strategic as well as cost benefits while in addition often less critical metals are required in SIBs compared to LIBs. Despite these considerable advantages of SIBs over LIBs their wide application is still hindered by there inferior electrochemical performance. Key challenges in improving the performance of SIBs are often connected to the much larger ionic radius of sodium compared to lithium which causes more drastic changes in the host materials upon (de-)intercalation during (dis-)charging. More precisely, for the aforementioned layered oxide cathode materials often phase transitions are observed during operation [1–5]. The phases can be classified by the sodium-ion coordination-environment such as octahedral (O) and and prismatic (P) and the stacking periodicity of the layers along the *c*-direction [6] while the most commonly observed phases are P2 (intermediate sodium concentration) and O3 (high sodium concentration). However, during operation of the cathode material the varying sodium concentration often yields to (ir-)reversible phase transitions. The most important transitions are P2 to O2 and O3 to P3 transitions while also transitions to mixed stackings such as OP2 or OP4 are observed [4, 5].

Whilst there is a common understanding that these transitions are caused by gliding of transition-metal oxygen slabs, there are little mechanistic insights until now as this requires atomistic-level simulations [4, 5]. Such simulations are limited by the model size and simulation time which can render it difficult to observe any phase transitions. Recent studies leveraged machine learned force-field aided *ab initio* molecular dynamics (MD) simulations at elevated temperatures and observed gliding of layers [7] or employed nudged elastic band (NEB) calculations to estimate the phase-transition barrier [8]. However, detailed insights about the sodium-concentration dependency on the transition barrier and the transition mechanism at dynamic conditions are still missing due to the associated computational costs. Even though machine learning potentials gained significant interest over the past years and allow for significant speed-ups over quantum-mechanic calculations while often maintain reasonable accuracy, most machine learning potentials are still significantly slower than simple classical potentials [9–13]. It must be mentioned that in spite of the faster simulations using classical potentials often a lower accuracy than in machine learning potentials is achieved and classical potentials are less transferable and require notorious fitting for new materials. Nevertheless, a few attempts have so far been made to describe (layered) oxide cathode materials with the help of classical potentials [14–18]. More recently, also some works focused on classical pairwise potentials to investigate sodium layered oxide cathodes [19–21]. Despite several challenges these classical potentials offer the opportunity to study cathode materials at atomistic level and at timescales and system sizes that cannot be achieved yet by other methods. To the best of our knowledge, such classical potentials have not been applied to study phase transitions in layered oxide sodium-cathodes yet but bear the potential for more direct atomistic insights under more realistic time and tempera-

ture conditions.

In this work, a classical pairwise potential is developed and applied to simulate and understand the O2-P2 phase transition in the prototype sodium-ion cathode-material Na_xCoO_2. The Co-based layered oxide is among the most studied simple cathode materials with many literature reports available and is therefore a suitable material for this study [22–26]. Moreover, Na_xCoO_2 has less additional complexities as it is not Jahn-Teller active and charges are usually just delocalized over all Co ions (according to higher level *ab initio* calculations [27]). While the material is reported in the P2, O3, and P3 phase, also phase transitions during desodiation are reported [22, 28] making it a suitable candidate to study phase transitions. Even though no full O2 phase (just irregular OP phase at high states of charge [28]) was proposed for this material yet it still seems reasonable to study the O2-P2 transition as the mechanisms should be similar to other O*n*-P*n* transitions and the O2-P2 case is the most simple to starting point with just one layer that is gliding [8]. Moreover, the O2-P2 phase transition is of great relevance to layered sodium-ion cathode-materials in general [5, 29]. To that extend, this study can be seen as a basis to study more complex materials and phase transitions while focusing here on the most simple cases to outline fundamentals of phase transitions in layered oxides and possible methodologies how these could be studied.

It is begun with a detailed methodology section describing the fitting procedure of a Coulomb-Buckingham potential for the O2-P2 Na_xCoO_2 system. It is continued by performing static calculations using density functional theory (DFT) and by employing the fitted potential to learn about how the phase-transition barrier changes with sodium concentration. Next, the fitted potential is applied in classical MD simulations to gain mechanistic insights and to obtain the activation energy for phase transitions under dynamic conditions. Finally, it is shown that with the help of classical potentials it is possible to observe phase transition under standard lab conditions at the time scale of µs. Moreover, it is also shown that the fitted potential is capable to reproduce sodium-diffusion properties and captures the different sodium conductivity of O- and P-phases well. The simplified workflow followed in this work is sketched in Figure 4.1.

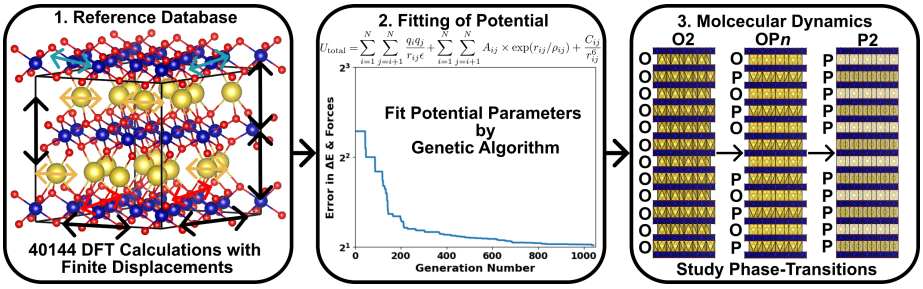

Figure 4.1: Schematic procedure of database creation, potential fitting, and application in molecular dynamics (MD) for the Na_xCoO_2 cathode material performed in this work. First, more than 40000 structures with finite displacements of lattice parameters and ion positions (indicated by arrows in the figure) were evaluated by density function theory (DFT) calculations. Second, a Coulomb-Buckingham potential was fitted to energy differences and forces of the reference database leveraging a Genetic Algorithm (GA). Finally, the obtained potential was applied in large-scale classical MD simulations in the µs regime to study phase transitions.

4.2 Computational Methods

The general computational methodology employed in work is outlined in Figure 4.1 consisting of three steps: creation of an *ab initio* reference dataset, fitting of the Coulomb-Buckinghma potential, and performing MD simulations. While the first two steps are discussed in some more detail in the following subsections of this section, MD simulations are analysed and discussed in the next section (Results and Discussion).

4.2.1 The employed Potential

The proposed potential follows a conventional Coulomb-Buckingham potential approach for all pairwise interactions in the Na_xCoO_2 cathode material. The potential is thus given by:

$$U_{\text{total}} = U_{\text{Coulomb}} + U_{\text{Buckingham}}. \tag{4.1}$$

The two different contributions can be further specified by:

$$U_{\text{Coulomb}} = \sum_{i=1}^{N} \sum_{j=i+1}^{N} \frac{q_i q_j}{r_{ij}\epsilon} \tag{4.2}$$

where the sums ensure to consider all pairwise interactions of the N ions in the system with q_i and q_j being the ionic charges of the corresponding ions, r_{ij} is their euclidean distance and ϵ is the dielectric constant of the material. For the ionic charges, always the bare formal charge (no effective charge) was applied and ϵ was fitted as a free parameter. Fixed charges of 1+ for Na and 2− for O were assumed and a variable charge between 3+ and 4+ for Co to charge-balance the total structures at all sodium concentrations. To account for the long-range character of electrostatic interactions and the periodic boundary conditions Ewald summation [30] is applied to solve the Coulomb potential contribution. As Coulomb interactions missing the Born repulsion at very short distances, Buckingham potentials are employed that have the following form [31]:

$$U_{\text{Buckingham}} = \sum_{i=1}^{N} \sum_{j=i+1}^{N} A_{ij} \times \exp(-r_{ij}/\rho_{ij}) - \frac{C_{ij}}{r_{ij}^6}. \tag{4.3}$$

In the Buckingham potential again r_{ij} denotes the euclidean distance of the two ions i and j that are currently considered in the double-sum over all pairwise interactions. A_{ij}, ρ_{ij}, and C_{ij} are free parameters that need to be fitted for all pairs of different ionic species in the system. In this work, parameters are fitted explicitly for each pair of different species and no interpolation is applied.

4.2.2 Creation of Reference Dataset

Considering the described Coulomb-Buckingham potential approach, reference data for fitting the potential parameters in the Na_xCoO_2 layered oxide cathode-system is required. To capture the most important features of the material, namely different sodium concentration, sodium orderings, sodium diffusion, phase transitions, and lattice parameter changes a broad variety of reference structures is required. Hence, structures in O2, P2, and OP2 stacking phases were modelled. Moreover, five equidistant intermediate

structures between O2 and P2 were modelled (e.g., different shifts of the two transition-metal layers towards each other) to account for dynamic phase transitions.

The structures were represented by $2\sqrt{3} \times 2\sqrt{3} \times 1$-supercells containing 24 formula units of Na_xCoO_2. For all of these eight phases different sodium concentrations of x = 1.00, 0.83, 0.67, 0.50, 0.33, 0.17, and, 0.00 in Na_xCoO_2 were included in the reference dataset. To account for different sodium orderings up to ten (e.g., there are no sodium orderings in x=0.00) local minimum sodium orderings were considered for each material. The different sodium arrangements were determined by optimizing the electrostatic energies with help of the gradient decent algorithm implemented in the GOAC (Global Optimization of Atomistic Configurations by Coulomb) code [32] while only local minima orderings that differ by at least 0.1 eV in electrostatic energy were chosen. This procedure resulted in a total of 386 reference structures in the Na_xCoO_2 layered oxide cathode-system. Finally, the reference dataset was created by generating randomly distorted samples for all of the 386 structures. In order to do so, 10 % (25 % for strong distortions) of the ions were selected and displaced randomly by up to 0.25 Å. To capture sodium migration and the sodium diffusivity, 20 % (75 % for strong distortions) of the sodium ions were selected randomly and displaced by up to 0.5 Å(0.75 Åfor strong distortions) with a two times (4.5 times for strong distortions) higher magnitude for displacements along the *a*- and *b*-direction than along the *c*-direction. Moreover, the lattice parameters were distorted randomly as well in the sample structures by ±2 % (±5 % for strong distortions) in the *a*- and *b*-direction. Along the *c*-direction inter- (O-Na-O) and intra-layer (O-Co-O) separations were varied for all layers each by up to ±3 % (±7.5 % for strong distortions). These inter- and intra-layer distortions were employed as they are expected to undergo the most pronounced changes during phase transitions and desodiation. For the strong distortions also lattice angles were varied by ±2.5 %. For the initial structures the distortions were applied to, DFT optimized lattice parameters of a=b=4.875 Å, $d_{\text{O-Co-O}}$=1.95 Å, and $d_{\text{O-Na-O}}$=3.45 Å long with perfectly symmetric ion positions were considered. These lattice parameters were calculated as the average values of O2 and P2 stackings at x = 0.50 as obtained from DFT optimizations. To create the reference dataset for fitting the potential parameters 104 (52 with normal and 52 with strong distortions) randomly distorted samples were created for each of the 386 structures resulting in a total of 40144 reference calculations. The methodology of these distortions of ionic positions and lattice parameters is also indicated by the arrows in the first step shown in Figure 4.1. All sample structures were evaluated by spin-polarized DFT single-point calculations employing the projector-augmented wave (PAW) method [33] as implemented in the Vienna *ab initio* simulation package (VASP) [34]. The Perdew-Burke-Ernzerhof (PBE) exchange-correlation functional [35] was applied along with an energy-cutoff of 600 eV and an electronic convergence criterion of 10^{-6} eV. The Γ-Point and standard pseudo potentials were employed. In addition, the D2 dispersion correction [36] was applied to capture the long-range layer-layer interactions more precisely and as a similar term appears in the Buckingham potential.

4.2.3 Error Metric

Using the reference dataset (cf. Figure 4.1, first step), the Coulomb-Buckingham potential parameters were fitted by minimizing the root-mean-square error (RMSE) between

DFT-computed energy differences (for sample structures at a specific sodium concentration) and each element of the force matrix. Energy differences between samples at different sodium concentrations were excluded as the described potential does not include any term that could account for the ionization energy required to oxidize cobalt. Thus, the scope of the potential is to accurately describe the dynamics, e.g., sodium diffusion and phase transitions, at a given sodium concentration. For the RMSE calculation, the RMSE in forces was weighted ten times more as the elements in the force matrix are usually smaller than energy differences and forces are also rather important to obtain correct dynamics when applying the fitted potential. In total, the error metric that was minimized during fitting the potential parameters can be described by:

$$\begin{aligned}\text{Error} \quad = \quad & \sum_{x\in X} \frac{S_x}{S} \times \\ & \sigma \times \sqrt{\frac{\sum_{s=1}^{S_x}\sum_{i=1}^{N_x}\sum_{d=1}^{3}(f_{xsid} - f_{xsid}^{\text{DFT}})^2}{S_x \times N_x \times 3}} + \\ & \sqrt{\frac{\sum_{s_1=1}^{S_x}\sum_{s_2=s_1+1}^{S_x}(\Delta E_{xs_1s_2} - \Delta E_{xs_1s_2}^{DFT})^2}{\sum_{s_1=1}^{S_x}\sum_{s_2=s_1+1}^{S_x} N_x}}.\end{aligned}$$

In this Equation, x denotes the sodium concentration and the following sodium concentrations were included: $x = \{0.00, 0.17, 0.33, 0.50, 0.67, 0.83, 1.00\}$. S is the total number of samples (40144) and S_x is the number of samples at a given sodium concentration x. The first squared term describes the RMSE of the force matrix f relative to the DFT reference force matrix f^{DFT} weighted by a factor $\sigma = 10$. For the given sodium concentration x, all samples s, all ions i, and all three dimensions d are considered in the RMSE of the forces. The second squared term accounts for the RMSE in energy differences between the samples s_1 and s_2 at the given sodium concentration x. The RMSE is normalized to per ion energies by dividing by the total number of ions in the system (N_x). The exact formulation of the error metric is somewhat arbitrary but proved to be efficient in fitting the potential parameters.

4.2.4 Fitting of Potential Parameters

With the potential form, the *ab initio* reference dataset, and the error metric described in the previous subsections, fitting of the potential parameters can be attempted (second step in Figure 4.1). As mentioned before, classic ionic charges (q) and no effective charges that would require fitting were considered. Still, this approach yields 19 ($1+3\times6$) potential parameters, e.g., ϵ and 3 Buckingham parameters for 6 pairs (Na-Na, Na-Co, Na-O, Co-Co, Co-O, O-O). Moreover, a different set of parameters is required for each sodium concentration in Na_xCoO_2. Thus, fitting the potentials for all of the 7 considered sodium concentrations included in the reference dataset would require fitting of 133 (7×19) parameters. However, as only q_{Co} is changing with different sodium concentrations, e.g., Co is oxidized and reduced between Co^{3+} and Co^{4+}, it seems justified to assume that Buckingham parameters for pairs that do not include Co are the same

among all sodium concentrations. This greatly reduces the number of potential parameters for Na_xCoO_2 from 133 to a total of 79 parameters. However, this assumption also requires a coupled fitting of all sodium concentrations at the same time as certain optimized parameters must be the same for all sodium concentrations. It was attempted to fit this potential by global optimization using the genetic algorithm (differential evolution) as implemented in the scipy package[37, 38]. A population size of 512 samples (256 samples for 23 and 21 parameter models) was used along with "sobol" initialization. For mutations dithering was employed in the range of 0.25 to 1.5 along with a recombination constant of 0.6. The best sample of the population was optimized by the L-BFGS (limited memory Broyden–Fletcher–Goldfarb–Shanno) algorithm [39] after each iteration. The following boundaries for Buckingham parameters of A, ρ, C, and ϵ were applied: [100, 30000], [0.1, 0.5], [0, 1000], and [1, 10], respectively. The Buckingham cut-off was set to 15 Åwhile electrostatics part was solved exactly by Ewald summation. Convergence of the fitting involving 79 parameters can be seen in Figure 4.2 (a).

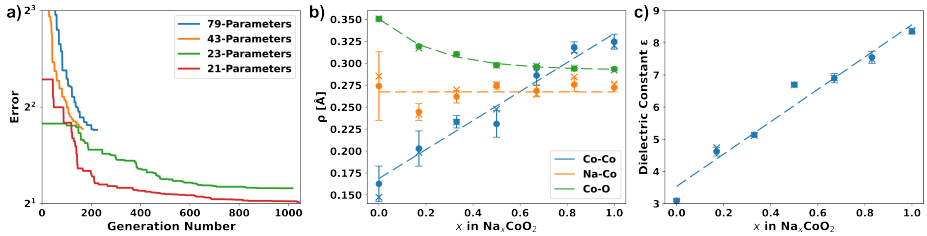

Figure 4.2: Fitting plots of the process of obtaining the potential parameters. a) Convergence plots of Genetic Algorithm for fitting different potential models with decreasing numbers of parameters. b) Dependence of ρ in interactions with Co on sodium concentration as obtained from the potential model with 43 parameters. Crosses indicate the parameter value of the best fit, circles the mean value of the first 1000 best optimized parameter sets and error bars their standard deviation. Fitted functions that were considered in further potential models are shown by dashed lines. c) Dependence of ϵ on sodium-concentration as obtained from the potential model with 43 parameters. Symbols, error bars and lines correspond to same quantities as in plot b).

As 79 parameters describing the Na_xCoO_2 system are still quite inconvenient, it was tested if it is possible to fit a potential assuming that also the C Buckingham-parameters for pairs including Co are the same for all sodium concentrations. This assumption might be justified by the fact that also in the D2 dispersion correction the term C/r^6 is used while C is independent of the chemical environment, e.g., the ionic charge [36]. Fixing the A parameters for pairs including Co as well does not significantly reduce the degrees of freedom in the fit as this fix can be mostly compensated by adjusting the ρ parameters. Ultimately, these assumptions result in a potential with 43 parameters and convergence of the error metric for fitting this model is shown in Figure 4.2 (a) as well. Even though both fittings, the one of the 79 parameter model and the one of the 43 parameter model, were stopped early, their similar convergence behaviour shown in Figure 4.2 (a) indicates that the model with 43 parameters still has enough degrees of freedom to capture the characteristics of the Na_xCoO_2 system.

It was further tried to reduce the parameters of the Na_xCoO_2 potential by analysing the variation of the remaining sodium concentration dependent parameters ($\rho_{\text{Co-Co}}$, $\rho_{\text{Na-Co}}$, $\rho_{\text{Co-O}}$, ϵ) as function of sodium concentration x. The ρ parameters for all pairs

involving Co are plotted in Figure 4.2 (b) and indicate that $\rho_{\text{Na-Co}}$ is sufficiently described by a fixed value over the whole sodium range reducing the 7 parameters for each sodium concentration to just 1. Moreover, $\rho_{\text{Co-Co}}$ has the strongest dependency on sodium concentration while its change is well described by a simple linear function of the form $f(x) = ax + b$. Thus, the 7 parameters per sodium concentration can be reduced to two parameters that describe the linear function, namely a and b. Lastly, $\rho_{\text{Co-O}}$ shows a small change on varying the sodium concentration that is apparently well described by an exponential decay of the general form $f(x) = a\exp(bx) + c$, transforming the 7 fitted parameters per sodium concentration to the 3 parameters of the function: a, b, c. Finally, the fitted dielectric constants undergo strong changes at different sodium concentrations which are visualized in Figure 4.2 (c). The trend of ϵ and sodium concentration x is almost perfectly linear indicting that the 7 ϵ for each sodium concentration in the fitting can be replaced by just 2 parameters that describe the linear function, similar to $\rho_{\text{Co-Co}}$. The approach of fitting functions instead of parameters for each sodium concentration bears two substantial advantages: I) The total number of parameters in fitting is reduced which speed-ups convergence and II) the resulting potential is more generalized as the functions allow to interpolate to intermediate sodium concentrations that were not considered in the reference dataset used for the fitting.

Table 4.1: Coulomb-Buckingham potential for Na_xCoO_2 fitted and employed in this work.

Pair	A	ρ	C
Na-Na	101.02	0.33982	0.31577
Na-Co	701.536	0.32767	6.6555
Na-O	6276.7	0.22321	40.010
Co-Co	8582.7	$0.019341x$+0.27366	403.57
Co-O	11474	0.19886	41.395
O-O	4144.2	0.23746	4.1772
Charge	Na	Co	O
q	+1	$+4-x$	−2
	ϵ=1.0379x+8.1337		

Considering these functions and fixes for the parameters the total number of parameters in the potential fitting reduces further from the aforementioned 43 parameters to 23 parameters and the corresponding convergence curve is shown in Figure 4.2 (a). The pronounced and fast convergence towards errors significantly lower than the models with more parameters prove that the assumptions made for the parameter functions do not decrease the flexibility of the potential too much and still allow for a reasonable fitting of the potential. Ultimately, the exponential function assumed for $\rho_{\text{Co-O}}$ became very flat during fitting indicating that $\rho_{\text{Co-O}}$ might be considered a fixed parameter over the whole sodium range as well, reducing the total amount of parameters of the potential to just 21. Indeed, the convergence plot in Figure 4.2 (a) highlights that also with a fixed value of $\rho_{\text{Co-O}}$ a potential with a low error can be fitted, even significantly lower than for the model with 23 parameters. This might be explained by the fact that an exponential function is more difficult to fit and very sensitive to small parameter changes.

The fitting without the exponential function for $\rho_{\text{Co-O}}$ shows therefore a better convergence behaviour and an overall lower error metric for the final potential. The resulting Coulomb-Buckingham-Potential parameters which have been applied in this work are listed in Table 4.1. Notably, also the change of $\rho_{\text{Co-Co}}$ with the sodium-concentration is small, indicating the possibility of fitting Coulomb-Buckingham potentials for different sodium concentrations of layered oxides by just varying the charges of the transition metals as well the dielectric constant in a linear fashion. However, in this work also a linear function is used for $\rho_{\text{Co-Co}}$ as the resulting potential appears to be well-fitted (cf. Fig. 4.2 (a)) and sufficiently simplified. The fitted average (over sodium concentration) effective dielectric constant of approx. 8.65 is in very good agreement to previously reported first principles studies [40] that suggest an average (over structure models and lattice directions) dielectric constant of 8.86 while other computational studies [41] also reported lower values of 5.66 (for octahedral sodium coordination).

Table 4.2: Coulomb-Buckingham potential with a Buckingham potential for Na-O obtained from fitting a Coulomb-Buckingham potential to Na_2O. The described potential is also applied to Na_xCoO_2 in this work.

Pair	A	ρ	C
Na-O	2566.3	0.27302	67.186
Charge	Na	Co	O
q	+1	$+4-x$	-2
		ϵ= 2.2733	

To determine which pairwise interactions are most important and to understand how much complexity of a potential is actually required to study phase transitions in layered oxides another Coulomb-Buckingham potential was fitted to 100 distorted structures of Na_2O. While a full potential with parameters for all pairs (Na-Na, Na-O, and O-O) was fitted, only the Buckingham potential for the Na-O interaction was considered in the tests and the resulting total potential is described in Table 4.2. Again, the fitted dielectric constant of 2.27 is in comparable order of magnitude to previously reported calculations that determined a value of 3.27 [41]. This potential can be seen as the most simplistic potential that allows to study phase-transition barriers by only adding one Buckingham potential to bare electrostatic interactions and by assuming that Na-O interactions are mostly independent on structure-type and coordination. Thus, the potential has also no dependencies on the sodium concentration in Na_xCoO_2.

4.2.5 Calculation of Phase-Transition Barriers

Calculation of static phase-transition barriers was achieved by starting with an O2 structure and shifting one CoO_2 layer as a whole by $a/3$ along the a-axis which leads a P2 structure. A total of 21 equidistant images along this reaction path were considered in $2\sqrt{3} \times 2\sqrt{3} \times 1$-supercells containing 24 formula units of Na_xCoO_2. At each image, sodium-ordering was determined over both sodium sub-lattices of the P2 structure while one sub-lattice coincides with the one of O2 which was fixed and the other was shifted proportional to the reaction coordinate. Sodium orderings were optimized by configurational optimization of the total Coulomb energy assuming the charges de-

scribed in Table 4.1. Replica Exchange Monte Carlo (REMC) as implemented in the GOAC package [32] with parallel tempering at 0.1, 0.2, 0.3, 0.4, 0.6, 0.8, 1.0, and 1.2 eV was leveraged for the configurational optimization. Obtained lowest energy configurations for each image were than evaluated by DFT with the same settings described before, the Coulomb-Buckingham potential, and the potential considering just the Na-O Buckingham interaction and electrostatics. For comparison, the lattices of the cells (just cell volume) at each image were relaxed by DFT with an convergence criterion of a 10^{-5} eV change in total energy. Furthermore, the lattices were also relaxed by the fitted Coulomb-Buckingham potential with help of the LAMMPS software package [42, 43]. A Buckingham cutoff of 15 Åalong with Ewald summation for electrostatic interactions were applied. The fractional volume change was limited to 10^{-3} for each iteration of the FIRE algorithm [44].

4.2.6 Molecular Dynamics Simulations

For the MD simulations $4\sqrt{3} \times 4\sqrt{3} \times 6$-supercells of $Na_{0.67}CoO_2$ with 576 formula units (2112 atoms) were created. Simulations were carried out in the LAMMPS software package [42, 43] as well with the same settings described for the minimizations in the subsection before. For each simulation the structure was first fully minimized (lattice and ionic positions), followed by an MD relaxation of 30 ps during which the temperature was linearly increased from 0 K to the target temperature. The relaxations were performed in the *NpT* ensemble with an isotropic pressure of 1 bar. Both, temperature and pressure were controlled by a Nose-Hover-thermostat (barostat) [45, 46] with damping parameters of 0.1 ps for the temperature and 1 ps for the pressure. LAMMPS applies the equations of motions as described by Shinoda *et al.* [47] along with the time integration schemes described by Tuckerman *et al.* [48] while a time step of 2 fs was used in this work. After the relaxation runs MD production runs were carried out at the fixed target temperature and a pressure of 1 bar in the *NpT* ensemble and by the same settings described for the relaxation runs. Snapshots of the simulation were written every 1 ps and structures shown in this work were visualized with help of the VESTA software [49].

4.3 Results and Discussion

4.3.1 Calculation of Phase-Transition Barriers by Static Simulations

First, the O2-P2 phase-transition reaction-path of Na_xCoO_2 is studied in static cells and an exemplary energy transition-pathway is shown in Figure 4.3 (a) for the O2-P2 transition in $Na_{0.67}CoO_2$ evaluated by DFT single-point calculations. The resulting reaction pathway shows the expected thermodynamic stabilities between the O2 and P2 phase with the P2 phase being almost 1.5 eV more stable. This matches experimental studies that also report the P2 phase to be stable at intermediate sodium concentrations such as 0.67 [28, 50]. However, the reaction path also reveals a barrier for the transition of the O2 to P2 phase while the pure O2 phase is a local minimum that is kinetically stabilized through the aforementioned barrier. Thus, the reaction path allows to determine the transition barrier (ΔE) between the two (local) minima in both directions (O2 to P2 and P2 to O2) as indicated by the blue and red lines in Figure 4.3 (a). The corresponding phase transition barriers are in the following referred to as $\Delta E_{O2\rightarrow P2}$ and $\Delta E_{P2\rightarrow O2}$, re-

spectively. Due to the higher thermodynamic stability of the P2 phase, $\Delta E_{P2\rightarrow O2}$ is more than three times larger in this example but also the O2 to P2 transition shows a considerable barrier of $\Delta E_{O2\rightarrow P2}$=0.67 eV highlighting that despite the much higher stability of the P2 phase the transition is still not barrier-free. The transition state of the phase transition is shifted towards the O2 phase as well because of the higher stability of P2.

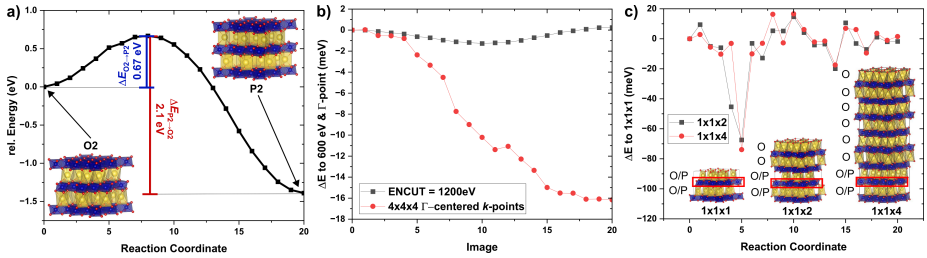

Figure 4.3: Visualization of a reaction pathway and computational convergence considerations. a) Reaction path of the O2-P2 phase transition as obtained from DFT calculations of the perfect images (no relaxation of lattice parameters) normalized to the energy of O2 at a sodium concentration of 0.67. The O2 to P2 ($\Delta E_{O2\rightarrow P2}$) as well as the P2 to O2 ($\Delta E_{O2\rightarrow P2}$) phase-transition barriers can be obtained from the reaction path and are indicated by blue and red lines, respectively. b) Convergence of the applied DFT settings with respect to energy cut-off and *k*-point sampling. Energy differences to the plot in a) are shown. c) Convergence with respect to supercell size in *c*-direction by treating more O-layers beyond the transitioning layer explicitly. The transitioning layer is highlighted by a red box in the shown structure models.

To verify that the employed DFT settings are sufficiently converged to allow computation of ΔE for the O2-P2 phase transition, a convergence test with respect to the energy cutoff and *k*-points was carried out. Results are plotted in Figure 4.3 (b) showing only minor deviations of few meV in the calculated ΔE compared to the employed settings. Towards higher image numbers the *k*-point convergence slightly worsens as the energies were normalized to the O2 phase (image 0). Still, energy differences are far less than 20 meV and corresponding errors in ΔE are even lower due to partial error cancellations. Moreover, ΔE are in the range of several hundreds or even thousands of meV and therefore significantly larger than the estimated computational error. Thus, the employed cutoff and *k*-points seem to be sufficiently converged to reliably conclude the trends in ΔE, most likely also supported by error cancellation when normalizing the images to the O2 phase.

Finally, from a practical point of view it is also important to check whether the long-range interactions between the layers along the *c*-direction influence the obtained ΔE or not. Under realistic conditions the phase transition occurs most likely gradually such that the O2 to P2 transition happens under periodic interaction to further O-layers. In a small cell ΔE might be affected be the long-range self-interactions of the gliding layer. Accordingly, the convergence with respect to supercell-size along the *c*-direction was checked by treating more and more layers explicitly that remain in the O-phase during the transition of one layer. The results and structural models for supercells that are two- and four-times larger along the *c*-direction are presented in Figure 4.3 (c). Only a small fluctuation (below 20 meV) for all images is found which is negligible in comparison to the absolute values of energy barriers ($\Delta E_{O2\rightarrow P2}$=0.67 eV or $\Delta E_{P2\rightarrow O2}$=2.1 eV in the example in Figure 4.3 (a)). However, for the sixth image (reaction coordinate 5) stronger

deviations of almost 80 meV are observed. This deviation can be explained by insufficient convergence of the sodium arrangements during electrostatic optimization or of the electronic structure during DFT calculation (or both) in the original data as also a small deviation (irregular increase) in the relative energy in Figure 4.3 (a) can be seen. However, Figure 4.3 (a) also shows that such small deviations usually do not affect the obtained ΔE much as long as they are not at the minima or transition state. Regarding the influence of the supercell-size along the *c*-direction it can be therefore concluded that ΔE is not significantly influenced by the neighbouring layers. More generally, this indicates that the phase transition of one layer is mostly unaffected by long-range interactions to other layers. Thus, phase transitions should happen randomly in a layered oxide structure in terms of which layer transitions first/last when many layers are present along the *c*-direction as long as no other factors influence the transition such as inhomogeneous desodiation per sodium layer or defect/surface effects.

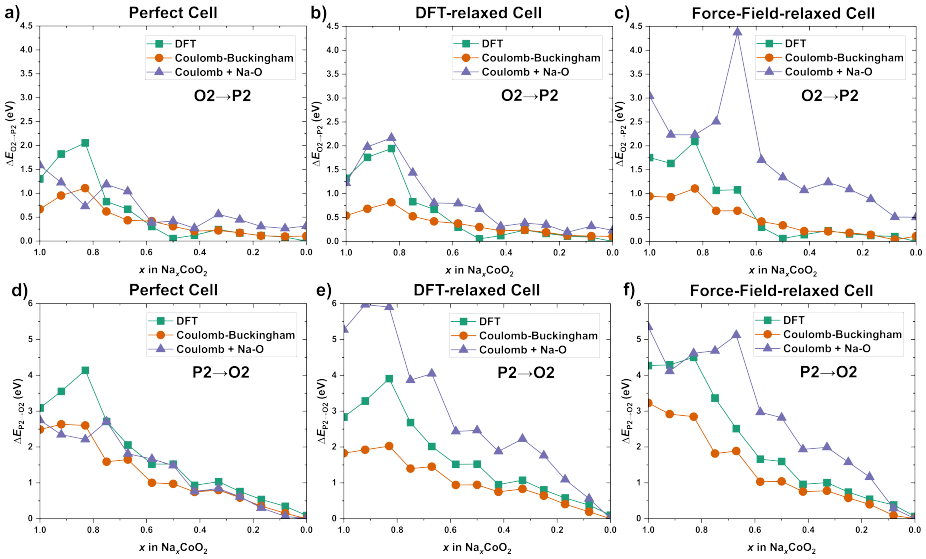

Figure 4.4: O2-P2 phase-transition barriers in Na_xCoO_2 as function of sodium concentration *x*. Non-relaxed and relaxed cells were considered and all transition barriers were obtained by DFT, the fitted Coulomb-Buckingham potential, and by employing just a Buckingham potential for the Na-O interactions along with full electrostatics. a)-c) O2 to P2 barriers ($\Delta E_{O2\rightarrow P2}$) and d)-f) P2 to O2 barriers ($\Delta E_{P2\rightarrow O2}$) for a perfect cell (a) and d)), for a cell with lattice parameters relaxed by DFT for each image (b) and e)), and for cells with lattice parameters optimized with the Coulomb-Buckingham potential fitted in this work (c and f).

Following the methodology sketched in Figure 4.3 (a) to determine ΔE it was continued by calculating ΔE as function of sodium concentration in Na_xCoO_2 (Figure 4.4). An overall trend towards lower ΔE at higher states of charge (lower sodium concentration) can be observed, which is in agreement with the fact that phase transitions are mostly observed at lower sodium concentrations in experiment [5]. This indicates that realistic computational predictions of most stable phases should consider both, thermodynamics and kinetics as the larger ΔE at high sodium concentrations might allow to kinetically stabilize a meta-stable phase under experimental conditions. Moreover, calculated ΔE

are generally higher for P2 to O2 than for O2 to P2 transitions due to the higher thermodynamic stability of P2 over O2 for the Na_xCoO_2 system. Besides this trend towards lower ΔE with decreasing sodium concentration most graphs in Figure 4.4 show first an increase of ΔE from sodium concentrations of 1.00 to 0.83. A possible explanation might be that the P2 phase is thermodynamically less favourable at such high sodium concentrations compared to lower sodium concentrations. This is probably because a more favorable sodium ordering benefiting from occupation of both sodium sub-lattices cannot be realized in the P2 phase due to the strong electrostatic repulsion at the short distances between neighbouring positions of the two different sodium sub-lattices of this phase. Moreover, the O2 to P2 phase transition at a sodium concentration of 0.5 shows consistently lower $\Delta E_{O2\rightarrow P2}$ in DFT (cf. Figure 4.4 (a)-(c)) potentially caused by a distinct electronic structure that is not captured in the force field approaches.

Regarding the accuracy of the potential approaches compared to DFT it can be concluded that the Coulomb-Buckingham potential fitted in this work follows the trends in the DFT ΔE closely while there is a tendency for under-prediction of ΔE at high sodium concentrations (sodium concentrations of 0.83 to 1.00). However, especially at low sodium concentrations the fitted Coulomb-Buckingham potential shows promising qualitative and quantitative agreement to DFT results. Interestingly, the approach of using bare electrostatics and adding just a Buckingham potential for the Na-O interaction fitted in the Na_2O system shows satisfactory performance for predicting ΔE and its trends (despite a few outliers, e.g., the data point at x=0.67 in Figure 4.4 (c) or high sodium concentrations in Figure 4.4 (e)). Especially at high sodium concentrations predictions are in some cases more close to DFT than the full Coulomb-Buckingham potential, e.g., Figure 4.4 (b). This highlights that ΔE is mainly controlled by the repulsive interaction of sodium and oxygen at short distances (Born repulsion). Sodium and oxygen ions are brought closely together when shifting an entire CoO_2 layer causing the Na-O repulsion to be the determining factor for ΔE. However, as the Na-O interactions should be comparable for different cathode compositions and as only electrostatic interactions for the transition metal (Co) were considered in this model, this finding implies that kinetic phase stabilization through composition tuning relies on electrostatics (inter-ionic distances and their charges).

The discussed trends in ΔE are also mostly consistent over different cell geometries especially for the more accurate approaches such as DFT and the full Coulomb-Buckingham potential (c.f. Figure 4.4). This proves that the approach of using perfect cells with averaged (over O2 and P2 and at a sodium concentration of 0.5) lattice parameters is generally justified. However, for some sodium concentrations, the absolute ΔE values change more significantly when relaxation of the lattice parameters is allowed as the initial and final states (O2 and P2) can become thermodynamically more favourable. In order to decrease ΔE by lowering the energy of the transition state, more strong relaxations than just the lattice parameters are required. This will be discussed in the next section.

4.3.2 Calculation of Phase-Transition Barriers by Dynamic Simulations

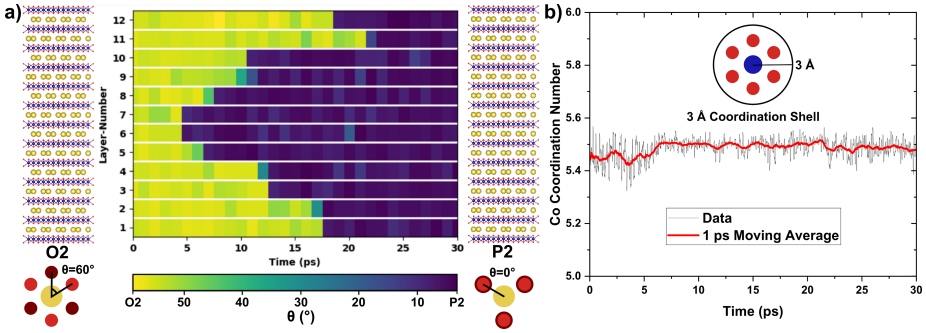

Figure 4.5: Sodium and cobalt coordination during a *NpT* molecular dynamics simulation at 600 K and 1 bar with fitted Coulomb-Buckingham potential for $Na_{0.67}CoO_2$. a) Sodium coordination-angles per sodium layer over a runtime of 30 ps. The structure models indicate the sodium layers the bars in the plot correspond to while the sodium coordination is given as the angle θ. As also sketched in the Figure, θ describes the rotation angle between the upper three (light-red) and lower three (dark-red) oxygen ions that coordinate a sodium ion (yellow). Thus, an angle of 60° corresponds to an octahedral coordination (O2 phase) and an angle of 0° to a prismatic coordination (P2 phase). b) Number of oxygen ions in a coordination sphere of 3 Åaround cobalt ions over run time with the actual data in black and the running average over 1 ps in red.

To allow for pronounced structural relaxations that might occur during the phase transition, it was continued by large-scale MD simulations with 12 layers in the *c*-direction and using the fitted Coulomb-Buckingham potential. To obtain results that are as close to experimental conditions as possible *NpT* simulations at 1 bar and various temperatures were performed. The fitted Coulomb-Buckingham potential showed promising agreement to DFT in the phase-transition barriers as discussed for Figure 4.4 but during MD runs at low sodium concentrations the layered structures collapsed after several ps or ns. This most likely highlights that pairwise interactions are insufficient to maintain a 2D layered structure without or little sodium and higher order interactions (3-body and/or 4-body) are required to simulate layered oxide materials at low sodium concentrations. Similar issues were already reported in the literature on delithiation of a layered oxide lithium-ion cathode [18]. While this finding is important for further theory studies that aim to improve on this issue, the Coulomb-Buckingham potential presented in this work is still able to maintain the atomisitc structure stability during MD simulations at higher sodium concentrations. As there is a strong thermodynamic-driving force (cf. Figure 4.3 (a)) for the O2 to P2 transitions at a sodium concentration of 0.67 and the structures do not collapse at this concentration, in the following MD results for the $Na_{0.67}CoO_2$ material are discussed. Figure 4.5 (a) shows the O2 to P2 phase transitions observed during an MD simulation at 600 K.Firstly, Figure 4.5 (a) proves that with applying the fitted Coulomb-Buckingham potential it is indeed possible to directly observe the O2 to P2 phase transition of $Na_{0.67}CoO_2$ during MD simulations. Moreover, it can be seen that under the applied conditions the transition of a single layer happens quite rapidly (1-3 ps) while the whole structure is gradually transitioning towards P2 *via* different (irregular) types of OP*n* inter-growth phases (often referred to as "Z"-phase [51]). This consecutive phase-transition mechanism is in agreement with the current gained

insight from experimental studies of phase transitions in layered oxide sodium-ion cathodes [7, 52].

The conducted MD simulations allow for more pronounced structural changes during the phase transition and thus might alter the mechanism of gliding an entire CoO_2 layer as assumed for the calculated ΔE in Figure 4.4. Especially the cobalt coordination to nearest neighbor oxygen ions during the transitions is of interest as a recent computational study proposed a transition state with a tetrahedral transition-metal coordination for the P2 to O2 phase transition in Na_xMnO_2. Therefore, the coordination of Co over simulation time is plotted in Figure 4.5 (b). The coordination, which was approximated by a 3 Åcoordination sphere, is in average slightly below 6 due to artifacts at the cell boundaries as no periodic boundary conditions were considered for the analysis. Most importantly, the coordination number is almost constant over simulation time and always significantly above 5. This proves that during the MD simulations the phase transitions also occurred *via* gliding of an entire CoO_2 layer and no transition states with a tetrahedral cobalt coordination exist. Moreover, the calculated $\Delta E_{P2\rightarrow O2}$ by DFT at a sodium concentration of 0.17 is 0.54 eV which is significantly smaller than the barrier of 1.04 eV reported for a reaction path involving a tetrahedral transition-metal coordination at a sodium concentration of 0.125 [8]. The other reason for the difference in energy barriers might be explained by the fact that a different layered oxide material has been studied by Langella *et al.* [8], namely Na_xMnO_2. In contrast to the studied compound (Na_xCoO_2), a strong Jahn-Teller activity is expected in Na_xMnO_2. Further research must show if different transition metals indeed change the phase-transition mechanism or if gliding of an entire TMO_2 layer is the more likely mechanism as indicated by the significantly lower ΔE.

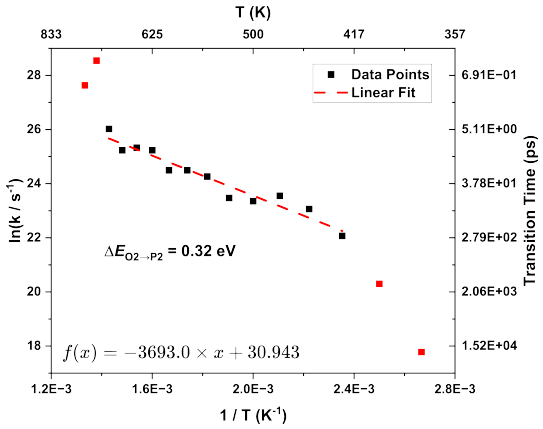

Figure 4.6: Arrhenius plot for the O2 to P2 phase transition in $Na_{0.67}CoO_2$ obtained from molecular dynamics simulations employing the fitted Coulomb-Buckingham potential. Excluded points are shown in red along with the fitted linear function (dashed red line) and the resulting phase-transition barrier ($\Delta E_{O2\rightarrow P2}$).

To asses whether the increased flexibility of the system during the MD simulations lowers $\Delta E_{O2\rightarrow P2}$ even further compared to the more static calculations in Figure 4.4, it was continued by computing an Arrhenius plot for the O2 to P2 phase transition in

$Na_{0.67}CoO_2$. In order to do so, MD simulations in the temperature range of 375 K to 750 K in steps of 25 K were performed and the time to complete the phase transition of the whole structure (e.g., all layers have become prismatic in Figure 4.5 (a)) was tracked to obtain the rate constants (k). The corresponding Arrhenius plot is shown in Figure 4.6. It can be seen that for the very low temperatures (375 K and 400 K) the transition becomes too sluggish rendering the observed rate constants unreliable while at high temperatures (725 K and 750 K) the transition becomes so fast that it is also difficult to determine accurate timings for the transition. However, in the intermediate temperature range from 425 K to 700 K a clear linear trend can be observed in the Arrhenius plot (cf. Figure 4.6). Under the assumption that the phase transition is a first order reaction, which might be justified by the fact that $\Delta E_{O2\rightarrow P2}$ of the transition of one layer was shown to be mostly unaffected by the other layers in Figure 4.3 (c), the activation energy (E_a) can be calculated from a linear fit for the temperature region of 425 K to 700 K by multiplying the obtained slope value by the Boltzmann's constant (k_B) following the Arrhenius equation:

$$\ln(k) = \ln(A) - \frac{E_a}{k_B T}. \tag{4.4}$$

The calculated $\Delta E_{O2\rightarrow P2}$ from MD simulation is 0.32 eV, which is lower than those determined by the Coulomb-Buckingham potential in Figure 4.4 a)-c): 0.43 eV (perfect cell), 0.42 eV (DFT-relaxed cell), and 0.64 eV (force-field relaxed cell). It is also to expect that the full structural flexibility during the MD simulations allows for lower $\Delta E_{O2\rightarrow P2}$ than the static and just-optimized the lattice parameters calculations. This difference in $\Delta E_{O2\rightarrow P2}$ shows that additional degrees of freedom in the MD simulations can lower $\Delta E_{O2\rightarrow P2}$ by more than 25 % or more than 0.1 eV. An exact quantification of how much dynamic conditions decrease $\Delta E_{O2\rightarrow P2}$ in general remains difficult. Still, it becomes evident that the values presented in Figure 4.4 can be understood as an upper limit, while under experimental conditions most-likely even lower ΔE can be achieved due to additional degrees of freedom in the structural relaxation during the transition.

Finally, a MD simulation was performed at standard lab conditions (NpT, 300 K, and 1 bar) with the fitted Coulomb-Buckingham potential to study if it is possible to observe the O2 to P2 phase transition under experimental conditions. The results in Figure 4.7 indeed prove that the transition can be observed under standard lab conditions on the µs-timescale. These timescales for a system with 12 layers (576 formula units, 2112 atoms) are only accessible by simple classical potentials highlighting the value of the Coulomb-Buckingham potential fitted in this work. Figure 4.7 shows that the O2 phase is kinetically stabilized for the first 100 ns. Next, one layer transitions and an O10P2 intergrowth phase remains stable for the next 250 ns. The rather long-time scale over which the thermodynamically unstable phases such as O2 and O10P2 exist under standard lab conditions indicates that kinetic phase stabilization can play an important role supporting the observation of "Z"(OPn)-phases by experiments as discussed before. Next, two more CoO_2 layers glide almost exactly at the same time resulting in a O6P6 phase with an OOPPOPPOOOPP stacking sequence. Finally, the transition of remaining O2 layers results in a P12 structure. However, before a complete transition, an O2P10 phase is observed for a short time (20 ns). The transition sequence is therefore O12-O10P2-O6P6-O2P10-P12. The sequence of phases observed during transition is symmetric and there

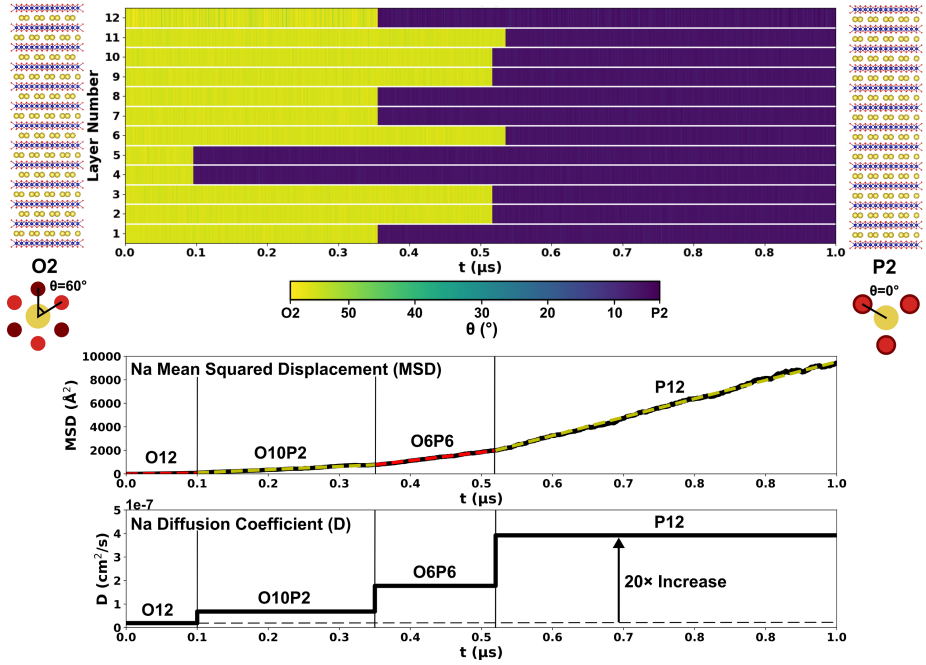

Figure 4.7: O2 to P2 phase transition and sodium diffusion in $Na_{0.67}CoO_2$ during a 1 µs *NpT* molecular dynamics simulation with the fitted Coulomb-Buckingham potential at 300 K and 1 bar (standard lab conditions). The top plot depicts the sodium coordination-environment by the angle θ over simulation time for each of the 12 simulated sodium layers as indicated by the structural models at the left and right side. θ is defined as the rotation angle of the upper coordinating oxygen ions to the lower ones as sketched in the Figure and explained for Figure 4.5. The middle plot shows the mean-squared-displacement (MSD) of sodium over simulation time along with the linear fits (dashed lines) for the regions of different intermediate phases. In the lower plot the sodium diffusion-coefficient resulting from the linear fits in the MSD plot is visualized over the simulation time.

is a tendency towards a decreased kinetic stability (shorter times to next transition) of the inter-growth phases towards a pure P-phase. Still, transition sequences are strongly temperature-dependent as a comparison with Figure 4.5 (a) highlights and as discussed before most likely also random to some extend.

4.3.3 Sodium Diffusion-Coefficients

The µs MD simulation trajectory also allows to analyse the sodium diffusivity directly at experimental conditions as many sodium hoppings occur during the simulation time. The mean squared displacement (MSD) of sodium ions over simulation time is shown in Figure 4.7. From the MSD plot, it is possible to determine the sodium diffusion coefficient (D) by [53]:

$$D = \frac{1}{2d}\frac{\mathrm{dMSD}}{\mathrm{d}t}. \tag{4.5}$$

Here, d denotes the dimensionality of diffusion which is 2 in the case of 2D layered oxides and $\frac{\mathrm{dMSD}}{\mathrm{d}t}$ can be obtained as the slope of a linear fit in the MSD versus time plot with an y-intercept of zero. The phase transitions significantly change the diffusivity of sodium ions as it is known that the P-phase has a better sodium conductivity (at lower sodium concentrations such as 0.67) than the O-phase counterpart due to a different diffusion mechanism [54, 55]. Thus, not a single linear fit of the MSD over the whole simulation time can be applied. Therefore, linear fits were performed for all different observed stacking sequences discussed before but omitting the O2P10 phase due to its short (in terms of simulation time) appearance. The linear fits are shown as dashed lines in the MSD plot in Figure 4.7. Following Equation 4.5 the linear fits allow to determine the sodium diffusion coefficient and its evolution with the different stacking sequences is shown in Figure 4.7 as well.

The calculated sodium ion diffusion coefficients show a pronounced increase over simulation time as more and more P-layers form which is consistent with the fact that P-layers conduct sodium ions better than O-layers. For the pure P-phase (P12) finally a value of 3.92×10^{-7} cm^2/s is obtained which is in excellent agreement to an experimental study of single-crystal Na_xCoO_2 that reports a value of $1.2\pm0.5\times10^{-7}$ cm^2/s at standard lab conditions and for sodium concentrations greater than 0.5 [56]. Other simulation based studies report values of 5.2×10^{-8} cm^2/s [57] (at a sodium concentration of 0.8) or approx. 5×10^{-6} cm^2/s [54] (at 720 K) while further experimental studies on powders suggest values of 1.7×10^{-11} cm^2/s [57] or approx. 1×10^{-9} cm^2/s [58], and 1.9×10^{-11} cm^2/s [59]. It can be concluded that there is a broad variety sodium diffusion-coefficients reported in the literature for P2-Na_xCoO_2 while the value obtained in this work is very similar to the experimental value for single crystals. Thus, the Coulomb-Buckingham potential fitted in this work captures the sodium-ion dynamics reasonably well. Moreover, the simplicity of the potential allows to study the diffusion at standard lab conditions and over extremely long time scales (µs). For the O2 phase experimental and theoretical data is harder to compare as the O2 phase is not commonly reported for Na_xCoO_2. However, it remains interesting to compare the relative increase in the diffusion coefficient of the P2 structure versus the O2 structure. The fits in Figure 4.7 result in an diffusion coefficient of 1.90×10^{-8} cm^2/s for the pure O2 phase suggesting that the pure P2 phase shows an approx. 20-times increased sodium diffusion-coefficient. Recent simulation studies reported a 12-times higher sodium diffusion coefficient of P2-$Na_{0.8}CoO_2$ over O3-$Na_{0.8}CoO_2$ [57]. Moreover, at 720 K an (approximately) increase of 5-times in the P2 sodium diffusion coefficient over the O3 phase was reported [54]. Another experimental study on $Na_{0.67}Fe_{0.67}Mn_{0.33}O_2$ reports ratios of the sodium diffusion coefficient in the P2 over O3 structure in the range of 12-20 depending on the experimental method [55]. Overall, it can be concluded that the observed 20-times increase in the sodium diffusion-coefficient observed in the MD simulation in Figure 4.7 appears to be in a realistic order of magnitude and matches to values for similar systems reported in the literature supporting the conclusion that the Coulomb-Buckingham potential presented in this work is well-suited to study sodium-ion diffusion in Na_xCoO_2, besides the phase transition.

4.4 Conclusions

In summary, a Coulomb-Buckingham potential for layered oxide cathode materials was developed at the example of Na_xCoO_2. The results show that most Buckingham parameters are insensitive to the charge-carrier (sodium) concentration (x) allowing for significant parameter reductions of the potential. It was found that the most important parameter that changes with x is the dielectric constant of the material to account for the change in screening of electrostatic interactions. However, the dependency of the dielectric constant with x appears to be linear allowing for simple fittings and extrapolation. First, the O2-P2 phase-transition barrier was computed as function of x by static calculations (single-point calculations) and moving one entire CoO_2 layer along the a-lattice direction. A pronounced trend towards lower barriers at lower x values and higher barriers for P2 to O2 than for O2 to P2 was found. The barrier values and trends were reasonably well reproduced by the fitted Coulomb-Buckingham potential. The Na-O Buckingham potential was identified to be the most important interaction beyond electrostatics to capture the phase-transition barriers. Afterwards, the O2 to P2 phase transition in $Na_{0.67}CoO_2$ was studied by molecular dynamics simulations employing the fitted Coulomb-Buckingham potential. While it was shown that the transition mechanism during the simulations (shift of one entire CoO_2 layer) remains the same as in the static calculations, lower energy barriers were obtained by activation-energy calculations following Arrhenius equation. The fitted Coulomb-Buckingham potential has enabled performing molecular dynamics simulations at standard lab conditions on the timescale of µs. The observed trends in gradual phase transitions (OPn-/"Z"-phases) and kinetic stabilities of intermediate phases might help in further understanding of experimental results on phase transitions and inter-growth phases. Finally, the sodium-ion diffusion-coefficient was computed as a function of completeness of phase transition. Absolute values of sodium diffusion-coefficients and the relative increase during phase transition were shown to be in similar order of magnitude than experimental values for single crystals reported in the literature.

Overall, this work shows, at the prototype layered oxide sodium-ion cathode material Na_xCoO_2, that it is possible to investigate phase transitions and sodium dynamics at standard lab conditions utilizing simple pairwise Coulomb-Buckingham potentials. Further studies could consider different, more complex transition-metal compositions and include more layered phases such as O3 and P3. It is believed that the procedure of fitting classical potentials outlined in this work can be a promising route to obtain more detailed understanding of unknown atomistic mechanisms in complex layered oxide sodium-ion cathode materials.

REFERENCES

1. Wang, J. *et al.* Routes to high-performance layered oxide cathodes for sodium-ion batteries. *Chemical Society reviews* **53,** 4230–4301 (2024).
2. Yang, H. *et al.* Improvement of cycle life for layered oxide cathodes in sodium-ion batteries. *Energy & Environmental Science* **17,** 1756–1780 (2024).
3. Wang, P.-.-F., You, Y., Yin, Y.-.-X. & Guo, Y.-.-G. Layered Oxide Cathodes for Sodium–Ion Batteries: Phase Transition, Air Stability, and Performance. *Advanced Energy Materials* **8** (2018).
4. Hwang, J.-Y., Myung, S.-T. & Sun, Y.-K. Sodium-ion batteries: present and future. *Chemical Society reviews* **46,** 3529–3614 (2017).
5. Zhang, J. & Li, X. Perspective on Phase Transition in Layered Oxide Cathodes for Sodium-Ion Batteries: Mechanism, Influenced Factors, and Inhibition Strategies. *Energy & Fuels* **38,** 13906–13933 (2024).
6. Delmas, C., Fouassier, C. & Hagenmuller, P. Structural classification and properties of the layered oxides. *Physica B+C* **99,** 81–85 (1980).
7. Tang, Y. *et al.* Sustainable layered cathode with suppressed phase transition for long-life sodium-ion batteries. *Nature Sustainability* **7,** 348–359 (2024).
8. Langella, A., Massaro, A., Muñoz-García, A. B. & Pavone, M. Atomistic Insights into Solid-State Phase Transition Mechanisms of P2-Type Layered Mn Oxides for High-Energy Na-Ion Battery Cathodes. *ACS energy letters* **10,** 1089–1098 (2025).
9. Fellman, A., Byggmästar, J., Granberg, F., Nordlund, K. & Djurabekova, F. Fast and accurate machine-learned interatomic potentials for large-scale simulations of Cu, Al, and Ni. *Physical Review Materials* **9** (2025).
10. Li, Y., Zhang, X., Liu, M. & Shen, L. A critical review of machine learning interatomic potentials and Hamiltonian. *Journal of Materials Informatics* **5** (2025).
11. Deringer, V. L., Caro, M. A. & Csányi, G. Machine Learning Interatomic Potentials as Emerging Tools for Materials Science. *Advanced materials (Deerfield Beach, Fla.)* **31,** e1902765 (2019).
12. Behler, J. Perspective: Machine learning potentials for atomistic simulations. *The Journal of Chemical Physics* **145,** 170901 (2016).
13. Mueller, T., Hernandez, A. & Wang, C. Machine learning for interatomic potential models. *The Journal of Chemical Physics* **152,** 050902 (2020).
14. Lee, S. & Park, S. S. Atomistic Simulation Study of Mixed-Metal Oxide (LiNi 1/3 Co 1/3 Mn 1/3 O 2) Cathode Material for Lithium Ion Battery. *The Journal of Physical Chemistry C* **116,** 6484–6489 (2012).

15. Kerisit, S., Chaka, A. M., Droubay, T. C. & Ilton, E. S. Shell Model for Atomistic Simulation of Lithium Diffusion in Mixed Mn/Ti Oxides. *The Journal of Physical Chemistry C* **118,** 24231–24239 (2014).

16. He, J., Zhang, L. & Liu, L. Thermal transport in monocrystalline and polycrystalline lithium cobalt oxide. *Physical chemistry chemical physics : PCCP* **21,** 12192–12200 (2019).

17. Hart, F. X. & Bates, J. B. Lattice model calculation of the strain energy density and other properties of crystalline LiCoO2. *Journal of Applied Physics* **83,** 7560–7566 (1998).

18. Morgan, L. M. *et al.* From Atoms to Cells: Multiscale Modeling of LiNi x Mn y Co z O 2 Cathodes for Li-Ion Batteries. *ACS energy letters* **7,** 108–122 (2022).

19. Sau, K. & Ikeshoji, T. Insights of cationic diffusion in nickel-based honeycomb layered tellurates using molecular dynamics simulation. *Solid State Ionics* **383,** 115982 (2022).

20. Masese, T. *et al.* Mixed alkali-ion transport and storage in atomic-disordered honeycomb layered NaKNi2TeO6. *Nature communications* **12,** 4660 (2021).

21. Sau, K. & Ikeshoji, T. Ring mechanism of fast Na+ ion transport in Na2LiFeTeO6 : Insight from molecular dynamics simulation. *Physical Review Materials* **6** (2022).

22. Delmas, C., Braconnier, J., Fouassier, C. & Hagenmuller, P. Electrochemical intercalation of sodium in NaxCoO2 bronzes. *Solid State Ionics* **3-4,** 165–169 (1981).

23. Boddu, V. R. R., Puthusseri, D., Shirage, P. M., Mathur, P. & Pol, V. G. Layered NaxCoO2-based cathodes for advanced Na-ion batteries: review on challenges and advancements. *Ionics* **27,** 4549–4572 (2021).

24. Kaufman, J. L. & van der Ven, A. NaxCoO2 phase stability and hierarchical orderings in the O3/P3 structure family. *Physical Review Materials* **3** (2019).

25. Rivadulla, F., Zhou, J.-S. & Goodenough, J. B. Chemical, structural, and transport properties of Na1−xCoO2. *Physical review. B, Condensed matter* **68** (2003).

26. Toumar, A. J., Ong, S. P., Richards, W. D., Dacek, S. & Ceder, G. Vacancy Ordering in O3 -Type Layered Metal Oxide Sodium-Ion Battery Cathodes. *Physical Review Applied* **4** (2015).

27. Köster, K. & Kaghazchi, P. Hybrid functionals with nonempirical Hartree-Fock parameters for electronic structure calculation of layered oxides. *Physical Review B* **109** (2024).

28. Biecher, Y. *et al.* Structure and Electronic Structure Evolution of P2-Na x CoO 2 Phases from X-ray Diffraction and 23 Na Magic Angle Spinning Nuclear Magnetic Resonance. *Chemistry of Materials* **34,** 6431–6439 (2022).

29. Lee, D. H., Xu, J. & Meng, Y. S. An advanced cathode for Na-ion batteries with high rate and excellent structural stability. *Physical chemistry chemical physics : PCCP* **15,** 3304–3312 (2013).

30. Ewald, P. P. Die Berechnung optischer und elektrostatischer Gitterpotentiale. *Annalen der Physik* **369,** 253–287 (1921).

31. Buckingham, R. A. The classical equation of state of gaseous helium, neon and argon. *Proceedings of the Royal Society of London. Series A. Mathematical and Physical Sciences* **168,** 264–283 (1938).

32. Köster, K., Binninger, T. & Kaghazchi, P. Optimization of Coulomb energies in gigantic configurational spaces of multi-element ionic crystals. *npj Computational Materials* **11** (2025).

33. Blöchl, P. E. Projector augmented-wave method. *Physical review. B, Condensed matter* **50,** 17953–17979 (1994).

34. Kresse, G. & Furthmüller, J. Efficient iterative schemes for ab initio total-energy calculations using a plane-wave basis set. *Physical review. B, Condensed matter* **54,** 11169–11186 (1996).

35. Perdew, J. P., Burke, K. & Ernzerhof, M. Generalized Gradient Approximation Made Simple. *Physical review letters* **77,** 3865–3868 (1996).

36. Grimme, S. Semiempirical GGA-type density functional constructed with a long-range dispersion correction. *Journal of computational chemistry* **27,** 1787–1799 (2006).

37. Virtanen, P. *et al.* SciPy 1.0: fundamental algorithms for scientific computing in Python. *Nature methods* **17,** 261–272 (2020).

38. Storn, R. & Price, K. Differential Evolution – A Simple and Efficient Heuristic for global Optimization over Continuous Spaces. *Journal of Global Optimization* **11,** 341–359 (1997).

39. Liu, D. C. & Nocedal, J. On the limited memory BFGS method for large scale optimization. *Mathematical Programming* **45,** 503–528 (1989).

40. Li, Z., Yang, J., Hou, J. G. & Zhu, Q. First-principles lattice dynamics of NaCoO2. *Physical Review B* **70** (2004).

41. Petousis, I. *et al.* High-throughput screening of inorganic compounds for the discovery of novel dielectric and optical materials. *Scientific data* **4,** 160134 (2017).

42. Thompson, A. P. *et al.* LAMMPS - a flexible simulation tool for particle-based materials modeling at the atomic, meso, and continuum scales. *Computer Physics Communications* **271,** 108171 (2022).

43. Plimpton, S. Fast Parallel Algorithms for Short-Range Molecular Dynamics. *Journal of Computational Physics* **117,** 1–19 (1995).

44. Bitzek, E., Koskinen, P., Gähler, F., Moseler, M. & Gumbsch, P. Structural relaxation made simple. *Physical review letters* **97,** 170201 (2006).

45. Nosé, S. A unified formulation of the constant temperature molecular dynamics methods. *The Journal of Chemical Physics* **81,** 511–519 (1984).

46. Hoover, W. G. Canonical dynamics: Equilibrium phase-space distributions. *Physical review. A, General physics* **31,** 1695–1697 (1985).

47. Shinoda, W., Shiga, M. & Mikami, M. Rapid estimation of elastic constants by molecular dynamics simulation under constant stress. *Physical Review B* **69** (2004).

48. Tuckerman, M. E., Alejandre, J., López-Rendón, R., Jochim, A. L. & Martyna, G. J. A Liouville-operator derived measure-preserving integrator for molecular dynamics simulations in the isothermal–isobaric ensemble. *Journal of Physics A: Mathematical and General* **39,** 5629–5651 (2006).

49. Momma, K. & Izumi, F. VESTA : a three-dimensional visualization system for electronic and structural analysis. *Journal of Applied Crystallography* **41,** 653–658 (2008).

50. Berthelot, R., Carlier, D. & Delmas, C. Electrochemical investigation of the P2–NaxCoO2 phase diagram. *Nature materials* **10,** 74–80 (2011).

51. Mortemard de Boisse, B., Carlier, D., Guignard, M., Bourgeois, L. & Delmas, C. P2-Na(x)Mn(1/2)Fe(1/2)O2 phase used as positive electrode in Na batteries: structural changes induced by the electrochemical (de)intercalation process. *Inorganic chemistry* **53,** 11197–11205 (2014).

52. Somerville, J. W. *et al.* Nature of the "Z"-phase in layered Na-ion battery cathodes. *Energy & Environmental Science* **12,** 2223–2232 (2019).

53. Usler, A. L., Kemp, D., Bonkowski, A. & de Souza, R. A. A general expression for the statistical error in a diffusion coefficient obtained from a solid-state molecular-dynamics simulation. *Journal of computational chemistry* **44,** 1347–1359 (2023).

54. Mo, Y., Ong, S. P. & Ceder, G. Insights into Diffusion Mechanisms in P2 Layered Oxide Materials by First-Principles Calculations. *Chemistry of Materials* **26,** 5208–5214 (2014).

55. Katcho, N. A. *et al.* Origins of Bistability and Na Ion Mobility Difference in P2– and O3–Na 2/3 Fe 2/3 Mn 1/3 O 2 Cathode Polymorphs. *Advanced Energy Materials* **7** (2017).

56. Shu, G. J. & Chou, F. C. Sodium-ion diffusion and ordering in single-crystal P2-NaxCoO2. *Physical Review B* **78** (2008).

57. Tatara, R. *et al.* Revisiting the ion dynamics in Li x CoO2 and Na x CoO2. *Chemical science* (2025).

58. Ohishi, K. *et al.* Ion Dynamics in P2-Na x CoO 2 Detected with Operando Muon Spin Rotation and Relaxation. *ACS Applied Energy Materials* **6,** 8111–8119 (2023).

59. Shibata, T., Kobayashi, W. & Moritomo, Y. Sodium Ion Diffusion in Layered Na x CoO 2. *Applied Physics Express* **6,** 097101 (2013).

5

ELECTRONIC STRUCTURE CALCULATIONS:

HYBRID FUNCTIONALS WITH NON-EMPIRICAL HARTREE-FOCK PARAMETERS FOR ELECTRONIC STRUCTURE CALCULATION OF LAYERED OXIDES

Accurate electronic structure descriptions of layered oxides are highly relevant yet complex to obtain by *ab inito* methods. The functionalities of layered transition metal oxides are usually heavily influenced by their electronic structure and the hybridization/delocalization of *d*-electrons of the transition metals. Therefore, understanding the electronic structure can enable more rational design of this highly important material class, which is widely utilized in practical applications such as cathodes in secondary batteries of portable electronic devices and electric vehicles. However, it is well known that standard quantum-mechanic approximations to the many-body problem over-localize (Hartree-Fock) or over-delocalize (Density Functional Theory) electrons in these systems. A mixture of different methods (hybrid functionals) can partially resolve the problem but introduces at least one additional parameter (the mixing parameter) that has to be determined by e.g., higher levels of theory (*GW*). In this study, the focus lies on electronic structure of lithiated layered transition-metal oxides based on Co, Ni, Mn, and their binary systems that form the foundation of state-of-the-art lithium-ion batteries. The influence of Hartree-Fock mixing in the PBE0 hybrid functional on the electronic structure is compared as well as using different Hartree-Fock mixings as starting points for *GW* calculations. Two non-empirical *GW*-based fitting approaches to determine the optimal Hartree-Fock mixing are considered. It is shown that one of the fitting approaches suggests small mixing parameters and is in satisfactory agreement with experimental results, while the other approach has a stronger theoretical foundation and indicates higher mixing parameters, which are close to the value obtained by perturbation theory by Perdew, Ernzerhof, and Burke. Finally, it is shown that larger mixing parameters are required when screening is introduced to the Hartree-Fock term.

This chapter is reprinted with permission from: **Köster, K.** & Kaghazchi, P. Hybrid functionals with nonempirical Hartree-Fock parameters for electronic structure calculation of layered oxides. Phys. Rev. B **109**, 155134 (2024).

5.1 Introduction

Transition metal (TM) oxides are very important materials due to their broad applicability in multiple fields, but it is challenging to describe their electronic structures correctly by *ab inito* methods [1–6]. Among the different classes of TM oxides, layered ones with the composition A[TM]O_2 are among the most appealing. They are already utilized as cathodes in state-of-the-art energy storage devices and are modified to meet the needs of next generation of energy-storage materials [7, 8]. In these materials alkali metals (A) are reversibly intercalated and deintercalated as charge carriers between the cathode and the anode while the electrons are moving through an external circuit, allowing to obtain the stored electrical energy from these materials. In particular, layered oxide cathode materials based on Co, Mn, and Ni along with Li as charge carrier have become the market standard for energy storage and are employed in multiple devices nowadays [7]. $LiCoO_2$ was first proposed by Goodenough in Ref. [9] in 1980 and became later the first commercialized secondary Li-ion battery by Sony Corp. [10]. The $LiNiO_2$ [11] and $LiMnO_2$ [12] materials were first introduced a few years later as cathode active materials for lithium ion batteries. Nowadays, cathodes with different mixtures of these TMs are most frequently employed in high-performance batteries where Mn can also be replaced by Al [7]. For practical use cases — not limited to the field of batteries — the correct description of the electronic structure is especially important as it determines some of the key properties of TM oxides (e.g. band gap, redox process) but is hard to come by with computational methods. This yields to some controversies for the calculation of redox processes in these materials [13–15].

Standard methods such as Hartree-Fock (HF) or density functional theory (DFT) with a generalized-gradient-approach (GGA) based exchange-correlation (xc) functional fail to accurately predict the electronic structures of TM oxides as they over-localize or over-delocalize the electrons onto the ion cores due to their well-known intrinsic errors (missing correlation in HF and self-interaction errors in DFT) [16]. This yields an inadequate description of the *d*-electrons that are of special importance for the aforementioned practical applications of these materials [17–19]. Using the band gap as an indicator for the correct description of electronic structure, it can be shown that HF tends to overestimate, whereas DFT-GGA tends to underestimate the band gaps compared to experimental studies [20]. As both approaches seem to be complementary to some extend, it was proposed to mix a portion of exact exchange (HF) with the exchange of DFT to improve the accuracy with the cost of increased computational effort [21]. This approach is known as hybrid-functional and its superiority over the two bare methods for electronic structures is widely accepted [22–26]. It is also worth noting that another, computationally less demanding method, the Hubbard U (DFT+U) method is commonly applied to describe TM oxides [1, 27–30]. In a simplified picture this model applies a species-specific bias potential of the strength U, which localizes the electrons by introducing a penalty for partial occupations [31]. Hybrid functionals provide a more general treatment of the self-interaction error in DFT by avoiding species-specific auxiliary parameters and the risk of perturbing the electronic structure [14, 23, 28]. The focus of this work is on hybrid functionals, especially the one-parameter formulation proposed by Becke in Ref. [32]: PBE0 (also sometimes called PBEh), which is described by the following formula:

$$E^{\mathrm{PBE0}} = \alpha \times E_{\mathrm{x}}^{\mathrm{HF}} + (1-\alpha) \times E_{\mathrm{x}}^{\mathrm{PBE}} + E_{\mathrm{c}}^{\mathrm{PBE}}. \tag{5.1}$$

The value of α (HF mixing-parameter) is usually set to 25 % which can be reasoned by perturbation theory [33]. However, $\alpha = \frac{1}{2}; \frac{1}{3}; \frac{1}{4}; \frac{1}{5}$ can all be reasoned by pure theory approaches (Ref. [34]) and it is also widely accepted to fit the parameter to experimental and/or theoretical benchmarks [6, 35–38]. Moreover, position-dependent local mixing parameters are also employed that allow to vary the effective mixing spatially with respect to the different ion-species [22, 39]. Regarding the non-local hybrid functional approach, it should also be noted that more complex, screened approaches exist (e.g., HSE [40, 41]) that split the exchange in long-range (LR) and short-range (SR) to apply a screening to the Hartree-Fock exchange. To reduce the computational demand, this method considers only the SR Hartree-Fock exchange (cf. Equation 5.2) introducing another parameter, the screening parameter ω, that can be freely optimized [40, 41].

$$E^{\mathrm{HSE}} = \alpha \times E_{\mathrm{x,HF}}^{\mathrm{SR}} + (1-\alpha) \times E_{\mathrm{x,PBE}}^{\mathrm{SR}} + E_{\mathrm{x,PBE}}^{\mathrm{LR}} + E_{\mathrm{c}}^{\mathrm{PBE}} \tag{5.2}$$

It should be mentioned that also physically motivated approaches were developed to determine HF mixing/range-separation in hybrid functionals such as dielectric-dependent hybrid functionals [42], optimally tuned hybrid functionals (ionization potential theorem) [43, 44], and hybrid functionals aimed to satisfy Koopman's condition [45]. In all these hybrid functionals, the HF mixing has a significant influence on several electronic properties calculated for the material under study [6, 46, 47]. A correct description of electronic structure is essential for layered TM oxides as cathode materials since it determines the redox process, especially the activity of oxygen redox in the compound [15, 48, 49]. To further rationalize the design of novel layered TM oxide cathode materials by computational methods accurate electronic structures are required that can be effectively tuned by varying the HF mixing in hybrids.

As mentioned above, one strategy is to fit the HF mixing to calculated reference electronic structures by higher levels of theory for example within the so-called *GW* approximation: The first term in the expansion of the self-energy in the Green's function G and the dynamically screened Coulomb interaction W, obtained within the random phase approximation [50, 51]. This approach has already been proven to be practical for obtaining reference electronic structures and fitting HF mixing by several other studies [6, 38, 52]. In the *GW* approximation quasi-particle energies $E_{n\mathbf{k}}^{\mathrm{QP}}$ are given by: [53]

$$E_{n\mathbf{k}}^{\mathrm{QP}} = \mathrm{Re}[\langle \psi_{n\mathbf{k}} | T + V_{n-e} + V_H + \Sigma(E_{n\mathbf{k}}^{\mathrm{QP}}) | \psi_{n\mathbf{k}} \rangle]. \tag{5.3}$$

Band and k-points indices are denoted as n and $\mathbf{k}$, T is the kinetic-energy operator, V_{n-e} and V_H are the nuclei and Hartree potential, respectively. The self-energy operator Σ is constructed from G and W as mentioned before. The quasi-particle energies are then updated by adding Equation 5.3, scaled by a renormalization factor, to the quasi-particle energies of the previous cycle. Naturally, this *ansatz* requires a starting point for the quasi-particle energies which is commonly obtained by DFT calculations [54–56]. In the single-shot *GW* method (G_0W_0), Equation 5.3 is only evaluated once (and so the self-energy) and added to the starting point. In contrast, in the fully self-consistent *GW*

approach (*GW*) the procedure is iterated to convergence by updating the single electron energies in Σ along with reconstructing *W* based on the most recent quasi-particle energies. There is also the possibility to fix *W* during these iterations for the partially self-consistent *GW* (GW_0) approach. It should be noted that for all *GW* calculations in this work off-diagonal elements of the self-energy were considered to be equal to the corresponding elements of the DFT exchange-correlation potential, which is only justified if the wave functions of the starting point are in sufficient agreement with the ones of *GW* [51]. This kind of *GW* is sometimes also denoted as "ev*GW*".

Even though the *GW* approach has a strong theoretical foundation, the critical point is still to select an appropriate DFT starting-point. Higher levels of *GW* can reduce the starting-point dependence, but the results of all levels still depend on the starting wave functions and band gaps can vary strongly by starting point and level of *GW* [57]. It was suggested to employ G_0W_0 starting from hybrid functionals and GW_0 on top of DFT-GGA calculations, while *GW* is shown to tend to overestimate band gaps, regardless of the starting point [51, 58]. Consequently, it seems valuable to also scan the results of *GW* at intermediate starting points as DFT-GGA can be tuned by adding HF mixing step-wise towards the default value of 25 % for hybrids, as it was already investigated by Chen *et al.* [38] for some semiconductors and insulators.

In this work, the band gap is adopted as the key property to optimize the electronic-structure calculations using hybrid functionals by adjusting the HF mixing-parameter. Prototype layered oxides of Co, Mn, and Ni and their binary mixtures are investigated at their fully lithiated state, since previous works suggested the largest adjustment to the default mixing parameter at high lithium contents [6]. Band gaps at various HF mixings are calculated in the PBE0 approach and G_0W_0 calculations are employed to each PBE0 solution. Two optimal sets of mixing parameters for PBE0 are found for the materials under study and the corresponding band gaps are compared to experimental values. Moreover, the influence of using a screened hybrid and higher levels of *GW* on band gaps and optimal HF mixing parameters is discussed.

5.2 Method

All calculations were carried out using the projector augmented wave (PAW) method [59] as implemented in the Vienna *ab inito* simulation package (VASP) [60]. Pseudopotentials optimized for *GW* calculations that explicitly describe outer *s*- (Li), *s*- and *p*- (O), and *s*- and *d*-electrons (TM) were employed, while *d*-projectors were considered for the oxide ions. The spin-polarized calculations were performed with a 4×2×4 *k*-point grid including the Γ-point along with an energy cutoff of 600 eV. Non-spherical contributions from the gradient corrections were accounted for in all calculations. Furthermore, partial occupancies were treated with Gaussian smearing along with a smearing width of 0.01 eV. Density of states (DOS) was calculated with the tetrahedron method. Layered oxides of $LiCoO_2$, $LiNiO_2$, $LiMnO_2$, $LiCo_{0.5}Mn_{0.5}O_2$, $LiCo_{0.5}Ni_{0.5}O_2$, and $LiMn_{0.5}Ni_{0.5}O_2$ were modeled by 1×3×1 supercells containing six formula units and in the *C2/m* space-group (O1 phase) as shown in the exemplary model in Figure 5.1.

It should be noted that the experimentally observed $Li_{1-x}Ni_{1+x}O_2$ defects (non-stoichiometric compositions) [61] for $LiNiO_2$ were not accounted for in the model for the sake of simplicity. Moreover, $LiCoO_2$, which generally has been observed to have

a $R\bar{3}m$ space group (O3 phase according to the notation for layered TM oxides by Delmas *et al.* [62]), has been modelled by a O1 structure. It was carefully checked that both space groups yield essentially the same band gaps at various levels of theory. However, it should be mentioned that other layered TM oxides show a weak space group dependence of band gap [63].

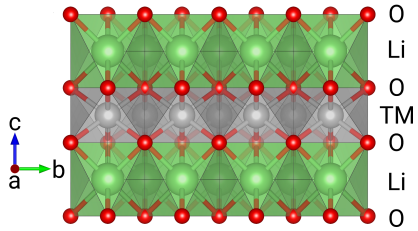

Figure 5.1: Exemplary structure of the models employed in this study showing the transition metals (TM) in silver in an octahedral coordination as well as the lithium ions in green also in octahedral coordination along with the red oxygen layers.

The overall calculation process can be structured into three steps: geometry optimization (a), electronic structure optimization (b), and *GW* calculations (c).

Geometry Optimization: Geometries of all symmetry-distinctive TM arrangements were fully optimized for each compound without symmetry constrains using the generalized-gradient-approach (GGA) within the Perdew-Burke-Ernzerhof (PBE) exchange-correlation functional [64]. An electronic convergence criterion of 10^{-8} eV was employed and the geometry was optimized until the forces of each ion were lower than 10^{-3} eV/Å. The total energy of the structures was found to be reasonably converged (< 0.0025 eV per formula unit) with respect to *k*-points and cutoff energy. The optimized geometry of the lowest energy structure for each compound was fixed for the following calculation steps.

Electronic Structure Optimization: Different ferro-magnetic (FM) and anti-ferromagnetic (AFM) arrangements in the compounds containing magnetic ions were tested on the PBE level to identify the most favorable magnetic configurations. Using the PBE geometries and magnetic structures, electronic structures were optimized within the single-parameter PBE0 hybrid-functional approach [32] varying the Hartree-Fock mixing parameter. Same settings were applied for screened hybrid functional calculations [65]. A convergence criterion of 10^{-8} eV was employed and the "Accurate" setting of VASP was used for the DFT part of the calculations. In a consecutive step, an exact diagonalization of the Hamiltonian was performed while the number of bands was increased to 256 resulting in more than 150 unoccupied bands for all investigated compounds.

***GW* Calculations:** Single-shot *GW* calculations considering just eigenvalues (G_0W_0 calculations) were performed for all compounds to obtain the quasi-particle energies. However, for $LiCoO_2$ and $LiNiO_2$, *G* and *W* were also both iterated to convergence to obtain fully self-consistent (in eigenvalues) *GW* results (denoted "*GW*" in this work but in

other works sometimes also referred to as "ev*GW*)". The iterations were stopped when the band gap was converged within at least 0.1 eV. For *GW* calculations, the energy cut-off for the response function was set to 400 eV and the number of frequency/time grid points was set to 100. Quasi-particle energies were calculated for all bands that lie within twice the number of occupied states. Convergence tests with higher cutoffs, more grid points, more bands, and calculating quasi-particle energies for more unoccupied bands showed that the band gap is well converged ($\ll$ 0.1 eV) with the chosen settings.

Atomistic structures and iso-surfaces were visualized with help of the VESTA software-package [66] and charge density differences were calculated with the help of vaspkit [67].

5.3 Results and Discussion

5.3.1 DFT optimizations and influence of different portions of HF mixing within the PBE0 functional

The optimized geometries revealed an intermediate Jahn-Teller distortion for $LiNiO_2$ and a strong Jahn-Teller distortion for $LiMnO_2$, whereas $LiCoO_2$ showed an almost perfect symmetrical coordination (cf. Figure 5.3). These geometries are in agreement with previous studies and experimental observations as well as with the general Jahn-Teller activity of *d*-configurations assuming charges of 3+ for the TM ions [68]. Distortions were, however, much weaker in the mixed materials ($LiCo_{0.5}Mn_{0.5}O_2$, $LiCo_{0.5}Ni_{0.5}O_2$, and $LiMn_{0.5}Ni_{0.5}O_2$) and not present around Co. Only Ni in $LiCo_{0.5}Ni_{0.5}O_2$ showed a significantly distorted environment. Regarding the magnetic ordering, the calculations indicated no magnetism (unpaired electrons) for $LiCoO_2$, FM ordering for $LiNiO_2$ and $LiCo_{0.5}Ni_{0.5}O$, and AFM ordering was found to be most favorable for $LiMnO_2$ and $LiMn_{0.5}Ni_{0.5}O_2$. Moreover, a high-spin configuration was obtained for Mn in $LiMnO_2$ which is an agreement with the literature where also an AFM high-spin configuration is reported for $LiMnO_2$ [69]. Using these models to optimize electronic structures, it was found that band gap increases linearly with the HF mixing-parameter (α) of PBE0 (Figure 5.2 and fitted parameters in Table 5.2). The linear trend agrees with previous studies on various materials [6, 70–72].

Only for $LiCo_{0.5}Mn_{0.5}O_2$ no linear trend is observed as the electronic structure undergoes significant changes with α, which is concluded from the computed unpaired electrons (UPE) on Co and Mn (Table 5.3 for α=25 %): In the α-range from 0 % to 10 % three $Co^{2.67+}$ and three $Mn^{3.33+}$ can be assigned with the partial charges being delocalized over all ions of the same type. For α between 15 % and 20 % three Co^{3+} and three Mn^{3+} are observed and for α=25 % two Co^{3+}, one Co^{2+}, two Mn^{3+}, and one Mn^{4+} are obtained in the electronic structure corresponding to the same average charges as for the α-range from 0 % to 10 % but with the partial charges in the average being fully localized on single ions. These changes of the electronic structure with α and changes on how electrons are localized/delocalized between/within the two different metal species become problematic when comparing electronic structures of two different α for $LiCo_{0.5}Mn_{0.5}O_2$. The reason for this behavior might be found in electron affinity (e.g., estimated by electronegativity) as the one of Co is closer to that of Mn compared to Ni-Mn, which presumably causes intermediate degree of reduction of Co in favor of oxidation of Mn with roughly

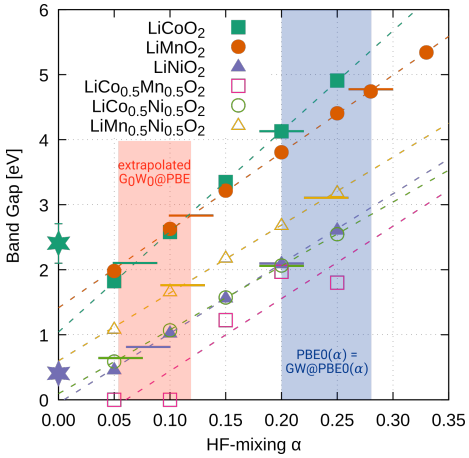

Figure 5.2: PBE0 band gaps of the investigated layered TM oxides as a function of the HF mixing-parameter α. The band gaps increase linearly with α as indicated by the linear fits (dashed lines). Horizontal solid bars in the α-range marked red (left) correspond to the optimal mixing parameters to reproduce the extrapolated G_0W_0@PBE band gaps. The horizontal bars in the α-range marked in blue (right) show the mixing parameters that result in no correction of the band gap in consecutive *GW* calculations. Stars on *y*-axis mark experimental band gaps as shown in Table 5.1.

$\frac{1}{3}$ of the Co being reduced to 2+ and $\frac{1}{3}$ of the Mn being oxidized to 4+. In contrast, the electron affinities of Co and Ni are more similar resulting in 3+ ions for both species in $LiCo_{0.5}Ni_{0.5}O_2$ and those of Ni and Mn are more different resulting in full oxidation of Mn to Mn^{4+} and reduction of Ni to Ni^{2+} in $LiMn_{0.5}Ni_{0.5}O_2$ which can be again verified by UPE in the electronic structures (cf. Table 5.3). Varying α in these compounds changes localization/delocalization of electrons for each transition-metal ion but does not result in different localizations of oxidations between or within the ionic species. Consequently, electronic structures at different α are comparable for all materials but $LiCo_{0.5}Mn_{0.5}O_2$.

These oxidation states also agree with the missing Jahn-Teller distortion in $LiMn_{0.5}Ni_{0.5}O_2$ as both ions are not Jahn-Teller active in these charge states in contrast to their 3+ ions. In general, the results indicate that a critical range of difference in electron affinity exists. In this range delocalizations of electrons over the TMs can appear. At smaller differences in electron affinity, both species show the same oxidation state and at larger differences one species is fully oxidized and the other fully reduced. Therefore, it becomes evident that the anomalous lower electronegativity of Mn compared to Co and Ni is the main challenge in predicting the correct electronic structure for mixtures comprising of Mn, Ni, and/or Co. As mentioned above, the dependence of α on localization/delocalization of partial charges between Co and Mn for $LiCo_{0.5}Mn_{0.5}O_2$ prevents a fair comparison of electronic structures at different α for this composition. By applying an effective Hubbard correction of 5 eV to both Mn and Co, the localized charge states that were obtained in the calculations with 25 % HF mixing were successfully stabilized for the smaller mixing parameters. However, the calculated electronic structures were in a high-spin and not a low-spin configuration that was observed in the Hubbard-free calculations at α=25 %. This complex behavior of a simple binary system shows that

first, a carefully chosen α, for example by fitting to some additional input, is required and second, that a description via adjustment of α is desirable over correction by a bias potential (e.g., Hubbard). It is to expect that this effect becomes more severe in more practical ternary or quaternary systems underlining the importance of tuning α in the employed computational methods for layered TM oxides.

The aforementioned linear trend of increasing band gap with the HF mixing-parameter for the other materials except $LiCo_{0.5}Mn_{0.5}O_2$ can be explained by the tendency of over-localization of HF and over-delocalization of DFT-GGA. Adding more of the over-localized part widens the band gap by diminishing electron density between the ions. This trend is visualized by the charge-density-difference (CDD) plots in Figure 5.3 showing the computed CDD for $LiCoO_2$, $LiMnO_2$, and $LiNiO_2$ at various HF mixing-parameters with respect to PBE.

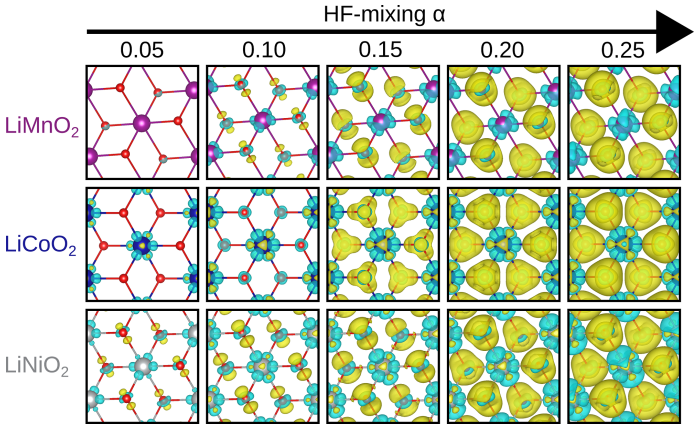

Figure 5.3: Charge density differences (CDDs) of $LiMnO_2$, $LiCoO_2$, $LiNiO_2$ (from top to bottom) at different HF mixing-parameters ranging from 5 % to 25 % (from left to right) relative to their PBE density (HF mixing of zero). All iso-surfaces are shown at an iso-value of 2.5×10^{-3} electrons/Å^3, while electron accumulation is indicated by yellow color and electron depletion by turquoise color.

The CDD plots show a depletion of electrons around the TM ions that is centered along the TM-O bonds and for $LiCoO_2$ and $LiNiO_2$ also a small accumulation between the TM-O bonds. The shapes of these depletions are in agreement with Jahn-Teller distortions in $LiNiO_2$ and $LiMnO_2$ as $LiMnO_2$ shows no depletion along the elongated axis of the of the coordination octahedron, while $LiNiO_2$ shows a spatially expanded depletion along the elongated axis. In general, differences become stronger at higher mixing parameters and are relatively similar for $LiCoO_2$ and $LiNiO_2$ (despite the Jahn-Teller distortion in $LiNiO_2$), while weaker for $LiMnO_2$. Although the computed CDD on TMs coincides with the picture of localizing the electrons stronger onto the ion cores by adding more HF mixing, the CDD on oxygens shows the opposite trend: an electron depletion is observed on O anions which increases with α. However, a significant accumulation of electrons along the O-TM bonds from oxygen is also observed for α=0.15, 0.20, and 0.25, distributing more homogeneously around O-TM bonds at higher HF mixings. This indicates delocalization of oxygen electrons. These results outline the holistic approach

of changing HF mixing to tune the electronic structure rather than using more local corrections. However, it must be noted that the shown changes in CDD are overall small but allow for qualitative statements about trends in localization/delocalization.

To further comment on the hybridization of O *2p*-orbitals and TM *3d*-orbitals a degree of hybridization η as described in Equation 5.4 was defined by integrating the projected densities of states (pDOS). Consequently, η can take values between 0 and 1 where 1 is maximal hybridization ($pDOS_{O_{2p}} = pDOS_{TM_{3d}}$) and 0 indicates no overlap of the different pDOS (no hybridization).

$$\eta = 1 - \frac{\int_a^b \left| pDOS_{O_{2p}} - pDOS_{TM_{3d}} \right| dE}{\int_a^b pDOS_{O_{2p}} dE + \int_a^b pDOS_{TM_{3d}} dE} \tag{5.4}$$

It can be assumed that the high energy states are most important for hybridization and therefore the energy range was set to a=-2 to b=0 eV where 0 eV corresponds to the Fermi-Level. A similar hybridization measurement in the same energy range was also employed by Seo *et al.* [6] for $LiCoO_2$, allowing for comparison to their study. As spin-polarized calculations were performed, both, spin-up and spin-down pDOS were considered separately and added to plot the degree of hybridization versus the HF mixing-parameter in Figure 5.4.

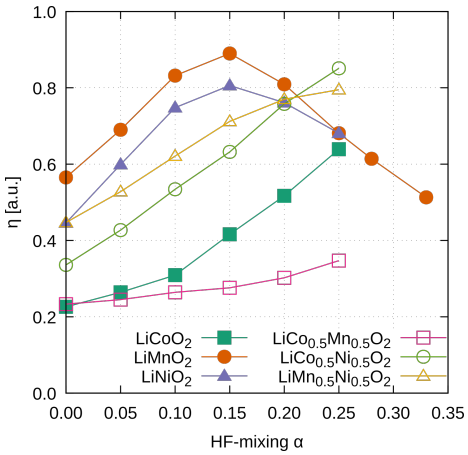

Figure 5.4: Dependency of the degree of hybridization η of O *2p*- and TM *3d*-orbitals as defined in Equation 5.4 on the HF mixing-parameter α for the different layered TM oxides under investigation.

Hybridization in $LiCoO_2$ increases almost exponentially with the HF mixing in Figure 5.4 which is in agreement to the aforementioned study by Seo *et al.* [6]. Generally, different trends can be observed for the materials varying from a linear increase of hybridization with α (e.g., $LiCo_{0.5}Ni_{0.5}O_2$) to a parabola shape with a maximum in hybridization at a HF mixing of 15 % (e.g., $LiMnO_2$ and $LiNiO_2$). The hybridization trend in Figure 5.4 is mainly governed by the change in the intensity of the TM and O pDOS plots in Figure 5.6. The TM pDOS for $LiCoO_2$ has the strongest intensity right below the Fermi level and the intensities of the O pDOS become closer to TM pDOS at higher HF mixing

but never reach the TM pDOS intensities. $LiMnO_2$ shows the same trend but at 15 % HF-mixing both pDOS are almost the same and at higher mixing the intensities of the O pDOS exceeding the TM pDOS. These behaviors result in the trends observed in the hybridization plot in Figure 5.4. It could be argued that the *d*-orbital splitting influences which *d*-orbitals are located directly below the Fermi-Level and are therefore available for a hybridization with O *2p*-orbitals. As a consequence, the strongly Jahn-Teller distorted materials ($LiMnO_2$ and $LiNiO_2$) show a more different behavior of hybridization and HF mixing because of their electronic configuration.

5.3.2 Single-shot *GW* band gaps at different PBE0 HF mixing-parameters and optimal HF mixing

Having shown that variation of the HF-mixing parameters has an significant influence on certain important properties such as band gap and hybridization it was proceeded by performing G_0W_0 calculations to identify the most suitable HF mixing-parameter. Consecutive G_0W_0 calculations were performed on top of all the PBE0 calculations at different HF mixings discussed in the previous section. This procedure allows to consider and analyse the strong starting-point dependence of G_0W_0 calculations. The band gaps obtained from these calculations are shown in the upper plot of Figure 5.5.

In general, the G_0W_0 band gaps maintain the rising trend of the underlying starting point with higher mixing parameters α but a perfect linear increase in band gaps with the HF mixing as observed for the PBE0 calculations (cf. Fig. 5.2) is not obtained. The consecutive G_0W_0 step shows no linearity at higher HF mixings (e.g., $LiMnO_2$) as well as low HF mixings (e.g., $LiNiO_2$). The latter trend is particularly pronounced for TM oxides which change their class by adding a small portion of HF mixing from metal (have no band gap) to insulator (have band gap) as shown by the non-linear fit for $LiNiO_2$ in Figure 5.5, upper plot. It should be also noted that the irregular behavior of the band gap of $LiCo_{0.5}Mn_{0.5}O_2$ due to the aforementioned changes in electronic structure with α is also present in the G_0W_0 calculations.

For intermediate α (5-20 %) the trend of the band gaps is reasonably approximated by a linear function indicated by the linear fits (dashed lines in Figure 5.5, upper plot) except for $LiCo_{0.5}Mn_{0.5}O_2$ due to the aforementioned irregular behavior of the electronic structure with α. Despite this trend it is still unclear what HF mixing acts as the most accurate starting point for G_0W_0 calculations for the layered TM oxides under study.

The linear (band gap vs. α) functions fitted (cf. upper Fig. 5.5 and Table 5.4) for the 5 to 20 % α-range allow to extrapolate to a G_0W_0@PBE solution. This extrapolation is particularly useful for compositions undergoing a change from metal to insulator by admixing HF (e.g. $LiNiO_2$). In that case PBE has no band gap and is therefore a unsuitable starting point that is far off the more linear trend observed at higher HF mixing-parameters. This might be because of an incorrect alignment of states in the starting point and/or a larger difference of the starting point wave-functions to the *GW* wave-functions. For $LiCoO_2$, this extrapolated G_0W_0@PBE band gap is only slightly higher (less than 0.2 eV) than the band gap calculated from the "real" PBE starting point. A pure PBE starting point is already quite suitable for $LiCoO_2$ because it predicts the metal-insulator properties correctly. However, for $LiNiO_2$, where pure PBE predicts a metal, the extrapolated band gap increases more drastically. The proposed extrapolation method is intrinsically

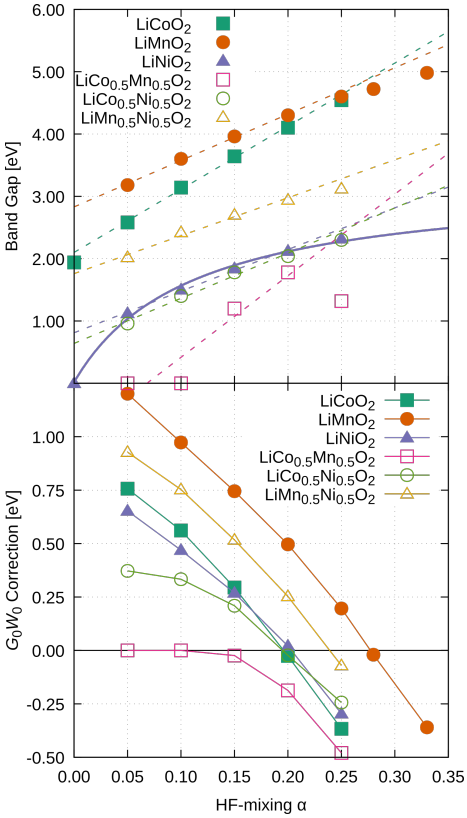

Figure 5.5: The upper plot shows G_0W_0 band gaps as function of the HF mixing-parameter α in the PBE0 starting point. Linear fits for the values in the α-range 5-20 % are shown by dashed lines and for $LiNiO_2$ also a fit of an inverse function that describes the whole α-range seemingly well is plotted by a solid line. The lower plot shows the corrections G_0W_0 made to the band gap of the PBE0 starting point.

ab initio-based as no experimental inputs are required. It should be noted that neither the linear fit nor the extrapolation approach have an physical meaning but employing these strategies seems to offer the best compromise between under- and over-prediction of band gaps compared to experimental values, especially for $LiCoO_2$ and $LiNiO_2$ for which most experimental values exist.

For $LiCoO_2$, the extrapolated G_0W_0@PBE band gap of 2.10 eV perfectly matches the band gap of a very recent experimental study that determined a band gap of 2.15 eV [73] and another experimental value of 2.10 eV [74] (the experimental structures were O3 but it was checked that the calculations of the O1 structures for $LiCoO_2$ do not change significantly by using O3). Despite this excellent agreement with the experiments it is also worth noting that experimental band gap studies show quite some deviations and even a value of 2.7 eV [75] has been reported such that the calculated value is at the lower edge of experimental band gaps. For $LiNiO_2$, the experimental studies are more sparse but one study suggested a band gap of 0.40 eV [27] which is significantly lower compared to the

extrapolated G_0W_0@PBE band gap of 0.81 eV. However, deviations would be even worse by using a starting point with (higher) HF mixing and also a pure PBE starting point would show almost the same deviation but in a different direction (under-prediction) and predicts metallic instead of insulator properties. For $LiMnO_2$, some theory works exist that predict various band gap values, depending on structure, magnetism, and computational approach, about 1 eV lower compared to the extrapolated G_0W_0@PBE band gap [76, 77]. As the $LiMnO_2$ model considered a strong Jahn-Teller distortion along with AFM ordering which are both known to increase the band gap, it is also expected that the band gap of this material is comparably high. No final conclusion about its accuracy in the extrapolated G_0W_0@PBE approach can be made for $LiMnO_2$.

In conclusion, it seems that the extrapolated G_0W_0@PBE band gaps are in reasonable agreement to experimental data and also work considerably well for all layered TM oxides under study (except $LiCo_{0.5}Mn_{0.5}O_2$ due to the aforementioned changes in the electronic structure with α). However, it must be mentioned that the seemingly good agreement to experimental band gaps might be due to error cancellation as direct comparisons to experiment are not completely fair. The calculations yield 0 K band gaps while the experimental values were obtained at finite temperatures. Moreover, the model used in the simulations of stoichiometric $LiNiO_2$ might not represent the experimental structure exactly which has been observed to be non-stoichiometric, as discussed in the method part. This can also accidentally improve the agreement to experiment.

Using these extrapolated G_0W_0@PBE band gaps to determine the corresponding optimal HF-mixing parameters ($\alpha^{\text{ext.}}$) for PBE0 is straight forward due to the linear trend of band gap vs. α. The corresponding optimal $\alpha^{\text{ext.}}$ values are shown in Table 5.1 along with their band gaps and are also visualized in Figure 5.2. For $LiCo_{0.5}Mn_{0.5}O_2$ no mixing parameter could be determined because of the irregular behavior of electronic structure and α explained in the previous section.

Table 5.1: Optimal PBE0 HF mixing-parameters determined by extrapolated G_0W_0@PBE ($\alpha^{\text{ext.}}$) and the PBE0 HF mixing-parameter that directly leads to the fully self-consistent *GW* band gaps (α^{GW}). Band gaps (BG) corresponding to the determined α are given along with experimental band gaps, where available. No values for $LiCo_{0.5}Mn_{0.5}O_2$ are given as the changes in the electronic structure with α prevented to apply any fitting approach.

Compound	$\alpha^{\text{ext.}}$ [%]	$\text{BG}^{\text{ext.}}$ [eV]	α^{GW} [%]	BG^{GW} [eV]	$\text{BG}^{\text{exp.}}$ [eV]
$LiCoO_2$	6.7	2.10	20	4.13	2.10 [74], 2.15 [73], 2.70 [75]
$LiMnO_2$	11	2.83	28	4.77	-
$LiNiO_2$	8.0	0.81	20	2.09	0.40 [27]
$LiCo_{0.5}Mn_{0.5}O_2$	-	-	-	-	-
$LiCo_{0.5}Ni_{0.5}O_2$	5.6	0.64	20	2.06	-
$LiMn_{0.5}Ni_{0.5}O_2$	11	1.76	24	3.10	-

The optimal mixing parameters vary within a range of roughly 5 % which is relatively large as a change in band gap of up to 0.75 eV can arise for these compounds from this

variation. The optimal $\alpha^{\text{ext.}}$ for the binary systems cannot be extrapolated as mean value of the corresponding pure materials independent if the charges of the individual species change from the pure and binary system ($LiMn_{0.5}Ni_{0.5}O_2$) or not ($LiCo_{0.5}Ni_{0.5}O_2$). Therefore, the optimal mixing parameter seems to be system-depended and using the mean value over all compositions of ca. 8.5 % appears to be the efficient trade off for all compositions. This HF mixing is significantly lower than the default value of 25 % but in agreement with other studies on similar (layered) TM oxides that rely directly or indirectly on experimental properties and also suggested significantly lower HF mixing-parameters for hybrid functionals [6, 14, 35].

The corrections in the band gap G_0W_0 is introducing to the PBE0 starting point, namely the differences in each point of Figure 5.2 and the upper plot in Figure 5.5, are visualized in the lower plot of Figure 5.5. In general, a pronounced increase of the band gap by G_0W_0 to the PBE0 starting point (positive correction) is observed for small α that gets smaller for higher α and even turns into a decrease (negative correction) for high α. This behavior can be utilized to define a different optimal HF mixing α^{GW} for each compound at the point were the PBE0 starting band gap is not altered by a consecutive G_0W_0 calculation (correction is zero in lower plot of Figure 5.5). It should be noted that this α^{GW} fitting-approach was also proposed by Chen *et al.* [38]. In agreement to their study, it was also found that the determined optimal α^{GW} values using this zero-correction approach are higher than those agreeing better to experimental values (e.g., aforementioned $\alpha^{\text{ext.}}$). It should be mentioned that the seemingly worse agreement to the experimental band gaps of the higher level of theory approach (α^{GW}) compared to the extrapolated G_0W_0@PBE approach might be due to error cancellations in the latter approach or fundamental differences of experiment and calculation (e.g., temperature, model/structure) as discussed above. Such error cancellations were also discussed in the work of Wiktor *et al.* [78] where G_0W_0@PBE delivered the best agreement to experimental values for perovskites of the type CsPbX (X = Cl, Br, and I), even better than fully self consistent (in eigenvalues and wave functions) *GW* calculations with vertex correction. The authors also showed that when accounting for effects such as temperature and spin-orbit coupling the higher level method is again in better agreement with experiment and concluded that without these corrections G_0W_0@PBE showed better agreement to experimental band gaps because of error cancellations. A similar cancellation could also be present in the extrapolated G_0W_0@PBE approach for the materials in this work.

The optimal α^{GW} along with their corresponding band gaps for the studied layered TM oxides in this work are shown in Table 5.1 and are visualized in Figure 5.2. Interestingly, these values and especially the mean value of 22 % are close to the default value of 25 % that has been derived by perturbation theory approaches [33] as well as the value of 19 % obtained by xc kernel-analysis in a very recent study [79]. Therefore, values of 20 % to 25 % appear to have a strong theoretical foundation in general and also for layered TM oxides. It is worth mentioning that the optimal α^{GW} of the binary systems seems to be predictable as mean values of the α^{GW} of the pure materials. For example, $LiCoO_2$ and $LiNiO_2$ both have an optimal α^{GW} value of 20 % and so does their binary mixture ($LiMn_{0.5}Ni_{0.5}O_2$) has a value of 20 % as well. $LiMn_{0.5}Ni_{0.5}O_2$ shows an optimal mixing α^{GW} of 24 % which is exactly the mean value of the pure materials, 20 % ($LiNiO_2$) and 28 % ($LiMnO_2$), respectively. Moreover, this predictive behavior was also verified for the

ternary system (Co:Mn:Ni = 1:1:1) of species under study that showed an optimal α^{GW} of 22.5 % which is essentially the sum of the optimal α^{GW} parameters of the pure compounds weighted by their concentration in the ternary system. This linear dependence of optimal α^{GW} on the concentrations of constituting elements is different to optimal $\alpha^{\text{ext.}}$ where no trend was observed but allows to immediately predict α^{GW} for mixed compounds.

Regarding the computed DOS below the Fermi energy, it can be concluded that no significant change by the consecutive G_0W_0 step is observed and almost the same features as in the PBE0 starting points (Figure 5.6) appear. Consequently, also the same trends in terms of hybridization of O *2p*-orbitals and Co/Mn *3d*-orbitals as discussed for Figure 5.4 in the previous section can be observed proving again that hybrids are a rather advanced starting point for *GW* calculations.

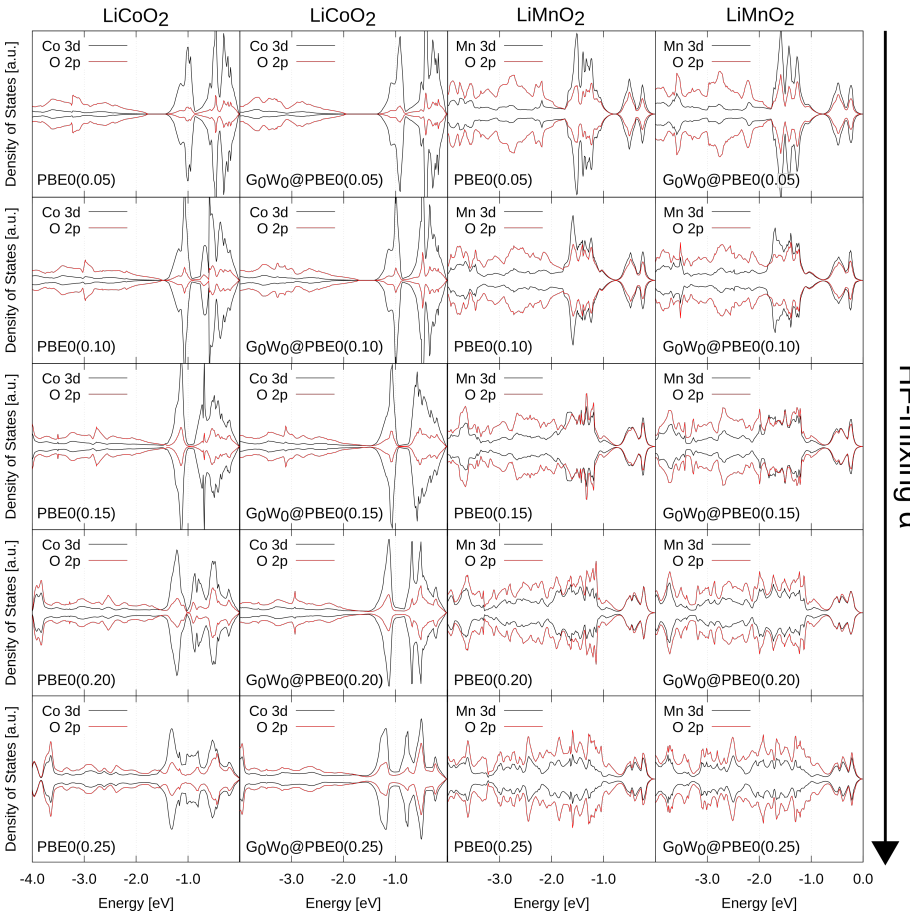

Figure 5.6: pDOS of O *2p*-orbitals (red) and TM *3d*-orbitals (black) for $LiCoO_2$ (first column) and $LiMnO_2$ (third column) at increasing HF mixing (top to bottom) along with the pDOS obtained from a consecutive G_0W_0 step (second and fourth column).

5.3.3 Fully self consistent *GW* calculations at different PBE0 HF mixing-parameters and influence of screening the HF part

To further verify the obtained trends within the G_0W_0 approach, a higher level of *GW* was also employed where eigenvalues were iterated to self-consistency in *G* and *W* (sometimes also denoted as "ev*GW*") for $LiCoO_2$ and $LiNiO_2$. In general, it is expected that this approach has a tendency to over-predict band gaps due to missing vertex corrections [58]. A tendency towards larger band gaps is also observed for the layered TM oxides in this study (cf. Figure 5.7). However, an excellent agreement with the experimental value of 2.7 eV [75] is found for $LiCoO_2$ by applying fully self-consistent *GW* at a PBE starting point. Overall, the calculated band gaps get closer to their corresponding converged values with increasing the number of *GW* iterations but the self-consistent results still maintain (strongly) starting point dependent as also found in another study on a different TM oxide and can be related to different starting wave functions [57, 58].

For $LiCoO_2$ and $LiNiO_2$, the converged *GW* band gaps become larger with higher HF mixing in the starting point, are lowered by *GW* for mixings above 20 % (the determined optimal α^{GW} in the previous section), and increased for lower mixing values. The results also show that the number of steps to converge the band gaps strongly varies with the HF mixing in the starting point and is larger the more different the initial mixing parameter is from the optimal mixing-parameter α^{GW}. In fact, optimal α^{GW} (20 %) that were obtained in the previous section do not show a significant change in band gap over all performed *GW* steps proving that this approach of determining the optimal α^{GW} delivers direct access to fully self-consistent *GW* band gaps at the computational cost of a hybrid functional. That the optimal α^{GW} mixing parameters are not just consistent in G_0W_0 but also in *GW* underlines their strong theoretical foundation.

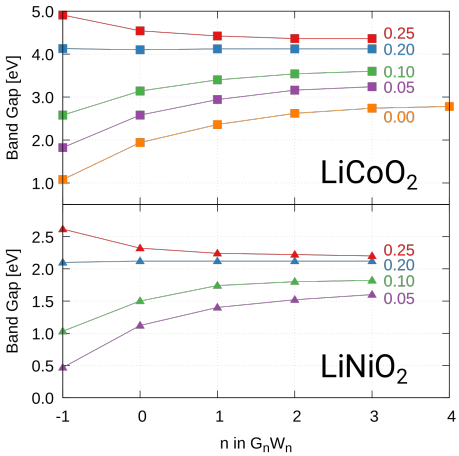

Figure 5.7: Band gaps of iterations (*n*) of fully self-consistent *GW* calculations with different PBE0 starting points for $LiCoO_2$ (upper plot) and $LiNiO_2$ (lower plot). Iteration n=−1 corresponds to the PBE0 band gap and n=0 to the G_0W_0 band gap.

Lastly, also the effect of applying range-separated hybrid functionals with screening in the HF part (HSE approach) compared to the unscreened PBE0 functional was in-

vestigated as this approximation can offer some computational benefits [40]. The two inverse screening length of $\omega = 0.3$ Å^{-1} (HSE03) [40] and $\omega = 0.2$ Å^{-1} (HSE06) [41] were employed and the results were compared to those with PBE0. Their dependence of the band gap and the HF mixing-parameter is plotted in Figure 5.8, indicating an almost perfectly linear trend (minor deviations for $LiNiO_2$ with HSE at high mixing and screening parameters) as observed for PBE0 in this study as well as in other studies with HSE functionals [6, 80].

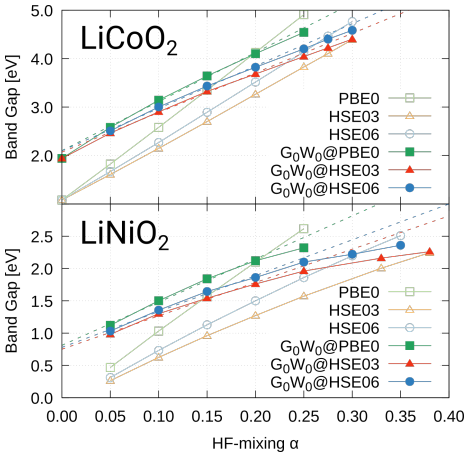

Figure 5.8: G_0W_0 and hybrid functional band gaps for $LiCoO_2$ (upper plot) and $LiNiO_2$ (lower plot) for hybrid functional starting points with different mixing parameters and different screenings of the HF part (HSE06, HSE03). The linear functions for the extrapolated G_0W_0@PBE band gaps are indicated by the dashed lines.

HSE06 band gaps are slightly higher but in fair agreement with the computational HSE06 study of Seo *et al.* [6] for $LiCoO_2$ and $LiNiO_2$. In agreement with the studies of Komsa *et al.* [80], the slopes of linear fits become smaller with higher ω and consequently higher HF mixing-parameters are required to obtain the same band gaps compared to PBE0. Applying G_0W_0 to the HSE starting points also yields deviations from the linear trend as for PBE0 resulting in a crossing point of both approaches that allows for the determination of an optimal α^{GW}. At this α G_0W_0 (and as discussed above also higher levels of *GW*) causes no correction to the band gap of the bare hybrid functional (cf. Figure 5.8). The corresponding optimal mixing parameters α^{GW} are 25 % ($LiCoO_2$-HSE06), 30 % ($LiNiO_2$-HSE06), 30 % ($LiCoO_2$-HSE03), and 38 % ($LiNiO_2$-HSE03). For HSE03 the parameters are higher than the default of 25 %, while for HSE06 both values are fairly close to 25 %. This proves the superior fitting of the screening parameter in HSE06 over HSE03 for the investigated layered TM oxides as the mixing parameter was fixed to 25 % in HSE, while technically both, the mixing parameter and the screening parameter could be fitted (to some extend) to obtain the same result [41, 81]. This shows that the default HF mixing within the HSE06 functional can be reasoned quite well by the α^{GW} fitting-approach for the layered TM oxides. However, in contrast to the PBE0 case the optimal α^{GW} mixing parameter becomes composition-dependent for $LiCoO_2$ and $LiNiO_2$ when screening is introduced. The flatter slope that comes along with higher screen-

ing has the beneficial effect that the band gaps become less sensitive to the HF mixing. Even though the determined $LiNiO_2$-HSE06 optimal mixing parameter α^{GW} is with 30 % slightly higher than the default, the pure hybrid band gap and the corresponding G_0W_0 solution are already relatively close at 25 % (cf. Figure 5.8).

Note that computed band gaps using the optimal α^{GW} values corresponding to each screening are almost the same for all functionals (PBE0, HSE03, HSE06) with a small drift towards higher values at higher ω. This proves that the determined band gaps using $\alpha^{GW}(\omega)$ show a high consistency across several high-level theory methods constituting them as promising candidates for describing layered TM oxides. Although the $\alpha^{GW}(\omega)$ over-predicts the experimental band gaps of the materials under study, it is reasonably close to the default mixing values of the functionals as mentioned above.

The screened hybrids also allow for the extrapolated G_0W_0@PBE approach which showed better agreement to experimental band gaps for PBE0 in the previous section. As this approach tries to extrapolate to PBE level, using HSE functionals should not alter the extrapolated band gaps as the differences to PBE0 are just in the HF part that should be eliminated by the extrapolation. Indeed, the linear fits in Figure 5.8 (dashed lines) show the same extrapolated G_0W_0@PBE band gaps for all functionals within an accuracy way below 0.1 eV. This proves that extrapolating the trends of the G_0W_0 band gaps by a linear function in the intermediate α-range of 5-20 % is reasonable for the layered TM oxides in this study. Moreover, the usage of screened hybrids can slightly reduce the enormous computational effort of this approach as they offer a computational performance advantage over PBE0 [40]. Applying extrapolation, optimal mixing parameters $\alpha^{\text{ext.}}$ of 8.5 % ($LiCoO_2$-HSE06), 11 % ($LiNiO_2$-HSE06), 9.2 % ($LiCoO_2$-HSE03), and 12 % ($LiNiO_2$-HSE03) can be determined. Compared to PBE0, the optimal $\alpha^{\text{ext.}}$ are higher because the band gaps are the same but the slopes of the linear trends of the band gap and α become smaller for higher screenings as mentioned above. The robustness of extrapolated G_0W_0@PBE towards different hybrid functionals based on PBE along with the reasonable agreement to experimental results is quite encouraging for the idea of extrapolating band gaps from descriptions with wave functions and alignment of states more close to *GW*, namely hybrid functionals. This approach can be utilized to determine *ab initio* band gaps in layered TM oxides close to experimental values.

5.4 Summary and Conclusion

Two different non-empirical fitting approaches to determine the HF mixing parameter in PBE-based hybrids were presented to calculate electronic structures of layered TM oxides. While one approach yields satisfactory agreement to experiment for $LiCoO_2$ and $LiNiO_2$, the other, despite its stronger theory foundation, overpredicts band gaps of $LiCoO_2$ and $LiNiO_2$ compared to experimental values significantly. The first approach suggests low optimal mixing parameters of $\alpha^{\text{ext.}} \approx 8.5$ % and the second fitting approach yields optimal mixing of $\alpha^{GW} \approx 22$ % which is in fair agreement to default mixing of 25 % employed in hybrid functionals such as PBE0, HSE03, and HSE06. The first fitting approach was defined by extrapolation of G_0W_0 band gaps to G_0W_0@PBE band gaps using G_0W_0@PBE0 band gaps with intermediate mixing parameters in the range of 5-20 %. It was also shown that almost same extrapolated G_0W_0@PBE band gaps can be fitted from G_0W_0 calculations at screened PBE-based hybrid functionals (HSE). However, for these

screened hybrids, the corresponding optimal mixing increases with the screening parameter. For the second fitting approach, the HF mixing that directly yields the band gap of a consecutive G_0W_0 calculation was chosen. It was proven that this mixing parameter is also valid at fully self-consistent *GW*, allowing access to accurate *GW* band gaps at the much lower computational cost of hybrid functionals. For screened hybrid functionals strong variation in optimal mixing $\alpha^{GW}(\omega)$ depending on screening ω was found but only minor changes in the corresponding computed band gap. Moreover, dependence of optimal mixing α^{GW} and concentration of elements in the studied composition shows linearity, allowing for the prediction of optimal HF mixing.

It is encouraging that (extrapolated) G_0W_0@PBE appears to obtain band gaps from purely computational methods that are in reasonable agreement with experiment and also that the default mixing of 25 % is justified not just by perturbation theory but also high level *GW* calculations. Further works, however, are required to understand the large discrepancy between the optimal $\alpha^{\text{ext.}}$ (close to experimental band gap) and α^{GW} (strong theory foundation) HF mixing-parameters in hybrids that was shown by the two different non-empirical *GW* fitting approaches in this work as well as if the better agreement to experiment of the lower level of theory approach ($\alpha^{\text{ext.}}$) might be caused by error cancellations.

Supporting Information

Supplementary Table 5.2: Fitted linear functions of the form $BG(\alpha) = a \times \alpha + b$ of the PBE0 band gaps (BG) as function of the HF mixing-parameter α.

Compound	a [eV]	b [eV]
$LiCoO_2$	15.436 ± 0.062	1.042 ± 0.010
$LiMnO_2$	12.054 ± 0.126	1.399 ± 0.021
$LiNiO_2$	10.732 ± 0.105	-0.052 ± 0.017
$LiCo_{0.5}Mn_{0.5}O_2$	11.136 ± 2.651	-0.672 ± 0.440
$LiCo_{0.5}Ni_{0.5}O_2$	9.820 ± 0.045	0.094 ± 0.007
$LiMn_{0.5}Ni_{0.5}O_2$	10.440 ± 0.168	0.599 ± 0.028

Supplementary Table 5.3: Calculated unpaired electrons (UPE) for the ions in the studied compounds and charges estimated from UPE assuming octahedral ligand-field splitting of *d*-orbitals at 25 % HF-mixing. As discussed in the text, average UPE/charges over all ions of one species are given for $LiCo_{0.5}Mn_{0.5}O_2$

Compound	UPE			Charges		
	Co	Mn	Ni	Co	Mn	Ni
$LiCoO_2$	0.0	-	-	3	-	-
$LiMnO_2$	-	3.7	-	-	3	-
$LiNiO_2$	-	-	0.9	-	-	3
$LiCo_{0.5}Mn_{0.5}O_2$	0.4	2.3	-	2.7	3.3	-
$LiCo_{0.5}Ni_{0.5}O_2$	0.0	-	0.9	3	-	3
$LiMn_{0.5}Ni_{0.5}O_2$	-	3.0	1.6	-	4	2

Supplementary Table 5.4: Parameters of the linear fits ($f(\alpha) = a \times \alpha + b$) for G_0W_0@PBE0 band gaps against different PBE0 HF mixing-parameters α in the range of 5 % to 20 %. The *y*-intercepts *b* correspond to the discussed extrapolated G_0W_0@PBE band gaps.

Compound	a [eV]	b [eV]
$LiCoO_2$	10.128 ± 0.317	2.101 ± 0.043
$LiMnO_2$	7.440 ± 0.259	2.831 ± 0.036
$LiNiO_2$	6.680 ± 0.318	0.811 ± 0.043
$LiCo_{0.5}Mn_{0.5}O_2$	13.086 ± 3.161	-0.891 ± 0.433
$LiCo_{0.5}Ni_{0.5}O_2$	7.246 ± 0.578	0.640 ± 0.079
$LiMn_{0.5}Ni_{0.5}O_2$	6.086 ± 0.522	1.760 ± 0.071

REFERENCES

1. Wang, L., Maxisch, T. & Ceder, G. Oxidation energies of transition metal oxides within the GGA+U framework. *Physical Review B* **73** (2006).
2. Lany, S. Band-structure calculations for the 3 d transition metal oxides in GW. *Physical Review B* **87** (2013).
3. Diebold, U., Anderson, J. F., Ng, K. O. & Vanderbilt, D. Evidence for the Tunneling Site on Transition-Metal Oxides: TiO2(110). *Physical review letters* **77,** 1322–1325 (1996).
4. Sakuma, R. & Aryasetiawan, F. First-principles calculations of dynamical screened interactions for the transition metal oxides M O (M =Mn, Fe, Co, Ni). *Physical Review B* **87** (2013).
5. Graetz, J., Ahn, C. C., Ouyang, H., Rez, P. & Fultz, B. White lines and d -band occupancy for the 3d transition-metal oxides and lithium transition-metal oxides. *Physical Review B* **69** (2004).
6. Seo, D.-H., Urban, A. & Ceder, G. Calibrating transition-metal energy levels and oxygen bands in first-principles calculations: Accurate prediction of redox potentials and charge transfer in lithium transition-metal oxides. *Physical Review B* **92** (2015).
7. Myung, S.-T. *et al.* Nickel-Rich Layered Cathode Materials for Automotive Lithium-Ion Batteries: Achievements and Perspectives. *ACS Energy Letters* **2,** 196–223 (2017).
8. Wang, P.-.-F., You, Y., Yin, Y.-.-X. & Guo, Y.-.-G. Layered Oxide Cathodes for Sodium–Ion Batteries: Phase Transition, Air Stability, and Performance. *Advanced Energy Materials* **8** (2018).
9. Mizushima, K., Jones, P. C., Wiseman, P. J. & Goodenough, J. B. LixCoO2 (0<x<-1): A new cathode material for batteries of high energy density. *Materials Research Bulletin* **15,** 783–789 (1980).
10. Nishi, Y. The Dawn of Lithium-Ion Batteries. *Interface magazine* **25,** 71–74 (2016).
11. Ohzuku, T., Ueda, A. & Nagayama, M. Electrochemistry and Structural Chemistry of LiNiO2 (R3m) for 4 Volt Secondary Lithium Cells. *Journal of The Electrochemical Society* **140,** 1862–1870 (1993).
12. Armstrong, A. R. & Bruce, P. G. Synthesis of layered LiMnO2 as an electrode for rechargeable lithium batteries. *Nature* **381,** 499–500 (1996).
13. Chakraborty, A. *et al.* Layered Cathode Materials for Lithium-Ion Batteries: Review of Computational Studies on LiNi 1– x – y Co x Mn y O 2 and LiNi 1– x – y Co x Al y O 2. *Chemistry of Materials* **32,** 915–952 (2020).

14. Singh, V., Kosa, M., Majhi, K. & Major, D. T. Putting DFT to the test: a first-principles study of electronic, magnetic, and optical properties of Co3O4. *Journal of chemical theory and computation* **11,** 64–72 (2015).

15. Genreith-Schriever, A. R. *et al.* Oxygen hole formation controls stability in LiNiO2 cathodes. *Joule* **7,** 1623–1640 (2023).

16. Iori, F., Gatti, M. & Rubio, A. Role of nonlocal exchange in the electronic structure of correlated oxides. *Physical Review B* **85** (2012).

17. Lines, M. E. Influence of d orbitals on the nonlinear optical response of transparent transition-metal oxides. *Physical review. B, Condensed matter* **43,** 11978–11990 (1991).

18. Peng, H. & Lany, S. Semiconducting transition-metal oxides based on d5 cations: Theory for MnO and Fe 2 O 3. *Physical Review B* **85** (2012).

19. Rödl, C., Fuchs, F., Furthmüller, J. & Bechstedt, F. Quasiparticle band structures of the antiferromagnetic transition-metal oxides MnO, FeO, CoO, and NiO. *Physical Review B* **79** (2009).

20. Jain, M., Chelikowsky, J. R. & Louie, S. G. Reliability of hybrid functionals in predicting band gaps. *Physical review letters* **107,** 216806 (2011).

21. Becke, A. D. A new mixing of Hartree–Fock and local density-functional theories. *The Journal of chemical physics* **98,** 1372–1377 (1993).

22. Eckhoff, M., Blöchl, P. E. & Behler, J. Hybrid density functional theory benchmark study on lithium manganese oxides. *Physical Review B* **101** (2020).

23. Chevrier, V. L., Ong, S. P., Armiento, R., Chan, M. K. Y. & Ceder, G. Hybrid density functional calculations of redox potentials and formation energies of transition metal compounds. *Physical Review B* **82** (2010).

24. Franchini, C., Bayer, V., Podloucky, R., Paier, J. & Kresse, G. Density functional theory study of MnO by a hybrid functional approach. *Physical Review B* **72** (2005).

25. Franchini, C., Podloucky, R., Paier, J., Marsman, M. & Kresse, G. Ground-state properties of multivalent manganese oxides: Density functional and hybrid density functional calculations. *Physical Review B* **75** (2007).

26. Wróbel, J., Kurzydłowski, K. J., Hummer, K., Kresse, G. & Piechota, J. Calculations of ZnO properties using the Heyd-Scuseria-Ernzerhof screened hybrid density functional. *Physical Review B* **80** (2009).

27. Anisimov, V. I., Zaanen, J. & Andersen, O. K. Band theory and Mott insulators: Hubbard U instead of Stoner I. *Physical review. B, Condensed matter* **44,** 943–954 (1991).

28. Vaugier, L., Jiang, H. & Biermann, S. Hubbard U and Hund exchange J in transition metal oxides: Screening versus localization trends from constrained random phase approximation. *Physical Review B* **86** (2012).

29. Zhou, F., Cococcioni, M., Marianetti, C. A., Morgan, D. & Ceder, G. First-principles prediction of redox potentials in transition-metal compounds with LDA+U. *Physical Review B* **70** (2004).

30. Bendavid, L. I. & Carter, E. A. Status in calculating electronic excited states in transition metal oxides from first principles. *Topics in current chemistry* **347,** 47–98 (2014).

31. Himmetoglu, B., Floris, A., de Gironcoli, S. & Cococcioni, M. Hubbard-corrected DFT energy functionals: The LDA+U description of correlated systems. *International Journal of Quantum Chemistry* **114,** 14–49 (2014).

32. Becke, A. D. Density-functional thermochemistry. IV. A new dynamical correlation functional and implications for exact-exchange mixing. *The Journal of chemical physics* **104,** 1040–1046 (1996).

33. Perdew, J. P., Burke, K. & Ernzerhof, M. Generalized Gradient Approximation Made Simple. *Physical review letters* **77,** 3865–3868 (1996).

34. Cortona, P. Note: Theoretical mixing coefficients for hybrid functionals. *The Journal of chemical physics* **136,** 086101 (2012).

35. House, R. A. *et al.* Delocalized electron holes on oxygen in a battery cathode. *Nature Energy* **8,** 351–360 (2023).

36. Feng, X. & Harrison, N. M. Magnetic coupling constants from a hybrid density functional with 35% Hartree-Fock exchange. *Physical Review B* **70** (2004).

37. Chen, W. & Pasquarello, A. Accuracy of GW for calculating defect energy levels in solids. *Physical Review B* **96** (2017).

38. Chen, W. & Pasquarello, A. Band-edge positions in GW : Effects of starting point and self-consistency. *Physical Review B* **90** (2014).

39. Sotoudeh, M. *et al.* Electronic structure of Pr1−xCaxMnO3. *Physical Review B* **95** (2017).

40. Heyd, J., Scuseria, G. E. & Ernzerhof, M. Hybrid functionals based on a screened Coulomb potential. *The Journal of chemical physics* **118,** 8207–8215 (2003).

41. Krukau, A. V., Vydrov, O. A., Izmaylov, A. F. & Scuseria, G. E. Influence of the exchange screening parameter on the performance of screened hybrid functionals. *The Journal of chemical physics* **125,** 224106 (2006).

42. Skone, J. H., Govoni, M. & Galli, G. Self-consistent hybrid functional for condensed systems. *Physical Review B* **89** (2014).

43. Kronik, L., Stein, T., Refaely-Abramson, S. & Baer, R. Excitation Gaps of Finite-Sized Systems from Optimally Tuned Range-Separated Hybrid Functionals. *Journal of chemical theory and computation* **8,** 1515–1531 (2012).

44. Refaely-Abramson, S., Jain, M., Sharifzadeh, S., Neaton, J. B. & Kronik, L. Solid-state optical absorption from optimally tuned time-dependent range-separated hybrid density functional theory. *Physical Review B* **92** (2015).

45. Miceli, G., Chen, W., Reshetnyak, I. & Pasquarello, A. Nonempirical hybrid functionals for band gaps and polaronic distortions in solids. *Physical Review B* **97** (2018).

46. Wruss, E., Zojer, E. & Hofmann, O. T. Distinguishing between Charge-Transfer Mechanisms at Organic/Inorganic Interfaces Employing Hybrid Functionals. *The Journal of Physical Chemistry C* **122,** 14640–14653 (2018).

47. De P. R. Moreira, I., Illas, F. & Martin, R. L. Effect of Fock exchange on the electronic structure and magnetic coupling in NiO. *Physical review. B, Condensed matter* **65** (2002).

48. Seo, D.-H. *et al.* The structural and chemical origin of the oxygen redox activity in layered and cation-disordered Li-excess cathode materials. *Nature chemistry* **8,** 692–697 (2016).

49. Konarov, A. *et al.* High–Voltage Oxygen–Redox–Based Cathode for Rechargeable Sodium–Ion Batteries. *Advanced Energy Materials* **10** (2020).

50. Hybertsen, M. S. & Louie, S. G. Electron correlation in semiconductors and insulators: Band gaps and quasiparticle energies. *Physical review. B, Condensed matter* **34,** 5390–5413 (1986).

51. Shishkin, M. & Kresse, G. Self-consistent GW calculations for semiconductors and insulators. *Physical Review B* **75** (2007).

52. Gerosa, M. *et al.* Electronic structure and phase stability of oxide semiconductors: Performance of dielectric-dependent hybrid functional DFT, benchmarked against GW band structure calculations and experiments. *Physical Review B* **91** (2015).

53. Shishkin, M. & Kresse, G. Implementation and performance of the frequency-dependent GW method within the PAW framework. *Physical Review B* **74** (2006).

54. Jiang, H., Gomez-Abal, R. I., Rinke, P. & Scheffler, M. First-principles modeling of localized d states with the GW@LDA+U approach. *Physical Review B* **82** (2010).

55. Klimeš, J., Kaltak, M. & Kresse, G. Predictive GW calculations using plane waves and pseudopotentials. *Physical Review B* **90** (2014).

56. Han, M. J., Kino, H. & Kotani, T. Quasiparticle self-consistent GW study of LaNiO3 and LaNiO3/LaAlO3 superlattice. *Physical Review B* **90** (2014).

57. Liao, P. & Carter, E. A. Testing variations of the GW approximation on strongly correlated transition metal oxides: hematite (α-Fe2O3) as a benchmark. *Physical chemistry chemical physics : PCCP* **13,** 15189–15199 (2011).

58. Fuchs, F., Furthmüller, J., Bechstedt, F., Shishkin, M. & Kresse, G. Quasiparticle band structure based on a generalized Kohn-Sham scheme. *Physical Review B* **76** (2007).

59. Blöchl, P. E. Projector augmented-wave method. *Physical review. B, Condensed matter* **50,** 17953–17979 (1994).

60. Kresse, G. & Furthmüller, J. Efficient iterative schemes for ab initio total-energy calculations using a plane-wave basis set. *Physical review. B, Condensed matter* **54,** 11169–11186 (1996).

61. Sugiyama, J. *et al.* Low-temperature magnetic properties and high-temperature diffusive behavior of LiNiO2 investigated by muon-spin spectroscopy. *Physical Review B* **82** (2010).

62. Delmas, C., Fouassier, C. & Hagenmuller, P. Structural classification and properties of the layered oxides. *Physica B+C* **99,** 81–85 (1980).

63. Chen, Z., Zou, H., Zhu, X., Zou, J. & Cao, J. First-principle investigation of Jahn–Teller distortion and topological analysis of chemical bonds in LiNiO2. *Journal of Solid State Chemistry* **184,** 1784–1790 (2011).

64. Perdew, J. P., Ernzerhof, M. & Burke, K. Rationale for mixing exact exchange with density functional approximations. *The Journal of chemical physics* **105,** 9982–9985 (1996).

65. Heyd, J. & Scuseria, G. E. Assessment and validation of a screened Coulomb hybrid density functional. *The Journal of chemical physics* **120,** 7274–7280 (2004).

66. Momma, K. & Izumi, F. VESTA : a three-dimensional visualization system for electronic and structural analysis. *Journal of Applied Crystallography* **41,** 653–658 (2008).

67. Wang, V., Xu, N., Liu, J.-C., Tang, G. & Geng, W.-T. VASPKIT: A user-friendly interface facilitating high-throughput computing and analysis using VASP code. *Computer Physics Communications* **267,** 108033 (2021).

68. Marianetti, C. A., Morgan, D. & Ceder, G. First-principles investigation of the cooperative Jahn-Teller effect for octahedrally coordinated transition-metal ions. *Physical review. B, Condensed matter* **63** (2001).

69. Singh, D. J. Magnetic and electronic properties of LiMnO2 s. *Physical review. B, Condensed matter* **55,** 309–312 (1997).

70. Cai, X. *et al.* Band-gap trend of corundum oxides $\alpha-$M2O3 (M=Co , Rh, Ir): An ab initio study. *Physical Review B* **108** (2023).

71. Koller, D., Blaha, P. & Tran, F. Hybrid functionals for solids with an optimized Hartree-Fock mixing parameter. *Journal of physics. Condensed matter : an Institute of Physics journal* **25,** 435503 (2013).

72. Viñes, F., Lamiel-García, O., Chul Ko, K., Yong Lee, J. & Illas, F. Systematic study of the effect of HSE functional internal parameters on the electronic structure and band gap of a representative set of metal oxides. *Journal of computational chemistry* **38,** 781–789 (2017).

73. Slima, I. B., Karoui, K. & Rhaiem, A. B. Ionic conduction, structural and optical properties of LiCoO2 compound. *Ionics* **29,** 1731–1739 (2023).

74. Kushida, K. & Kuriyama, K. Narrowing of the Co-3d band related to the order–disorder phase transition in LiCoO2. *Solid State Communications* **123,** 349–352 (2002).

75. van Elp, J. *et al.* Electronic structure of CoO, Li-doped CoO, and LiCoO2. *Physical review. B, Condensed matter* **44,** 6090–6103 (1991).

76. Nath Shukla, N. & Prasad, R. Electronic structure of LiMnO2: A comparative study of the LSDA and methods. *Journal of Physics and Chemistry of Solids* **67,** 1731–1740 (2006).

77. Kong, F. *et al.* Ab initio study of doping effects on LiMnO 2 and Li 2 MnO 3 cathode materials for Li-ion batteries. *Journal of Materials Chemistry A* **3,** 8489–8500 (2015).

78. Wiktor, J., Rothlisberger, U. & Pasquarello, A. Predictive Determination of Band Gaps of Inorganic Halide Perovskites. *The journal of physical chemistry letters* **8,** 5507–5512 (2017).

79. Moldabekov, Z. A., Lokamani, M., Vorberger, J., Cangi, A. & Dornheim, T. Nonempirical Mixing Coefficient for Hybrid XC Functionals from Analysis of the XC Kernel. *The journal of physical chemistry letters* **14,** 1326–1333 (2023).

80. Komsa, H.-P., Broqvist, P. & Pasquarello, A. Alignment of defect levels and band edges through hybrid functionals: Effect of screening in the exchange term. *Physical Review B* **81** (2010).

81. Moussa, J. E., Schultz, P. A. & Chelikowsky, J. R. Analysis of the Heyd-Scuseria-Ernzerhof density functional parameter space. *The Journal of chemical physics* **136,** 204117 (2012).

6

CASE STUDIES

In this chapter several additional works and contributions to other publications are summarized. Each section depicts one contribution to larger collaborative works. All works are briefly motivated and key findings are summarized with a clear focus on the contributions of the author. The sections therefore just cover a fraction of the original works and the interested reader is referred to the original publications instead. However, the summaries presented here aim to depict the most important computational findings and employed methodologies and therefore put the approaches developed in the previous chapters into perspective. Thus, the following sections can be understood as case studies for the methodologies presented in the previous chapters. The connections of the employed approaches to the purely theoretical previous chapters are discussed, as well as challenges encountered in simulational studies of real cathode materials. Furthermore, the importance of collaborative studies that combine experimental findings and simulation results is emphasized.

This chapter is based on the following publications:

1. Yu, J. H. & **Köster, K.** & Voronina, N., *et al.* Elevating Li-ion battery paradigms: Sophisticated ionic architectures in lithium-excess layered oxides for unprecedented electrochemical performance. eScience **5**, 4, 100376 (2025).
2. Binninger, T., Ting, Y.-Y., **Köster, K.**, *et al.* Simulating charging characteristics of lithium iron phosphate by electro-ionic optimization on a quantum annealer. Phys. Rev. B **112**, 174118 (2025). Copyright (2025) by the American Physical Society.
3. Voronina, N. & **Köster, K.**, Yu, J. H., *et al.* Synergetic Lattice and Surface Engineering: Stable High-Voltage Cycle Performance in P3-Type Layered Manganese Oxide. Adv. Energy Mater. **Early View**, 2501823 (2025).
4. Li, Y. & **Köster, K.**, Mazzio, K., *et al.* 'Oxygen bound to magnesium' as high voltage redox center causes sloping of the potential profile in Mg-doped layered oxides for Na-ion batteries. Adv. Funct. Mater. **Early View**, e19132 (2025).

6.1 A Li-rich Li-ion Layered Oxide Cathode Material:

Elevating Li-ion battery paradigms: Sophisticated ionic architectures in lithium-excess layered oxides for unprecedented electrochemical performance

Achieving high energy-density in cathode materials and accounting for economic and ecological aspects remains a significant challenge for the next generation of lithium-ion batteries. Many of the currently used cathode materials rely on cobalt and high nickel contents which drive up their price and also raise ecological and/or ethical concerns. Therefore, Mn-rich and Co-free cathode chemistries would be beneficial. Moreover, Li-rich materials (lithium concentration greater one with lithium also in the transition metal (TM) sites) bear the potential for increased capacities and higher voltages due to anionic (oxygen) redox [1]. However, such materials also possess the risk of low capacity retention caused, for example, by Mn-migration or irreversible oxygen loss [2, 3]. In this collaborative work with the group of Prof. Taek Myung from Sejong University a novel, Co-free, Mn-rich, and Li-rich layered oxide cathode for lithium-ion batteries: O2-$Li_{0.75}[Li_{0.15}Ni_{0.15}Mn_{0.7}]O_2$ was studied.

The group of Prof. Myung obtained the material by topotactic ion-exchange from the analogous sodium-based cathode material and also were in charge of the further experimental characterization techniques discussed in the publication. Employing the GOAC code (Chapter 2) to perform electrostatic configurational optimization, the author of this thesis was able to identify a honeycomb ordering with Ni and Li in the Mn-combs as the by far (4.7 eV in electrostatics compared to the lowest non-honeycomb structure) most favorable configuration. Such an ordering was also confirmed by an additional superstructure reflection in the experimental X-ray diffraction (XRD) measurements while the calculated structural model ultimately enabled a more accurate Rietveld refinement of the experimental structures. Moreover, the experimentally observed (*operando*-XRD) trends in changes in lattice parameters on (dis-)charging were mostly reproduced in the Machine Learning Force Field *Ab Initio* Molecular Dynamics (MLFF-AIMD) simulations performed by the author. In general, a trend of decreasing *a*- (*a* and *b* parameters are same in hexagonal cells) and *c*-lattice parameters was observed on charge. While the change in *a* can be assigned to stronger electrostatic oxygen and TM interactions upon oxidation of the TM and the change in *c* to a decrease in inter-layer spacing due to the reduced lithium concentration on charging.

The author continued by unveiling the charge compensation (redox) mechanism of the cathode material. Density functional theory (DFT) geometry optimizations on selected (low energy) snapshots of the MLFF-AIMD runs were performed and further electronic structures were calculated by employing a hybrid functional (details on electronic structure calculations were discussed in Chapter 5). The optimized structures are shown in Figure 6.1 along with the calculated unpaired electrons (UPE) for four distinct lithium concentrations (states of charge). It can be seen that the UPE on Mn change slightly

This section is based on the publication: Yu, J. H. & **Köster, K.** & Voronina, N., *et al.* Elevating Li-ion battery paradigms: Sophisticated ionic architectures in lithium-excess layered oxides for unprecedented electrochemical performance. eScience **5**, 4, 100376 (2025).

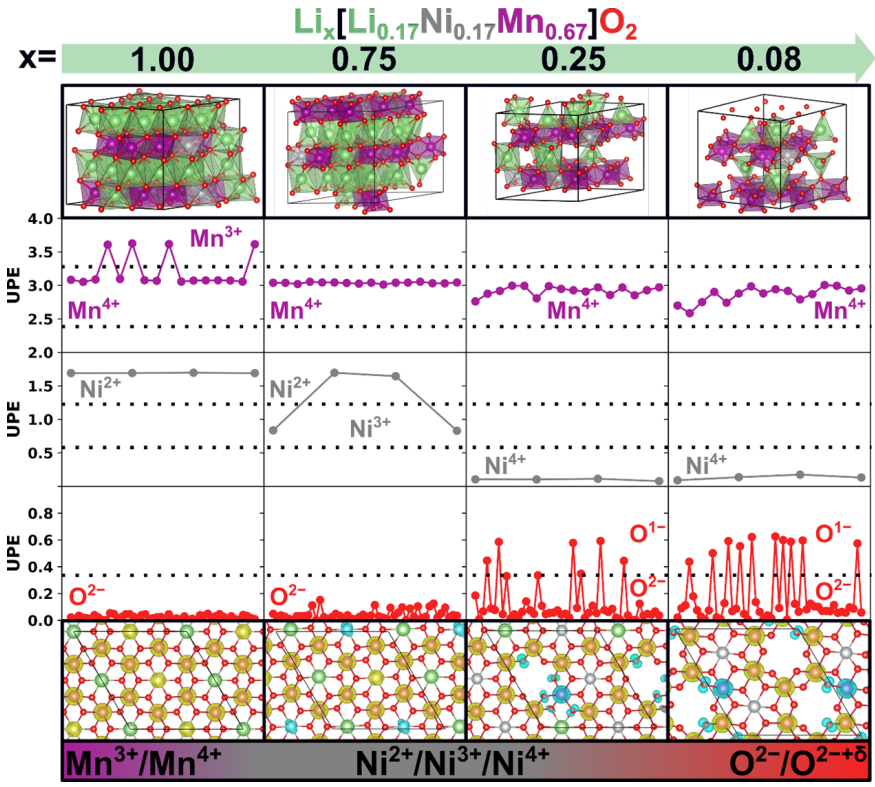

Figure 6.1: From top to bottom: Lowest energy structures obtained from Machine Learning Force Field *Ab Initio* Molecular Dynamics (MLFF-AIMD) simulations followed by optimizations with density functional theory (DFT). Unpaired electrons (UPE) on Mn, Ni, and O ions as calculated by DFT electronic structure calculations, applying a hybrid functional. Spin-Density-Difference (SDD) plots to visualize the UPE. Redox activity as assigned by the computational methods. All properties are shown at the four different considered lithium concentrations between x=1.00 and x=0.08 (from left to right). The Figure is reprinted from: Yu, J. H. & **Köster, K.** & Voronina, N., *et al.* Elevating Li-ion battery paradigms: Sophisticated ionic architectures in lithium-excess layered oxides for unprecedented electrochemical performance. eScience **5**, 4, 100376 (2025)

from values of approximately 3.7 UPE to values of approximately 3 UPE for four Mn while the other remain constant at approximately 3 UPE. These changes on the four distinct Mn ions happen on the first delithiation from x=1.00 to x=0.75 and indicate oxidation of Mn^{3+} to Mn^{4+} while most Mn ions simply remain as Mn^{4+}. The oxidation states can be assigned from UPE by applying crystal-field theory and taking into account that Mn is in an octahedral coordination environment of oxygen which splits the *d*-orbitals of Mn into a t_{2g} (3 *d*-orbitals lower in energy) and e_g (2 *d*-orbitals higher in energy) level. Therefore, 4 UPE (or roughly 3.7 UPE as found in the calculations) would correspond to a t_{2g}^3 e_g^1 high-spin electronic configuration of an Mn^{3+} while 3 UPE indicate a t_{2g}^3 e_g^0 electronic configuration of a Mn^{4+} ion. On further charge of the cathode material, Mn shows always about 3 UPE pointing to a fixed charge of Mn^{4+}. The higher fluctuations and deviations from exactly 3 UPE on Mn at higher states of charge can be assigned to artifacts

in the assignment of UPE to ion cores, uncertainties in the degree of (de-)localization of electron-densities associated with the Hartree-Fock mixing parameter of the hybrid functional as discussed in detail in Chapter 5, or distorted coordination environments that cause a fine-splitting of the *d*-orbitals beyond classical crystal-field theory. After all, Mn is oxidized to Mn^{4+} and a gradual change of UPE on Ni from approximately 2 UPE to 0 UPE is observed in Figure 6.1. This indicates oxidation of Ni^{2+} ($t_{2g}{}^6$ $e_g{}^2$, 2 UPE) over Ni^{3+} ($t_{2g}{}^6$ $e_g{}^1$ (low-spin), 1 UPE) to Ni^{4+} ($t_{2g}{}^6$ $e_g{}^0$ (low-spin), 0 UPE). Again, deviations of the calculated UPE and the theoretical UPE can be assigned to challenges in the electronic structure calculation proving the importance of in-depth theoretical electronic structure studies on these materials as presented in Chapter 5 of this thesis. Finally, at high states of charge such as x=0.25 or x=0.08 strong deviations from 0 UPE are observed on the oxygen anions in Figure 6.1. While 0 UPE simply correspond to O^{2-} ($2p^6$), calculated UPE values of up to approximately 0.6 UPE are even more close to O^{1-} with formally 1 UPE ($2p^5$). Therefore, it can be concluded that strong anionic redox is present in the cathode material. However, full oxidation to O^{1-} is probably unlikely and could be an artifact of too strongly localized electron densities due to a too large portion of Hartree-Fock mixing in the hybrid functional. Details on how this mixing influences the electronic structure and also comparisons to higher level of theory calculations were discussed in Chapter 5. Finally, it was ensured that the assigned charges result in an overall charge-neutral structure and that the total theoretical UPE match the total calculated UPE (including possible spin-up and spin-down cancellations). In conclusion, the computational results of this study suggested a redox mechanism of $Mn^{3.75+}$ to Mn^{4+} followed by redox of Ni^{2+} to Ni^{4+} and finally strong anionic redox (O^{2-} to $O^{2-+\delta}$) during charging as also indicated by the color-bar in Figure 6.1. This redox mechanism was in excellent agreement to the experimental studies that confirmed the same redox activities by *operando* X-ray Absorption Near Edge Structure (XANES) measurements.

Finally, the simulations performed by the author of this thesis for the present study enabled further atomistic insights such as the fact that oxygen ions get closer to each other on charge due to the lowered electrostatic repulsion upon anionic redox. This was confirmed by Pair-Distribution-Functions (PDFs) that were calculated from the MLFF-AIMD trajectories. Moreover, the simulations revealed no oxygen distances in the binding-regime of oxygen dimers, an indication that no irreversible oxygen loss took place in the studied cathode material which was also confirmed by experimental Differential Electrochemical Mass Spectrometry (DEMS) measurements. However, during the MLFF-AIMD simulations migration of lithium from the TM layer to the lithium layer was observed at low lithium concentrations. Again, this finding matched experimental ^{7}Li Nuclear Magnetic Resonance (NMR) measurements that also found reversible lithium migration. The simulations and NMR measurements further confirmed that at higher states of charge lithium prefers to occupy a tetrahedral site in the lithium layer rather than an octahedral site. To capture such strong structural changes in the calculations, MD simulations are required as also discussed at the problem of phase transitions and utilizing classical force fields in Chapter 4 of this thesis. Regarding the results of this study, it is worth mentioning that when analyzing the Spin-Density Difference (SDD) plots in Figure 6.1 the strongest anionic redox was found in direct proximity to TM layer vacancies formed by lithium migration. This highlights that a detailed computational

study must consider both, dynamic structural relaxations and accurate electronic structure calculations to obtain results in agreement to experiment and to deliver further mechanistic insights.

In summary, in this work topotactic ion-exchange was leveraged to obtain a Mn-rich, Co-free O2-type layered cathode ($Li_{0.75}[Li_{0.15}Ni_{0.15}Mn_{0.7}]O_2$) that combines honeycomb cation-ordering, excess lithium, and reversible oxygen-redox activity. The material delivered a high energy density (approximately 284 mAh/g) and long-term cycling stability such as a capacity retention of 70 % after 500 cycles in a full-cell setup. The computational studies by the author of this thesis involved electrostatic configurational optimization, DFT geometry-optimization, MLFF-AIMD simulations, and electronic structure calculations. The calculations were of great importance to unveil and confirm the mechanistic details of structural changes and the charge-compensation mechanism during operation of the cathode material. Ultimately, this work highlighted a promising direction for designing the next generation of sustainable (Co-free, Mn-rich), high-voltage (due to anionic redox), and cycle-stable (no irreversible oxygen loss) layered oxide lithium-ion cathode materials and therefore marked an important step in cathode material development.

6.2 Configurational Optimizations in LFP:

Simulating charging characteristics of lithium iron phosphate by electro-ionic optimization on a quantum annealer

Lithium-iron phosphate (LFP) is a broadly applied cathode material for lithium-ion batteries and can serve as a lower cost alternative to layered-oxide cathode materials. The LFP cathode material is a subject of extensive research and it is known that the charging mechanism involves generally a two-phase reaction [4, 5]. Such a two-phase charging mechanism is characterized by the presence of a Li-rich ($LiFePO_4$) and a Li-poor ($FePO_4$) phase. In contrast to other cathode materials such as layered oxides, intermediate lithium concentrations are achieved by adjusting the ratios of the Li-rich and the Li-poor phases (domains). In other words, for a lithium concentration of 0.5 not a single phase/domain with homogeneous lithium distribution exists but two equally-sized domains, one of $LiFePO_4$ and one of $FePO_4$ resulting in an average lithium concentration of one half. From a more general perspective, the formation of two domains instead of a single-phase with a homogeneous lithium distribution can be understood as a configurational optimization problem, similar to those discussed in Chapter 2 of this thesis. As iron is known to show electronic disproportion in the LFP material as well, the charging mechanism becomes a joint electro-ionic combinatorial optimization problem of distributing Fe^{2+} (electrons) and Fe^{3+} (electron-holes) over the iron sites and distributing Li-ions and vacancies onto the lithium sites.

In this work the author of this thesis collaborated with the group of Dr. Tobias Binninger from the department of Theory and Computation of Energy Materials (IET-3) in the Institute of Energy Technologies at Forschungszentrum Jülich GmbH. While their work focused on transferring the configurational optimization problem in LFP to a D-Wave quantum annealer, the author's contribution involved approaching the optimization problem on classical hardware by the newly developed GOAC code (see Chapter 2). Results were used to verify the energy model, to compare to optimizations on the quantum annealer, and to estimate the scaling of optimizations on a quantum annealer. For evaluation of different configurations of LFP periodic electrostatic interactions, as implemented in the GOAC code, were considered and the first step was to verify that this energy-evaluation model can correctly reproduce the aforementioned two-phase charging mechanism of LFP. As it is known from experiment that the two phases only appear in particles that are larger than several nanometers, while for smaller particles a homogeneous lithium distribution is observed, electro-ionic optimizations needed to be performed in extremely large cells [6, 7]. These required large supercells yield a combinatorial explosion of possible configurations that cannot be tackled on current state-of-the-art quantum annealers. However, as outlined in Chapter 2, the GOAC code developed by the author of this thesis is among the fastest (to the best of our knowledge) codes to approach such extremely large configurational optimization problems. Therefore, configurational (Fe^{2+}/Fe^{3+} and lithium/vacancy distribution) optimization in increasingly larger supercells of $Li_{0.5}FePO_4$ was performed and mainly the interface to the commer-

This section is based on the publication: Binninger, T., Ting, Y.-Y., **Köster, K.**, *et al.* Simulating charging characteristics of lithium iron phosphate by electro-ionic optimization on a quantum annealer. Phys. Rev. B **112**, 174118 (2025). Copyright (2025) by the American Physical Society.

cial Gurobi solver in GOAC was leveraged to also allow for exact optimizations in smaller cells while heuristic optimization was performed in the larger cells. The results obtained and presented in the corresponding article are also shown in Figure 6.2.

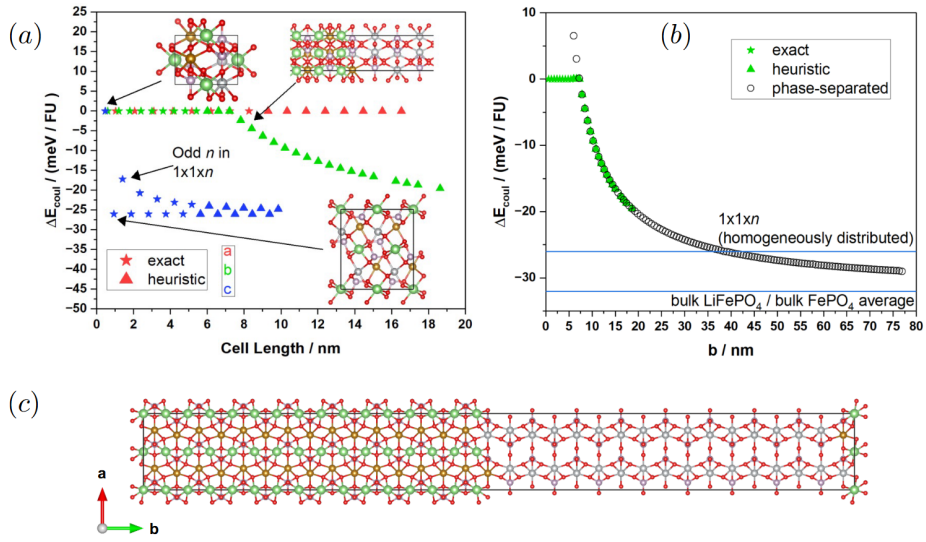

Figure 6.2: Results of configurational optimization of Fe^{2+}/Fe^{3+} and lithium/vacancy positions in $Li_{0.5}FePO_4$ as obtained by the GOAC code (cf. Chapter 2) and interfacing to Gurobi solver. a) Energies of optimized configurations as function of supercell size along the different cell dimensions (a (red), b (green), and c (blue)). Stars indicate exact optimization (proven global minimum) and triangles show the lowest energy obtained through heuristic optimization (no guarantee for global minimum). b) Energy of a two-phase configuration as function of supercell size along the b-direction. The lowest energy phase obtained when extending the cell along c-direction is indicated by a blue horizontal line as well as the average energy of the two separate bulk phases ($LiFePO_4$ and $FePO_4$). c) Structure of the minimum energy configuration obtained in a $1 \times 16 \times 1$ supercell that shows a phase separation into two domains ($LiFePO_4$ and one of $FePO_4$). Lithium, Fe^{2+}, Fe^{3+}, and oxygen ions are shown in green, brown, silver, and red color, respectively. The Figure is reprinted with permission from: Binninger, T., Ting, Y.-Y., **Köster, K.**, *et al.* Simulating charging characteristics of lithium iron phosphate by electro-ionic optimization on a quantum annealer. Phys. Rev. B **112**, 174118 (2025). Copyright (2025) by the American Physical Society.

It can be seen that for the unit cell ($1 \times 1 \times 1$ supercell) a homogeneous distribution of lithium (and electrons/electron-holes on iron) is obtained as the lowest energy structure and the structural model is also shown in the Figure. When the cell is extended along the a-direction the same configuration is obtained resulting in a straight line for the lowest energy configuration versus the particle size along the a-direction. However, when the cell is extended along the c-direction ($1 \times 1 \times n$ supercells), a configuration with lower energy (cf. structural snapshot in Figure 6.2 (a)) is obtained that still has a homogeneous lithium distribution over the whole cell (single-phase). The energy of this new single-phase configuration shows a constant energy for even numbers of n and slightly higher energies for odd numbers of n that eventually converge to the same energy as for even n for larger and larger $1 \times 1 \times n$ supercells. The most interesting phenomena is observed when extending the cell along the b-direction. While for small $1 \times n \times 1$ supercells up to $n = 12$ (7.2 nm) the same homogeneous lithium distribution as in the

unit cell is found to be most stable, larger supercells show a pronounced decrease in energy. Analyzing the structures of the optimized configurations reveals that for $1 \times n \times 1$ supercells with $n > 12$ a configuration with two domains (two-phase configuration of $LiFePO_4$ and $FePO_4$) is energetically favored over a homogeneous lithium distribution. Such a lowest energy configuration of a two-phase product is also shown for a $1 \times 16 \times 1$ supercell in Figure 6.2 (c). While this observation proves that large-scale electro-ionic configurational optimization with an electrostatic energy evaluator is able to correctly reproduce the two-phase charging mechanism of LFP, the obtained energies of the two-phase product are still higher than the single-phase product found for extending the cell along the *c*-direction. Still, the optimized two-phase configurations show a pronounced trend towards lower energies with larger cells that will eventually become the most stable known configuration. Therefore, the study was continued by manually creating the two-phase product in larger and larger cells along the *b*-direction up to almost 80 nm in length and evaluating the electrostatic energies of the structures. Results are shown in Figure 6.2 (b) and indicate that at particle sizes of about 40 nm along the *b*-direction the two-phase configuration indeed becomes the most stable configuration found over all optimizations. At that size the energy is lower than the one (with homogeneous lithium distribution) obtained for extending the cell along *c*-direction. This indicates that the reason for the two-phase behavior of LFP are the electrostatic forces in the bulk material. When further increasing the cell size, the energy appears to converge towards the average energy of the two separate bulk phases, $LiFePO_4$ and $FePO_4$. This can be explained by the fact that the energy of the two-phase configuration is characterized by the energies of the two bulk phases plus an interfacial energy for the contact area of the two bulk phases. In the limit of an infinitely large cell the total energy would be purely dominated by the energies of the bulk phases and the contribution of the interfacial energy becomes neglectable. Thus, the electrostatic optimizations also allowed to determine the interface energy of $LiFePO_4/FePO_4$ by scaling with an effective dielectric constant obtained through density functional theory (DFT) calculations. Regarding the estimated critical particle size of 40 nm for the two-phase configuration to become most stable, it is quite remarkable that experimental studies suggested critical particle sizes in the range of 10 nm [7] to 40 nm [6] indicating even quantitative agreement of the employed electrostatic optimization model.

In summary, the configurational optimizations conducted with the GOAC code, that was developed in this thesis (cf. Chapter 2), for this study were able to prove that an electrostatic energy model is capable to capture the two-phase charging mechanism in LFP as well as its critical particle size (single-phase for particles below 40 nm, two-phase for larger particles). It should be mentioned that in order to prove these aspects, configurational optimizations in systems with almost 1000 ions and approximately 10^{75} possible configurations were conducted and energies of models with more than 3300 ions were considered. Modelling such large systems at the atomistic scale requires efficient methods and highlights the scalability and capabilities of the GOAC code. Moreover, this study on LFP proves that electrostatic configurational optimization in such large problems is not just a theoretical experiment but also required for certain systems to discover additional atomistic insights. Thus, the study on LFP that was summarized in this section provides a strong motivation for the development and usage of the GOAC code.

In addition, the collaborators in this study were able to map the electro-ionic configurational optimization problem successfully to a quantum annealer and also proved that the LFP problem can be solved on a quantum annealer. However, the current state-of-the-art quantum annealers are only capable to solve much smaller problem instances (supercell sizes) than demonstrated in the results using the GOAC code. Further research on quantum annealers might enable more powerful devices in the future and therefore also the scalability with supercell-size was assessed. To that extend, the GOAC code was employed to generate and evaluate millions of random configurations in various supercell sizes to finally obtain the configurational densities of state (cDOS) as a function of supercell size. It was found that the cDOS are well-described by a Log-normal distribution which allowed extrapolation of cDOS for even larger supercells. A key property of these Log-normal distributions is a shift of their center towards higher energies (more far away from the global minimum) at larger supercells. Therefore, larger cells are not only much more complex to optimize due to the combinatorial explosion of total configurations but also because of the fact that it becomes significantly more likely to sample higher energy configurations instead of the ground-state (global minimum). With these considerations it was possible to provide evidence that even future generations of quantum annealers (probably) cannot achieve an exponential speed-up on configurational optimizations in increasingly large supercells. However, it was found that quantum annealers in general bear the potential for significant speed-ups over classical hardware for problems such as the electro-ionic configuration optimization in LFP. The cDOS estimated by GOAC just indicated that the exponential scaling for considering larger supercells cannot be overcome by quantum hardware relying on thermal sampling statistics, highlighting again how challenging such optimizations are and underline once more the importance of fast heuristic optimizers such as the GOAC code presented in Chapter 2 of this thesis.

6.3 NTP Coating of Cathodes to protect from Electrolyte Attacks:

Synergetic Lattice and Surface Engineering: Stable High-Voltage Cycle Performance in P3-Type Layered Manganese Oxide

Degradation of the cathode material by reactions with the electrolyte during cycling can decrease its cyclability significantly. A possible strategy to mitigate such degradations is the coating of the cathode active material by some protective layer. Such a coating layer should have two important properties: I) being inert towards reactions with the electrolyte and II) ensure a high ionic conductivity to not limit the performance of the coated cathode (also electronic conductivity but that is not the focus in this case study) [8]. For layered oxide sodium-ion cathodes a suitable candidate for a coating layer might be $NaTi_2(PO_4)_3$ (NTP) as it is known to show high sodium conductivity and the phosphate structure is very different from a layered oxide which bears the potential for a different (improved) stability towards an electrolyte [9].

In this project, the author of the thesis collaborated with the group of Prof. Taek Myung from Sejong University Seoul, South-Korea. Their group synthesized a P3-$Na_{0.67}[Zn_{0.3}Mn_{0.7}]O_2$ layered oxide cathode material and successfully coated it with NTP. The experimental data suggested that the NTP-coated material had a severely improved cycling stability with a capacity retention of 70 % after 200 cycles while the bare, non-coated cathode material showed only 25 % capacity after just 100 cycles. Besides other effects that are also discussed by the computational results below, they proposed that Ti migration from NTP towards the layered material enhances the lattice-parameter change during cycling which contributes to the improved cyclability due to the more similar ionic radii of Ti^{4+} (0.61 Å) and Mn^{4+} (0.53 Å) [10]. Moreover, they found a P3 to O/P phase transition on charge and a O/P to P3 to O3 phase transition on discharge. Even though not commented on by theoretical calculations in this case study, these transitions highlight the importance of the methodologies to investigate phase stability (Chapter 3) and to observe phase transitions (Chapter 4) that were developed in this thesis.

Regarding the computational studies performed in this case study, also the redox mechanism was studied by electronic structure calculations as discussed in detail for the case study summarized in Section 6.1. Similar challenges for electronic structure calculations were encountered and therefore the results of this case study also motivate the theory work on accurate electronic structure calculations presented in Chapter 5. Moreover, to determine the positions of Mn and Zn on their lattice sites as well as sodium orderings, configurational optimization with help of the GOAC code, that was introduced in Chapter 2, was employed. In summary, for the cathode material in this case study a redox mechanism involving Mn^{3+}/Mn^{4+} as well as anionic redox (formally $O^{2-}/O^{1.75-}$) was found in the conducted calculations. This redox mechanism was well-matched by the experimental XANES (X-ray Absorption Near Edge Structure) measure-

This section is based on the publication: Voronina, N. & **Köster, K.**, Yu, J. H., *et al.* Synergetic Lattice and Surface Engineering: Stable High-Voltage Cycle Performance in P3-Type Layered Manganese Oxide. Adv. Energy Mater. **Early View**, 2501823 (2025).

ments. Furthermore, during geometry optimizations by DFT (Density Functional Theory) prior to the electronic structure calculations at different states of charge (different sodium concentrations), migration of Zn from the transition-metal (TM) layer towards the sodium layer was observed at high states of charge (low sodium concentration) (cf. Figure 6.3 (b)). This migration was also confirmed by experiment in XANES measurements. Analysis of the electronic structure revealed that the strongest anionic redox took place at the oxygen ions next to the vacancies from Zn migration in the TM layer. This finding is also in agreement with the activation of the anionic redox next to vacancies found in the case study discussed in Section 6.1. Moreover, some oxygen ions next to Zn^{2+} that remained in the TM layer showed stronger redox activity as well, hinting towards an electrostatic activation of anionic redox. Also, in both, experiment (*operando* Differential Electrochemical Mass Spectrometry (*o*-DEMS)) and simulation no evidence of irreversible oxygen loss was found as the O-O pair-distribution functions (PDFs) in Figure 6.3 (a), right plot, showed just a minor shift towards shorter distances on charge but no intensities in the O-O bonding region.

Finally, extensive *ab initio* molecular dynamics (AIMD) simulations were performed for this case study to probe the degradation of different interfaces in contact with electrolyte species. It was assumed that HF (hydrogen-fluoride) is the most aggressive species that can form under electrochemical conditions from the $NaPF_6$-based electrolyte. Consequently, the surface of the cathode material in its discharged (sodium concentration of 1.00) and its charged (sodium concentration of 0.17) state as well as the NTP material were simulated in contact with HF. For the layered cathode a surface without Ti and a surface with Ti-doping was simulated as the experimental results suggested migration of Ti into the cathode material on NTP coating. In total, systems with approximately 200 to 300 ions were simulated for 25 ps each in steps of 1 fs. To facilitate reactions of the HF with the surface, an elevated temperature of 600 K was employed. Due to the expected reactions at the surface it was decided to perform fully *ab initio* simulations and to not leverage on-the-fly machine-learning force fields (MLFF) as discussed for the case study in Section 6.1. An overview of some important results obtained from the AIMD simulations is shown in Figure 6.3.

The PDFs for pairs including F in the left plot of Figure 6.3 (a) showed no intensities below distances of 3 Å for the NTP material. This proved that there are no bonding interactions of F and the NTP coating and therefore no degradation of the material. It might be concluded that NTP is mostly inert towards the HF electrolyte. However, the bare layered cathode material showed a strong intensity in the metal-F bonding region for both, the charged and discharged state. Interestingly, these intensities were dominated by the F-Zn pair indicating that Zn is the main contact point for HF attacks at the surface of the cathode. This observation was further verified by the structure snapshots in Figure 6.3 (b) as the HF molecules or F^- ions were mostly attached to Zn while the Zn was migrating out of the surface plane of the cathode. The tendency that Zn migrates from the TM layer towards the sodium layer that was found in the simulations and experiment was already discussed. The AIMD simulations highlighted in addition that also at the surface Zn has a tendency to migrate out of the surface plane, thus offering a suitable attacking point for electrolyte species such as HF. Once an HF is attached to a surface Zn, the simulations showed a few cases where another HF attacked or dissociation of the at-

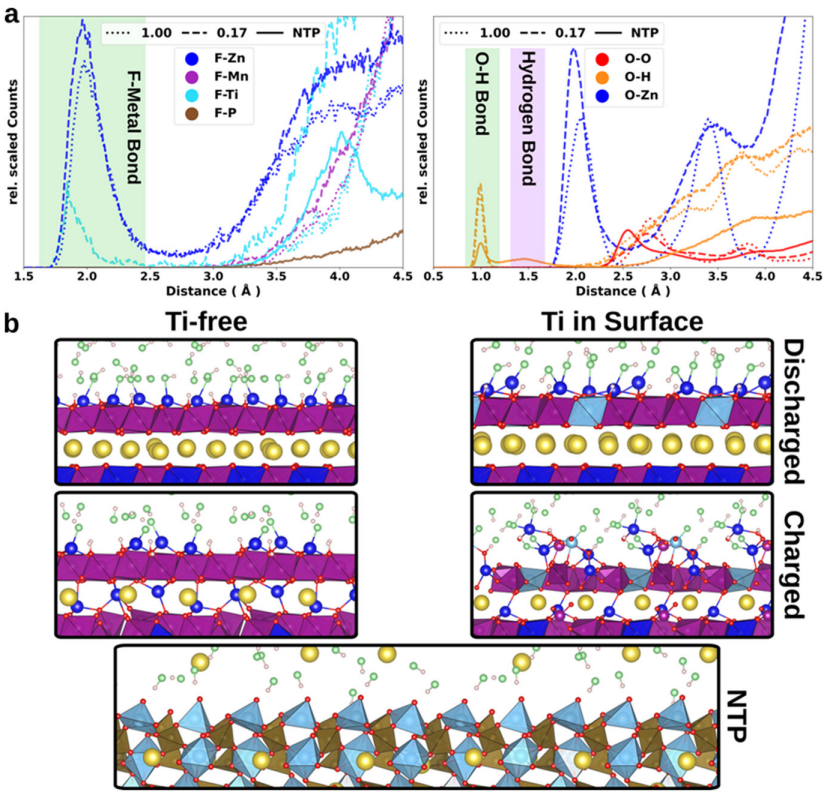

Figure 6.3: Results from *ab initio* molecular dynamics (AIMD) simulations. a) Pair-distribution functions (PDFs) of pairs involving F (left) and pairs involving O (right). Colors indicate pair types while line styles highlight the bulk material. b) Snapshots from AIMD simulations of the (001) surface of the cathode material with (right) and without (left) surface Ti-doping and the $(1\bar{1}02)$ surface in NTP all in contact with HF. The Figure is reprinted from: Voronina, N. & **Köster, K.**, Yu, J. H., *et al.* Synergetic Lattice and Surface Engineering: Stable High-Voltage Cycle Performance in P3-Type Layered Manganese Oxide. Adv. Energy Mater. **Early View**, 2501823 (2025).

tached HF into F^- and a proton happened. This could indicate the initial state of ZnF_2 formation which was detected in experimental time-of-flight secondary ion mass spectrometry (TOF-SIMS). The rather short, in comparison to experiment, time-scales in the range of several ps that were accessible in the AIMD simulations probably prevented to observe the complete formation of ZnF_2. Furthermore, the PDFs showed that some HF also attacks at Ti at the Ti-doped cathode surface of the charged material. This material further showed the strongest indication of degradation of the cathode material by HF (see Figure 6.3 (b)). In general, dissolution of the cathode material appeared to be stronger in the charged than in the discharged states.

The PDFs involving oxygen ions (Figure 6.3 (a), right plot) revealed how the protons of the HF interact with the material. When the HF attacked the Zn, it dissociated right before or after the attack which resulted in an excess proton. This proton can bind to surface oxygen and as a consequence peaks with high intensity were observed at the O-

H bond-distance region in the O-H PDFs of the layered cathode material. Thus, these peaks indicated another degradation mechanism of the cathode material. The NTP surface also showed a small intensity in the O-H bonding region indicating that oxygen is more prone to react with the electrolyte than P or Ti in this compound. However, the peak was more smeared and showed some intensity in the hydrogen-bond interaction distance. This highlighted that also the proton interactions of the electrolyte (HF) with NTP were less-covalent than for the layered cathode and therefore presumably less destructive (less/no degradation). The overall trends regarding the stability of the different surfaces against HF were also confirmed by the snapshots in Figure 6.3. In summary, the bare layered cathode showed strong interaction/degradation in contact with HF while mainly Zn was the point of attack as well as surface oxygen by the excess protons. The degradation was stronger at higher states of charge (lower sodium concentration) and also stronger when Ti-doping was introduced. In contrast, the NTP material appeared to be almost inert to HF and only the surface oxygen-ions showed some interaction with protons from the electrolyte. Therefore, it was concluded that the improved cycling stability achieved in experiment by the NTP coating is mainly a direct protective effect of NTP against electrolyte attacks.

Overall, this case study gave valuable insights into stabilization strategies that can significantly improve the performance (mainly cyclability) of layered oxide sodium-ion cathodes. The introduction of a NTP coating improved the cycling stability drastically while maintaining reasonable ionic conductivity. The DFT calculations were able to match and confirm the redox mechanism proposed from experimental measurements while both indicated a strong activation of anionic redox that is, however, reversible (no oxygen loss). Furthermore, the AIMD simulations were able to prove that NTP has a greater resistance against the electrolyte (HF) than the bare cathode material and revealed the degradation mechanism at an atomistic level. To sum up, the cooperative approach of experimental and simulational studies employed in this case study was able to give important insights and to point out novel design strategies to improve the cycling stability of layered oxide sodium-ion cathodes.

6.4 Distinct Redox Potential of Oxygen bound to Magnesium:

'Oxygen bound to magnesium' as high voltage redox center causes sloping of the potential profile in Mg-doped layered oxides for Na-ion batteries

Substitution of transition metals (TM) by various elements is a common strategy to improve or alter the electrochemical characteristics of layered oxide sodium-ion cathode materials. Such substitutions can, for example, change the phase-stability and transitions, the voltage profile or the capacity retention. While usually cathode materials are tuned to improve their performance, subtle changes in their electrochemical behavior such as small shifts or changes of shape of the voltage curve are also commonly observed [11–16]. These shifts in the voltage curve upon substitution can hint towards important changes in the redox mechanism and therefore deserve to be studied in more detail.

This case study was a collaboration with the group of Prof. Philipp Adelhelm from Humboldt-University, Berlin. Their group performed the experimental parts of this study on the $NaNi_{0.5}Mn_{0.5}O_2$ cathode material while replacing Ni with various concentrations of Mg, including Mg=0, 0.10, 0.15, 0.20, 0.25. They synthesized and tested the materials in both, the P2 and O3 phase and also investigated extensively how the different Mg concentrations and starting phases alter the phase stabilities and phase transitions during operation. These phase transitions were not part of the simulations for this study but nevertheless highlight the relevance of the works on phase stability and phase transition presented in Chapter 3 and Chapter 4 once more. Moreover, the experimental studies revealed that a high-voltage plateau transformed to a slopy feature (a curvature with a slope instead of a plateau at a constant voltage) upon introduction of more and more Mg to the system. This behavior was also found independent of the phase which proved that it is in direct relation to the redox mechanism. It was further found that gradually adding Mg reduced the capacity as redox-active Ni is replaced by electrochemically inactive Mg. However, substitution with Mg also improved the capacity retention (also due to an overall decreased total capacity) significantly and O3-$NaMg_{0.1}Ni_{0.4}Mn_{0.5}O_2$ was determined as the sweet-spot for total capacity and capacity retention. Consequently, the simulational studies aimed on understanding the change in the redox mechanism observed in the experimental voltage curve of the Mg-doped material in comparison to its Mg-free parent material.

As discussed in more detail for the case study shown in Section 6.1, the redox mechanism of the cathode materials was determined by electronic structure calculations. Prior to the electronic structure calculations atomistic configurations were determined by configurational optimization of Coulomb energies, for example by optimizers such as the GOAC code presented in Chapter 2. Next, the geometry of the structure was fully relaxed by Density Functional Theory (DFT) calculations and finally the electronic struc-

This section is based on the publication: Li, Y. & **Köster, K.**, Mazzio, K., *et al.* 'Oxygen bound to magnesium' as high voltage redox center causes sloping of the potential profile in Mg-doped layered oxides for Na-ion batteries. Adv. Funct. Mater. **Early View**, e19132 (2025).

ture was calculated by a more accurate hybrid functional. The effects of hybrid functionals on the electronic structures of cathode materials were discussed in some detail in Chapter 5 of this thesis. From the unpaired electrons (UPE) obtained from the electronic structure calculations the electronic configurations of the ions were assigned. Thereby their charge was estimated as outlined in Section 6.1. In agreement to experimental X-ray absorption near edge structure (XANES) measurements it was found that the redox mechanism in both cathode materials, the one without Mg and the one with 10 % Mg, was dominated by $Ni^{2+}/Ni^{3+}/Ni^{4+}$ redox while Mn remains electrochemically inactive at a charge state of Mn^{4+}. Moreover, in experimental resonant inelastic X-ray scattering (RIXS) analysis strong oxygen redox was observed for the cathode materials that was weakened with the introduction of more and more Mg. However, the experiments also showed evidence for another, distinct center of anionic redox in the Mg-doped materials yielding to the hypothesis that 'O bound to Mg' is a novel redox center. The aforementioned change in the experimental voltage profile on Mg substitution was also attributed to this additional new redox center. To validate this statement detailed electronic structure analysis with several methodologies was performed and results are summarized in Figure 6.4.

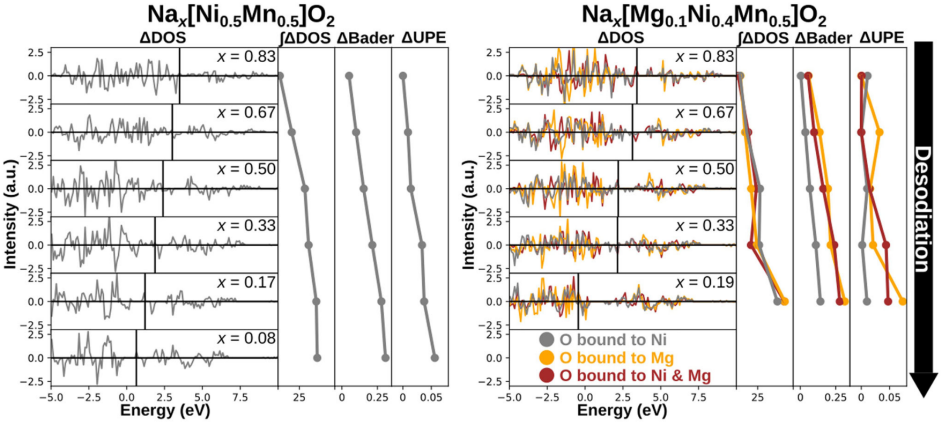

Figure 6.4: Changes in projected densities of states (DOS) of oxygen *p*-orbitals on desodiation for O3-$Na_xNi_{0.5}Mn_{0.5}O_2$ (left) and O3-$Na_xMg_{0.1}Ni_{0.4}Mn_{0.5}O_2$ (right). The DOS are visualized as their difference to the respective previous sodium concentration. Contributions to the DOS are further split into different groups of oxygen ions as colored in the legend in the right plot. Next to the DOS also the changes in the integrated DOS of depleted states, the differences in Bader charges on oxygen as well as the differences in unpaired electrons (UPE) are plotted as a function of sodium concentration x and per oxygen group. The Figure is reprinted from: Li, Y. & **Köster, K.**, Mazzio, K., *et al.* 'Oxygen bound to magnesium' as high voltage redox center causes sloping of the potential profile in Mg-doped layered oxides for Na-ion batteries. Adv. Funct. Mater. **Early View**, e19132 (2025).

The Figure depicts the changes in the projected densities of states (DOS) of oxygen *p*-orbitals relative to their respective previously considered sodium concentration for the Mg-free and Mg-doped cathode materials. For example, the plot omits the sodium concentration of x=1.00 and the presented DOS for x=0.83 are the relative differences to the DOS at x=1.00. To account for the different capacities observed in experiment, the low-

est considered sodium concentration for the Mg-doped material was x=0.19 while for the Mg-free material sodium concentrations down to x=0.08 were calculated. Furthermore, the DOS are split into different oxygen groups, namely 'O bound to Ni' for oxygen ions bound to at least one Ni but no Mg, 'O bound to Mg' for oxygen ions bound to at least one Mg but no Ni, and 'O bound to Ni & Mg' for oxygen ions bound to at least one Ni and at least one Mg. Such a distinction allowed to identify different redox centers and activities as function of the first coordination shell of the oxygen ions. For the Mg-free case all oxygen ions were bound to at least one Ni according to the electrostatic configurational optimization, thus resulting in just one oxygen group. Next to the DOS also the change of the integrated DOS of depleted states above the Fermi-level (indicated by vertical black lines in Figure 6.4) are shown, always relative to the DOS at x=1.00. Absolute DOS were considered to not double-count shifts between the two spin-channels. For both simulated cathode materials an increase of depleted states with higher states of charge (lower sodium concentrations) was observed also facilitated by the fact that the Fermi-level is shifting towards lower energies as electrons are removed during desodiation. This increase was accounted to anionic redox-activity that occurs in both cathode materials and proving that the experimentally observed oxygen redox was also present in the electronic structure calculations. Interestingly, for the Mg-doped material (Figure 6.4, right plot) the oxygen ions that are bound to an Mg ion ('O bound to Mg' and 'O bound to Ni & Mg') showed a slightly stronger increase than 'O bound to Ni' for the fully charged material (x=0.19). This tendency of stronger oxidation of oxygen bound to Mg was further solidified by other analysis methods of the electronic structure. Namely, Bader charge analysis [17] and tracking of UPE, both relative to the sodium concentration of x=1.00, highlighted a significantly stronger oxidation of oxygen ions bound to any Mg than oxygen ions bound just to Ni (and Mn which was not discussed here). This strengthened the experimental hypothesis that 'O bound to Mg' is a distinct and novel redox center in the Mg-doped material that is not present in the Mg-free material. Regarding the general oxygen redox-activity it was found that at the level of theory applied in this case study (hybrid functional with default Hartree-Fock mixing parameter) only small fluctuations on oxygen ions were observed during charge and more strong changes on Ni ions were observed which would indicate that the redox mechanism is mainly dominated by $Ni^{2+}/Ni^{3+}/Ni^{4+}$ redox and only small delocalizations onto oxygen ions occur. However, for the Mg-doped material one oxygen was observed that showed a high number of unpaired electrons (approximately 0.6 UPE) which hinted towards strong oxidation from O^{2-} ($2p^6$, 0 UPE) to formally O^{1-} ($2p^5$, 1 UPE). While it was concluded that this is most likely a too strongly localized oxidation as an artifact of challenges in the electronic structure calculations as outlined in Chapter 5, it still proved again the distinct nature of 'O bound to Mg' as an additional redox center. However, these assignments yielded stronger oxygen redox in the Mg-doped material than in the Mg-free material while experimentally the opposite was reported. Employing Bader charge analysis [17] to obtain ionic charges from the electronic structures inverted the overall average anionic redox-activity seen from UPE and therefore agreed with the aforementioned experimental results. This highlights that besides accurate electronic structure calculations also the choice of integration scheme (e.g., UPE versus Bader) is of great importance to analyze redox mechanism in layered oxide cathode materials. It should be mentioned that the

redox activity of oxygen in combination with Ni by computational methods is a matter of debate and in generally challenging [18, 19].

Machine learning force-field *ab initio* molecular dynamics (MLFF-AIMD) simulations were also performed on the charged materials and a slightly more intense peak for the shortest oxygen-oxygen distances was found in the pair-distribution functions (PDFs) for the Mg-free than for the Mg-doped material. This was in concert with the stronger oxygen redox reported in experiment and found in Bader-charge analysis as stronger anionic redox should yield shorter O-O distances due to decreased electrostatic repulsion. Moreover, no contributions in the O-O bounding region were found during the MLFF-AIMD simulations which indicated no (irreversible) formation of oxygen dimers. However, the rather short (on experimental time-scales) simulation time-scales might have prevented observation of such dimerization and the experimental results gave some hints that the 'O bound to Mg' redox center was more irreversible. Although the experimental results gave no definitive evidence if oxygen dimerization took place in the Mg-doped material, such an irreversible redox would be in agreement with the strong localization of UPE on a single 'O bound to Mg' that was seen in the electronic structure calculations. To comment on the question if the new redox center of 'O bound to Mg' induced indeed more irreversible oxygen redox, oxygen-vacancy formation-energies for the different coordination environments were calculated as well. Results highlighted that the oxygen-vacancy formation-energy was approximately 0.3 eV lower for the 'O bound to Mg' than for other oxygen ions pointing out that oxygen redox at these redox centers is probably more prone to result in irreversible oxygen dimerization than at other anionic redox centers.

In summary, in this case study a combination of experimental and theoretical simulation techniques gave strong evidence that substitution of Ni by Mg into O3-$NaNi_{0.5}Mn_{0.5}O_2$ introduces an additional anionic redox center, namely 'O bound to Mg'. This new redox center was linked to the presence of a more sloping voltage profile at high voltages. Furthermore, both theory and experiment indicated that anionic redox happening at these novel redox centers is more irreversible than anionic redox at other locations. Similar mechanisms probably occur when the substituent is switched to other low-charge redox-inactive species such as Li, Zn, Cu, Fe, and Ti while this case study aimed to give fundamental insights on how to further improve layered oxide cathode materials for sodium-ion batteries. Especially, it showed how TM substitution can influence the profile of the voltage curve due to different anionic redox centers and that these additional redox centers require stabilization in long-term cycling.

6.5 Summary and Conclusion

To summarize, in this chapter some of the additional collaborative works in which the author participated during the Ph.D. were presented. The discussed works were mainly shared works together with experimental scientists while the author contributed theoretical calculations to the works. The first 2 discussed case studies focused on cathode materials for lithium-ion batteries (LIBs). The material classes of layered oxides and phosphates (olivines) were presented. The author of the thesis contributed electronic structure calculations as well as molecular dynamics (MD) simulations to the first work. Computational studies proved the presence of reversible oxygen redox and also confirmed migration of excess lithium ions to the transition-metal (TM) layer which can further activate anionic redox. Therefore, this work introduced a new Mn-rich, Co-free cathode material for LIBs with reversible oxygen redox and high-energy density along with promising cycling-stability. In the other work on lithium-based systems, the configurational optimization problem in lithium-iron phosphate (LFP) was highlighted together with the resulting two-phase charging mechanism that is also observed experimentally. While the contribution of the author focused on the application of the GOAC code (cf. Chapter 2) on classical computer hardware, it was also shown that the configurational optimization problem can be solved on a quantum annealer. Simulations with the GOAC code further helped to predict the expected scaling behavior of larger systems on future generations of quantum annealers.

In the other two case studies presented in this chapter computational contributions to two experimental works on layered oxide cathodes for sodium-ion batteries (SIBs) were highlighted. In the first work, the redox mechanisms of the cathode material were again confirmed by calculations of the author. Moreover, with the help of extensive *ab initio* MD simulations the stability of a layered cathode material and its sodium-titanium-phosphate (NTP) coating layer against electrolyte attacks was assessed. The computational studies showed that the bare cathode material will degrade through electrolyte attacks while the NTP coating layer is mostly inert, thus providing the explanation for the significantly improved experimental cycling stability when an NTP coating is applied. Results therefore pointed out interesting directions to improve the electrochemical performance of SIB cathodes further. The last presented study also focused on layered oxide SIB cathode materials but not on the effects of coatings on stability but on the effect of substitution on the voltage profile. Detailed electronic structure analysis of the calculations was performed by the author and in combination with the experimental results of the collaborator enabled to identify a new center of anionic redox that is created on substitution with fixed-charge ions (in the presented study Mg) in the TM layer. In particular, the distinct redox activity of 'O bound to Mg' was pointed out and related to a change in the voltage profile towards a more sloping behavior at high voltages. Moreover, experiment and simulation gave some indication that the anionic redox at this new center is less reversible even though the cyclability was improved in experiment on Mg substitution. Thus, this case study gave fundamental insights for the design and challenges when aiming to improve layered oxide SIB cathodes by substitution of TM ions.

For all case studies it was pointed out how the previous, methodology-focused chapters of this thesis relate to the application in computational studies of real (experimen-

tal) cathode materials. Therefore, this chapter showed both, further contributions of the author to the field of cathode materials research and how the methodological contributions of the author can potentially advance the utilization of computational methods for this research. For all of the materials it was required at a very first step to determine the atomistic configuration from partial occupancies in the TM and charge-carrier (Li or Na) sites. A suitable tool for this task is the GOAC code developed by the author (details in Chapter 2). The case studies prove that with help of the code not only structural models for further computational studies can be obtained, but also more accurate models for experimental X-ray diffraction (XRD) refinements can be provided. Moreover, the two-phase charging mechanism in lithium-iron-phosphate (LFP) and its particle-size dependence was successfully simulated. Regarding the theoretical works on phase stability (Chapter 3) and phase transition (Chapter 4) presented in this thesis, the case studies give strong motivation to leverage such computational approaches to better understand these phenomena. The importance of predicting phase stabilities and phase transitions became evident by the experimental results discussed for the case studies and highlight how the theory works could be beneficial to design novel cathode materials in the future. Finally, the necessity of electronic structure calculations to support experimental findings and to obtain in-depth atomistic insights that are not even (directly) accessible in experiment was pointed out for most of the case studies. This strongly motivates the assessment and possible optimizations of electronic structure calculations for battery materials by hybrid functionals as outlined in Chapter 5. In conclusion, the summarized case studies nicely highlight how the previous theory-development chapters can contribute to the characterization as well as the rational design of cathode materials and that they can support gaining more accurate insights into structural stabilities and electronic structures to explain experimental findings.

REFERENCES

1. Manthiram, A. Materials Challenges and Opportunities of Lithium Ion Batteries. *The Journal of Physical Chemistry Letters* **2,** 176–184 (2011).
2. Arunkumar, T. A., Wu, Y. & Manthiram, A. Factors Influencing the Irreversible Oxygen Loss and Reversible Capacity in Layered Li[Li 1/3 Mn 2/3]O 2 −Li[M]O 2 (M = Mn 0.5-y Ni 0.5-y Co 2y and Ni 1-y Co y) Solid Solutions. *Chemistry of Materials* **19,** 3067–3073 (2007).
3. Zhang, H. *et al.* First–Principles Insights into the Role of Coordination Polyhedron Size on Mn Ion Migration within Li 2– x MnO 3 Layered Cathode Material. *Batteries & Supercaps* **8** (2025).
4. Padhi, A. K., Nanjundaswamy, K. S. & Goodenough, J. B. Phospho–olivines as Positive–Electrode Materials for Rechargeable Lithium Batteries. *Journal of The Electrochemical Society* **144,** 1188–1194 (1997).
5. Jugović, D. & Uskoković, D. A review of recent developments in the synthesis procedures of lithium iron phosphate powders. *Journal of Power Sources* **190,** 538–544 (2009).
6. Gibot, P. *et al.* Room-temperature single-phase Li insertion/extraction in nanoscale Li(x)FePO4. *Nature materials* **7,** 741–747 (2008).
7. Ichitsubo, T. *et al.* What determines the critical size for phase separation in LiFePO4 in lithium ion batteries? *Journal of Materials Chemistry A* **1,** 14532 (2013).
8. Hu, S. *et al.* Insight of a Phase Compatible Surface Coating for Long–Durable Li–Rich Layered Oxide Cathode. *Advanced Energy Materials* **9** (2019).
9. Lu, X. *et al.* First-principles insight into the structural fundamental of super ionic conducting in NASICON MTi2(PO4)3 (M = Li, Na) materials for rechargeable batteries. *Nano Energy* **41,** 626–633 (2017).
10. Shannon, R. D. Revised effective ionic radii and systematic studies of interatomic distances in halides and chalcogenides. *Acta Crystallographica Section A* **32,** 751–767 (1976).
11. Kubota, K. *et al.* Impact of Mg and Ti doping in O3 type NaNi 1/2 Mn 1/2 O 2 on reversibility and phase transition during electrochemical Na intercalation. *Journal of Materials Chemistry A* **9,** 12830–12844 (2021).
12. Clément, R. J. *et al.* Direct evidence for high Na + mobility and high voltage structural processes in P2-Na x [Li y Ni z Mn 1−y−z]O 2 (x, y, z ≤ 1) cathodes from solid-state NMR and DFT calculations. *Journal of Materials Chemistry A* **5,** 4129–4143 (2017).

13. Mariyappan, S. *et al.* The Role of Divalent (Zn 2+ /Mg 2+ /Cu 2+) Substituents in Achieving Full Capacity of Sodium Layered Oxides for Na-Ion Battery Applications. *Chemistry of Materials* **32,** 1657–1666 (2020).

14. Wang, Q. *et al.* Reaching the Energy Density Limit of Layered O3–NaNi 0.5 Mn 0.5 O 2 Electrodes via Dual Cu and Ti Substitution. *Advanced Energy Materials* **9** (2019).

15. Yu, T.-Y. *et al.* High-voltage stability of O3-type sodium layered cathode enabled by preferred occupation of Na in the OP2 phase. *Energy Storage Materials* **61,** 102908 (2023).

16. Ren, J. *et al.* Core–Shell Structure and X–Doped (X = Li, Zr) Comodified O3–NaNi 0.5 Mn 0.5 O 2 : Excellent Electrochemical Performance as Cathode Materials of Sodium–Ion Batteries. *Energy Technology* **8** (2020).

17. Bader, R. F. W. Atoms in molecules. *Accounts of Chemical Research* **18,** 9–15 (1985).

18. Genreith-Schriever, A. R. *et al.* Oxygen hole formation controls stability in LiNiO2 cathodes. *Joule* **7,** 1623–1640 (2023).

19. Lee, D.-H., Gong, M., Lee, E. & Seo, D.-H. Oxygen redox in LiNiO2 cathodes. *Joule* **7,** 1408–1411 (2023).

7

CONCLUSIONS AND OUTLOOK

This chapter intends to summarize the most important conclusions made in the previous chapters and how they relate to the overall thesis objectives as well as their relations and advancements to the general three-step simulation procedure for energy materials followed in this work. Moreover, outlooks are given on possible further research directions and applications while also potential links between the chapters to combine them into more advanced methods are given.

In the first chapter (Chapter 1), the introduction, it was highlighted that due to the transition to renewable energies and the electrification of the transport sector, both to mitigate climate change, an increasing demand for energy storage is expected. Following, it was motivated that current lithium-ion batteries (LIBs) face limitations in terms of costs, sustainability, and availability to fully meet such increasing demand. Thereby, the development of new LIB technologies as well as the investigation of sodium-ion batteries (SIBs) was motivated. Some key challenges such as phase stabilities and transitions were discussed and the value and general methodology of computational methods to support materials design was highlighted. Afterwards, the thesis objectives were formulated and an overview over the following chapters was given. To recap, in the introduction the following general three-step simulation procedure was introduced: 1. Configuration Selection, 2. Geometry Relaxation and Evolution, and 3. Electronic Structure Calculation. The thesis objectives were defined as: I) The reduction of computational costs to allow for more, larger, and faster simulations that offer new insights or support rational materials selection, II) The assessment and advancement of the calculation accuracy to improve the understanding of fundamental mechanisms in layered oxide cathode materials, and III) The utilization of computational methods in close combination with experimental measurements to support characterizations and to enable more rational material design.

In the first method-development chapter (Chapter 2) the GOAC (Global Optimization of Atomistic Configurations by Coulomb Energies) package was introduced. The code is designed to apply heuristic optimizers to the configurational search problem in crystals with partially occupied sites as they frequently appear in battery research. Optimality is assessed in terms of periodic electrostatic energy which proves to be useful in ionic crystals. The main thesis objective addressed by this chapter is the reduction of computational costs to allow for faster and larger optimizations and therefore the focus of the GOAC code is on scalable and efficient implementation of the heuristic optimiz-

ers. Precisely, the code implements various kinds of Monte Carlo based heuristics as well as a steepest decent and a genetic algorithm. The algorithms themselves work on matrices of pre-calculated energy contributions that arise from a pairwise decomposition of the total periodic electrostatic energy. Scalability of GOAC was highlighted by approaching extremely large configurational problems. Moreover, the possibility to interface to external solvers was shown and a feature to incorporate charge smearing was presented as well. In conclusion, this chapter provided a highly useful tool to the community of computational materials researches by allowing for fast and scalable configurational optimizations in ionic crystals. Therefore, this chapter delivers a valuable contribution to the first thesis objective of reduction of computational costs for the first simulation step, namely the configuration selection. As an outlook, the developed code can be applied to study larger systems than before and an exemplary application was already discussed in one of the case studies in Chapter 6 were large-scale simulations on LFP (Lithium iron phosphate) were carried out. Moreover, the code is already leveraged by several researchers and proven to be useful for various kinds of large-scale/high-through-put studies and surface reconstructions. In the future, combination with additional energy terms, e.g., classical potential terms, might be an interesting direction for extensions of the code and first steps were already made by the development of a classical potential in Chapter 4. Another promising direction for further improvement is to combine the configuration search with the prediction of the phase and (constrained) geometry optimization. Also in that direction foundations were established by the development of a phase-stability predictor in Chapter 3 that is summarized in the following paragraph. Thus, it can be concluded that there are plenty of future applications for the code developed in this chapter as well as many directions for further developments leveraging the established general optimization framework.

In Chapter 3 an *ab initio* predictor for the phase stability, in terms of the layer stacking sequence along the *c*-direction and sodium coordination environment, of layered oxide cathodes for SIBs was developed. It was shown that comparing the electrostatic energy of the respective lowest energy configurations of various stacking phases can be a computationally inexpensive proxy to estimate phase stability. In order to maximize the agreement to density functional theory (DFT) calculations, the lattice parameters for the electrostatic calculations were optimized such that the correlation to the relative phase stabilities in DFT is maximized. These developments allowed to achieve a high correlation between the relative phase energies in DFT and electrostatics across different cathode-material compositions and are therefore an interesting tool to pre-select phases/compositions for further DFT calculations or experiments. Thus, this chapter also contributed to the first objective of the thesis, decreasing the computational cost for material simulations, while the described use-case is located in the first step of the three simulation steps. In contrast to the previous chapter, the selection of the lowest energy configuration was extended by another degree of freedom in the optimization, namely the phase stability, thus the chapter is a natural extension of the GOAC code. Furthermore, the developed predictor was thoroughly tested against experimental data in this chapter and a promising accuracy of predicted and observed phase of 80 % was achieved. Therefore, the constructed *ab initio* predictor should be highly useful for rational design of cathode materials. As outlined in the introduction and this chapter, engineering the

phase stability of layered oxide SIB cathodes by their composition is highly desirable to improve their electrochemical performance. Consequently, this chapter is also an important contribution to the third objective of the thesis, which is about the application of computational methods for rational material design. It was also proven in this chapter that the low computational demand of the method allows for high-throughput screenings of compositions to quickly identify interesting candidates for further experiments. As the predictor was also made available in an online GUI (Graphical User Interface), it might become a useful tool for experimental battery scientists to select novel cathode materials. Another outlook for the application of the predictor introduced in this chapter could be coupling with the GOAC code of the previous chapter to allow simultaneous optimization of configuration and phase in a handy command-line interface. Despite the fact that the predictor also showed promising performance on cycled materials, it must be mentioned that the comparisons of energy at the lowest energy configurations only consider thermodynamic effects of phase stability. To also account for kinetic contributions a full classical potential was developed in the next chapter.

The following chapter, Chapter 4, comprised fitting of a Coulomb-Buckingham potential for the Na_xCoO_2 system to enable large-scale molecular dynamics (MD) simulations over long time-scales. Thus, also mainly targeting the first objective of the thesis about creating computationally less expensive methods to obtain new insights in larger simulations. However, in contrast to the previous chapters, in this chapter the second step of the three-step simulation procedure was addressed by dynamic structure relaxation/evolution. The procedure of fitting a Coulomb-Buckingham potential for the entire sodium-concentration range by minimizing the error in energy differences and forces utilizing a genetic algorithm was outlined in detail. Thus, allowing to reproduce this methodology for other layered oxide cathode materials. It was shown that in fact many of the Buckingham parameters can be kept constant for all sodium concentrations while it mostly matters to correctly adjust the dielectric constant of the cathode material. Furthermore, a special focus was on phase transitions, in terms of the stacking sequence along the *c*-direction, in particular on the O2-P2 transition. Computational results showed for the (probably) first time that the phase-transition barrier decreases with higher states of charge (lower sodium concentration) which explains why phase transitions are experimentally often observed at higher voltages. Dynamic simulations also gave further atomistic level insights into the mechanism of phase transition that cannot be (easily) obtained in experiment. Finally, large-scale simulations at standard lab conditions (*NpT*, 300 K, 1 bar) were carried out that allowed to study both, the phase transition and sodium diffusion in a realistic environment (most similar to experiment) and at the µs time-scale. While such simulations are prohibitively expensive in most conventional methods such as DFT, these simulations can also deliver important insights to support experimental understanding and accelerate material design. The simulation enabled to follow the sodium diffusivity as a function of progress of phase transition and promising agreements to experimentally observed diffusivities were identified. As mentioned before, possible future applications of the developed Coulomb-Buckingham potential include the extension to cathode materials beyond Na_xCoO_2 as well as its implementation into the GOAC code presented in Chapter 2. The general usage of pair-wise potentials was already implemented in GOAC but future works could aim to couple con-

figuration, phase, and (restricted) geometry search in one package. While such combinations require careful assessment of coupling strategies, for example, resetting/evolving the geometry after several configuration- and phase-search steps, they also bear the potential for fast and more accurate descriptions of layered oxide SIBs. The manual or even automatic combination of the methods described in this chapter with the ones from the previous two chapters could be a very promising further research direction that results from the works in this thesis. Moreover, the codes for fitting the Coulomb-Buckingham potential were already leveraged in a study concerning interphases of battery materials and delivered excellent results in the pre-selection and pre-optimization of interphases for further DFT calculations. To conclude, this chapter outlined a methodology to fit and apply Coulomb-Buckingham potentials to battery materials which can be transferred to other systems in the future and also provided valuable insights for experimental studies into the mechanisms of phase transition and sodium diffusion.

The last theory chapter, Chapter 5, focused on both, a different objective and simulation step compared to the previous chapters. Namely, objective II) of the thesis was targeted for the third simulation step. *GW* calculations were performed to investigate the accuracy of hybrid functionals for electronic structure calculations of layered oxide cathode materials. In particular, *GW* calculations at the single-shot and fully self-consistent level were conducted while using electronic structures from hybrid functionals with systematically varied Hartree-Fock mixing parameters (α) as starting point. The α-parameter determines the fraction of Hartree-Fock that is mixed to the DFT calculations. It was shown that two different ranges of α can be justified from the higher level of theory (*GW*) calculations. One by extrapolation at the single-shot *GW* level to a starting-point with no Hartree-Fock mixing (α=0, PBE) and the other one where further *GW* calculations, even at the fully self-consistent level, do not alter the band gap compared to the hybrid functional starting-point. While the first approach suggested optimal α-parameters around 8.5 %, the latter approach resulted in mixing parameters of 22 %. Furthermore, it was pointed out that the α-parameter has a significant influence on the electronic structure of layered oxides, in particular to the degree of hybridization between oxygen *p*- and transition-metal (TM) *d*-orbitals. For practical studies these fine differences in the electronic structure are crucial to correctly determine the redox mechanism and distinguish the redox activity of TM ions and oxygen ions. Therefore, despite the fact that this study was purely theoretical, the use case of determining redox mechanisms in cathode materials renders it very practical for advanced electronic structure calculations (simulation step three). Thus, this chapter is also a contribution to the third thesis objective of supporting experimental studies by simulations to enable more rational material design. A possible conclusion for future electronic structure studies of layered oxide cathodes could be to test different α-parameters, for example within the two distinct regions that were determined in this chapter. Regarding the determined α-parameters it should be mentioned that while the lower value (8.5 %) delivered band gaps in promising agreement to experimentally reported values, the other value (22 %) is rather close to the default mixing parameters of 25 % or even 20 % that are typically applied in hybrid functionals. Therefore, the study motivated to check also other, in particular lower, mixing parameters when simulating layered oxides as this could result in electronic structure descriptions closer to experiment. For an outlook, it would be

desirable to get rid of the (strong) dependence of α for the electronic structure calculations and the fact that two very different α can be justified. Therefore, future studies could involve hybrid functionals with more elaborated mixing schemes in the short and long range. This would open the possibility to also better account for the directional and distance dependent dielectric constant of these 2D TM oxides. As pointed out in the previous chapter, the dielectric constant probably strongly depends on the sodium concentration which could be considered in hybrid functionals particularly tailored to layered oxide materials. In summary, the data presented in this chapter gave valuable insights into the accuracy and challenges of electronic structure calculations in layered oxides and also came to some suggestions to improve electronic structure calculations which could further improve the mechanistic understanding of novel cathode materials.

The last chapter, Chapter 6, finally showcased the applications of the methodologies developed in this work, mainly to allow for advanced characterizations in cooperation with experimental results. Therefore, this chapter aims to contribute to the third thesis objective while employing all three simulation steps for almost all case studies. In the first discussed case-study, mainly the calculation of the redox mechanism by electronic structure calculations was highlighted as well as its interpretation together with experiment. In addition, an activation of anionic redox at TM layer vacancies was seen in the calculations which is hard to confirm in experiment and therefore proves that simulations can offer valuable insights for advanced experimental characterization. Moreover, at the specific example of the Li-rich cathode material explored in this case study, the challenges of assigning redox mechanisms from electronic structure calculations were pointed out. These mainly concern the localization or delocalization of unpaired electrons on oxygen ions and TM ions for which Chapter 5 proved the importance of the correct choice of the mixing parameter in the employed hybrid functional. As also all three simulation steps were employed in this case-study, the GOAC code from Chapter 2 was leveraged as well in the first step and the lowest energy configuration allowed for a more accurate X-ray diffraction (XRD) fitting in experiment. In conclusion, the computations resulted in detailed understanding of a novel and sustainable (Co-free, Mn-rich) Li-rich cathode material with promising capacity and cycling stability. The second presented case study solely focused on the application of the GOAC code, implemented and presented in Chapter 2, to simulate extremely large systems. Precisely, the particle-size dependence of the two-phase charging mechanism in LFP was correctly predicted by configurational optimizations in extremely large supercells. Therefore, this case study illustrated the possibilities the GOAC code could offer for battery materials research in the future. The GOAC code is already applied in other studies that aim to understand the substituent distribution in cathode material particles that are several nanometers large. Therefore, this case study was an outlook of what might be achieved by the GOAC code in the future. The following case study was focused on *ab initio* MD simulations of cathode materials in contact with an electrolyte. The main conclusion from a practical point of view was that an NTP ($NaTi_2(PO_4)_3$) coating can successfully prevent degradation of a layered oxide cathode material by electrolyte attacks while maintaining reasonable sodium conductivity. For an outlook, it can be concluded that such simulations, despite being computationally demanding, can allow to predict suitable cathode-material-coating-electrolyte combinations in the future. Such *a priori* screenings might

allow for faster and more rational material design for SIBs cathodes with high cycling stability. Furthermore, it highlighted the importance of MD simulations to study cathode materials which gives an outlook for further applications of the potential developed in Chapter 4 (note, in the case study, reactions were observed by *ab initio* MD which are hard to capture in classical potentials, therefore the potentials discussed in Chapter 4 cannot be directly applied to such a study but will be useful in general for other MD simulations). In the last case study, the focus was again on electronic structure calculations in combination with experiments to obtain in-depth understanding of changes in the redox-mechanism/potential on TM substitution. It was found that 'O bound to Mg' is a distinctive redox center with a different potential than other oxygen ions which translates into an altered shape of the experimental voltage curve. From a practical point of view, this study proved again the value of simulations of battery materials to obtain electronic structures that are not (directly) accessible in experiment. From the theoretical side, the calculations in this study highlighted once more the difficulties of electronic structure calculations in layered oxide materials. Despite the fact that the choice of a hybrid functional and its mixing parameter can significantly influence the hybridization between oxygen and TM ions (cf. Chapter 5) and thereby the assigned redox mechanism, in this chapter it was further concluded that also the integration scheme applied to the electronic structure to assign the electron density to nuclei is crucial. For further studies it would be therefore interesting to not just vary the electronic structure calculation-method as proposed in Chapter 5 but to also test and develop different integration schemes, e.g., Bader charges. This could further boost computational understanding of redox mechanisms in cathode materials.

To summarize, all of these case studies highlighted how simulation studies can advance the understanding of novel cathode materials and especially in terms of the methods developed in this thesis that could further strengthen such calculations by computational cost reduction, increased system sizes, and improved accuracy. Thus, these case studies serve as a small outlook themselves on how computational studies on cathode materials might be conducted and improved in the future. Ultimately, the developed computational methods and gained insights presented in this thesis, in combination with the experimental results and together with many other contributions in the literature, hopefully bring us to the point at which we can (more) rationally design new cathode materials tailored to our specific needs, e.g., sustainability and higher capacity. Therefore, mixed computational and experimental studies with advanced modelling approaches could enable us to meet the increasing demand for sustainable energy storage in the future.

LIST OF PUBLICATIONS

Published

First Author

1. **Köster, K.**, Binninger, T. & Kaghazchi, P. Optimization of Coulomb energies in gigantic configurational spaces of multi-element ionic crystals. npj Comput Mater **11**, 202 (2025).

2. **Köster, K.** & Kaghazchi, P. Hybrid functionals with nonempirical Hartree-Fock parameters for electronic structure calculation of layered oxides. Phys. Rev. B **109**, 155134 (2024).

Shared First Author

3. Yu, J. H. & **Köster, K.** & Voronina, N., *et al.* Elevating Li-ion battery paradigms: Sophisticated ionic architectures in lithium-excess layered oxides for unprecedented electrochemical performance. eScience **5**, 4, 100376 (2025).

4. Voronina, N. & **Köster, K.**, Yu, J. H., *et al.* Synergetic Lattice and Surface Engineering: Stable High-Voltage Cycle Performance in P3-Type Layered Manganese Oxide. Adv. Energy Mater. **Early View**, 2501823 (2025).

5. Li, Y. & **Köster, K.**, Mazzio, K., *et al.* 'Oxygen bound to magnesium' as high voltage redox center causes sloping of the potential profile in Mg-doped layered oxides for Na-ion batteries. Adv. Funct. Mater. **Early View**, e19132 (2025).

Others

6. Binninger, T., Ting, Y.-Y., **Köster, K.**, *et al.* Simulating charging characteristics of lithium iron phosphate by electro-ionic optimization on a quantum annealer. Phys. Rev. B **112**, 174118 (2025).

7. Voronina, N., **Köster, K.**, Yu, J. H., *et al.* Unveiling the Role of Ruthenium in Layered Sodium Cobaltite Toward High-Performance Electrode Enabled by Anionic and Cationic Redox. Adv. Energy Mater. **13**, 36, 2302017 (2023).

8. Kim, H.-J., Voronina, N., **Köster, K.**, *et al.* Synergetic impact of dual substitution on anionic–Cationic activity of P2-type sodium manganese oxide. Energy Storage Mater. **66**, 103224 (2024).

9. Cho, M.-J., Yaqoob, N., Yu, J. H., **Köster, K.**, *et al.* Theoretical and Experimental Optimization of P2-Type Sodium-Ion Battery Cathodes via Li, Mg, and Ni Co-Doping: A Path to Enhanced Capacity and Stability. Adv. Energy Mater. **15**, 13, 2405112 (2025).

10. Wu, L.-T., Zdravković, M., Milosavljević, D., **Köster, K.**, *et al.* Prediction of structural stability of layered oxide cathode materials: Combination of machine learning and ab initio thermodynamics. Adv. Energy Mater. **Early View**, e05470 (2025).

Submitted and Under Review

First Author

11. **Köster, K.**, ten Elshof, J. E., Huijben, M., *et al.* High-Throughput Predictions of Phase-Stabilities of Layered Oxide Cathodes by Optimized Electrostatics. *In Preparation for Re-Submission to eScience* (2025).

12. **Köster, K.** & Kaghazchi, P. Computational Studies on O2-P2 Phase-Transition Dynamics in Layered-Oxide Sodium-Ion Cathode Materials. *Under Review in Phys. Rev. B* (2025).

Shared First Author

13. Baiju, S. & **Köster, K.**, Huijben, M. & Kaghazchi, P. A Semi-Empirical Descriptor for Open Circuit Voltage. *Submitted to PRX Energy* (2025).

Manuscripts in Preparation

Shared First Author

14. Sun, Y. & **Köster, K.**, Haumann, M., *et al.* Understanding the Phase Transition Involving Cationic/Anionic Redox Activities in Sodium Layered Sulfide Cathodes.

15. Voronina, N. & **Köster, K.**, Kim, A.-Y., *et al.* Inductive Chemistry and Structural Ordering in P2-Type Layered Cathodes for Sodium-Ion Batteries.

16. Han, E. & **Köster, K.**, Voronina, N., *et al.*, Enhanced Rate Capability of O3-type $Na[Na_{1/3}Ru_{2/3}]O_2$ by Substitution of Na in Transition Metal Layer for Sodium Ion Battery.

Others

17. Winkler, L., Park, G.-T., Kuo, L.-Y., Ihrig, M., **Köster, K.**, *et al.* Zr Incorporation into Lithium Nickel Oxides: Solid Solution or Two-Phase System?

18. Olszewski, W., Bankowski, P., **Köster, K.**, *et al.* How reversible O redox in Li and Mn rich cathodes relates to the local structural properties.

19. Kim, H.-J., Oh, S.-M., **Köster, K.**, *et al.* Understanding Role of Al Substitution in Cation-Disordered Rock-Salt Type Cathode Material Through Fundamental Study of Lithium Storage Mechanism.

20. Zdravković, M., van de Nes, J., **Köster, K.**, Huijben, M. & Kaghazchi, P. Electrostatic Considerations for Phase-Stability.

LIST OF CONFERENCE CONTRIBUTIONS

1. (*Oral*) **Köster, K.** & Kaghazchi, P. Anionic Redox to increase Capacity in novel Layered Cathode Materials for Sodium-Ion Batteries. Jülich-Twente Summit, Enschede, The Netherlands, (2023).

2. (*Oral*) **Köster, K.**, Olivier Guillon & Kaghazchi, P. Oxygen Redox in Sodium-Based Layered Cathode Materials: A First Principles DFT and *GW* Study. 48th International Conference and Exposition on Advanced Ceramics and Composites (ICACC), Daytona Beach, Florida, United States, (2024).

3. (*Oral*) **Köster, K.**, Olivier Guillon & Kaghazchi, P. Anionic Redox in Sodium-Based Layered Cathode Materials: A First Principles DFT and *GW* Study. MUST (Münster-Stanford-Twente) Battery Workshop, Palo Alto, California, United States, (2024).

4. (*Poster*) **Köster, K.** & Kaghazchi, P. *Ab Initio* Simulations of Layered Oxides for Sodium-Ion Batteries. HITEC (Helmholtz Interdisciplinary Doctoral Training in Energy and Climate Research) Retreat, Enkhuizen, The Netherlands, (2024).

5. (*Poster*) **Köster, K.**, Takeshi Abe & Kaghazchi, P. *Ab Initio* Studies of Sodium-Ion Battery Cathodes and their Interaction with Solid Electrolytes. JSPS (Japanese Society for the Promotion of Science) Summer Program Poster Session, Tokyo, Japan, (2024).

6. (*Oral*) **Köster, K.**, Olivier Guillon & Kaghazchi, P. *Ab Initio* Simulations of Layered Oxide Cathodes: Screening Atomistic Arrangements and Accurate Electronic Structures. ECS (The Electrochemical Society) PRIME (Pacific Rim Meeting), Honolulu, Hawaii, United States, (2024).

7. (*Oral*) **Köster, K.**, Olivier Guillon & Kaghazchi, P. *Ab Initio* Simulations of Sodium-Based Cathode Materials — Efficient Configurational Screening to Discover Novel and Stable Compositions. MRS (Materials Research Society) Spring Meeting and Exhibit, Seattle, Washington, United States, (2025).

8. (*Invited, Poster*) **Köster, K.** & Kaghazchi, P. *Ab Initio* Simulations of Cathode Materials — Efficient Configurational Screening to Discover Novel and Stable Compositions. International Battery Workshop, Berlin, Germany, (2025).

9. (*Oral*) **Köster, K.** & Kaghazchi, P. Configurational Optimizations in Battery Materials: Applications of the GOAC code. Material Development for Batteries (MDB): Material Development for Batteries, Seoul, South-Korea, (2025).

About the Author

Mr. Konstantin Köster was born on 27th of October 1998 in Paderborn, Germany and grew up in Warburg-Scherfede, Germany. He finished high school by obtaining his "Abitur" (German high school degree) in 2017 at Gymnasium Marianum Warburg. Due to his interest in the natural sciences, he was awarded the "Förderpreis der Wirtschaft" (Industry Sponsorship Award) by the Universität Paderborn, Germany. The author continued by studying Business-Chemistry at Christian Albrechts Universität zu Kiel, Germany, while focusing on physical and inorganic chemistry and received his Bachelor's degree in 2020. He wrote his Bachelor's thesis in the group of Prof. Bernd Hartke about the implementation of molecule-fragment databases. For his Bachelor's degree he was awarded a prize for the best degree of the year by the "Gesellschaft Deutscher Chemiker" (GDCh, German Chemical Society), "Ortsverband Kiel" (local association Kiel). Mr. Köster continued studying at the same university in the Master's courses of Chemistry and Business-Chemistry with a focus on theoretical/computational and physical chemistry and wrote his Master's thesis with Prof. Bernd Hartke about classical molecular dynamics simulations of fatty acid layers on water. He obtained his two Master's degrees in 2022 and was honored for the best Master's degree of the year with the Otto-Diels prize awarded by the Professors of Chemistry at Christian Albrechts Universität zu Kiel. In 2023 the author continued his academic journey as a Ph.D. student at Forschungszentrum Jülich GmbH, Germany and at University of Twente, The Netherlands, supervised by Prof. Payam Kaghazchi and Prof. Mark Huijben. In the Ph.D. he proceeded to focus on computational studies of materials while leveraging the world-class supercomputing resources at Forschungszentrum Jülich GmbH and with a special emphasize on battery cathode materials. During his Ph.D. he was able to engage in several other activities beyond the scientific achievements presented before (cf. List of Publications and List of Conference Contributions). These include a scholarship of the Japan Society for the Promotion of Science (JSPS) for a 3-month research stay at Kyoto University, Japan and a HITEC (Helmholtz Interdisciplinary Doctoral Training in Energy and Climate Research) Go funding for a 1-month research stay at National University of Singapore (NUS), Singapore. Furthermore, he competed with the CeraBatt project for the commercialization of solid-state batteries in the Jülich Innovation & Entrepreneurship Certificate Program (JUICE) Innovation Contest and achieved the first place. Moreover, he became the elected Ph.D. representative in the IBLA (Institutsbereichsleitungsausschuss) meetings at the IMD-2 (former IEK-1) institute at Forschungszentrum Jülich GmbH and further organized a retreat conference for 25 Ph.D. students. Finally, he also got the opportunity to supervise a master student project within this Ph.D. thesis.

ACKNOWLEDGEMENTS

This thesis is the result of intensive work and the support of many individuals. I want to express my thanks to everybody who supported me in making this work a success, especially my supervisors, collaborators, and colleagues. I am truly thankful for the valuable help provided, the interesting projects I was allowed to contribute to, the challenges that strengthened and extended my skills, and the many new and nice people that I met and was able to work with.

I want to express my special appreciation to my daily supervisor and promoter, **Prof. Dr. Payam Kaghazchi**. I am very thankful for the excellent supervision, the trust in my work, and the frequent discussions about our research that contributed to the final results presented in this thesis. Furthermore, I am thankful for the encouragement to conduct two research stays during the Ph.D. and for the possibility to present my research at several international conferences — I highly enjoyed these opportunities.

For financial support to these trips, I also want to acknowledge the JSPS (Japan Society for the Promotion of Science) and the HITEC (Helmholtz Interdisciplinary Doctoral Training in Energy and Climate Research) graduate school.

I would like to thank **Prof. Dr. ir. Mark Huijben** for being my supervisor and promoter during my Ph.D. I am truly grateful for our regular scientific discussions, in particular towards the end of my Ph.D., and for the help in overcoming various challenges.

To continue, I would like to express my gratitude to the committee members, **Prof. Dr. Qiong Cai**, **Prof. Dr. Emiel Hensen**, **Prof. Dr. ir. Andre J. E. ten Elshof**, **Prof. Dr. ir. Hans J. W. M. Hilgenkamp**, and **Prof. Dr. Han J. G. E. Gardeniers**, for taking the time to assess this thesis and to participate in the defense.

Moreover, I would like to thank all the (inter-)national collaborators I was allowed to work with during this Ph.D. thesis. It was always a pleasure to work with you, and we were able to succeed in many interesting, yet challenging, works together. In particular, I want to point out **Prof. Dr. Seung-Taek Myung**, **Prof. Dr. Philipp Adelhelm**, and **Dr. Tobias Binninger** as well as their groups for the fruitful, professional, and close collaborations on several novel cathode materials and simulation techniques that were extremely valuable for my work.

Furthermore, I want to recognize my colleagues at Forschungszentrum Jülich GmbH, IMD-2, Team Modeling, for their support. Starting with Dr. **Najma Yaqoob** and **Dima Abubaker** for their help, especially during the beginning of my Ph.D., as well as **Lars**

Winkler and **Sourav Baiju**, as we supported each other throughout the whole time of this thesis. Moreover, I want to thank **Milica Zdravković**, **Severin Kuffer**, **Bibin Jose**, **Tan Le-Dinh**, Dr. **Dijana Milosavljević** and the other group members for the numerous nice, not only scientific, discussions, the fruitful collaborations, and the good working atmosphere. Our great team spirit made me enjoy my Ph.D. journey and helped me to finalize this thesis.

Last but certainly not least, I would like to point out my deep gratitude for the support of my family, especially my parents, **Elke Hillebrand-Köster** and **Hubertus Köster**, throughout this Ph.D., but also during my entire life before. Their belief in my capabilities constantly encouraged me throughout my academic journey and their patience, advice, and practical support were of invaluable help to accomplish this thesis.

Thank You All!

Band / Volume 687
Entwicklung von Beschichtungsverfahren für die Herstellung von Wärmedämmschichten auf additiv gefertigten Komponenten
M. Rüßmann (2026), ix, 188 pp
ISBN: 978-3-95806-877-3

Band / Volume 688
Model Perovskite Oxide Electrocatalysts for the Oxygen Evolution Reaction and their Material Sustainability Evaluation
L. Heymann (2026), vi, 174 pp
ISBN: 978-3-95806-878-0

Band / Volume 689
Development of an oxygen ion conducting solid oxide electrolysis cell based on gadolinium-doped cerium oxide as fuel electrode and electrolyte material
D. Ramler (2026), ix, 162 pp
ISBN: 978-3-95806-879-7

Band / Volume 690
Design of Local Multi-Energy Systems: Impact of Coupled Energy Vector Integration and Grid Service Participation
P. S. Glücker (2026), xxviii, 145 pp
ISBN: 978-3-95806-880-3

Band / Volume 691
A Parallel-in-Space Simulator for Accelerating Power System Simulation on Graphics Processing Units
J. Zhang (2026), 112 pp
ISBN: 978-3-95806-882-7

Band / Volume 692
Entwicklung von Reparaturmethoden für einkristalline Bauteile mittels thermischer Spritzverfahren
M. L. Létang (2026), X, 211 pp
ISBN: 978-3-95806-883-4

Band / Volume 693
Assessing the Environmental Implications of Offshore Wind Energy Advancements on the Future German Electricity Sector
A. Benitez (2026), xi, 176 pp
ISBN: 978-3-95806-885-8

Band / Volume 694
Entwicklung von Korrosionsschutzschichten für Protonen-Austausch-Membran-Wasserelektrolyseure
T. Sievert (2026), 201 pp
ISBN: 978-3-95806-888-9

Band / Volume 695
Hierarchical Modeling of Electrocatalytic Reactions from a Local Perspective
X. Zhu (2026), ix, 121 pp
ISBN: 978-3-95806-889-6

Band / Volume 696
Nanocrystalline Silicon Carbide in Transparent Passivating Contact Solar Cells
A. Eberst (2026), xiii, 225 pp
ISBN: 978-3-95806-891-9

Band / Volume 697
Theory of Electronic and Ionic Perturbations at Supported Electrocatalyst Nanoparticles
Y. Zhang (2026), XI, 131 pp
ISBN: 978-3-95806-896-4

Band / Volume 698
Aufbau und Einsatz eines on-board Messsystems zur Untersuchung der Abgaszusammensetzung von Fahrzeugen betrieben mit konventionellen und alternativen Kraftstoffen
V. Polinowski (2026), VIII, 269 pp
ISBN: 978-3-95806-897-1

Band / Volume 699
***Ab Initio*-based large-scale Atomistic Simulations of Cathode Materials for Secondary Batteries: From Computational Methodologies to Applications towards improved Structural and Chemical Stability**
K. Köster (2026), x, 204, x pp
ISBN: 978-3-95806-898-8

Weitere ***Schriften des Verlags im Forschungszentrum Jülich*** unter
http://wwwzb1.fz-juelich.de/verlagextern1/index.asp

Energie & Umwelt / Energy & Environment
Band / Volume 699
ISBN 978-3-95806-898-8

Mitglied der Helmholtz-Gemeinschaft

JÜLICH
Forschungszentrum